

**Lowest Q^2 Measurement of the $\gamma^*p \rightarrow \Delta$ Reaction:
Probing the Pionic Contribution**

by

Sean C. Stave

B.S. Physics

University of Kentucky, 1999

Submitted to the Department of Physics
in partial fulfillment of the requirements for the degree of

Doctor of Philosophy in Physics

at the

MASSACHUSETTS INSTITUTE OF TECHNOLOGY

June 2006

© Massachusetts Institute of Technology 2006. All rights reserved.

Signature of Author
Department of Physics
May 5, 2006

Certified by
Aron Bernstein
Professor of Physics
Thesis Supervisor

Accepted by
Thomas J. Greytak
Professor, Associate Department Head for Education

Lowest Q^2 Measurement of the $\gamma^*p \rightarrow \Delta$ Reaction: Probing the Pionic Contribution

by

Sean C. Stave

Submitted to the Department of Physics
on May 5, 2006, in partial fulfillment of the
requirements for the degree of
Doctor of Philosophy in Physics

Abstract

The first excited state of the proton, the Delta, can be reached through a magnetic dipole spin flip of one of the quarks (M1) or through electric and Coulomb quadrupole terms (E2 and C2) which indicate a deviation from spherical symmetry. The quark models using the color hyperfine interaction underestimate the size of the quadrupole terms by more than an order of magnitude. Models using the pion cloud do a much better job of describing the data. This is expected due to the spontaneous breaking of chiral symmetry which leads to a cloud of virtual p wave pions which introduce the non-spherical amplitudes. The data presented in this work fill gaps in the low Q^2 , long distance region where the pion cloud is expected to dominate and to produce significant Q^2 variation.

The $p(\vec{e}, e'p)\pi^0$ reaction was measured in the Δ region at $Q^2 = 0.060$ (GeV/c)², the lowest Q^2 to date for pion electroproduction, utilizing out-of-plane magnetic spectrometers at the Mainz Microtron in Germany. This work reports results for the dominant transition magnetic dipole amplitude and the quadrupole to dipole ratios obtained from fitting the new data with models using a three parameter, resonant multipole fit: $M_{1+}^{3/2} = (40.33 \pm 0.63_{\text{stat+syst}} \pm 0.61_{\text{model}}) (10^{-3}/m_{\pi^+})$, $E2/M1 = \text{Re}(E_{1+}^{3/2}/M_{1+}^{3/2}) = (-2.28 \pm 0.29_{\text{stat+syst}} \pm 0.20_{\text{model}})\%$, and $C2/M1 = \text{Re}(S_{1+}^{3/2}/M_{1+}^{3/2}) = (-4.81 \pm 0.27_{\text{stat+syst}} \pm 0.26_{\text{model}})\%$. These new results for the transition multipoles disagree with predictions of the quark models but are in reasonable agreement with a chiral extrapolation of lattice QCD, chiral effective field theory and dynamical model results confirming the dominance and general Q^2 variation of the long range pionic contribution. While there is qualitative agreement with the models, there is no quantitative agreement thus indicating the need for further improvement of the models.

Thesis Supervisor: Aron Bernstein
Title: Professor of Physics

“Science is a way of trying not to fool yourself. The first principle is that you must not fool yourself, and you are the easiest person to fool.”

Richard Feynman

Contents

1	Introduction	21
2	Theory	25
2.1	Kinematics	25
2.2	Cross Section Formalism	28
2.3	Multipoles	31
2.4	The Δ Resonance	34
2.5	Scattering formalism	36
2.5.1	The S matrix	36
2.5.2	The Fermi-Watson Theorem	37
2.6	Chiral Perturbation Theory	38
2.7	Models	42
2.7.1	Mainz Unitary Model 2003	42
2.7.2	Sato-Lee	46
2.7.3	Dubna-Mainz-Taipei	47
2.7.4	SAID	48
3	Experimental Setup	51
3.1	Electron Beam	51
3.1.1	Mainz Microtron	51
3.1.2	Polarized beam	52
3.1.3	Beam position	54
3.1.4	Current monitoring	55

3.2	Hydrogen target and beam rasterization	56
3.3	Spectrometers	56
3.3.1	Collimators	59
3.3.2	Magnets	60
3.3.3	Detectors	61
3.4	Electronics	65
4	Experiment Overview	69
4.1	Low Q^2 (GeV/c) ² Measurements	73
4.1.1	$Q^2 = 0.060$ (GeV/c) ²	73
4.1.2	W scan	74
4.1.3	Background terms	75
4.2	$Q^2 = 0.127$ (GeV/c) ² Measurements	76
4.3	Elastic Cross Section	76
5	Cross Section Analysis Procedure	79
5.1	Software	79
5.1.1	COLA++	79
5.1.2	Simul++	79
5.1.3	Lumi++	82
5.1.4	ROOT	83
5.2	Detector Calibration	84
5.3	Cross Section Extraction	84
5.3.1	Timing	84
5.3.2	Particle ID and Missing Mass	86
5.3.3	Background subtraction	91
5.3.4	Luminosity	94
5.3.5	Dead time	100
5.3.6	Detector/trigger/chamber efficiencies and checks	101
5.3.7	Phase space overlap	103
5.3.8	Definition of cuts	105

5.3.9	Cross section extraction and collapse to point	110
5.3.10	Cut Robustness and Corrections	113
5.3.11	Radiative Corrections and Energy Loss	121
5.3.12	Energy Loss	123
5.4	Cross checks	124
5.4.1	Coincidences	124
5.4.2	Single Arm	133
5.4.3	δ scan	136
5.4.4	Parallel cross section	136
5.4.5	More Bates Overlap	139
5.5	Systematic Errors	142
6	Results	147
6.1	$Q^2 = 0.060 \text{ (GeV/c)}^2$ data	147
6.2	$Q^2 = 0.127 \text{ (GeV/c)}^2$ data	152
7	Interpretation and Discussion	155
7.1	Models and Fitting	155
7.1.1	Comparison with Models	155
7.1.2	$Q^2 = 0.060 \text{ (GeV/c)}^2$ fits	160
7.2	Background Amplitude Test	168
7.2.1	$Q^2 = 0.060 \text{ (GeV/c)}^2$	168
7.2.2	$Q^2 = 0.127 \text{ (GeV/c)}^2$	177
8	Summary and Conclusion	181
A	Fitting formalism	185
B	Correlations	189
B.1	Curvature Matrix and Eigenvectors	189
B.1.1	Correlation angle from curvature matrix	189
B.1.2	Correlation angle from eigenvectors	192

B.1.3	Errors	194
B.2	Correlation Coefficient	195
B.2.1	Definition	195
B.2.2	Interpretation of r	197
C	Kinematics Summary	199
C.1	April 2003 Central Kinematics Summary	199
C.1.1	$Q^2 = 0.060$ (GeV/c) ² Kinematics Details	200
C.1.2	Central Kinematics for $Q^2 = 0.127$ (GeV/c) ²	201
C.2	October 2003 Central Kinematics Summary	204
C.2.1	$Q^2 = 0.060$ (GeV/c) ² Kinematic Details	205
C.2.2	$Q^2 = 0.126$ (GeV/c) ² Kinematic Details	206
D	Cut Details	207
D.1	Central Cut Values	207
D.2	Cut Widths	209
E	Mainz $\gamma^*N \rightarrow \Delta$ Collaboration	211

List of Figures

1-1	Plot of Sato-Lee M_{1+} , E_{1+} , S_{1+} vs Q^2	22
1-2	Plot of existing data in the low Q^2 region along with models	23
2-1	The four-vectors and their relations in the one photon exchange for pion electroproduction.	26
2-2	Electron arm kinematics and the virtual photon using the one photon exchange approximation.	27
2-3	Various planes and angles required for defining the $\vec{e}(e', p)\pi^0$ reaction.	29
2-4	Pascalutsa and Vanderhaeghen CPT results for $\gamma^*p \rightarrow \pi^0p$ at $W=1232$ MeV, $Q^2 = 0.127$ (GeV/c) ²	40
2-5	Pascalutsa and Vanderhaeghen calculation of the m_π dependence of the EMR and CMR	41
2-6	Born terms used in the MAID model.	45
2-7	Meson exchange terms used in the MAID model.	45
2-8	Pion loop diagrams included in the Sato-Lee model	48
3-1	Schematic view of one of the three racetrack microtron stages of the Mainz Microtron	52
3-2	Overview of the Mainz facility showing the MAMI accelerator and the experimental halls	53
3-3	Example of the typical centered, rastered beam on the BeO target	54
3-4	Example of the typical off-center, rastered beam on the BeO target	55
3-5	Diagram of the hydrogen cryo-target used in the experiment	57
3-6	Schematic view of the cryo target seen from above and from the side	58

3-7	The central optics for Spectrometer A and Spectrometer B	61
3-8	Drawing of the Spectrometer A detector systems	62
3-9	Logic diagram for Spectrometer A	67
3-10	Coincidence logic diagram	68
4-1	Overview of the accessible regions of the phase space	70
4-2	Cross section errors versus Q^2	71
4-3	Schematic view of the various locations the spectrometers are placed .	73
5-1	Comparison of the data and the simulation weighted by MAID2003 .	81
5-2	Comparison of the data and the simulation weighted by MAID2003 for more variables	82
5-3	Raw timing spectrum	85
5-4	Software corrected coincidence timing spectrum	86
5-5	Plot of missing mass vs. coincidence timing	87
5-6	Plot of missing mass vs. coincidence timing with Cherenkov cut . . .	88
5-7	Plot of the missing mass for data and simulation for setup Q06-t36-p3	90
5-8	Missing mass vs. coincidence timing	91
5-9	Coincidence timing peak after π^-/μ^- background subtraction	93
5-10	Diagram of the off-axis, rastered beam and the target shape	95
5-11	Target density plotted against temperature for two pressures	96
5-12	Plot of the singles rate in spectrometer A divided by the beam current for all the $Q^2 = 0.060 \text{ (GeV/c)}^2$ runs in the April beam time period .	97
5-13	Plot of the singles rate in spectrometer A divided by the beam current for all the $Q^2 = 0.127 \text{ (GeV/c)}^2$ runs in the April beam time period .	99
5-14	Single wire efficiency histogram for the x1 layer of Spectrometer A from setting Q06-t24-p1	102
5-15	Log-log plot of counts versus $\log \Delta x$ for Spectrometer A	103
5-16	Plot of the overlap of the sequential settings for $Q^2 = 0.060 \text{ (GeV/c)}^2, W =$ $1221 \text{ MeV}, \theta_{pq}^* = 24^\circ$	104

5-17	Plot of the overlap of the sequential settings for $Q^2 = 0.060 \text{ (GeV/c)}^2$, $W = 1221 \text{ MeV}$, $\theta_{pq}^* = 37^\circ$	105
5-18	Comparison of the missing mass for data and simulation for the $Q^2 = 0.127 \text{ (GeV/c)}^2$ parallel cross section at $W = 1232 \text{ MeV}$	106
5-19	Comparison of data and simulation weighted by the Sato-Lee cross section for Q127-q spectrometer acceptance variables.	107
5-20	Physics variables for setup Q06-t24-p1 with cuts	109
5-21	Cross sections as a function of cut width for the setup Q06-t24-p1 with 75% shoulder cuts	115
5-22	Summary of the cut scan study	116
5-23	$Q^2 = 0.060 \text{ (GeV/c)}^2$, non-parallel, more forward settings cut scans .	117
5-24	Scan of the cuts for the settings Q06-t24-p3 and Q06-t36-p3	117
5-25	Scan of the cuts for the parallel cross section near the Δ resonance at $Q^2 = 0.060$ and 0.127 (GeV/c)^2	118
5-26	Helicity dependent cross section results for $Q^2 = 0.060$ and 0.127 (GeV/c)^2 . See Fig. 5-23 for legend.	118
5-27	Scan for the $Q^2 = 0.127 \text{ (GeV/c)}^2$, $\theta_{pq}^* = 63^\circ$ setting. See Fig. 5-23 for legend.	119
5-28	Diagrams containing the self-energy terms, the vertex correction, and the vacuum polarization	122
5-29	Diagrams showing the soft, real, Bremsstrahlung photon being emitted.	122
5-30	The effect of tightening VDC wires in plots of counts versus θ_e . .	125
5-31	Plot of counts versus θ_e for a parallel cross section, pion production run at $Q^2 = 0.126 \text{ GeV}^2/\text{c}^2$, $W = 1232 \text{ MeV}$	126
5-32	April 2003 elastic coincidence cross section in nb plotted against θ_e along with the acceptance averaged dispersion analysis fit	127
5-33	More April 2003 elastic coincidence cross section in nb plotted against θ_e along with the acceptance averaged dispersion analysis fit	129
5-34	October 2003 elastic coincidence cross section in nb plotted against θ_e along with the acceptance averaged dispersion analysis fit	130

5-35	Plot of hits versus the horizontal and vertical coordinates in the focal plane	131
5-36	Comparison of ratio of the elastic cross section to the Dispersion 96 prediction	131
5-37	Comparison of elastic form factor fits at $E=855$ MeV	132
5-38	April 2003 elastic single results plotted against the dispersion analysis	133
5-39	October 2003 elastic single results plotted against the dispersion analysis	134
5-40	Example of the two data streams for the single arm analysis of Q126_elas_2	135
5-41	Comparison of the parallel cross section from previous experiments and from the current experiment	139
5-42	Comparison of the Bates and Mainz $\sigma_{LT'}$ results at $W = 1221$ MeV, $Q^2 = 0.127$ (GeV/c) ² and the predictions from several models	141
5-43	Comparison of the elastic kinematic relations for the data and the simulation for the proton momentum P'	145
7-1	The new data at $W = 1221$ MeV, $Q^2 = 0.060$ (GeV/c) ² , $\theta_{pq}^* = 24^\circ$ plotted plotted versus ϕ_{pq}^* with the model predictions and fitted models	157
7-2	The new data at $W = 1221$ MeV, $Q^2 = 0.060$ (GeV/c) ² , $\theta_{pq}^* = 37^\circ$ plotted versus ϕ_{pq}^* with the model predictions and fitted models . . .	158
7-3	Summary of the new Mainz data at $Q^2 = 0.060$ (GeV/c) ² plotted with the model predictions and with fitted models	159
7-4	Example of convergence of the EMR and CMR with fitting	162
7-5	Results extracted with fit for $Q^2 = 0.060$ (GeV/c) ² at $W = 1232$ MeV compared with other data in the low Q^2 range and the same models as in Fig. 7-3	164
7-6	Comparison of multipoles for DMT model	166
7-7	Comparison of multipoles versus $\theta_{\pi q}^*$	167
7-8	Plot of spectrometer cross sections for $W = 1155$ MeV, $Q^2 = 0.060$ (GeV/c) ² with models and fitted models	169
7-9	Comparison of background multipoles for four models	170

7-10	Extracted M_{1+} , EMR and CMR for various fits using MAID 2003 . .	173
7-11	Summary of the new Mainz data at $Q^2 = 0.060 \text{ (GeV/c)}^2$ plotted with one of the best four parameter fits	174
7-12	Plot of spectrometer cross sections for $W = 1140 \text{ MeV}$, $Q^2 = 0.127$ (GeV/c)^2	177
7-13	Plot of $\sigma_{LT'}$ versus θ_{pq}^* for $W = 1140 \text{ MeV}$, $Q^2 = 0.127 \text{ (GeV/c)}^2$. .	178
B-1	$\Delta\chi^2=1.0$ curve for two parameters that are uncorrelated in x' space. .	190
B-2	$\Delta\chi^2=1.0$ curve for two parameters that are correlated in x space. . .	190
B-3	Plot of E_{1+} vs. M_{1-} fit parameters for data	195
B-4	Plot of E_{1+} vs. E_{0+} fit parameters for data	196

List of Tables

3.1	Ranges, limits, and resolutions for the A1 spectrometers	59
4.1	Primary kinematic settings for low Q^2 measurement	74
4.2	Kinematic settings for the $Q^2 = 0.060(\text{GeV}/c)^2$ W scan	75
4.3	Kinematic settings for the $Q^2 = 0.060(\text{GeV}/c)^2$ background test . . .	75
4.4	Kinematic settings for the $Q^2 = 0.127(\text{GeV}/c)^2$ settings which overlap with Bates	76
4.5	Kinematic settings for extending the Bates $Q^2 = 0.127(\text{GeV}/c)^2$ database	77
5.1	Comparison of the central missing mass values from the data and the simulation	89
5.2	Comparison of the values for the Full Width Half Maximum (FWHM) from the various setups.	89
5.3	Size of the different background subtractions	93
5.4	Average singles rates divided by average beam current which is pro- portional to counts per charge	97
5.5	Parallel cross section results for $Q^2 = 0.127 (\text{GeV}/c)^2$ as a function of beam current.	99
5.6	Settings which require the luminosity correction	99
5.7	Acceptance cut comparison.	107
5.8	Collapse factors using MAID2003 for the various settings	111
5.9	Cut correction factors and the settings used to calculate them.	120
5.10	Averaged elastic coincidence results	128
5.11	Selected averaged elastic single arm results for spectrometer A	135

5.12	Cross sections used to account for the different factors of ϵ in the existing data.	137
5.13	Comparison of the parallel cross section from previous experiments and from the current experiment.	138
5.14	Comparison of the Bates and Mainz $A_{0\pi}$ at $W = 1232$ MeV, $Q^2 = 0.126$ (GeV/c) ² and $\theta_{pq}^* = 28^\circ$	140
5.15	Comparison of the Bates and Mainz σ_{LT} at $W = 1232$ MeV, $Q^2 = 0.126$ (GeV/c) ² and $\theta_{pq}^* = 28^\circ$	140
5.16	Comparison of the Bates and Mainz $\sigma(\theta_{pq}^* = 0)$ at $W = 1212$ MeV and $Q^2 = 0.126$ (GeV/c) ²	140
5.17	Fit comparison at $Q^2 = 0.126$ (GeV/c) ² for Bates and Mainz	142
5.18	Model dependence of cross sections.	144
5.19	Summary of systematic errors.	146
6.1	$Q^2 = 0.060$ (GeV/c) ² cross sections	149
6.2	Correction factors for $Q^2 = 0.060$ (GeV/c) ² data	150
6.3	Systematic error summary for low Q^2	151
6.4	Summary of the extracted values for σ_0 , σ_{TT} , σ_{LT} , and $\sigma_{LT'}$ at $Q^2 = 0.060$ (GeV/c) ²	151
6.5	$Q^2 = 0.127$ (GeV/c) ² spectrometer cross sections	152
6.6	Correction factors for the $Q^2 = 0.127$ (GeV/c) ² data	153
6.7	Systematic error summary for $Q^2 = 0.127$ (GeV/c) ²	153
6.8	Summary of the extracted values for σ_0 , σ_{LT} , and $\sigma_{LT'}$ at $Q^2 = 0.127$ (GeV/c) ²	153
7.1	Values of EMR, CMR, and M_{1+} for the EFT predictions and fitted models	161
7.2	Background amplitudes from four models contributing the most to the $Q^2 = 0.060$ (GeV/c) ² data	171
7.3	Significant background amplitudes in the $Q^2 = 0.060$ (GeV/c) ² data	172

7.4	Results of a test of the sensitivity of the background to the new Mainz data.	179
7.5	Comparison of the EMR and CMR for the fits at $Q^2 = 0.127 \text{ (GeV/c)}^2$	179

Chapter 1

Introduction

Non-spherical components in the proton and its first excited state, the Δ , have been studied through experiments and theory in recent years [31]. All of the intermediate energy electromagnetic facilities have used photo- and electropion production to investigate the Δ resonance region. There is currently strong experimental evidence that the nucleon and Δ contain non-spherical components but neither the magnitude nor the physical mechanism for this are fully understood.

In the quark model, the deviations from spherical symmetry of the nucleon and Δ are caused by the non-central, tensor interaction between quarks [39, 43, 22, 23]. However, the magnitudes of this effect for the predicted $E2$ [22] and $C2$ [23] quadrupole amplitudes are at least an order of magnitude too small to explain the experimental results and even the dominant $M1$ matrix element is $\simeq 30\%$ low [22].

The quark model predictions are low because they do not respect chiral symmetry (see Sec. 2.6), whose spontaneous breaking leads to a large pion cloud effect in the p wave (which is not spherically symmetric), as has been recently discussed [14]. The pion cloud and its non-spherical components are then expected to dominate the quadrupole ($E2$ and $C2$) transition matrix elements in the low Q^2 (large distance) domain.

The domination of the pion cloud is demonstrated in the model calculation of Sato and Lee [67]. There, the pion cloud plays a large role in the size of the $E2$ and $C2$ matrix elements. As expected, these matrix elements are particularly strong at low

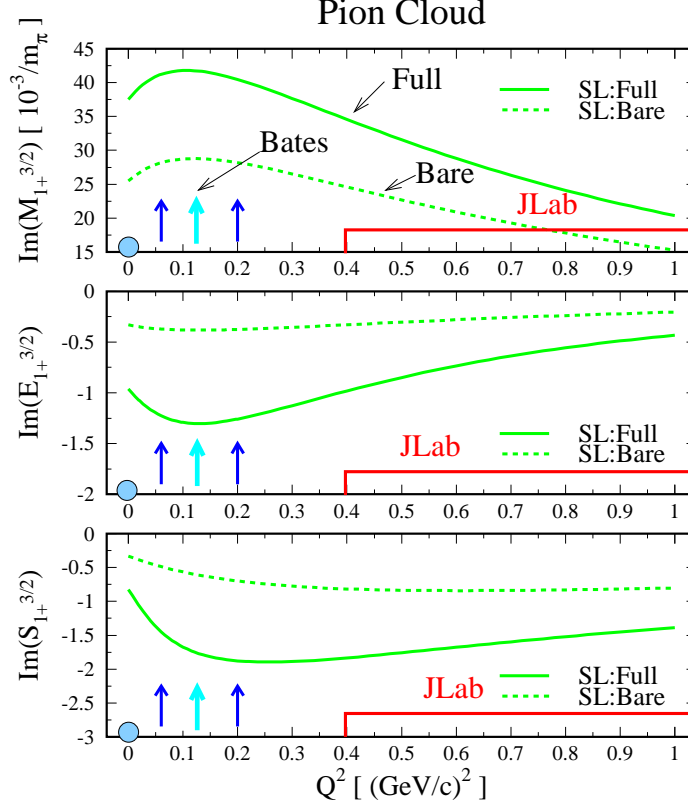


Figure 1-1: Sato-Lee M_{1+} , E_{1+} , S_{1+} [67] vs Q^2 plot where the pion cloud effect is visible. The central arrow is where the extensive $Q^2 = 0.127$ (GeV/c) 2 database is located. The leftmost Q^2 arrow is at $Q^2 = 0.060$ (GeV/c) 2 and is where the data for this work were measured. The rightmost arrow is at $Q^2 = 0.200$ (GeV/c) 2 which are data that were taken but are being analyzed by our collaborators. The circle represents the photon point.

Q^2 and peak near $Q^2 = 0.15$ (GeV/c) 2 . Figure 1-1 shows the calculation of Sato and Lee for the magnetic dipole and the two quadrupole terms both with and without the pion cloud. The pion cloud effect is a maximum in a region where there is a scarcity of data.

Recent electropion production experiments in the low Q^2 region have been carried out at Bates [81, 55, 80, 49, 48, 74] and Mainz [63, 12] and include measurements of the unpolarized and fifth structure functions. Experiments in the Q^2 range from 0.4 to 4.0 (GeV/c) 2 have been performed at Bonn [40] and JLab [45, 37]. In addition, measurements of the $E2$ amplitude from photopion reaction experiments with polarized photons have been reported [13, 16]. However, there is a gap in the Q^2

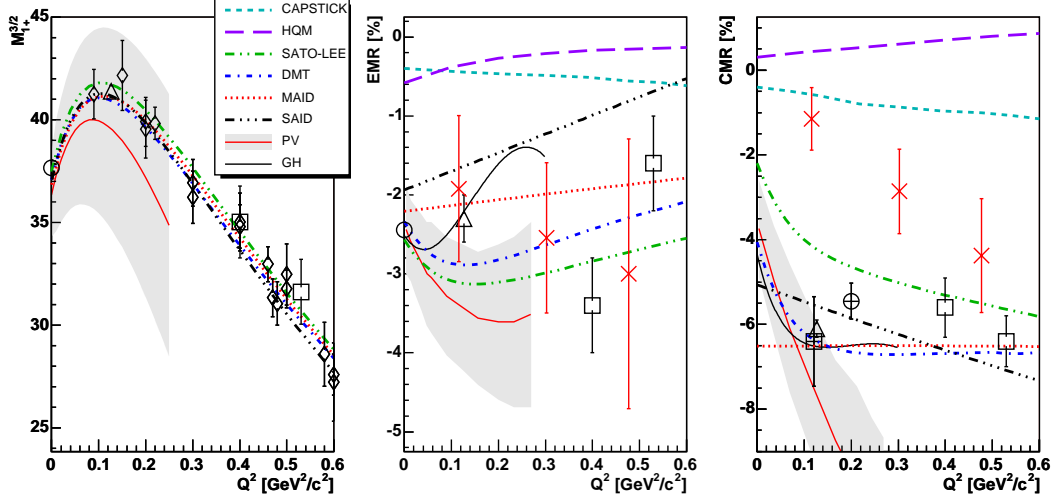


Figure 1-2: Plot of existing data versus Q^2 at $W = 1232$ MeV for M_{1+} (in units of $10^{-3}/m_{\pi}^+$), EMR and CMR compared with other data in the low Q^2 range and representative models. The SAID model is plotted at their fitted resonance position of $W = 1227.3$ MeV [3]. The other data are the photon point \bigcirc [13], CLAS \square [45], Bates \triangle [74], Elsner \oplus [33], M_{1+} inclusive \diamond [8], and Pospischil \boxplus [63]. Recent lattice QCD calculations are shown \times [2] as well as recent chiral effective field theory calculations from Pascalutsa and Vanderhaeghen (PV) [60] and Gail and Hemmert (GH) [38]. The GH prediction for $M_{1+}^{3/2}$ is very close to the MAID2003 results up to $Q^2 \approx 0.2$ (GeV/c) 2 and so has been suppressed. The HQM [25] and Capstick [22] quark models have been included to emphasize that those models do not agree with the data.

coverage between the photon point at $Q^2 = 0$ and the JLab data starting at $Q^2 = 0.4$ (GeV/c) 2 , with the exception of the $Q^2 = 0.127$ (GeV/c) 2 data from Bates and Mainz. It is this experimental gap that is partially filled in by these new measurements. For details, see Figure 1-2 which shows exactly where the data are and also shows the predictions from several models.

The goal of this experiment is to determine the Q^2 dependence of the multipoles in the region where the pion cloud is expected to dominate. There is an extensive database at $Q^2 = 0.127$ (GeV/c) 2 near where the pion cloud effect is expected to be a maximum, but there are few data below that point until the photon point. Furthermore, new chiral perturbation theory (CPT) results are available in this low Q^2 region [38, 60] where these calculations should be most accurate. There are also lattice QCD results available [2] and low Q^2 data provide an excellent test of the

linear extrapolation to the physical pion mass (see Chap. 2.6).

The deviation from spherical symmetry is measured by examining the electric and Coulomb quadrupole amplitudes ($E2$, $C2$) in the predominantly $M1$ (magnetic dipole-quark spin flip) $\gamma^* N \rightarrow \Delta$ ($1/2 \rightarrow 3/2$) transition. The $E2/M1$ and $C2/M1$ ratios are small (typically $\simeq -2$ to -8% at low Q^2) making their measurement difficult. In addition, the non-resonant (background) and resonant quadrupole amplitudes are of the same order of magnitude in this region. Therefore, experiments must be designed to separate the resonant and non-resonant components with precision.

An experiment was carried out at the Mainz Microtron to measure the helicity dependent and independent cross sections at $Q^2 = 0.060$ (GeV/c)², the lowest practical value at the facility. This value of Q^2 is also the lowest value probed to date in electroproduction. The cross sections were measured over as wide a kinematic region as was possible to maximize the sensitivity to the quadrupole terms.

In addition, data were taken at both $Q^2 = 0.060$ and 0.127 (GeV/c)² in order to constrain the background amplitudes. A complete experiment with target and recoil polarization would allow the determination of all of the multipoles. However, since that would require more time than is practical, models provide the background amplitudes while the resonant amplitudes are fit to the data. The models derive their background amplitudes in different ways which leads to differences in the model predictions. Fortunately, the effect of different backgrounds is fairly small in the resonance region. However at lower W , away from the higher resonances, the backgrounds become more important.

In summary, these new pion electroproduction data at the lowest Q^2 to date help to constrain the model backgrounds and determine the Q^2 dependence of the resonant multipoles in the region where the pion cloud is expected to dominate.

Chapter 2

Theory

2.1 Kinematics

The kinematics for the pion electroproduction reaction $p(\vec{e}, e'p)\pi^0$ can be described using six energy-momentum four-vectors:

- Incident electron: $k_i = (E_i, \vec{k}_i)$
- Scattered electron: $k' = (E', \vec{k}')$
- Target nucleus: $p_T = (E_T, \vec{p}_T)$
- Detected proton: $p_f = (E_f, \vec{p}_f)$
- Undetected pion: $p_\pi = (E_\pi, \vec{p}_\pi)$
- Virtual photon: $q = (\omega, \vec{q})$

Figure 2-1 shows the relations between the four vectors.

In a pion electroproduction coincidence experiment, k_i, k', p_T , and p_f are all known or measured. Four-momentum conservation leads to the following definitions.

$$k_i - k' = (E_i, \vec{k}_i) - (E', \vec{k}') = q = (\omega, \vec{q}) \quad (2.1)$$

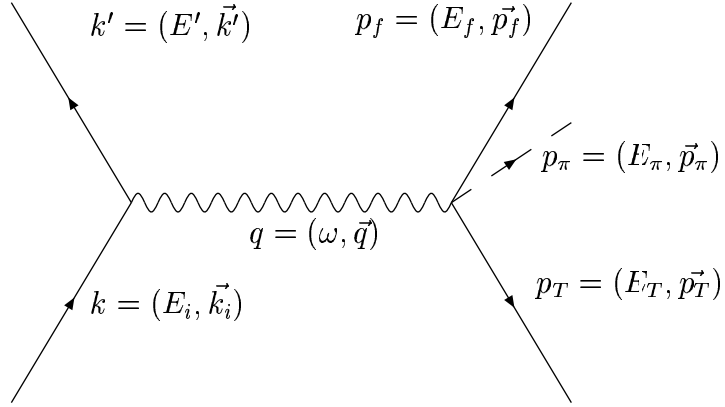


Figure 2-1: The four-vectors and their relations in the one photon exchange for pion electroproduction.

The variables ω and \vec{q} are then defined as

$$\omega = E - E' \quad (2.2)$$

and

$$\vec{q} = \vec{k}_i - \vec{k}'. \quad (2.3)$$

Therefore,

$$-Q^2 \equiv q^2 = \omega^2 - \vec{q}^2 \leq 0. \quad (2.4)$$

At the energies of this experiment, the electrons are ultra-relativistic and so $E_i \approx |\vec{k}_i|$ and $E' \approx |\vec{k}'|$. A useful equation for the four-momentum transfer squared is then

$$Q^2 = 4E_i E' \sin^2 \frac{\theta_e}{2}. \quad (2.5)$$

Figure 2-2 shows the electron arm and the relations between the kinematic variables and the lab angles. In addition, the virtual photon is shown.

Since the initial and final electron four-momenta and the initial and final proton four-momenta are all known, the undetected pion four-momentum can be derived.

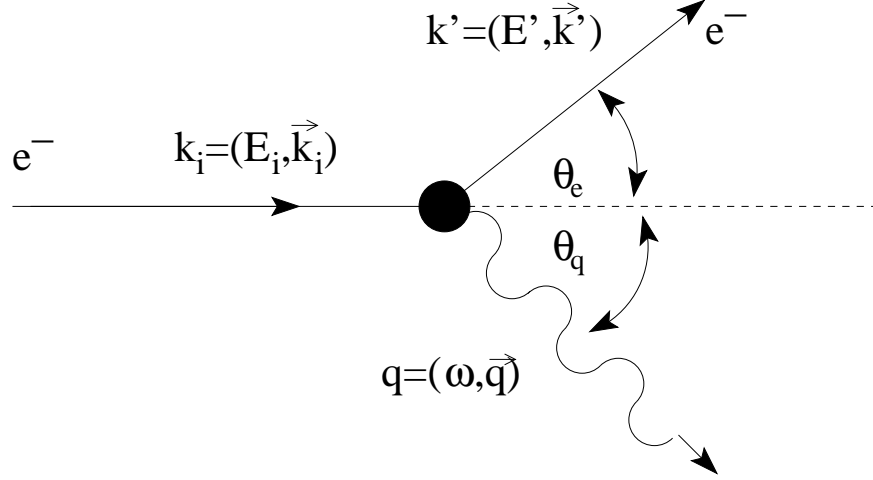


Figure 2-2: Electron arm kinematics and the virtual photon using the one photon exchange approximation.

Using four-momentum conservation,

$$q + p_T = p_\pi + p_p. \quad (2.6)$$

Another useful quantity is the center of mass energy W which can be derived from

$$W^2 = (q + p_T)^2 = -Q^2 + m_p^2 + 2\omega m_p. \quad (2.7)$$

Using Eq. 2.6 again

$$p_\pi = q + p_T - p_p. \quad (2.8)$$

Substituting in the values for the energies and momenta and conserving both independently gives:

$$E_\pi = \omega + m_p - E_p \quad (2.9)$$

and

$$\vec{p}_\pi = \vec{q} - \vec{p}_p. \quad (2.10)$$

The missing mass of the pion can then be calculated using

$$m_\pi = \sqrt{E_\pi^2 - \vec{p}_\pi^2}. \quad (2.11)$$

As will be shown in Sec. 2.2, the cross section depends upon certain specific variables. The scattered electron angle is represented through the W and Q^2 variables. The other derived relations up to now have not relied upon angles. Figure 2-3 shows the various planes and angles required for defining the pion electroproduction reaction.

The electron scattering plane is defined by the incoming and outgoing electron, $\vec{k}_i \times \vec{k}'$. It is measured from the floor plane by ϕ_e . ϕ_e does not play a role in the cross section physics but is critical for determining where the particles are in the lab frame and, hence, the detectors. The lab electron scattering angle θ_e has been shown before and is included here for completeness. θ_q is the angle from the initial electron to the momentum transfer vector \vec{q} . The pion center of mass polar angle θ_π^* is defined from the \vec{q} vector. The scattering pion and the \vec{q} vector define a plane called the reaction plane, $\vec{q} \times \vec{p}_\pi$. The pion center of mass azimuthal angle is defined as the angle between the scattering plane and the reaction plane. The other commonly used angles are the center of mass angles for the proton θ_p^* and ϕ_p^* . Since the proton and pion are both in the same center of mass frame, the angles are related as $\theta_p^* = \pi - \theta_\pi^*$ and $\phi_p^* = \phi_\pi^* + \pi$. The proton angles are only used for comparison with the experiment since the proton is the particle that is detected. The physics is always defined from the pion angle. In addition, θ_π^* and ϕ_π^* are also commonly written with an explicit reference to the q -vector, $\theta_{\pi q}^*$ and $\phi_{\pi q}^*$, as are the proton angles, θ_{pq}^* and ϕ_{pq}^* .

2.2 Cross Section Formalism

This section shows the formalism involved for the exclusive pion electroproduction cross section for the reaction $\vec{e}(e', N)\pi$ or $\vec{e}(e', \pi)N$.

The electron serves as a good probe of nucleons because the quantum electrodynamic interaction is very well understood. Since the size of the electromagnetic coupling constant $\alpha \equiv e^2/\hbar c \approx 1/137.036$ is small, the first order calculation can be used with a small error. The single photon exchange approximation is used throughout this thesis along with the plane-wave Born approximation (PWBA). The PWBA assumes plane wave incoming particles and spherical wave outgoing particles [79].

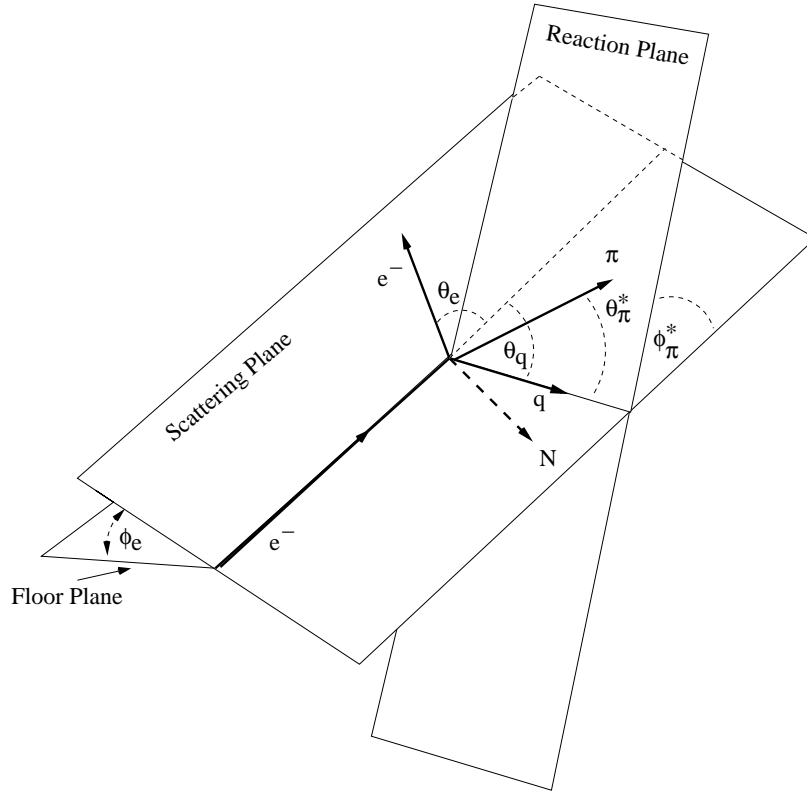


Figure 2-3: Various planes and angles required for defining the $\vec{e}(e', p)\pi^0$ reaction.

Since the electron arm is well known, all of the unknown terms are placed in the hadronic part. Using current conservation and symmetry properties, the contraction of the electron and nucleon tensors gives a cross section [27, 65]. While in the general case there are four combinations with and without initial and final polarization leading to 36 different cross sections, this experiment was performed with polarized initial electrons only leading to five cross sections. Using the convention of [29], the cross section can be written as

$$\begin{aligned} \frac{d^5\sigma}{d\Omega_f dE_f d\Omega} = & \Gamma \left(\frac{d\sigma_T}{d\Omega_\pi} + \epsilon \frac{d\sigma_L}{d\Omega_\pi} + v_{LT} \frac{d\sigma_{LT}}{d\Omega_\pi} \cos \phi_{\pi q}^* \right. \\ & \left. + \epsilon \frac{d\sigma_{TT}}{d\Omega_\pi} \cos 2\phi_{\pi q}^* + h v_{LT'} \frac{d\sigma_{LT'}}{d\Omega_\pi} \sin \phi_{\pi q}^* \right) \end{aligned} \quad (2.12)$$

where $\phi_{\pi q}^*$ is the pion center of mass angle, h is the longitudinal polarization (helicity) of the electron,

$$v_{LT} = \sqrt{2\epsilon(1+\epsilon)} \quad (2.13)$$

and

$$v_{LT'} = \sqrt{2\epsilon(1-\epsilon)}. \quad (2.14)$$

Also, ϵ is the transverse polarization of the virtual photon

$$\epsilon = \left(\frac{1 + 2\vec{q}^2}{Q^2 \tan^2 \frac{\theta_e}{2}} \right)^{-1} \quad (2.15)$$

Γ is the virtual photon flux

$$\Gamma = \frac{\alpha}{2\pi^2} \frac{E'}{E_i} \frac{k_\gamma}{Q^2} \frac{1}{1-\epsilon} \quad (2.16)$$

and k_γ is the photon-equivalent energy, the laboratory energy necessary for a real photon to excite a hadronic system with center of mass energy W

$$k_\gamma = \frac{W^2 - m_i^2}{2m_i}. \quad (2.17)$$

This notation is used on the MAID website [29] but differs from the notation defined in [30]. The difference is in the longitudinal terms and is due to the use of ϵ only instead of ϵ_L .

$$\epsilon_L = \frac{Q^2}{\omega_{cm}^2} \epsilon \quad (2.18)$$

with

$$\omega_{cm} = \frac{\omega m_p - Q^2}{W}. \quad (2.19)$$

The extra terms are absorbed by the longitudinal cross sections resulting in a different definition for them. This difference is mentioned for completeness since all the cross sections shown in this thesis follow the MAID convention.

2.3 Multipoles

The interaction of interest in this thesis is the virtual photon interacting with the proton, exciting the Δ , which decays into a proton and a π^0 . The electromagnetic current can be expanded into a series of complex multipoles. The conservation of total angular momentum and parity selects the allowed multipole amplitudes. The virtual photon initial state carries total angular momentum L made up of its intrinsic spin 1 and orbital angular momentum \tilde{l} relative to the proton. The wave-function can be represented using vector spherical harmonics as [30]

$$Y_{\tilde{l}LM} = \sum_{\nu} C(1\lambda, \tilde{l}\nu | LM) \hat{e}_\lambda Y_{\tilde{l}\nu}(\hat{r}). \quad (2.20)$$

Electric and magnetic multipole transitions correspond to the transverse polarizations $\lambda = \pm 1$ and the longitudinal or Coulomb transitions correspond to $\lambda = 0$.

There are two common notations to refer to the multipoles. One focuses on the

virtual photon and uses EL , ML , and CL to refer to the electric, magnetic and Coulomb multipoles with L being the angular momentum of the initial photon. The other notation is in terms of the πN final state: $E_{l\pm}, M_{l\pm}, L_{l\pm}$ where the E , M and L are the electric, magnetic and longitudinal multipoles respectively, l is the orbital momentum of the pion relative to the nucleon, and \pm refers to the total angular momentum $J = |l \pm 1/2|$.

Putting everything together, the conservation of total angular momentum in the initial and final states gives

$$|L \pm 1/2| = |l \pm 1/2| = J. \quad (2.21)$$

The conservation of parity formulas depend upon the type of multipole.

$$\text{Even intrinsic parity } \quad CL, EL \quad (-1)^L = (-1)^{l+1} \quad (2.22)$$

$$\text{Odd intrinsic parity } \quad ML \quad (-1)^{L+1} = (-1)^{l+1} \quad (2.23)$$

The initial state has the parity of the photon times the parity of the proton (which is 1 and is suppressed in the above formulas). The final state has the parity of the pion, -1, and the parity of the orbital momentum of the pion in the πN center of mass, $(-1)^l$ [48, 30]. A useful example of this multipole notation is the $\gamma^* N \rightarrow \Delta$ transition which is shown in the next section.

Multipoles can also be expressed in several different bases depending upon the physics of interest. In this thesis, multipoles will commonly be expressed in the charge channel basis or isospin basis. Both bases are related algebraically as [29, 30]

$$\begin{aligned} A_{\pi^0 p} &= A_p^{1/2} + \frac{2}{3} A^{3/2} \\ A_{\pi^+ n} &= \sqrt{2} \left(A_p^{1/2} - \frac{1}{3} A^{3/2} \right). \end{aligned} \quad (2.24)$$

Multipoles are then summed together using Legendre polynomials (P_l) and their

derivatives (P'_l, P''_l) into CGLNFs which are defined as

$$F_1 = \sum_{l \geq 0} \{ (l M_{l+} + E_{l+}) P'_{l+1} + [(l+1) M_{l-} + E_{l-}] P'_{l-1} \} , \quad (2.25)$$

$$F_2 = \sum_{l \geq 1} [(l+1) M_{l+} + l M_{l-}] P'_l , \quad (2.26)$$

$$F_3 = \sum_{l \geq 1} [(E_{l+} - M_{l+}) P''_{l+1} + (E_{l-} + M_{l-}) P''_{l-1}] , \quad (2.27)$$

$$F_4 = \sum_{l \geq 2} (M_{l+} - E_{l+} - M_{l-} - E_{l-}) P''_l , \quad (2.28)$$

$$F_5 = \sum_{l \geq 0} [(l+1) L_{l+} P'_{l+1} - l L_{l-} P'_{l-1}] , \quad (2.29)$$

$$F_6 = \sum_{l \geq 1} [l L_{l-} - (l+1) L_{l+}] P'_l \quad (2.30)$$

The response functions are then formed from the CGLNFs as [30]

$$R_T = |F_1|^2 + |F_2|^2 + \frac{1}{2} \sin^2 \theta (|F_3|^2 + |F_4|^2) \quad (2.31)$$

$$- \Re \{ 2 \cos \theta F_1^* F_2 - \sin^2 \theta (F_1^* F_4 + F_2^* F_3 + \cos \theta F_3^* F_4) \} \quad (2.32)$$

$$R_L = |F_5|^2 + |F_6|^2 + 2 \cos \theta \Re \{ F_5^* F_6 \} \quad (2.33)$$

$$R_{TT} = \sin^2 \theta \left(\frac{1}{2} (|F_3|^2 + |F_4|^2) \Re \{ F_1^* F_4 + F_2^* F_3 + \cos \theta F_3^* F_4 \} \right) \quad (2.34)$$

$$R_{LT} = - \sin \theta \Re \{ (F_2^* + F_3^* + \cos \theta F_4^*) F_5 + (F_1^* + F_4^* + \cos \theta F_3^*) F_6 \} \quad (2.35)$$

$$R_{LT'} = - \sin \theta \Im \{ (F_2^* + F_3^* + \cos \theta F_4^*) F_5 + (F_1^* + F_4^* + \cos \theta F_3^*) F_6 \} . \quad (2.36)$$

These response functions are related to the cross sections in Eq. 2.12 by

$$\frac{d\sigma_i}{d\Omega_\pi} \propto R_i \quad (2.37)$$

and

$$\begin{aligned} \frac{d\sigma}{d\Omega_\pi} = & \frac{|\vec{q}^*|}{k_\gamma} \left(R_T + \epsilon R_L \left(\frac{Q^2}{\omega_{cm}^2} \right) + v_{LT} R_{LT} \cos \phi_{\pi q}^* \left(\frac{Q}{\omega_{cm}} \right) + \right. \\ & \left. \epsilon R_{TT} \cos 2\phi_{\pi q}^* + h v_{LT'} R_{LT'} \sin \phi_{\pi q}^* \left(\frac{Q}{\omega_{cm}} \right) \right) \end{aligned} \quad (2.38)$$

where

$$\frac{d^5\sigma}{d\Omega_f dE_f d\Omega} = \Gamma \frac{d\sigma}{d\Omega_\pi} \quad (2.39)$$

and k_γ is the photon equivalent energy defined earlier and $|\vec{q}^*|$ is the pion momentum in the center of mass. The other terms are all defined in Sec. 2.2. As is shown in Eq. 2.38, R_L requires an additional factor of Q^2/ω_{cm}^2 while R_{LT} and $R_{LT'}$ both need a factor of Q/ω_{cm} [29] to account for the change in notation between [30] and [29]. The ϵ_L term is no longer used so the factor to convert from ϵ to ϵ_L had to be absorbed by the cross sections. The relation between the multipoles and the cross sections will be important when fitting the data in Sec. 7.1.

2.4 The Δ Resonance

The Δ is the first excited state of the proton. In this thesis, the Δ actually refers to the Δ^+ since in the reaction $\gamma^* + p \rightarrow \Delta \rightarrow p + \pi^0$ the Δ must carry a positive charge for charge conservation.

The Δ has total spin $J = 3/2$ and positive parity [32]. Therefore from Eq. 2.21, $L = 1$ or 2 and $l = 1$ or 2. $l = 1$ from the requirement for positive parity from $(-1)^l$ times the intrinsic parity of the pion -1. For C and E , $L = 2$ to conserve parity and for M , $L = 1$ to conserve parity (see Eqs. 2.22 and 2.23). Therefore, the multipoles allowed for the $\gamma^* + p \rightarrow \Delta$ transition are: M1, E2, and C2, or, in πN final state multipoles: M_{1+} , E_{1+} , L_{1+} [48, 30].

The M_{1+} multipole arises from a magnetic spin flip of one of the quarks in the proton [14]. The E_{1+} and L_{1+} terms are identified as quadrupole terms and indicate deviations from spherical symmetry. From the analysis above, these terms involve

the quarks going to a higher orbital momentum state. Since the proton is a spin 1/2 object, no quadrupole moment can be measured. However, the Δ is a spin 3/2 object so the $\gamma^*N \rightarrow \Delta$ reaction can be studied for quadrupole effects [14].

A fourth type of πN multipole is commonly used and that is the scalar multipole S . Scalar multipoles are related to longitudinal multipoles by

$$\omega_{cm} S_{l\pm} = |\vec{q}_{cm}| L_{\pm}. \quad (2.40)$$

$|\vec{q}_{cm}|$ can be calculated using Eq. 2.19 and a variation of Eq. 2.4

$$q^2 = \omega_{cm}^2 - \vec{q}_{cm}^2 \quad (2.41)$$

to give

$$|\vec{q}_{cm}| = \sqrt{\omega_{cm}^2 - q^2} = \sqrt{\omega_{cm}^2 + Q^2}. \quad (2.42)$$

Now that the multipoles are defined, their ratios can be defined. It is common to cite the electric to magnetic ratio (EMR) or the Coulomb to magnetic ratio (CMR). More formally, they are defined as

$$\text{EMR} = \frac{E2}{M1} = \frac{\Re(E_{1+}^* M_{1+})}{|M_{1+}|^2} \quad (2.43)$$

and

$$\text{CMR} = \frac{C2}{M1} = \frac{\Re(S_{1+}^* M_{1+})}{|M_{1+}|^2}. \quad (2.44)$$

Near resonance, where the real part of the multipoles goes to zero, the EMR and CMR simplify to

$$\text{EMR} = \Im(E_{1+})/\Im(M_{1+}) \quad (2.45)$$

and

$$\text{CMR} = \Im(S_{1+})/\Im(M_{1+}). \quad (2.46)$$

The EMR and CMR provide a concise summary of deviations from spherical symmetry. If they are non-zero, they indicate the presence of quadrupole terms. However, since they are ratios of multipoles, they are not observables. The EMR and CMR must be extracted from cross sections. One method for the extraction is described in Sec. 7.1.

2.5 Scattering formalism

2.5.1 The S matrix

Before discussing the details behind the various models, a quick overview of the scattering formalism is needed. The scattering matrix S , takes incident waves of the form

$$\psi_i^{in} = (4\pi v_i)^{-1/2} \frac{e^{-ik_i r}}{r} \quad (2.47)$$

and converts them to the outgoing wave [34]

$$S\psi_i^{in} = \sum_j S_{ij} \psi_j^{out}. \quad (2.48)$$

The columns and rows indicate the various initial and final states that are connected by the matrix. A zero in a particular place indicates no connection between the channels. Since the flux in must equal the flux out, the S matrix is unitary

$$S\tilde{S}^* = 1. \quad (2.49)$$

If the interactions are also invariant with respect to the direction in time, the S matrix is also symmetric. Combining both requirements gives

$$SS^* = 1. \quad (2.50)$$

The S matrix gives a cross section

$$\frac{d\sigma}{d\Omega}(i \rightarrow j) = \frac{1}{4k_i^2} |S'_{ij}|^2 \quad (2.51)$$

where S'_{ij} is summed over all intermediate states properly accounting for angular momentum.

From the S matrix, a transition probability operator can be defined [20]

$$T = \frac{1}{2i}(S - 1). \quad (2.52)$$

This operator will be used as the starting point for the model described in Sec. 2.7.1.

2.5.2 The Fermi-Watson Theorem

The $\gamma^*p \rightarrow \Delta \rightarrow \pi^0p$ transition can be connected to πN scattering through the Fermi-Watson theorem. The Fermi-Watson theorem shows the relationship between the phases for γN and πN reactions. Below the two pion threshold, the S matrix, which connects the incoming and outgoing channels (see Sec. 2.5.1), for the πN system has the form $e^{2i\delta_\alpha}$ for each partial wave. Next, the partial wave S matrix for the coupled channels $\pi N \rightarrow \pi N$, $\gamma N \rightarrow \gamma N$ and $\pi N \leftrightarrow \gamma N$ is used. The form for the πN channel S matrix element becomes $\eta_\alpha e^{2i\delta_\alpha}$ where $\eta_\alpha < 1$ and is a function of energy. Next, the S matrix is completely determined by applying the condition of unitarity, $S^\dagger = S^{-1}$. The S matrix is then

$$S_\alpha = \begin{pmatrix} \eta_\alpha & i\sqrt{1-\eta_\alpha^2}e^{i\delta_\alpha} \\ i\sqrt{1-\eta_\alpha^2}e^{i\delta_\alpha} & \eta_\alpha e^{2i\delta_\alpha} \end{pmatrix}. \quad (2.53)$$

The upper left is the Compton scattering channel, the lower right is the πN channel and the two off-diagonal terms are the $\gamma N \rightarrow \pi N$ and its inverse. The end result is that the phase of the $\gamma N \rightarrow \pi N$ reaction is the same as that of the πN channel within the limits of the theorem, namely below the two pion threshold. This derivation follows that of [76].

The phase shifts in πN scattering are connected with the cross sections. A reso-

nance occurs when the phase shift is at 90 degrees. This also means that the multipole is purely imaginary. So, near resonance, the terms which are real or interfere with the real parts are very small [48].

2.6 Chiral Perturbation Theory

As mentioned in Sec. 2.4, quadrupole terms are allowed in the $\gamma^*N \rightarrow \Delta$ transition, in addition to the magnetic dipole term. The presence of these quadrupole terms indicates a deviation from spherical symmetry. The quark models using the color hyperfine interaction underestimate the size of the quadrupole terms by an order of magnitude [14]. Models using the pion cloud do a much better job of recreating the data. This is expected due to the spontaneous breaking of chiral symmetry which leads to a cloud of virtual p wave pions.

In the limit that the light quark masses go to zero, the QCD Lagrangian exhibits chiral symmetry. That this symmetry is spontaneously broken is verified by the absence of parity doubling of all hadronic states. Goldstone's theorem states that if a continuous symmetry of the Lagrangian is broken, a zero mass, pseudoscalar, spinless boson appears. For chiral symmetry breaking, this boson is the pion. It is no longer massless because the light quarks have a small but non-zero mass. A Goldstone boson couples to a nucleon by $g\sigma \cdot \vec{p}$ where g is the $\pi - N$ coupling constant (from the Goldberger-Trieman relation), σ is the nucleon spin, and \vec{p} is the pion momentum. The coupling is strong in the p wave and mixes in non-zero angular momentum components. It is this p wave interaction that mixes in the quadrupole terms leading to a deviation from spherical symmetry.

The Goldberger-Trieman relation connects the ratio of the axial and vector coupling constants g_A (which can be found through nuclear β decay), the mass of the nucleon M_N , the pion decay constant F_π and the $\pi - N$ coupling constant $g_{\pi N}$ [20, 83]:

$$g_A = \frac{F_\pi g_{\pi N}}{\sqrt{2}M_N c^2}. \quad (2.54)$$

As will be shown, the dynamic models incorporate the pion cloud into the model

but also use other assumptions as to the shape. There are some recent calculations, though, that use the chiral symmetric Lagrangian directly to get results with a perturbative method.

One such calculation is that of Pascalutsa and Vanderhaeghen (PV) [60, 61] which starts with the relativistic chiral Lagrangian of pion and nucleon fields and then uses effective field theory (EFT).

Effective field theory assumes that light particles are degrees of freedom and heavy particles are static. It then creates a Lagrangian which has the dynamics of the light particles but also has all the underlying symmetries of QCD [76].

The next step is to determine the terms in the expansion that will play the largest roles. Pascalutsa and Vanderhaeghen have developed a new power counting method for the pion electroproduction amplitude. In this method, the excitation energy of the Δ ($M_\Delta - M \simeq 0.3$ GeV) is a light scale with $\Lambda \sim 1$ GeV being heavy so an expansion parameter $\delta = \Delta/\Lambda$ can be used. The other light scale is the pion mass which can be used as $m_\pi/\Lambda \sim \delta^2$. This δ^2 term is what makes this method different from previous methods which assumed the Δ and m_π were similar sizes.

After carrying out the effective field theory calculation with the diagrams of the proper orders, form factors and cross sections can be calculated. One benefit to the chiral perturbation theory (CPT) method is the small number of free parameters. There are only three low energy constants that need to be fit to give a good description of the data. Compare this to the Sato-Lee dynamical model which requires seven parameters or the SAID model which requires 148 (see Sec. 2.7.2 and 2.7.4). In addition, Pascalutsa and Vanderhaeghen can estimate the errors by looking at the expected size of the next-to-next-to leading order terms, those of order δ^2 , m_π/Λ or Q^2/Λ^2 . Pascalutsa and Vanderhaeghen's predictions compared with existing data at $Q^2 = 0.127$ are shown in Fig. 2-4.

Pascalutsa and Vanderhaeghen have also expanded their calculation to examine the validity of the linear extrapolation to the physical pion mass that is currently used by lattice QCD calculations. Lattice QCD approaches the problem of using the QCD Lagrangian from a different direction. Rather than formulating it in a way

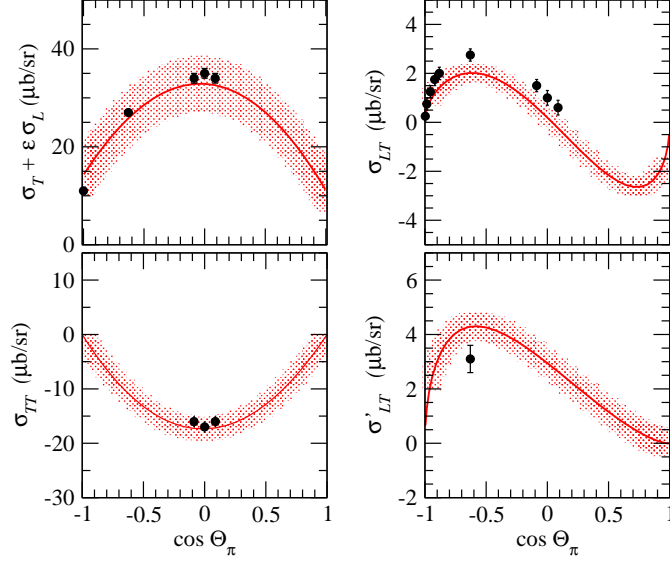


Figure 2-4: Pascalutsa and Vanderhaeghen CPT results for $\gamma^* p \rightarrow \pi^0 p$ at $W=1232$ MeV, $Q^2 = 0.127$ (GeV/c)². Data are from Bates [55, 74, 49]. Figure from [60].

which can be solved perturbatively, lattice QCD calculates the solution to the QCD Lagrangian on a grid or lattice. Better results are obtained with higher density and larger lattices but that is computationally expensive. In addition, for full QCD, the computation time goes with the quark mass m_q as $1/m_q^p$ where $p \sim 2 - 3$ [76]. Recent calculations indicate that p could be as high as 4.5 [58]. Compromises must be made and typically, lattice QCD calculations are performed with quark masses larger than the physical quark mass since the calculations converge more rapidly. The mass of the pion, m_π , is proportional to $\sqrt{m_q}$ so larger quark masses lead to larger pion masses as well. Then the lattice results must be extrapolated to the actual mass [76]. The lattice calculations from [2] use a simple linear extrapolation in m_π^2 .

Figure 2-5 shows the results of the Pascalutsa and Vanderhaeghen extrapolation of the lattice QCD data. It turns out that the linear extrapolation is not far off for the EMR but is totally out of agreement for the CMR. This clearly shows the importance of the pion cloud and accounting for it properly.

Another limitation of this order of chiral perturbation theory is that it is confined to the region $Q^2 < 0.25$ (GeV/c)². Since the large scale size is typically 1 GeV

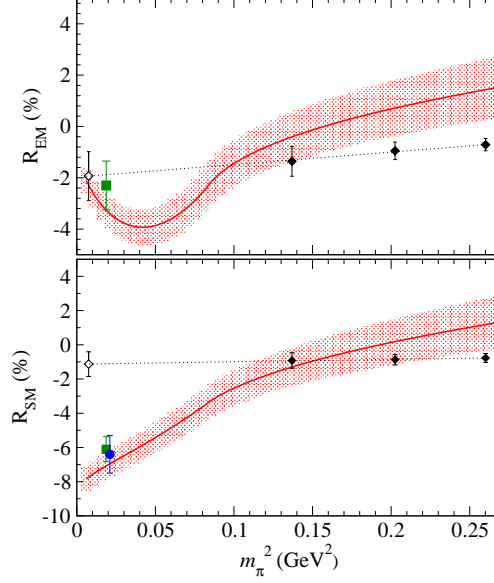


Figure 2-5: Pascalutsa and Vanderhaeghen calculation of the m_π dependence of the EMR and CMR. The solid black diamonds are the lattice calculation [2]. The circle is from MAMI [63] and the squares are from Bates [55, 74]. The figure is from [60].

($\sim 4\pi f_\pi$), terms that are 25% of the scale start to be too large for the approximations. Higher order terms are then needed. As mentioned earlier, this is included in the error estimates and those predictions versus Q^2 are plotted along with the new data from this experiment in Sec. 7.1.

Another chiral perturbation theory calculation has been performed by Gail and Hemmert (GH) [38]. They begin by parameterizing the $\gamma^*N \rightarrow \Delta$ matrix element using three form factors which are analogous to the Dirac and Pauli form factors. Gail and Hemmert utilized the small scale expansion where the nucleon-Delta mass splitting, Δ , is considered small and on the same order as the momentum transfer and the pion mass. The mass splitting was added in front of one of the form factors to get consistency between the transition amplitudes and the transition current. Gail and Hemmert then found the relations between the form factors they used and the standard form factors involving multipoles. From there, the relation to the EMR and CMR is simple.

The Gail and Hemmert chiral perturbation results also have some fit parameters.

Three parameters are used to fit the experimental results. They started with a two parameter fit which does not do as well when compared to data above $Q^2 = 0.05$ (GeV/c)². They then added a third parameter which increased the radius of one of their form factors. This term actually arises from a higher order in the calculation. It plays a role because the EMR is so sensitive to small changes in that form factor.

For both fits, the magnetic dipole and EMR data at $Q^2 = 0$ (GeV/c)² were used. However, the EMR and CMR at finite Q^2 are actually predictions of the model and have not been fit. The CMR happens to be the ratio that has more sensitivity in the Q^2 range of this experiment.

The Gail and Hemmert approach begins to have problems at $Q^2 = 0.30$ (GeV/c)² where other neglected terms start to play a role. As a check, they note that the form factors of the nucleon agree with dispersion-theoretical results up to $Q^2 = 0.30$ (GeV/c)². In the predictions provided by Gail and Hemmert and shown in Sec. 7.1, the predictions stop at $Q^2 = 0.20$ (GeV/c)² making sure to avoid the region where the errors start to get much bigger.

2.7 Models

Since QCD is difficult to solve in the low energy region, various models are used to predict the cross section. Some are phenomenological and others attempt to use perturbative forms of QCD. The differences between the models and their predictions are important for interpreting the results of experiments. Several models are commonly compared with the data and those models are described below.

2.7.1 Mainz Unitary Model 2003

The T matrix from Sec. 2.5.1 is the starting point for the MAID model. Below the two pion threshold, there are only γ s and π s giving the options of $T_{\gamma\gamma}$, $T_{\pi\pi}$ and $T_{\gamma\pi}$ as the components of the matrix. The $T_{\pi\pi}$ term can be calculated or acquired from an empirical analysis using

$$t_{\pi\pi}^\alpha = \frac{\eta_\alpha e^{2i\delta_\alpha} - 1}{2i}. \quad (2.55)$$

Below the 2 pion threshold, η_α (the inelasticity) is near 1 so

$$t_{\pi\pi}^\alpha \simeq \sin \delta_\alpha e^{-\delta_\alpha}. \quad (2.56)$$

In MAID, the πN phase shifts δ_α come from the SAID analysis [4]. To find $T_{\gamma\pi}$, the model has an ansatz that separates the resonance from the background terms as

$$T_{\gamma\pi} = T_{\gamma\pi}^{bg} + T_{\gamma\pi}^{res} \quad (2.57)$$

$$T_{\gamma\pi} = K_{\gamma\pi}(1 + iT_{\pi\pi}) + \sum_i T_{\gamma\pi}^{\{N,\Delta\}_i^*} \quad (2.58)$$

where the K matrix has been used. The K matrix is related to the T matrix as

$$T^{-1} = K^{-1} - i. \quad (2.59)$$

The K matrix approximation allows the following:

$$K_{\gamma\pi}^{bg} \approx V_{\gamma\pi}^{bg}. \quad (2.60)$$

The partial wave scattering amplitude $T_{\gamma\pi}^{res}$ is found using the ansatz that the resonance takes a Breit-Wigner shape that goes as

$$T_{\gamma\pi}^\Delta \sim \frac{[\Gamma_{\gamma N \rightarrow \Delta}(W, Q^2)]^{1/2} [\Gamma_{\Delta \rightarrow \pi N}(W)]^{1/2}}{M_\Delta - W - i\Gamma_\Delta(W)/2}. \quad (2.61)$$

The partial wave is given by

$$t_{\gamma\pi}^\alpha = v_{\gamma\pi}^{bg,\alpha}(1 + it_{\pi\pi}^\alpha) + t_{\gamma\pi}^{res,\alpha}. \quad (2.62)$$

Again, below the two pion threshold, the approximation can be made that

$$1 + it_{\pi\pi}^\alpha \sim \cos \delta_\alpha e^{i\delta_\alpha}. \quad (2.63)$$

Furthermore, the assumption is made that

$$t_{\gamma\pi}^{res,\alpha} \sim \sin \delta_\alpha e^{i\delta_\alpha}. \quad (2.64)$$

This shows one of the central differences in the MAID model: the background phases are the same as for the resonant phases. In addition, the background and resonance terms are unitarized separately using the form

$$t_{\gamma\pi}^\alpha = t_{\gamma\pi}^\alpha (Background)(1 + it_{\pi\pi}^\alpha) + t_{\gamma\pi}^\alpha (Resonance)e^{i\Psi^\alpha} \quad (2.65)$$

where Ψ^α is introduced for unitarization. It can be adjusted to ensure that the overall phase shift of the multipole is the same as the πN phase shift δ_α [78].

The background terms in MAID are primarily the Born terms, shown in Fig. 2-6, and the ω and ρ exchange terms shown in Fig. 2-7. Using those diagrams, the field theory Lagrangians can be written out and the cross sections found. The vector meson coupling constants are found by fitting non-resonant s and p wave multipoles over a wide energy range.

The diagrams labeled a, b, c in Fig. 2-6 have can be calculated with pseudoscalar or pseudovector coupling while d occurs only for pseudovector coupling. This behavior is added to the model by mixing the two couplings. In the MAID model, this mixing takes the form

$$T_{\gamma\pi}^{mix} = \frac{\Lambda_m^2}{\Lambda_m^2 + q_0^2} T_{\gamma\pi}^{PV} + \frac{q_0^2}{\Lambda_m^2 + q_0^2} T_{\gamma\pi}^{PS} \quad (2.66)$$

where q_0 is the pion momentum and $\Lambda_m = 450$ MeV is a parameter used to fit the data. The mixture is pure pseudovector at threshold and pure pseudoscalar at high pion momentum.

With the background terms fixed, the only remaining part is the resonance. As mentioned above, the resonance assumes a Breit-Wigner shape. More specifically, the

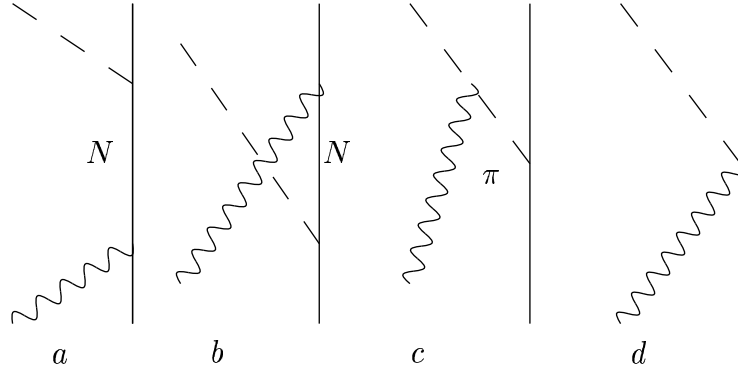


Figure 2-6: Born terms used in the MAID model.

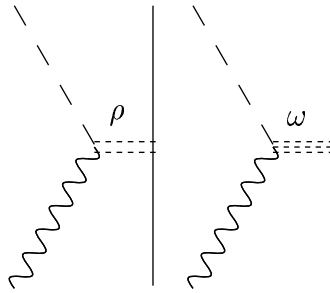


Figure 2-7: Meson exchange terms used in the MAID model.

resonant multipoles $E_{1+}^{3/2}$, $M_{1+}^{3/2}$ and $S_{1+}^{3/2}$ take the form

$$A_{l\pm}(W, Q^2) = \bar{A}_{l\pm}(Q^2) f_{\gamma N}(W) \frac{\Gamma_{tot} W_R e^{i\phi}}{W_R^2 - W^2 - iW_R \Gamma_{tot}} f_{\pi N}(W) C_{\pi N}. \quad (2.67)$$

In addition to the Breit-Wigner form, there are several other factors which are defined in [28]. However, the term $\bar{A}_{l\pm}$ has been updated since the original paper to improve the Q^2 evolution of the resonance. The form is now

$$\bar{A}_{l\pm} = A_{1/2}(0) \frac{1 + \alpha Q^2}{1 + \beta Q^2} \quad (2.68)$$

for each helicity amplitude $A_{1/2}(Q^2)$, $A_{3/2}(Q^2)$, $S_{1/2}(Q^2)$. The parameters α , β and $A(0)$ are all fit to a world database for each helicity amplitude.

To summarize, the MAID model is a unitarized model where the background and resonance are unitarized separately. The background comes from a combination of Born terms and vector meson exchange and fits to data. The resonance multipoles utilize phases from πN scattering and have Breit-Wigner forms. MAID also includes effects from higher resonances up to $W=2$ GeV. [28, 77]

2.7.2 Sato-Lee

The Sato-Lee model is a type of dynamical model which uses effective field theory along with meson exchange to build a model with only several fitted parameters. It explicitly includes the effect of a cloud of virtual pions around the nucleon and Δ and calculates the effect dynamically. The model begins with a Lagrangian for $\pi - N$ scattering using N , Δ , π and ρ fields. The Lagrangian is then converted into a Hamiltonian and a method of unitary transformation is applied. The end result of the unitary transformation is an effective Hamiltonian from which a T matrix can be calculated. The effective Hamiltonian created by the unitary transformation used for the Sato-Lee model is energy independent and hermitian. Therefore, the unitarity of the calculated reaction amplitudes is satisfied.

To extend the Lagrangian for pion photoproduction, the ω and γ fields have to be added. With the full effective Hamiltonian, the πN scattering phase shifts are fit with seven parameters to construct the hadronic part of the Hamiltonian. So that there is a consistent description of πN scattering and the $\gamma N \rightarrow \pi N$ transition, parts of the $\gamma N \rightarrow \pi N$ transition operator are then fixed.

With the hadronic part of the effective Hamiltonian fixed, the pion photoproduction part only has three parameters. The parameters are the form factors associated with the $M1$ and $E2$ transitions and the ωNN coupling constant. The $\gamma\pi$ element in the T matrix is written as

$$T_{\gamma\pi}(E) = t_{\gamma\pi}(E) + \frac{\bar{\Gamma}_{\Delta \rightarrow \pi N} \bar{\Gamma}_{\gamma N \rightarrow \Delta}}{E - m_{\Delta}^0 - \Sigma_{\Delta}(E)} \quad (2.69)$$

where $t_{\gamma\pi}$ is the non-resonant amplitude, $\Sigma_{\Delta}(E)$ is the Δ self energy, and

$$\bar{\Gamma}_{\gamma N \rightarrow \Delta} = \Gamma_{\gamma N \rightarrow \Delta} + \bar{\Gamma}_{\pi N \rightarrow \Delta} G_{\pi N}(E) v_{\gamma\pi}. \quad (2.70)$$

One of the differences between the Sato-Lee model and a more phenomenological model like MAID is in the calculation of $\bar{\Gamma}_{\gamma N \rightarrow \Delta}$. Figure 2-8 shows the diagrams that are included in the term. In addition to the quark model prediction, there are the pion loop corrections which are responsible for the pion cloud effect.

In the phenomenological models, these pion loops are approximated through the first order K matrix approximation. In the Sato-Lee model, they are calculated.

Finally, to reach the predictions for pion electroproduction, the procedure is extended to virtual photons. Once they are included, the multipoles for pion electroproduction can be calculated and from those, the cross sections. [67]

2.7.3 Dubna-Mainz-Taipei

The Dubna-Mainz-Taipei (DMT) dynamic model is more of a hybrid between the phenomenology of the MAID model and the dynamics of the Sato-Lee model. The background of the DMT model starts with the MAID background but then adds an integral over the pion loop diagrams which is not present in full form in MAID. As

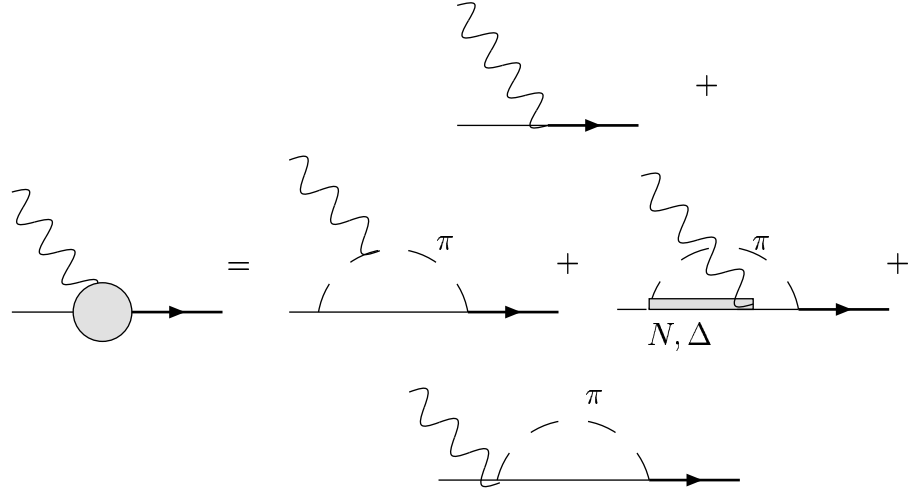


Figure 2-8: Pion loop diagrams included in the Sato-Lee model. The top diagram is the quark model prediction and the rest are the pion cloud effect.

mentioned above, MAID uses the K matrix approximation which partially includes the pion loops. The authors of DMT use their model to conclude that the bare (no pion cloud) Δ is almost spherical while the dressed Δ is oblate. This indicates that almost all of the deformation of the Δ comes from the pion cloud [47, 84]. The DMT model is also able to describe existing data for lab photon energies from threshold ($W \approx 1080$ MeV) up to 1 GeV ($W \approx 1660$ MeV).

2.7.4 SAID

The SAID analysis is a partial wave analysis which uses fits to data extensively. The idea is to use an energy dependent parametrization of the magnetic and electric multipoles and fit the πN scattering data and then extend it to other channels. The multipoles up to $L = 4$ were fit using a Breit-Wigner form which has been carefully crafted to obey the Fermi-Watson theorem (see Sec. 2.4).

In the SAID model, the first pass of the fit identifies the multipoles which contribute to the cross section. The second pass fits only the multipoles identified in the first pass. The results are energy dependent but single energy solutions are found by looking at sub-sets of the data.

The background terms are parametrized as $\cos(\delta)e^{i\delta}$ times a complex constant where δ is the πN phase. This is similar to the MAID background. In addition, SAID allows another overall phase of a form which preserves unitarity [4, 6, 5].

Many ansätze are used for the form of energy dependent widths of resonances, the shape of the resonances and the background. However, they are justified by the way the SAID analysis fits the various data sets reasonably well. The SM02 solution has a raw χ^2/dof of 3.8 in the $\pi^0 p$ channel [4]. After introducing a normalization term which takes into account systematic error in the data, the χ^2/dof drops to 2.3. Considering that there are over 8000 data points with 148 parameters, the fit seems reasonable.

Chapter 3

Experimental Setup

This chapter provides an overview of the A1 experimental setup at the Institute for Nuclear Physics at the University of Mainz, Germany. It starts with a description of the beam and the hydrogen target and moves on to the spectrometers and their detector packages. It ends with a description of the electronics. Even more detail about the spectrometers and detectors can be found in [17].

3.1 Electron Beam

3.1.1 Mainz Microtron

The accelerator at the Institute for Nuclear Physics consists of three racetrack microtron stages. One stage is shown in Fig. 3-1. Electrons from a strained Gallium-Arsenide source are sent into the Microtron where the accelerating section is used many times. The orbit of the electron increases until it is extracted. The electrons exit the second stage with an energy of 180.02 MeV. The third and final stage increases the electron energy by 7.504 MeV per turn up to a maximum of 90 turns or 855.10 MeV. The electron's final energy can be written as [71]:

$$E_{beam}(n) = (180.02 + 7.504n - 3.5 \cdot 10^{-5}n^2 \pm 0.16)\text{MeV} \quad (3.1)$$

where n is the number of turns. The Mainz Microtron (MAMI) can deliver up to

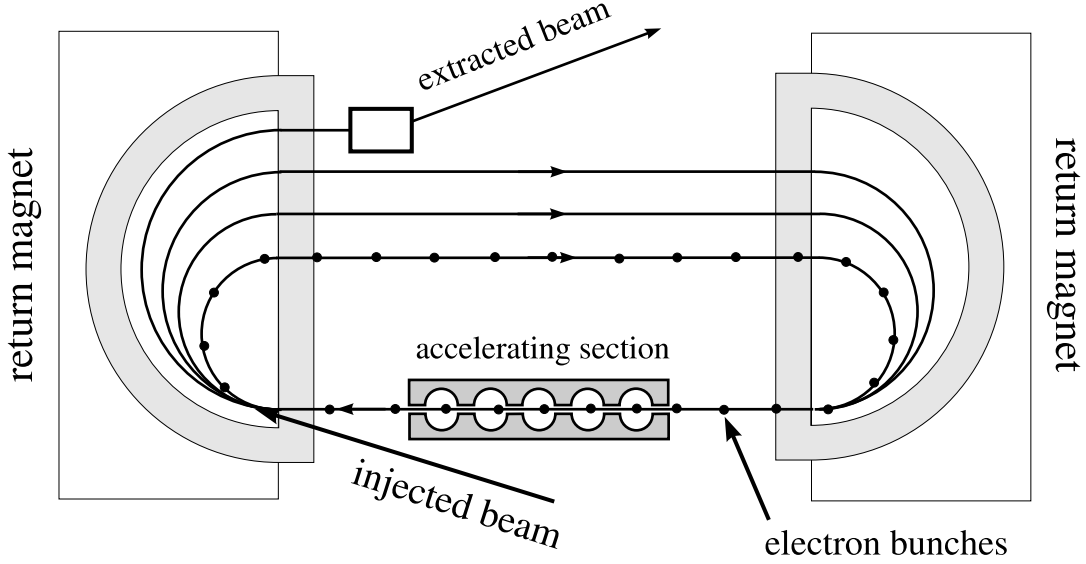


Figure 3-1: Schematic view of one of the three racetrack microtron stages of the Mainz Microtron. Figure from [18]

80 μ A of current with approximately 75% polarized beam.

An overview of the MAMI accelerator can be seen in Fig. 3-2. The spectrometers used in this experiment were located in the A1 experimental hall.

3.1.2 Polarized beam

Electrons from a strained Gallium-Arsenide source are used in the MAMI beam. The polarization is mostly preserved through the acceleration process but must be measured in the experimental hall. The A1 Hall contains a Möller polarimeter specifically for this purpose [11]. The polarimeter is located 15 meters upstream of the cryotarget [12]. The measurement required a special magnetically polarized, iron film target to be placed in the beam. As a result, the polarization measurement is destructive and cannot be run during pion production runs. The Möller polarimeter measurements were made about every twelve hours and each time two 300 second Möller runs were taken and the results averaged. The typical Möller run gave a polarization of about $75\% \pm 1.2\%_{stat} \pm 1.2\%_{sys}$. The polarization was seen to be stable over time.

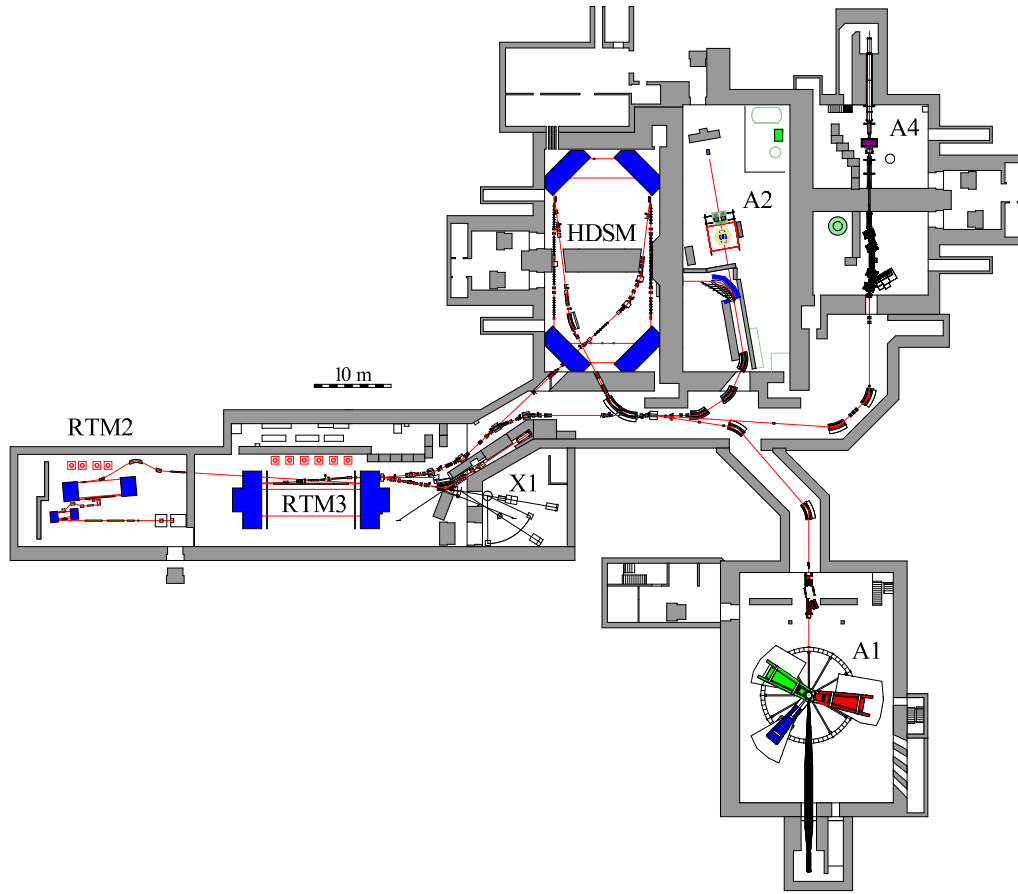


Figure 3-2: Overview of the Mainz facility showing the MAMI accelerator and the experimental halls. The A1 Hall with the three spectrometers is on the lower right. Figure from [82].

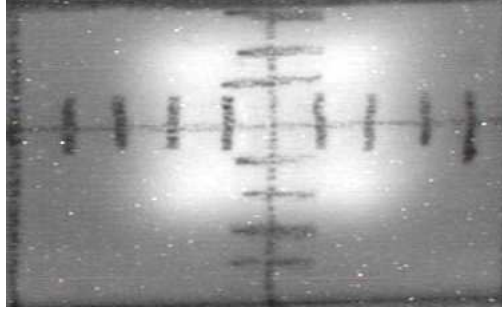


Figure 3-3: Example of the typical centered, rastered beam on the BeO target. This setting was used during the October 2003 runtime.

3.1.3 Beam position

The MAMI beam is typically kept centered on the target and rastered to minimize local heating in the cryo target (see Sec. 3.2). To monitor the beam position, the cryotarget was moved out and a BeO target grid was moved in. A camera allowed for direct monitoring of the beam position. Since this is a destructive measurement like the beam polarization measurement, the beam position was checked several times per day typically before and after a production run. An example of the centered and rastered beam is shown in Fig. 3-3.

However, because of the various out-of-plane settings in the April 2003 runtime, there was concern that with a centered beam, the outgoing protons would hit parts of the target assembly on the way to Spectrometer B. So, the beam was moved down and to the right to avoid those interactions. In addition, the beam rasterization was decreased in the y direction to further guard against the unwanted collisions. An example of the typical April runtime beam is in Fig. 3-4. Since the October runtime did not have any out-of-plane settings, the centered beam was used.

A final issue with the beam position is stability over time. The beam typically drifted less than 1 mm. Some testing by changing the beam position in software indicates that this has an effect on the cross section that is less than 1%.

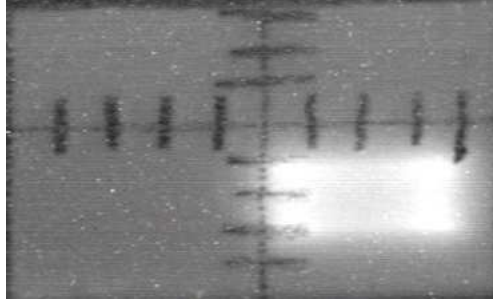


Figure 3-4: Example of the typical off-center, rastered beam on the BeO target. This setting was used during the April 2003 runtime.

3.1.4 Current monitoring

The beam current, and so the total charge, is constantly monitored using a Förster probe. The electron beam is surrounded by two toroidal coils which make up the probe. The electron beam's magnetic field induces a current in the coils which is proportional to the beam current. For currents above $10 \mu\text{A}$, the uncertainty on the measurement is $0.3 \mu\text{A}$ [71]. However, the probe is located in the accelerating section of the third microtron. As a result, the total current from the electrons from all the recirculations is measured. Therefore, the uncertainty of the probe is $0.3\mu\text{A}/n$, where n is the number of electron beam recirculations. For the lowest beam energy used and for low beam currents, then this uncertainty can become a 0.5% effect. However, for production runs the error from the current measurement is typically less than 0.1%. When combined with the other luminosity errors (see Chaps. 5.3.4 and 5.5), the current/charge error is insignificant.

The Förster probe has two scale settings, rough and fine, with rough for larger currents ($> 1\mu\text{A}$) and fine for smaller currents. The fine scale is 100 times the rough scale and was used for most elastic normalization runs since the beam current was low.

3.2 Hydrogen target and beam rasterization

The ideal target for the $p(\vec{e}, e'p)\pi^0$ reaction is liquid hydrogen since it is dense and pure protons. The hydrogen must be cooled and circulated rapidly to provide a constant, stable luminosity. The circulation prevents local heating from occurring which would lead to lower density regions of the target and even gas bubbles forming.

A Philips-Sterling cooling machine with a cooling power of 75 W was used to cool and liquify the hydrogen. The target was maintained at a temperature of about 20 K and a pressure of about 2 bars. Readings from temperature and pressure sensors around the target were fed into the data stream. The target density is then calculated and used to find the luminosity.

The target itself consists of 10 μm thick Havar which was 4.95 cm long, 1.15 cm wide and 1 cm high with rounded endcaps. See Fig. 3-6 for a schematic view.

In addition to rotors around the target to ensure adequate flow of hydrogen, the electron beam is rasterized or wobbled to prevent any particular area of the target from overheating. The electron beam is deflected transversely with respect to the beam axis and the wobbler position is logged in the data stream. This allows for accurate energy loss calculations in the analysis stage. Examples of the beam rasterization are in Figs. 3-3 and 3-4.

3.3 Spectrometers

The $p(\vec{e}, e'p)\pi^0$ measurements were performed using the A1 magnetic spectrometers at the Mainz Microtron facility. There are three spectrometers in the hall which are labeled A, B, and C. For most setups, electrons were detected in Spectrometer A which uses two pairs of vertical drift chambers for track reconstruction and two layers of scintillator detectors for timing information and particle identification. The protons were detected in Spectrometer B which has a detector package similar to Spectrometer A. Spectrometer B also has the ability to measure at up to 10° out-of-plane in the lab. This corresponds to a significantly larger value in the center of mass

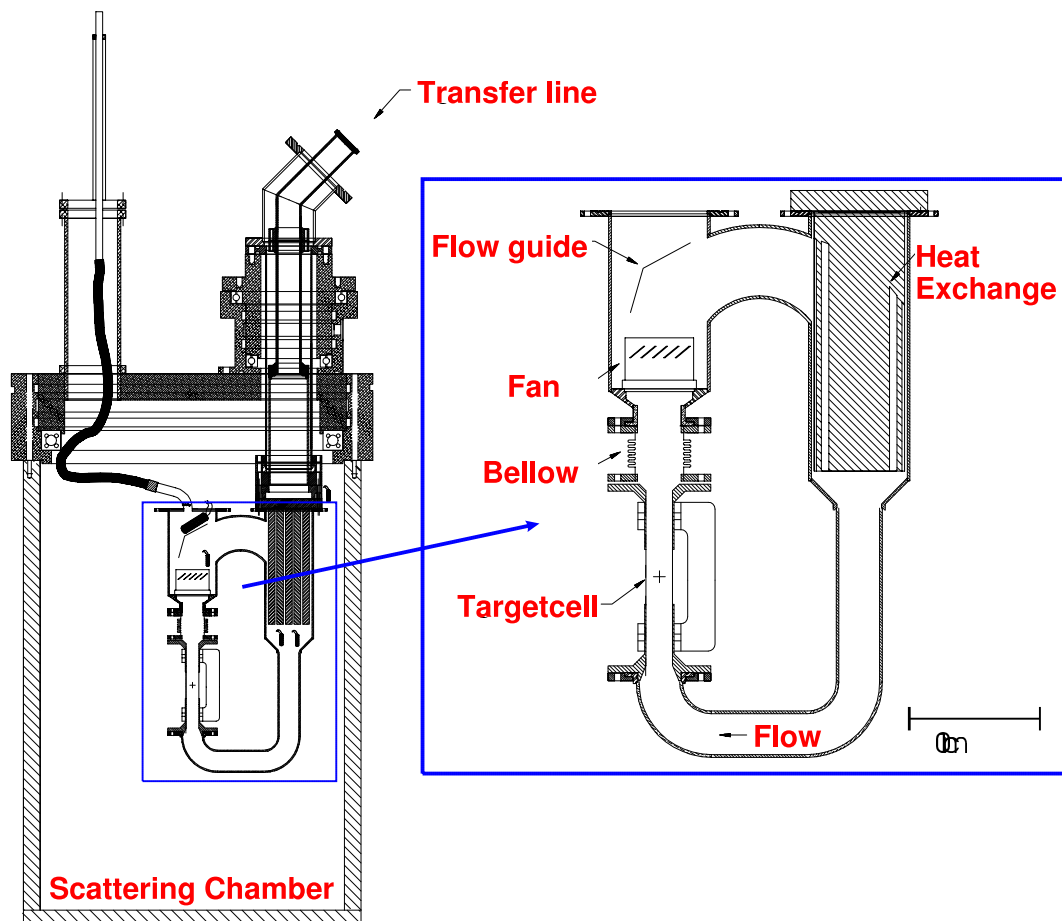


Figure 3-5: The hydrogen cryo-target used in this experiment. The + sign in the figure indicates where the center of the beam hits the target. Figure from [71].

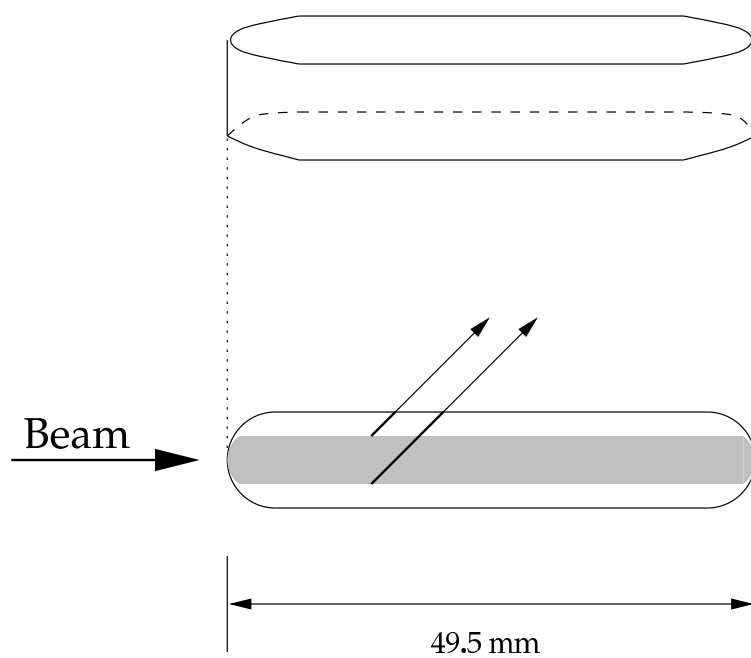


Figure 3-6: A schematic view of the cryo target seen from above and from the side. The shaded region represents the region swept by the beam wobbler. Figure from [71].

Spectrometer		A	B
Magnets		QSDD	D _{clam}
Maximum momentum	[MeV]	735	870
Solid angle	[msr]	28	5.6
Angular range	[°]	18(23.96)-160	7(15.11)-62
Momentum acceptance	[%]	20	15
Horizontal acceptance	[mrad]	± 100	± 20
Vertical acceptance	[mrad]	± 70	± 70
Momentum resolution		10^{-4}	10^{-4}
Angular res. at target	[mrad]	< 3	< 3
Position res. at target	[mm]	3-5	< 1

Table 3.1: Ranges, limits, and resolutions for the A1 spectrometers from [17]. The design angles were not reachable with the current setup. Angles in parentheses are the actual minimum angles.

frame. Spectrometer C is similar to Spectrometer A (scaled down by 11/14) and was used as a luminosity monitor during the April 2003 runtime. Table 3.1 contains an overview of the properties of the spectrometers.

For this experiment, it is not enough to merely know that an electron or proton went into the spectrometer. By using certain arrangements of magnets and detectors, the specific path of the particle can be reconstructed. This then gives much more detail about the event and allows the cross section to be measured as a function of several variables. The following sections contain more details about the spectrometer magnets and detectors.

3.3.1 Collimators

So as to define the size of the acceptance more precisely, collimators are used at the entrance of the spectrometers. Table 3.1 listed the maximum acceptance of the spectrometers but they can be made smaller. The maximum acceptance for Spectrometer A is 28 msr. For this experiment, the 21 msr collimator was used. The default acceptance for Spectrometer B of 5.6 msr was used. Special sieve slit collimators with many precisely located holes were used to check the optics of the magnets and to fine tune the offsets in the reconstruction matrix.

3.3.2 Magnets

In all three of the A1 spectrometers, charged particles are deflected by a dipole magnet. The plane in which the particles are bent is known as the dispersive plane. By placing various other magnets in the spectrometers, the size of the acceptance and the resolution can be changed. For Spectrometer A, the goal was large acceptance. For that reason, the first magnet is a quadrupole. The quadrupole was set to defocus in the dispersive plane and focus in the non-dispersive plane. By doing so, the transverse angular acceptance is increased. However, this also increases the angular divergence of the particles leaving the second dipole. This then leads to the requirement of large tracking and time-of-flight detectors.

The next magnet in Spectrometer A is a sextupole magnet whose purpose is to fine tune the trajectories and cancel some higher order effects of the dipoles. The two dipole magnets then bend the particles primarily depending upon their momentum. The particles then exit the spectrometer and their position and angle are measured by the detector package (see Sec. 3.3.3). Spectrometer A operates in point-to-point imaging mode in the dispersive plane. This means that events at a particular point in the target plane are projected to a specific point in the focal plane. In line-to-point mode, all of the target plane events which share a certain value (i.e. momentum) are mapped to the same point in the focal plane. Spectrometer A operates in parallel-to-point mode in the non-dispersive plane. The large angular range of Spectrometer A does mean that the vertex resolution is not as good as it could be.

Spectrometer B compensates for the lower vertex resolution of A by using a single dipole magnet. This means that Spectrometer B uses point-to-point imaging in both planes leading to higher vertex resolution but a smaller acceptance.

The central momentum in each spectrometer is determined by setting the central magnetic field of each spectrometer. Hall probes are located inside of each spectrometer and are used for finding the rough field. The magnets are typically cycled up to saturation and back down to the desired setting. Once the Hall probes indicate that the magnetic field is close to the desired strength, a nuclear magnetic resonance

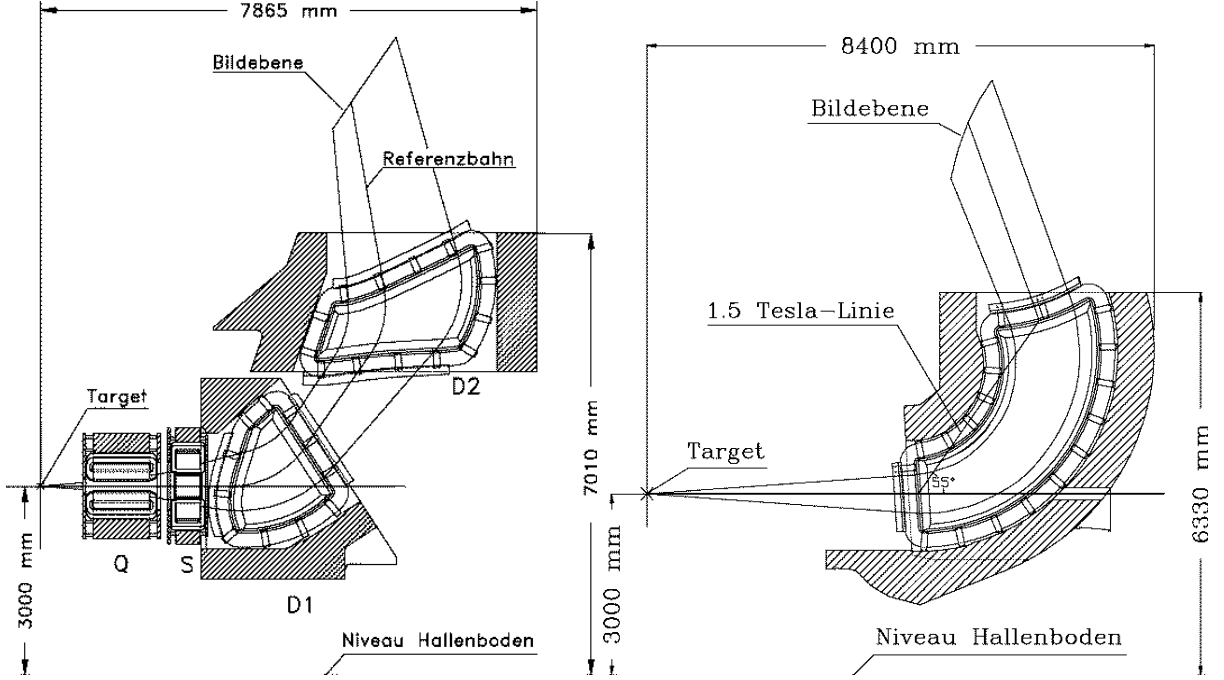


Figure 3-7: The central optics for Spectrometer A (left) and Spectrometer B (right). Figures from [24].

(NMR) reading is taken. Four NMR probes are inside of each of the spectrometers, each one covering a different range of magnetic field strengths. While the Hall probe is rather rough, the error in the NMR field measurements is smaller than the energy spread of the electron beam [71, 42]. The exact central momentum derived from the NMR is then fed into the data analysis and simulation software.

3.3.3 Detectors

After the charged particle exits the spectrometer magnets, its angle and position must be measured. This is accomplished with two pairs of vertical drift chambers which provide two points in space. After the drift chambers is a layer of scintillators which signal that a particle went through the spectrometer. Finally, there is a Cherenkov detector which separates the electrons and pions. The detectors can be seen in Fig. 3-8. More details about each of these detectors follow and can also be found in [17].

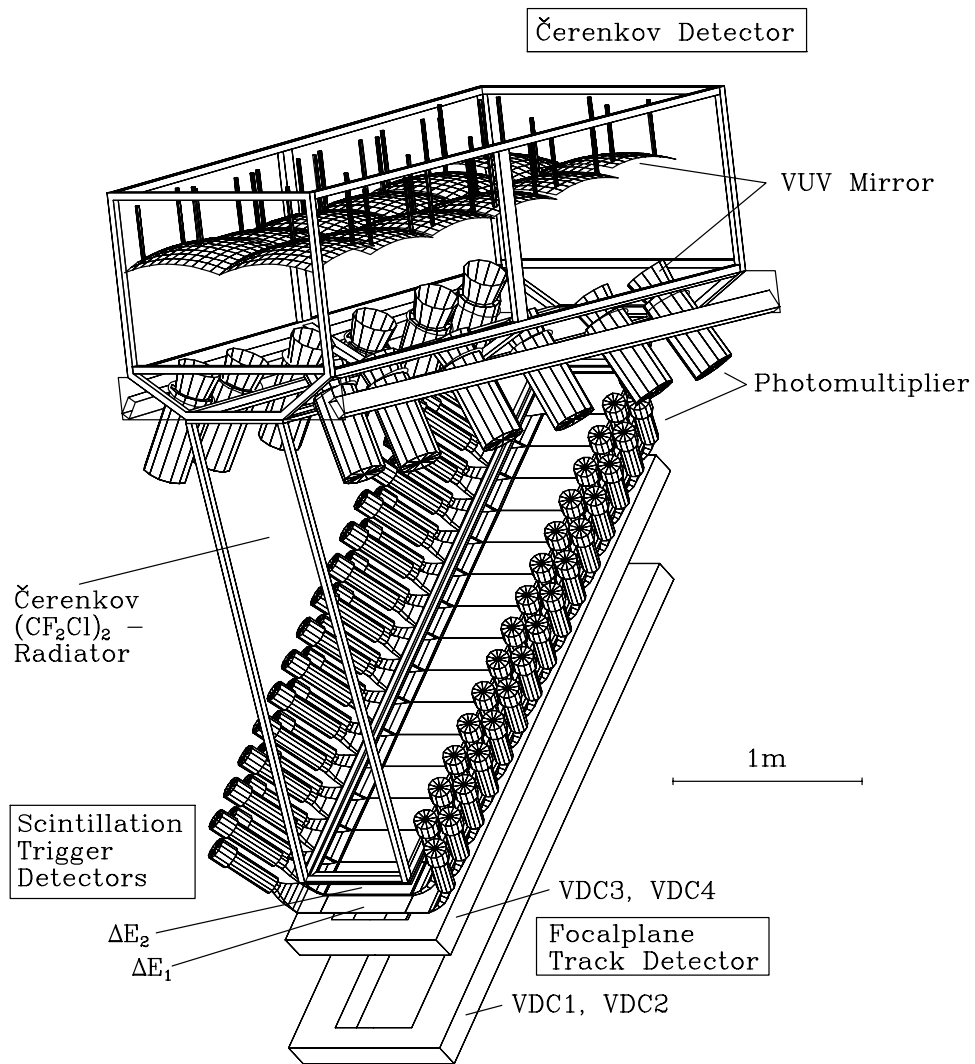


Figure 3-8: Drawing of the Spectrometer A detector systems from [35].

Vertical Drift Chambers

The detectors which give particle track information are vertical drift chambers (VDCs). These consist of 15 μm diameter signal and 50 μm diameter potential wires equally spaced between two high voltage cathodes in a gas filled volume. The signal and potential wires are connected to ground and the cathodes are at high negative voltage. The gas is a mixture of 80% ethane and 20% argon.

The VDCs are set at about 45° with respect to horizontal. As a charged particle traverses the chamber, the gas inside is ionized and electrons are freed. The electric field is such that these free electrons drift toward the sense wires. As they drift, the field becomes more intense and the electrons gain energy thus ionizing the gas more and freeing more electrons. This electron avalanche amplifies the signal and occurs in very close proximity to the sense wires. The potential wires are thicker than the signal wires so that there is no electron avalanche near them and less cross talk.

The free electrons drift through the gas in a known way with a typical drift time of 200 ns. Timing information can then be turned into a precise location. A particle traveling through the chamber typically fires five or six wires. When the wire is triggered, a time to digital converter (TDC) starts counting. The traversing particle is then detected in the scintillators (see Sec. 3.3.3) which act as a stop for the drift time measurement. The time each wire fires relative to the scintillator time, converted to distance, then gives the track through the chamber.

The first VDC in each pair has wires oriented such that it measures the position of the track in the dispersive plane. The second VDC has wires rotated 40° relative to the first in order to measure a projection of the track in the non-dispersive plane. The spatial resolution in the dispersive plane is $\leq 200 \mu\text{m}$. Because of the rotated wires and the projection, the resolution is not as good in the non-dispersive plane but is still $\leq 400 \mu\text{m}$ [71]. One pair of VDCs is enough to reconstruct the track but the angular resolution is improved by an order of magnitude by having a second pair located 20 cm above the first pair.

The timing information from the wires for an individual VDC has an up-down

ambiguity because the timing information does not indicate whether it drifted up or down. The up-down ambiguity is resolved by using multiple VDCs and finding the best fit to the track. If the wrong direction is used, the fit will be poor and the software can find the proper orientation.

Using the track information from the VDCs and the optics of the spectrometer, the track leaving the magnets can be mapped back to the target coordinates. Then COLA++ (see Sec. 5.1.1) can calculate physics variables such as W , Q^2 , θ_{pq}^* , and the like.

Scintillation counters

As mentioned earlier, the scintillators act as a stop for the drift chambers. There are actually two layers of scintillators in the detector packages. The first layer is thin (3 mm) and the second layer is thick (1 cm). The second layer typically provides the fast timing information for the coincidence. The two layers also can give particle identification. Protons will typically deposit more energy in the first layer than minimum ionizing particles. A plot of the first layer versus the second will then separate the two types.

The scintillator planes are made up of scintillator paddles, 15 for Spectrometer A and 14 for Spectrometer B. The light signals in Spectrometer A are detected with photomultiplier tubes on either side of the scintillator. The scintillator paddles in Spectrometer B are shorter and so only are instrumented on one side.

Cherenkov detectors

The two layers of the scintillator will not allow a separation of electrons or positrons from pions. A Cherenkov detector located after the scintillators accomplishes this task. When a particle exceeds the speed of light in the medium it is traveling in, Cherenkov light is produced. The Cherenkov detector is filled with Freon gas with an index of refraction of about 1.0012 [71]. The momentum threshold is then about 10 MeV/c for electrons and 2.4 GeV/c for pions. With a maximum electron beam energy of 855 MeV, the produced pions will never be above the 2.4 GeV/c threshold.

Therefore, if Cherenkov light is produced, the particle was an electron or positron.

For the October beamtime, the Cherenkov detector in Spectrometer A was removed and replaced with a recoil polarimeter. The polarimeter was not used but the effect of not having the Cherenkov was checked beforehand. It was found that the missing mass cut was enough so the Cherenkov detector was not needed. The Cherenkov is not a part of the standard cuts.

3.4 Electronics

The electronics for each of the three A1 spectrometers are similar and shown in Fig. 3-9. On board each spectrometer is an electronics crate which checks for good events. A good event is one where the left and right photomultiplier tubes in both layers of scintillator fired. This is ORed with the Cherenkov signal. When the programmable lookup unit (PLU) detects a good event, an unscaled singles signal is sent to the coincidence PLU. With three spectrometers, there are seven event types: single A, B, C, Coincidence AB, BC, AC and ABC. Pre-scaling units can selectively scale the number of events of any type. Since this experiment was looking at coincidences between Spectrometers A and B, all the other types were scaled down. The singles were scaled typically by factors of about 1000 so that they could be analyzed but not overwhelm the data acquisition system. Since the singles rates are much higher than the coincidence rates, they must be scaled down or else the data acquisition system will be perpetually dead.

When the coincidence PLU recognizes a valid single or coincidence event (see Fig. 3-10), interrupt signals are sent to the computers on the individual spectrometers. For proper reconstruction of the event, the event number and type is also sent to each spectrometer. The interrupt triggers the readout process on each spectrometer. The μ Busy flip-flops are set which halts data taking while the electronics are busy. The properly delayed photomultiplier signals are then sent to ADC's which are gated by the interrupt. Also, the TDCs started by the VDC wire signals are stopped by the re-timed spectrometer interrupt. Re-timing is critical since various electronic

components will add different delays. Re-timing is accomplished by ANDing the interrupt (which has a wide gate) with a properly delayed single from the same spectrometer. This keeps the timing precise and allows for good track reconstruction.

After all of the data have been read out, the μ Busy flip-flops are reset and data taking can resume. The dead time of all the electronics is measured using scalers which are vetoed by the busy signal and scalers which are not vetoed. More detail about the dead time can be found in Sec. 5.3.4.

Since each spectrometer generates its own data stream, the software must properly combine the three data streams into one. With the data taking rate at most 1 kHz, the millisecond time of each event could almost be used to uniquely combine the streams. However, there is the chance for differing machine times or multiple events at the same millisecond so a master event number generator is used. For each valid event that the coincidence PLU detects, the event number generator is advanced one and sent to the front end computers on each spectrometer along with the event type (single A, coincidence AB, etc.). The event builder AQUA (Data AcQUisition for A1 Experiments) combines the three spectrometer data streams as well as the slow control data stream (magnet settings, chamber voltages, target temperature, etc.) to create an event file with all the information needed to reconstruct the event. These event files are then sent to COLA++ (see Sec. 5.1.1) for processing into physics results.

This description of the electronics was based upon the description in [71]. More details about the A1 electronics can be found in [17], [71] and [19].

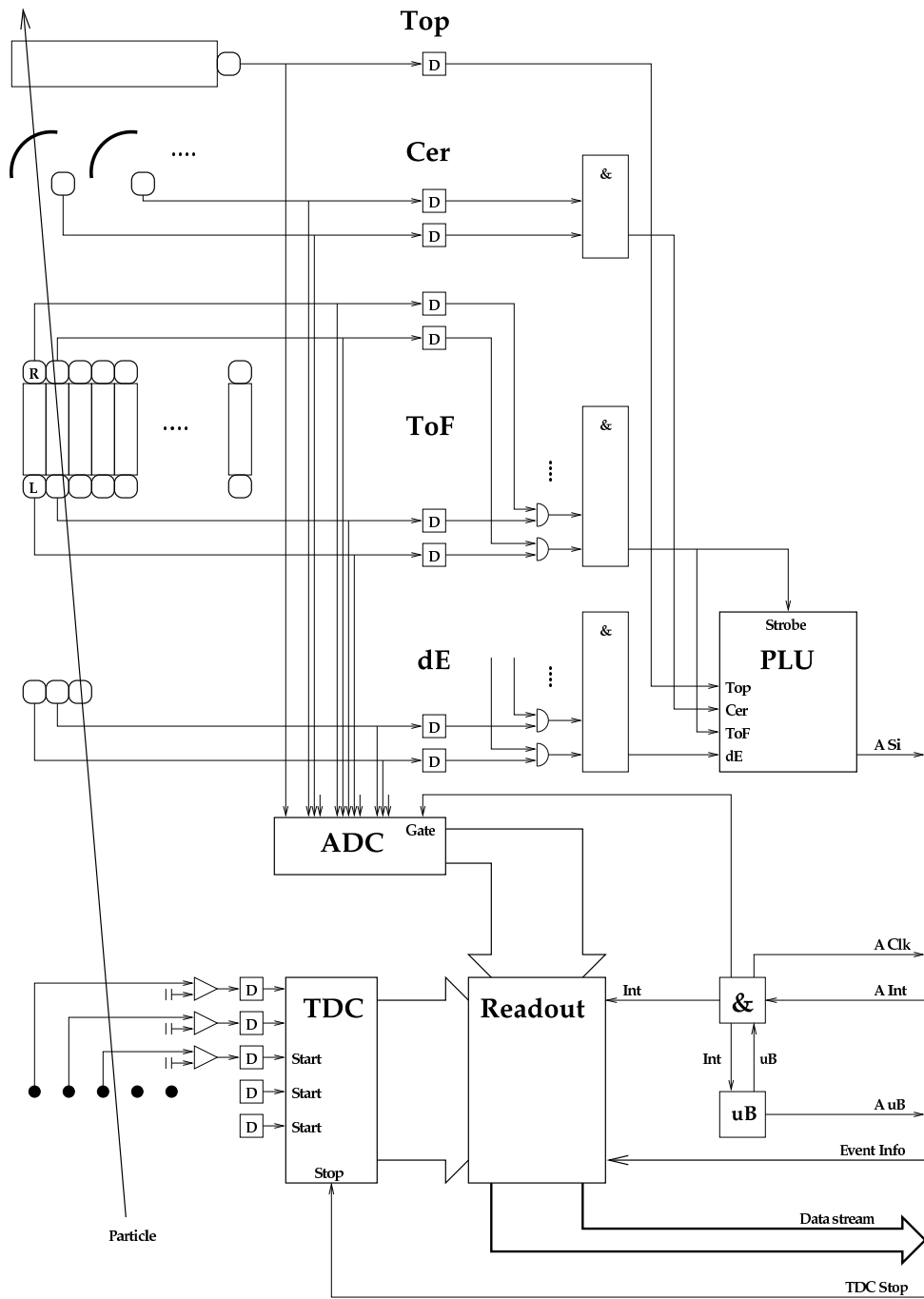


Figure 3-9: Logic diagram for Spectrometer A from [71].

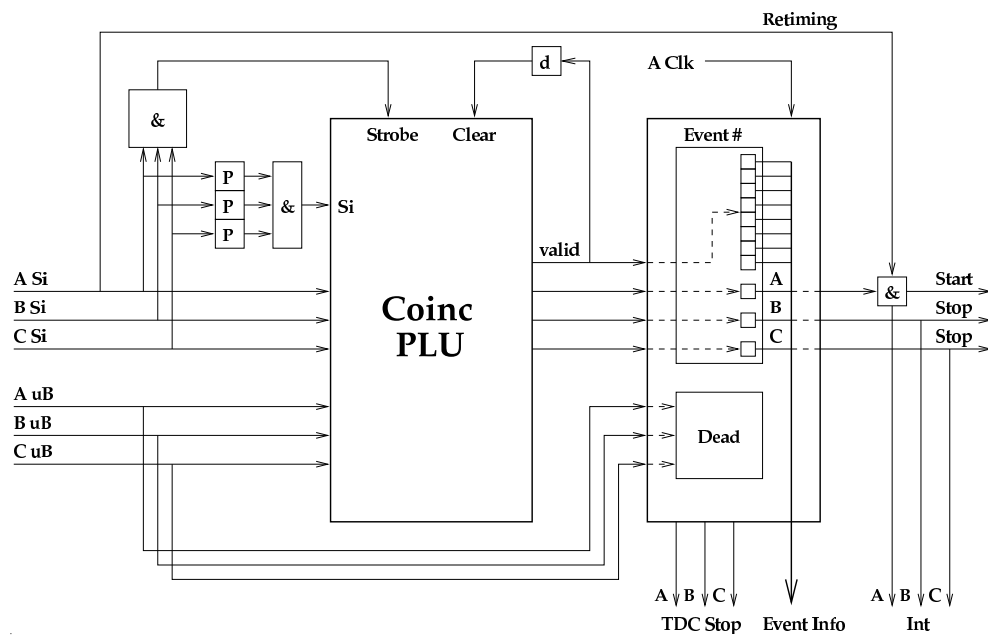


Figure 3-10: Coincidence Logic diagram from [71].

Chapter 4

Experiment Overview

This chapter will describe the design of the experiment and describe the specific kinematic settings used.

Since the goal of the experiment at Mainz was to map out the Q^2 evolution of the resonant multipoles as well as possible, the physical constraints of the spectrometers (see Sec. 3.3) had to be well understood. The angular constraints are shown in Table 3.1. However, knowing the ranges of the spectrometers is not enough. The phase space in which the experiment can be carried out is still large. It involves the electron beam energy, the central momenta of the spectrometers, the out-of-plane properties and, since the magnet polarity can be switched, even which spectrometer to use for electrons and which for protons.

Estimated luminosities were then used along with the MAID model to estimate the spectrometer cross sections for many settings. Then the results were run through a fitting routine (see Sec. 7.1) to see which kinematic combinations gave the smallest errors. In general, larger θ_{pq}^* angles were preferred because they gave more sensitivity to quadrupole terms. However, smaller ϕ_{pq}^* angles in the forward direction (between the continuing electron beam and the \vec{q} direction) were better for isolating the cross sections with smaller errors. Figure 4-1 shows the θ_{pq}^* and ϕ_{pq}^* coverage versus Q^2 . The regular setting (electrons in Spectrometer A, protons in Spectrometer B) was limited to smaller θ_{pq}^* but could reach smaller values of ϕ_{pq}^* . It also had a much narrower acceptance in θ_{pq}^* but much larger in W and Q^2 . The reverse setting (electrons in

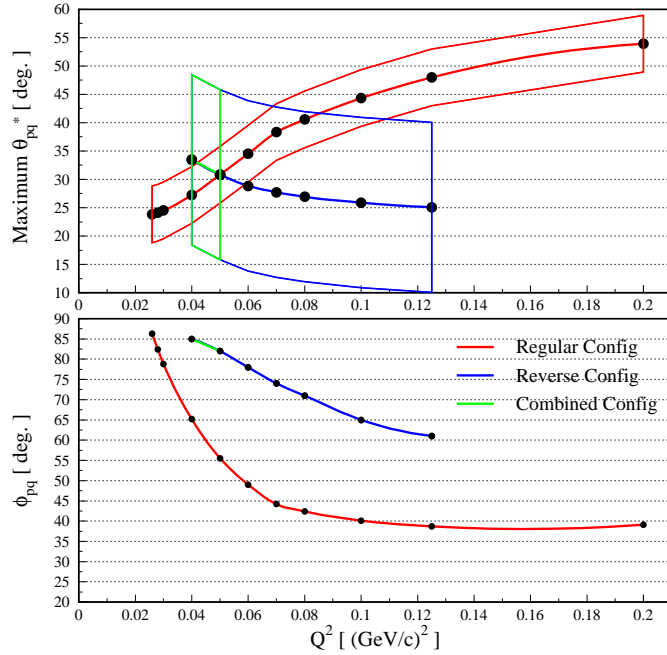


Figure 4-1: Overview of the accessible regions of the phase space. Regular kinematics was for electrons in Spectrometer A and protons in Spectrometer B. Reverse was vice versa. The Combined configuration used regular for the parallel cross section and reverse for the rest and required a change in beam energy. The large errors below $Q^2 \approx 0.06 \text{ (GeV/c)}^2$ (see Fig. 4-2) favored the regular setting. Figure from [15].

Spectrometer B, protons in Spectrometer A) could reach larger θ_{pq}^* values but was severely hurt by the larger ϕ_{pq}^* values.

Figure 4-2 shows the estimated statistical, systematic and total errors for extracted σ s for the reverse and regular configurations plotted versus Q^2 . (See Page 72 for more discussion about errors.) There is a clear dip in the errors near $Q^2 = 0.05 \text{ (GeV/c)}^2$. It was concluded that while the reverse setting is good for some limited cases, the regular setting should be used to get smaller errors at lower values of Q^2 .

Given the constraints of time and physical placement of the spectrometers, the lowest Q^2 that could be measured and still give good W and Q^2 coverage with a reasonably large θ_{pq}^* was at $Q^2 = 0.060 \text{ (GeV/c)}^2$ using the regular setting. This value is also about halfway between the existing database at $Q^2 = 0.127 \text{ (GeV/c)}^2$ and the photon point thus filling in the gap in a logical spot.

As mentioned above, the available phase space was searched for kinematic points

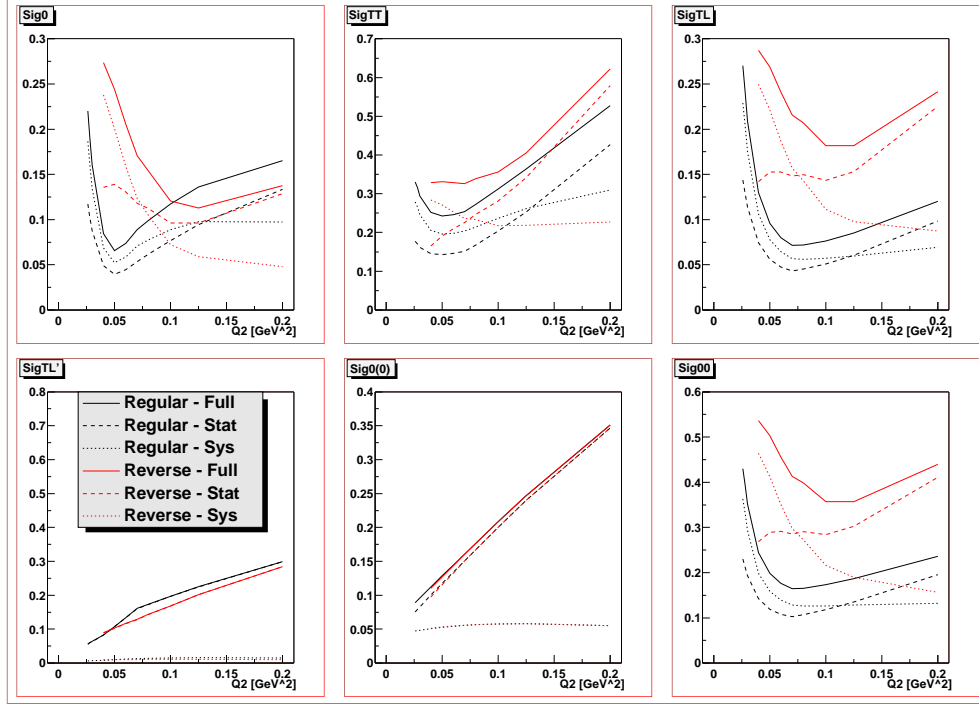


Figure 4-2: Cross section errors versus Q^2 . Note the dip near $Q^2 = 0.05 \text{ (GeV/c)}^2$ for the regular setting.

which would constrain the models as much as possible. When fitting the $Q^2 = 0.127 \text{ (GeV/c)}^2$ database, wide distributions in θ_{pq}^* were found to be useful. In addition, models were constrained by a scan of the parallel cross section as a function of W . It was the goal of the Mainz experiment to create another database with some of the constraining power of the $Q^2 = 0.127 \text{ (GeV/c)}^2$ database. So, a scan of the parallel cross section as a function of W at $Q^2 = 0.060 \text{ (GeV/c)}^2$ was carried out. Details about the kinematics are in Table 4.2.

The data for this thesis were taken during two run periods in 2003. The first period was in April and measured the mostly non-parallel cross sections for $Q^2 = 0.060$ and 0.200 (GeV/c)^2 in addition to the cross checks and an extension of the $Q^2 = 0.127 \text{ (GeV/c)}^2$ database. The October period was used to measure the W scans at $Q^2 = 0.060$ and 0.200 (GeV/c)^2 and the low W background terms.

The details of the extraction of the cross sections are in Sec. 5.3.9 but a short version is given here. With the form of the cross section as shown in Eq. 2.12 and

setting the helicity equal to zero, there are three cross sections to extract: $\sigma_0 = \sigma_T + \epsilon\sigma_L$ (ϵ was not varied so the two cross sections cannot be separated), σ_{TT} and σ_{LT} . The three cross sections can be extracted by measuring the spectrometer cross section at the same W, Q^2 , and θ_{pq}^* but different values of ϕ_{pq}^* .

Figure 4-3 shows the various locations used in measuring the cross section. The circle represents a slice of a cone whose opening angle is the constant proton angle θ_{pq}^* . Measuring along the circle is measuring at the same proton angle θ_{pq}^* but different ϕ_{pq}^* . The center of the circle is along the momentum transfer vector and is where the proton spectrometer is placed to measure the parallel cross section. Position 3 is the in-plane measurement at $\phi_{pq}^* = 180^\circ$. Spectrometer B was not constrained on the backward angle side and so that in-plane measurement was always possible. Two more measurements are still needed to extract the three cross sections. For the smaller θ_{pq}^* angle of 24° , there was enough space on the forward side of Spectrometer B that it could be placed in-plane. However, for the larger θ_{pq}^* angle of 37° , there was not enough space. Furthermore, during the experiment, an unforeseen conflict with the top of Spectrometer A forced a compromise. The setup Q06-t36-p1 was set to a smaller angle and the size of the acceptance allowed kinematic overlap.

Studies of the extraction process showed that the smallest errors and most sensitivity were achieved when the three ϕ_{pq}^* measurements were as far apart as possible. However, at the larger θ_{pq}^* angles, not all ϕ_{pq}^* values can be reached because of the constraint on the out-of-plane angle of Spectrometer B. Therefore, for each θ_{pq}^* setting, the maximally out-of-plane settings were used.

Further inspection of Eq. 2.12 shows that with a polarized beam and a non-zero ϕ_{pq}^* angle (i.e. out-of-plane), the fifth cross section $\sigma_{LT'}$ can be measured. The beam was always longitudinally polarized so all settings that were out-of-plane measured $\sigma_{LT'}$. Equations 2.36 and A.9 show that $\sigma_{LT'}$ is sensitive to the background terms through the real parts of the multipoles. Its measurement helps to constrain the background terms of the various models.

In addition to the low Q^2 measurements, some cross check measurements were made at $Q^2 = 0.127 \text{ (GeV/c)}^2$ which overlapped with existing data from Bates. The

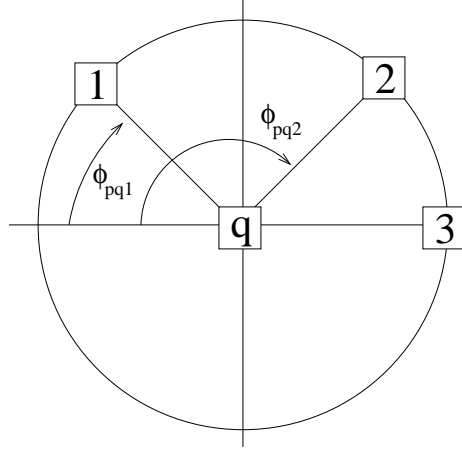


Figure 4-3: Schematic view of the various locations the spectrometers are placed. The number indicates which ϕ_{pq} angle is used and the q indicates measurement along the q vector.

$Q^2 = 0.127 \text{ (GeV/c)}^2$ database was also expanded a bit as will be detailed in the following sections.

Finally, a database with similar range to the $Q^2 = 0.060 \text{ (GeV/c)}^2$ database was taken at $Q^2 = 0.20 \text{ (GeV/c)}^2$. That database is being analyzed by our collaborators in Athens and will not be in this thesis.

4.1 Low $Q^2 \text{ (GeV/c)}^2$ Measurements

4.1.1 $Q^2 = 0.060 \text{ (GeV/c)}^2$

As mentioned above, the primary focus of this thesis is the low Q^2 analysis. The kinematic settings are shown in Table 4.1. Throughout the thesis, the setup name may be used to label a setting. The formula is Q06 for $Q^2 = 0.060 \text{ (GeV/c)}^2$, txx where xx is the θ_{pq}^* angle and py where y = 1 is the most forward ϕ_{pq}^* , y = 2 is the middle and y = 3 is the most backward. (The 24 comes from rounding 23.9 while the 36 value was from truncating 36.5.)

The reasons for the selection of Q^2 and θ_{pq}^* have been given above. The choice of central W came from the desire to measure the cross section as a function of W as well. The physical mass of the Δ is at 1232 MeV whereas the pion pole is at 1210

Setup	Q^2 [(GeV/c) ²]	W [MeV]	θ_{pq}^* [°]	ϕ_{pq}^* [°]
Q06-t0	0.060	1221	0	\vec{q}
Q06-t24-p1	0.060	1221	23.9	0.0
Q06-t24-p2	0.060	1221	23.9	90.0
Q06-t24-p3	0.060	1221	23.9	180.0
Q06-t36-p1	0.060	1221	29.6	28.8
Q06-t36-p2	0.060	1221	36.5	134.0
Q06-t36-p3	0.060	1221	36.5	180.0

Table 4.1: Primary kinematic settings for low Q^2 measurement. The out-of-plane settings are in bold.

MeV. From plots of the phase space (see Fig. 5-16), the W coverage is known to be 40 MeV wide. By centering the acceptance at 1221 MeV, the plan was to have two 20 MeV bins, one centered at 1232 MeV, the other at 1210. However, as the analysis proceeded, it was found that the systematic errors were too large going off-center. As a consequence, all the final results are at $W=1221$ MeV and models are used to extrapolate to $W=1232$ MeV.

The data sets listed in Table 4.1 are referred to as the primary data because the extraction of the M_{1+} , E_{1+} , and S_1 multipoles can be done with just this set alone. The data points were chosen to maximize the sensitivity to the quadrupole terms. All the other data enrich the data set and allow for more extensive testing of the backgrounds but, on their own, cannot constrain the EMR and CMR nearly as well.

4.1.2 W scan

As mentioned earlier, the W scan for the $Q^2 = 0.127$ (GeV/c)² database has been useful in constraining the models. The W scan of the parallel cross section at $Q^2 = 0.060$ (GeV/c)² covers a similar region in W . Table 4.2 gives the details of the measurements.

The parallel cross section scan spans a wide range of W from 1125 MeV to 1300 MeV. In addition, a cross check was added. For the $W=1205$ MeV setting, the roles of Spectrometers A and B were reversed. Spectrometer B was used to detect electrons and Spectrometer A was used to detect protons. This check verifies that the efficiency

Setup	Q^2 [(GeV/c) ²]	W [MeV]	θ_{pq}^* [°]	ϕ_{pq}^* [°]
Q06_W1125	0.060	1125	0	\vec{q}
Q06_W1155	0.060	1155	0	\vec{q}
Q06_W1185	0.060	1185	0	\vec{q}
Q06_W1205	0.060	1205	0	\vec{q}
Q06_W1225	0.060	1225	0	\vec{q}
Q06_W1245	0.060	1245	0	\vec{q}
Q06_W1275	0.060	1275	0	\vec{q}
Q06_W1300_low	0.060	1300	0	\vec{q}
Q06_W1205_rev	0.060	1205	0	\vec{q}

Table 4.2: Kinematic settings for the $Q^2 = 0.060(\text{GeV/c})^2$ W scan. The separate setting was for reverse kinematics where the roles of the spectrometers was reversed.

Setup	Q^2 [(GeV/c) ²]	W [MeV]	θ_{pq}^* [°]	ϕ_{pq}^* [°]
Q06_W1155_p1	0.060	1155	26	0
Q06_W1155_p2	0.060	1155	26	180

Table 4.3: Kinematic settings for the $Q^2 = 0.060(\text{GeV/c})^2$ background test. These runs were performed during the October 2003 run time.

of the two spectrometers is well understood. In addition, there are some other reverse kinematic settings and it is important to prove that the measurement is comparable to the standard configuration.

4.1.3 Background terms

The primary goal of this thesis is the extraction of the resonant multipoles at $Q^2 = 0.060 (\text{GeV/c})^2$ using models for the background terms. However, the model background terms can be tested by measuring as far from the resonances as possible while still having a reasonably large cross section. This led to the measurement at $Q^2 = 0.060 (\text{GeV/c})^2$ in the low W region. A reasonable compromise between angles and spectrometer constraints was to measure at the values listed in Table 4.3. The two in-plane measurements allow a separation of σ_{LT} and $\sigma_0 + \epsilon\sigma_{TT}$.

Setup	Q^2 [(GeV/c) ²]	W [MeV]	θ_{pq}^* [°]	ϕ_{pq}^* [°]	Bates Exp.
Q127-q	0.127	1232	0	\vec{q}	MV,S
Q126_W1232	0.126	1232	0	\vec{q}	MV,S
Q126_W1212	0.126	1212	0	\vec{q}	MV
Q126_W1232_p1	0.127	1232	28	0	MV
Q126_W1232_p2	0.127	1232	28	180	MV

Table 4.4: Kinematic settings for the $Q^2 = 0.127(\text{GeV}/c)^2$ settings which overlap with Bates. The top run was from the April 2003 run time and the bottom runs were from the October 2003 period. MV is for the Mertz-Vellidis results [55, 80]. S is for the Sparveris results [74].

4.2 $Q^2 = 0.127 (\text{GeV}/c)^2$ Measurements

Since there is a large database at $Q^2 = 0.127 (\text{GeV}/c)^2$ from Bates (see [81, 55, 80, 49, 48, 74]) and Mainz (see [63, 12]) already, the new Mainz experiment did not measure extensively there. There were several measurements which overlap exactly with previous Bates measurements and their purpose was to check the relative difference between the two labs. Table 4.4 shows these settings and the experiment with which it overlaps.

The $Q^2 = 0.127 (\text{GeV}/c)^2$ database was then extended during the April run time. More measurements to constrain the low W terms were added since measuring at low W minimizes the effects of higher resonances. The out-of-plane ability was used to measure the $\sigma_{LT'}$ at low W which directly checks the background terms. In addition to the low W data, new $\sigma_{LT'}$ data were taken near the resonance to check the background terms in that region. The new $\sigma_{LT'}$ data not only extend the database but also act as a cross check with existing Bates data that are near it (see Sec. 5.4.5). The settings for the database extension are shown in Table 4.5.

4.3 Elastic Cross Section

During the design of the experiment, it was found that the final errors were significantly impacted by the size of the systematic error from setup to setup. In order to check the cross section normalization, the elastic cross section was measured before

Setup	Q^2 [(GeV/c) ²]	W [MeV]	θ_{pq}^* [°]	ϕ_{pq}^* [°]
Q127-th30	0.127	1221	30	90
Q127-th43	0.127	1221	43	135
Q127-th63	0.127	1221	63	150
Q127-w1140-p1	0.127	1140	58.6	45
Q127-w1140-p2	0.127	1140	58.6	135

Table 4.5: Kinematic settings for extending the Bates $Q^2 = 0.127(\text{GeV}/c)^2$ database. The top section were single out-of-plane measurements which give $\sigma_{LT'}$ and the spectrometer cross section. The lower section is the low W background measurement. All of the measurements were out-of-plane and so are in bold.

and after each pion production run. Elastic kinematics differ greatly from the pion production kinematics. Both spectrometers had to have their central angle changed and either the electron or proton spectrometer would have to change central momentum. It was decided that the proton arm would remain at the same momentum and the electron arm would change.

An analysis of the elastic cross sections (see Sec. 5.4.1) showed that the Mainz setup is stable within the systematic errors and the large number of elastic runs was eliminated for the October run period. Elastics were still taken but before and after each Q^2 setting.

Chapter 5

Cross Section Analysis Procedure

This chapter describes all the parts of the analysis needed to go from counts (50 gigabytes of raw data) to a final cross section.

5.1 Software

5.1.1 COLA++

The main analysis package used by the Mainz A1 group is COLA++ (COLA for short) [26] which takes the raw data (timing, wire information, scintillator energies) and turns it into physics variables event by event. COLA contains the optics matrices for the spectrometers and reconstructs particle trajectories (see Sec. 3.3.3). With these trajectories, the most probable energy loss corrections are applied (see Sec. 5.3.12) and physics variables are obtained. Missing mass, W , Q^2 , θ_{pq}^* , ϕ_{pq}^* , coincidence timing, and spectrometer coordinates are all sent to an ntuple file. This allows for very flexible cuts to be applied to the data without re-running the analysis.

5.1.2 Simul++

Cross sections cannot be calculated without knowing the spectrometer phase space acceptance in detail. Simul++ (Simul for short) is the software which calculates the multi-dimensional phase space acceptance. In addition to precise spectrometer prop-

erties and collimators, Simul also handles energy loss and the radiative corrections (see Sec. 5.3.11). The same energy loss corrections are applied to the data and the simulation so that the data and simulation will agree. Figures 5-1 and 5-2 show the very good agreement in all the variables except for the z vertex. The agreement varies from setting to setting so a procedure locates the regions with good agreement in the center of the acceptance (see Sec. 5.3.8).

Each simulated event contains the proper weighting for radiative corrections and the Jacobian. The events are sent to an ntuple which undergoes cuts identical to the cuts used on the data. The only differences are that there are no coincidence timing or background subtraction required for the simulation because only the coincidence is simulated and there is no background added.

The error in the Monte Carlo should not dominate the total error. The error in the data is well known from counting statistics but the error in the Monte Carlo is different. Simul uses a quasirandom number generator which converges $\approx n^{-2/3}$ [64] and corresponds to a true simulation error of $\approx 0.2\%$ for 1×10^4 counts. Since the convergence is approximate, the more conservative estimate of \sqrt{n} is used.

Figure 5-1 shows a comparison of the data for Q06-t24-p1 (an in-plane, forward setup) with the results of Simul weighted by the MAID2003 cross section and plotted against five physics variables: W , Q^2 , θ_{pq}^* , ϕ_{pq}^* , z_B . These variables are used because the cross section depends upon the first four and z_B affects the size of the spectrometer acceptance. z_B is the vertex position determined by Spectrometer B. Since that spectrometer has better vertex resolution, it is always used throughout this work to define the z vertex. As a result, z_B will typically be shortened to just z .

Figure 5-2 shows the same type of plots as Fig. 5-1 but for target and spectrometer variables: $\theta_0^A, \theta_0^B, \phi_0^A, \phi_0^B, |p_A|, |p_B|$. The θ_0 angles are the angle the particle trajectory makes between the spectrometer central axis (z) and the dispersive direction (x) at the target. The ϕ_0 angles are the trajectory angles between the spectrometer central axis (z) and the non-dispersive direction axis (y) at the target. The momenta magnitudes $|p_A|, |p_B|$ are the momenta of particles in Spectrometers A and B. Simul only simulates the target coordinates which are compared with the target coordinates

from COLA. COLA starts with focal plane coordinates and uses optics matrices to map back to target coordinates for comparison. Those target coordinates are then used to kinematically calculate the other physics variables such as W , Q^2 , θ_{pq}^* , etc.

As is clear in Fig. 5-1, there is very good agreement for all the variables across the acceptance except for z_B . The real edges of the z_B distribution are not as sharp as the simulated edges. However, this is not a problem as long as that region is avoided. Extensive studies show this to be the case (see Sec. 5.3.10). Note that the z coordinate is centered at -4 mm because of an offset present in the data. The offset was placed in the simulation for agreement but the effect is small, only 0.5% (from studies using both elastic and pion production data). Figure 5-2 also shows good agreement for the spectrometer variables. Other setups have similarly good agreement between data and simulation. This particular setup happens to agree well with the MAID2003 model which is not always the case for other settings.

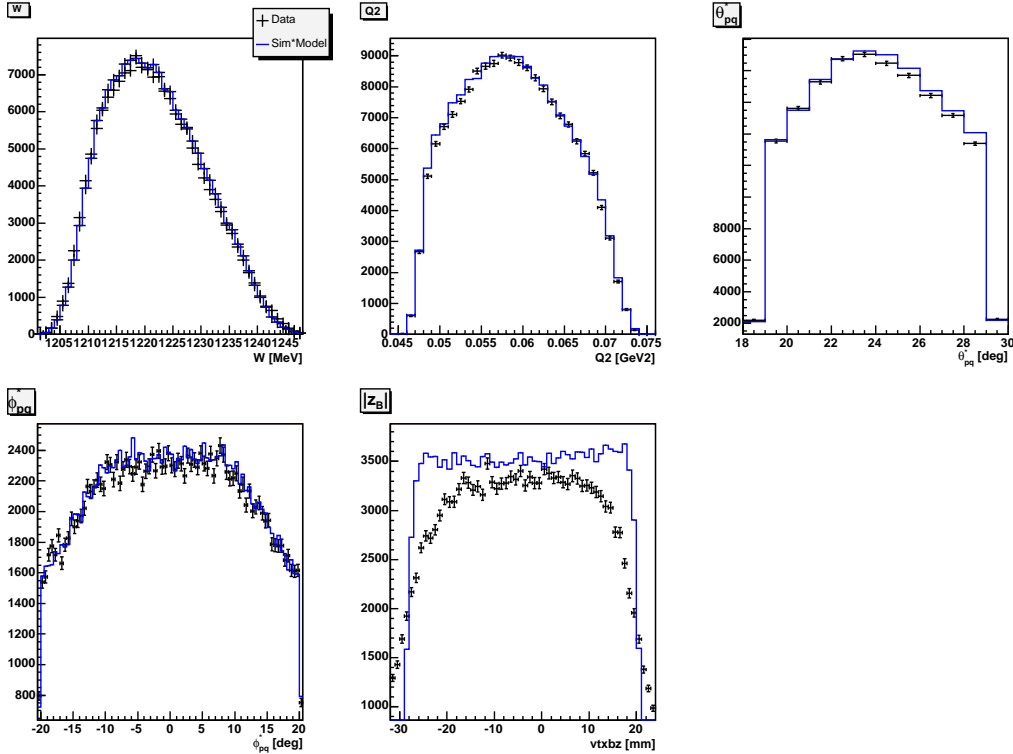


Figure 5-1: Comparison of the data and the simulation weighted by MAID2003 for the five variables typically used in the cut. The results are for the setup Q06-t24-p1.

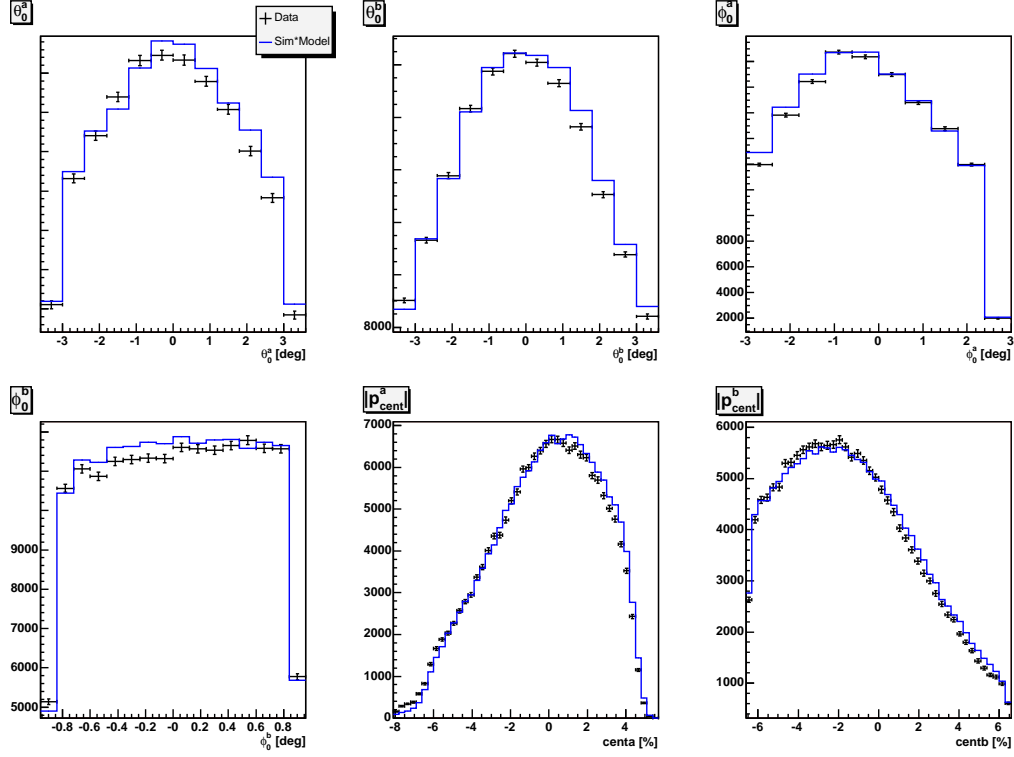


Figure 5-2: Comparison of the data and the simulation weighted by MAID2003 for the remaining critical variables. The results are for the setup Q06-t24-p1.

5.1.3 Lumi++

The luminosity is calculated using the Lumi++ program (Lumi for short) from Mainz. This software takes the raw data file, along with target information such as density and length and calculates the luminosity. Lumi takes the readout of the beam current from the Förster probe (see Sec. 3.1.4) and divides it by the number of turns the MAMI accelerator used. Each turn of the MAMI accelerator adds 7.5 MeV more energy to the electrons. So, with a starting energy of 180 MeV, after 90 turns, the electrons are at 855 MeV. Also, since the Förster probe is read before extraction, the current read out is larger than the extracted current by a factor that is the same as the number of turns. The Förster probe current must be scaled for this reason but the extracted current calculation is very precise.

Lumi also checks for wire chamber trips by looking for multiple consecutive events that do not contain information from a particular chamber. Occasionally, a wire in

one of the vertical drift chambers will begin to spark. More current is drawn and large currents can lead to chamber damage. The power supply will shut off before the current gets too large. A chamber trip means that useful data are no longer being taken. Standard procedure is to end the run and ramp the chamber back up to operating voltage. However, extra data may be taken in that time and we do not wish to use it. Lumi flags these regions and COLA uses this information to avoid them. Lumi and COLA work together to ensure that only good data are used in the analysis.

Lumi also uses scalers to determine the computer dead time and calculates the effective luminosity. It is this effective luminosity that is used to determine the cross section later.

5.1.4 ROOT

As mentioned above, the results from COLA and Simul are sent to ntuples which contain all the required information on an event-by-event basis. The detailed procedure for extracting a cross section is given in Sec. 5.3. Briefly, though, the software package ROOT [21] is used to load the ntuples from the simulation and COLA and place identical cuts on the data and simulation. The data are divided by the simulation and the luminosity to give a cross section as a function of several variables. The ROOT macros also allow for model results to be calculated on an event by event basis. This is important for collapsing the cross section to a point. That procedure is described in Sec. 5.3.9 but its purpose is to take a distribution of cross sections across the phase space and return a single result which can be compared directly with theory predictions. The end results of the ROOT macro are helicity dependent and independent cross sections which can be compared directly to models.

Using ROOT and ntuples allowed for a large amount of flexibility and speed. It aided the process of testing several models and also searching the phase space for any missing regions or other problems.

5.2 Detector Calibration

The Mainz A1 spectrometer setup has been in place in the A1 hall for approximately 10 years. As a result, massive calibration is not required prior to each experiment. Instead, some calibration runs are typically performed with a carbon target and then the hydrogen cryotarget.

With the carbon target, the kinematics are set for quasielastic scattering where the electron scatters off of a proton in the carbon nucleus. Because of the Fermi momentum of the target nucleon, the resulting distributions are not as sharp as for regular elastic kinematics. However, the advantage is that the entire focal plane in Spectrometer A is illuminated instead of a small part (see Sec. 5.4.1). Spectrometer B is fairly well illuminated in both settings but the distribution is wider for the quasielastic setup. Full illumination of the focal plane allows for checks of the wire chamber efficiency, modifying timing offsets, modifying scintillator offsets, checking timing and more.

After the quasielastic run, some regular elastic test runs were performed with the hydrogen cryotarget. Since the elastic kinematics are constrained, measuring any one of the variables p_e , p_p , θ_e or θ_p defines the other three. In this way, the momenta and angle offsets can be checked. In addition, the elastic cross section can be extracted confirming the target density and beam current measurements.

5.3 Cross Section Extraction

In this section, the procedure for extracting the cross section will be reviewed in detail.

5.3.1 Timing

Coincidence timing is critical for separating true events from background. For a true event, a proton must be detected in Spectrometer B and an electron in Spectrometer A within some time window. The timing for the experiment is defined by the scin-

tillators in the spectrometers. When the scintillators in Spectrometer A get a good hit (coincidence of left and right signals from the ToF scintillators), the coincidence TDC module is started with a coincidence gate. For the next 150 ns, the coincidence gate is open and any good event from Spectrometer B (only the ToF scintillator layer since B does not have left and right PMT's), will create a coincidence signal. The raw coincidence timing is shown in Fig. 5-3.

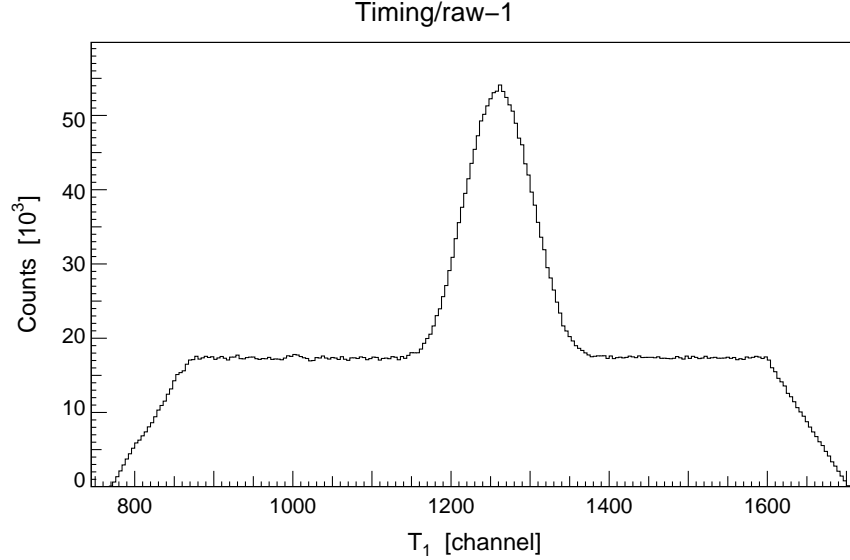


Figure 5-3: The raw timing spectrum for the $Q^2 = 0.060 \text{ GeV}/c^2$ parallel cross section. Each bin corresponds to a TDC channel of width 100 ps. The FWHM is approximately 10 ns.

The raw coincidence timing is spread out due to several factors:

- Particles will travel different path lengths depending upon their momentum and trajectory through the spectrometer.
- Light will take different amounts of time to reach the PMT's depending upon where in the scintillator the particle hits.
- Different time offsets for each scintillator depending upon electronics and the lengths of cable used.

These factors can be corrected for in software using track reconstruction information. The largest correction is the pathlength correction. In Spectrometer A, the

range of pathlengths can be up to 3 m [71]. This corresponds to 10 ns. The light travel time can also be accounted for by tracking where the particle hit the scintillator. The individual scintillator delay differences were adjusted with offsets so that all the timing peaks are aligned. The end result is the timing peak shown in Fig. 5-4. The remaining width of the coincidence peak is the intrinsic resolution of the PMT's and the electronics. The second peak at -2 ns is from the π^- background (see Sec. 5.3.2).

Also note when comparing Fig. 5-3 and 5-4 that the signal-to-noise ratio is much improved. The final timing plot also has broad, flat shoulders which are useful for background subtraction (see Sec. 5.3.3).

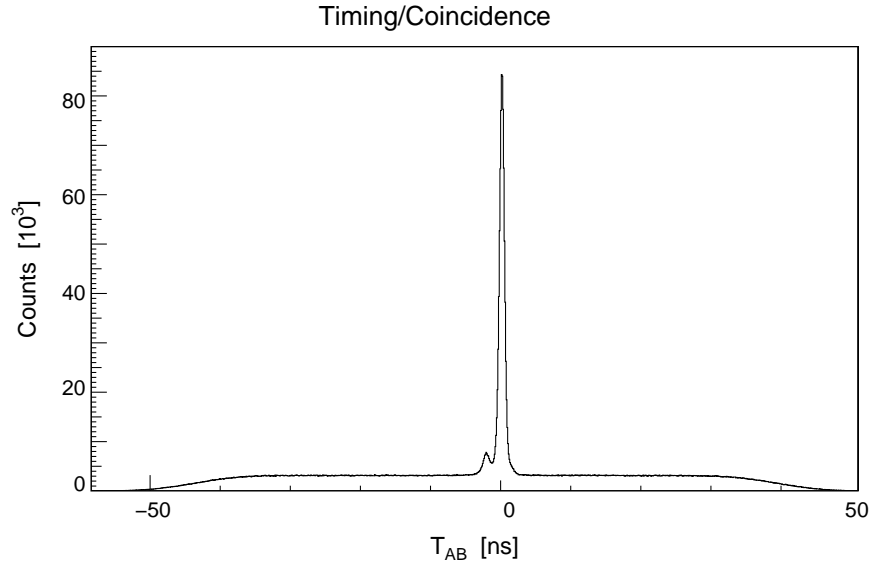


Figure 5-4: The software corrected coincidence timing spectrum for the $Q^2 = 0.060$ GeV/c² parallel cross section. The FWHM is approximately 1 ns. The second, smaller peak at -2 ns is from the π^-/μ^- background.

5.3.2 Particle ID and Missing Mass

For this experiment, timing and missing mass cuts are sufficient to uniquely identify the particles. Spectrometer A was used for electrons so any positively charged particles will not be detected. Another negative particle it could detect is the π^- or its decay product, μ^- , coming from two pion production and reactions with neutrons in

the target windows. With a central path length of 10.75 m and a central momentum of 437.5 MeV/c, the time for an electron to reach the focal plane is 35.9 ns. For the π^- , this time is 37.6 ns, a difference of 1.7 ns. A μ^- has a flight time of about 36.9 ns making it difficult to distinguish from the π^- . Also, only a fraction of the π^- decay in flight. Because the π^-/μ^- is not really in coincidence with the particle detected in Spectrometer B, the missing mass calculation will also be incorrect. A two dimensional plot of missing mass versus timing shows the π^-/μ^- to be clearly separated from the true coincidences (see Fig. 5-5). To further show that the extra peak consists of π^- s and μ^- s, a Cherenkov cut was placed on the data. The Cherenkov detectors are filled with Freon which has an index of refraction = 1.0012. The momentum threshold for Cherenkov radiation for electrons is about 10 MeV/c, for pions about 2.8 GeV/c and for muons about 2.1 GeV/c. Pions and muons will not trigger the Cherenkov detector while electrons will. The Cherenkov cut used in Fig. 5-6 required a hit in the Cherenkov detector. As can be seen in Fig. 5-6, the peak to the left of the central peak is gone. Taken together, all signs point to the second peak being pions and muons. As will be shown in Sec. 5.3.3, this two dimensional cut is unambiguous.

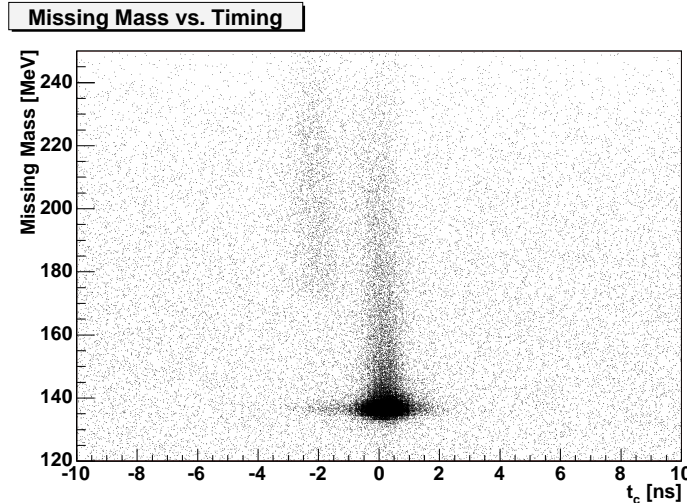


Figure 5-5: Missing mass vs. coincidence timing for one Q06-t0 run. Note the grouping of π^-/μ^- just to the left of the central coincidence peak.

Spectrometer B was set for detecting positive particles and its timing was set for

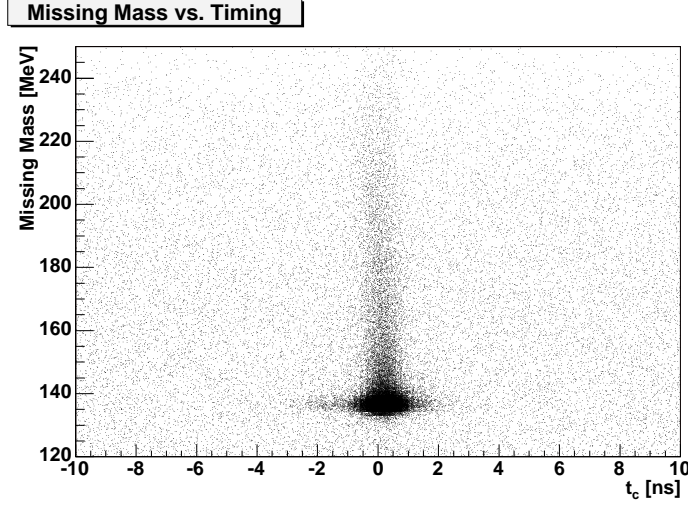


Figure 5-6: Missing mass vs. coincidence timing with Cherenkov cut for one Q06-t0 run. Note the second smaller peak to the left of the main peak is gone.

protons. Other positive particles that could be present are positrons and positively charged pions and muons. Given a central pathlength of 12.03 m and a central momentum of 573 MeV/c for Spectrometer B, a proton will take 77 ns to reach the focal plane. A pion requires 41.3 ns, a positron requires 40.1 ns and a muon 40.8 ns. A pion, muon or positron will then be so far out of time with the expected proton that they will be easily removed by the timing cut.

Missing mass was defined in Sec. 2.1 and for this experiment should be equal to the mass of the $\pi^0 = 134.98$ MeV. As mentioned Secs. 5.1.1 and 5.1.2, the energy loss in Simul and COLA is the most probable energy loss. However, as long as the simulation and data reconstruction perform the same operations, their results should agree. To check this, the missing mass was found from COLA and Simul for the various setups and the results can be found in Tables 5.1 and 5.2. Fig. 5-7 shows the comparison of missing mass data and the simulation for one setup. Other settings do not have alignment that is as good but all are within 1 MeV of the pion mass or less than 1%.

Setup	Data [MeV]	Sim [MeV]	ΔMM [MeV]
Q06-t0	136.68	135.97	0.71
Q06-t24-p1	136.85	136.45	0.40
Q06-t24-p2	136.93	136.05	0.88
Q06-t24-p3	135.81	135.85	-0.04
Q06-t36-p1	137.26	136.60	0.65
Q06-t36-p2	136.27	135.86	0.41
Q06-t36-p3	135.56	135.79	-0.22
Q127-q	135.80	135.85	-0.05

Table 5.1: Comparison of the central missing mass values from the data and the simulation.

Setup	FWHM(data) [MeV]	FWHM(sim) [MeV]	FWHM(dat/sim)
Q06-t0	2.97	2.66	1.12
Q06-t24-p1	4.27	3.19	1.34
Q06-t24-p2	3.97	3.63	1.10
Q06-t24-p3	4.27	3.81	1.12
Q06-t36-p1	5.45	4.63	1.18
Q06-t36-p2	5.16	4.56	1.13
Q06-t36-p3	4.99	4.38	1.14
Q127-q	3.14	2.70	1.17

Table 5.2: Comparison of the values for the Full Width Half Maximum (FWHM) from the various setups.

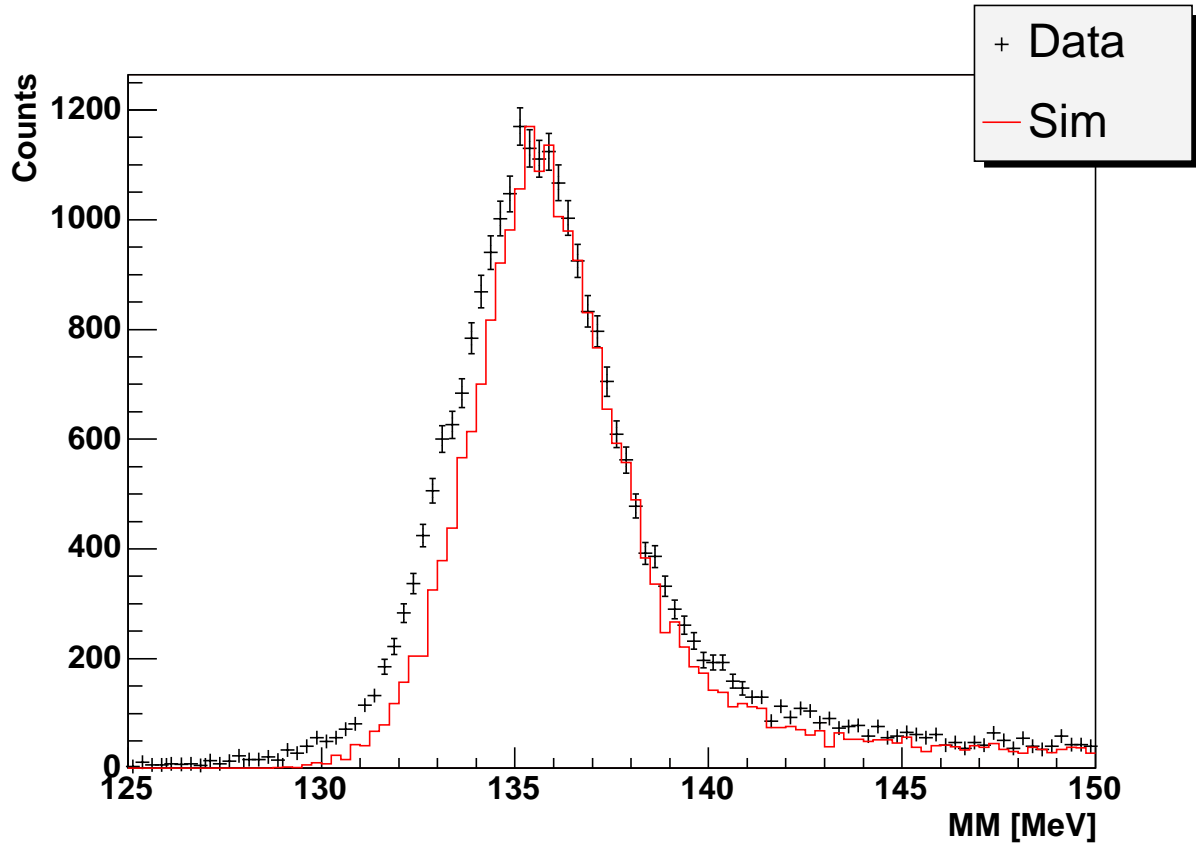


Figure 5-7: Comparison of the missing mass from the data (black crosses) and the simulation (red line) for setup Q06-t36-p3. Notice also that the width of the missing mass peaks are in good agreement.

5.3.3 Background subtraction

During the pion production runs, there were two types of backgrounds: π^-/μ^- background and general accidental background. The π^-/μ^- background was mentioned in Sec. 5.3.2 and can be seen in Fig. 5-5. It can be removed by making an elliptical cut like that seen in Fig. 5-8 and shown in Eq. 5.1.

$$\frac{(MM^2 - 200)^2}{2000} + (t_c + 2)^2 > 1 \quad (5.1)$$

However, this cut removes too much. To replace the background in that region, a second elliptical cut is made of equal size centered at -8 ns instead of -2 ns. The events in that region are added into the empty ellipse. The π^-/μ^- background is typically less than 2% of the coincidence events. A summary of the size of the π^-/μ^- background subtraction is in Table 5.3. The first π^-/μ^- column under Spect. cuts shows the percentage of pions/muons in the coincidence peak when only the basic spectrometer cuts are applied (more on the cuts in Sec. 5.3.8). When tighter cuts are applied using the physics variables (W , Q^2 , θ_{pq}^* , and ϕ_{pq}^*), the background decreases. Notice also that the π^-/μ^- background generally decreases as the angle of Spectrometer B becomes more backward.

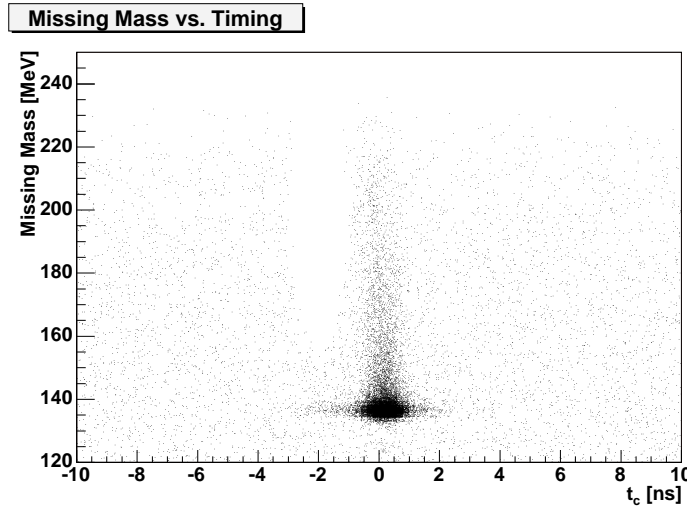


Figure 5-8: Missing mass vs. coincidence timing for one Q06-t0 run. Note the empty ellipse

After the π^-/μ^- cut, the data are ready for the second cut which is a strict timing cut of ± 3 ns. The tails of the timing peak merge with the background at that point. However, Figs. 5-5 and 5-6 have timing peaks on top of a flat background. That background extends underneath the coincidence peak and must be subtracted. One method would involve fitting the background and subtracting it away. However, another approach was used for this analysis. In Fig. 5-9, there is a flat region on either side of the coincidence peak. For the background subtraction, the events from -20 to -10 ns and 10 to 20 ns are integrated. Since this region is 20 ns wide and the coincidence region is only 6 ns wide, a factor of $6/20=0.3$ is used to scale the number of counts down. The resulting number is the estimated number of accidentals that are under the coincidence peak. The light gray region of Fig. 5-9 indicates that this estimate is very good. The accidental subtraction removes from about 6% to 20% of the events in the coincidence peak depending on the kinematics. The Accid. columns in Table 5.3 show the percentage of events removed from the coincidence peak for the spectrometer cuts (left) and with physics cuts (right). Again, the percentage tends to decrease as Spectrometer B is moved to more backward angles. Since the relativistic cone tends to boost particles forward, the backward region tends to have fewer accidentals and so a smaller background. The accidental subtraction is also the largest of the background subtractions.

After both the pion and accidental background subtractions, the data consist of pure coincidence events and a clean cross section can be extracted. The elastic runs do not have these backgrounds and are treated as pure coincidence events without any subtraction.

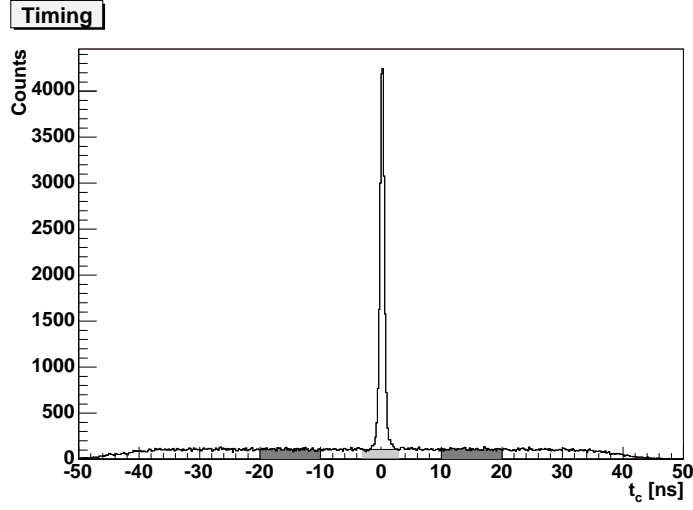


Figure 5-9: Coincidence timing peak after π^-/μ^- background subtraction. The dark gray regions are the background sample and the light gray region is the scaled background that is subtracted.

Setup	B angle [deg]	Spect. cuts		Spect. cuts + Phys. cuts	
		Accid. [%]	π^-/μ^- [%]	Accid. [%]	π^-/μ^- [%]
Q06-t36-p1	14.35	19.9	3.7	12.6	1.0
Q06-t24-p1	15.12	20.7	4.2	14.9	1.9
Q06-t24-p2	24.23	11.8	1.9	9.0	0.8
Q06-t0	24.23	14.0	2.3	11.4	1.2
Q06-t24-p3	33.34	9.6	1.0	9.0	0.9
Q06-t36-p2	33.95	7.3	0.7	5.8	0.1
Q06-t36-p3	38.08	6.2	0.7	5.4	0.2
Q127-q	47.47	17.6	4.0	16.1	0.2

Table 5.3: Size of the different background subtractions arranged from smallest to largest angle for Spectrometer B. The Spect. cuts column shows the results using simple cuts on the spectrometer acceptance. The Phys. cuts are cuts in W , Q^2 , θ_{pq}^* , and ϕ_{pq}^* . It is clear that the physics cuts clean up the background.

5.3.4 Luminosity

The luminosity is calculated based upon the total current measured by the Förster probe (see Sec. 3.1.4). The formula is

$$L = N_e N_t. \quad (5.2)$$

$$N_e = \frac{Q_{tot}}{e_c} = \frac{1}{e_c} \int_0^T I_e dt \quad (5.3)$$

where Q_{tot} is the total charge, e_c is the charge of the electron, and I_e is the instantaneous beam current.

$$N_t = \frac{\rho \bar{x} N_A}{A} \quad (5.4)$$

where ρ is the target density, \bar{x} is the average target length, N_A is Avogadro's number and A is the mass number. As will be mentioned in Sec. 5.5, \bar{x} and ρ contribute the most to the error in the luminosity.

The average target length is difficult to determine exactly because the cryotarget has never been measured while cold. The warm size is known to be 49.5 mm but the target may expand due to the pressure or contract due to the cold. Which effect is larger is unknown. In addition, due to the shape of the target and the beam rasterization (see Sec. 3.2), the effective length of the target is slightly less than the 49.5 mm warm length. The rounded endcaps lessen the amount of hydrogen the beam passes through off-axis. The Lumi software assumes a box target with the design length but Simul properly handles the beam rasterization in its generator. During the April run, the beam was also placed off-center to ensure a cleaner path to the out-of-plane Spectrometer B (see Sec. 3.1.3). This decreased the effective target length (see Fig. 5-10). Again, Simul properly accounts for the off-axis beam and the irregular target shape.

The value for ρ is determined from the target temperature and pressure and then found from the tables at [59]. In addition, a fit to the tables has been performed by

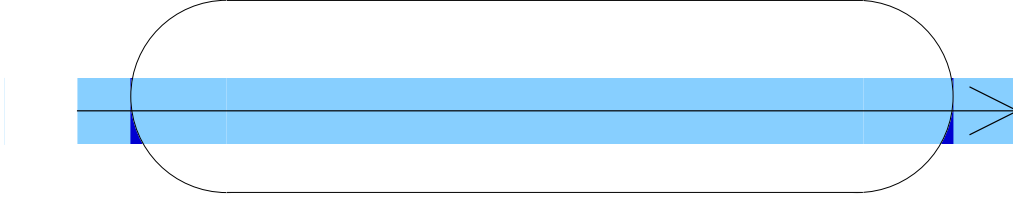


Figure 5-10: The off-axis, rastered beam along with the target's shape leads to an effective target length (lighter inside target) less than the design length (darker areas just outside the target). This effect is handled in the simulation.

S. Sirca and can be expressed as

$$\begin{aligned} \rho_{LH2}(T, p) = & (0.0732356 + 9.308 \times 10^{-4}T - 5.1501 \times 10^{-5}T^2) \\ & (1 + 1.9018 \times 10^{-3}(p - 2.0)) \end{aligned} \quad (5.5)$$

with T in K and p in bar. During the April runtime, the pressure was near 1.965 bar with a temperature near 22 K yielding $\rho=0.06878$ g/ml. During October, the pressure was lower, near 1.895 bar with a similar temperature yielding $\rho=0.06877$ g/ml. The normal operating pressure for the target is 2.1 bar. With a normal temperature of 22 K, this leads to an undercooling of 1 K. This buffer allows for a certain amount of local heating without the target starting to boil. However, running at the lower pressure led to less undercooling as can be seen in Fig. 5-11. Instead of 1 K undercooling, the experiment operated closer to 0.6 K undercooling. With high beam currents, the target was more likely to boil than usual due to local heating.

Previous measurements of the cross section with varying beam current showed that target boiling is not a problem up to 25 μA with normal target pressure. Due to the lower pressure, target boiling can be a problem for some of our data with higher beam currents.

One check was run during the October beamtime because of a general concern about high current running. The parallel cross section for $Q^2 = 0.20$ (GeV/c)² at $W=1225$ MeV was measured for 2.5 hours at 25 μA and for 5 hours at 12.5 μA so that

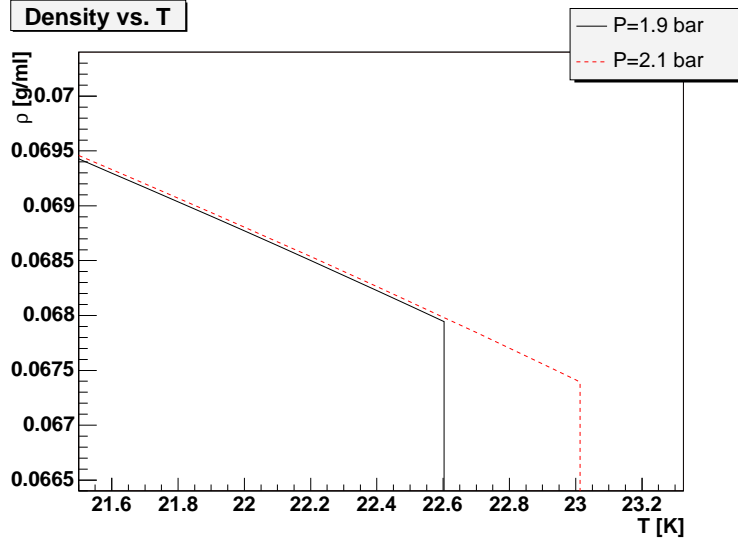


Figure 5-11: Target density plotted against temperature for two pressures, the standard pressure of 2.1 bar and the pressure used during this experiment of 1.9 bar. Notice that the standard temperature of 22 K is much closer to the gas phase (the sharp drop in density on the right of the plot). With higher beam currents, the target was more likely to boil than usual.

both runs had the same statistics. The average singles rates and beam currents are in Table 5.4. The effect of the higher beam current is seen by finding the rate divided by beam current (which is proportional to counts per current). Table 5.4 shows that at higher beam currents, the counts are lower by almost 2.5%. This clearly shows that some target boiling is occurring.

Of course, the pressure was at its lowest during the October runs which is when this check was performed. In addition, the boiling effect is expected to have a threshold behavior. Below some critical beam current, there is enough cooling power to keep the target from boiling. The singles rates in Spectrometer A were used to study this effect. Spectrometer B was rarely in the same place from one setup to another but Spectrometer A was returned to the same location repeatedly. By plotting the singles rate in A versus beam current, any target boiling effect should be visible. Figure 5-12 shows the A singles rate divided by the beam current for all the $Q^2 = 0.060$ (GeV/c)² runs. Also plotted are the average and the RMS deviation of all of the data. Notice that almost all of the points are consistent with a horizontal line which

Setup	I [μA]	Rate A [kHz]	Rate B [kHz]	A/I [kHz/ μA]	B/I [kHz/ μA]
Q20_W1225	25.06	40.51	21.29	1.617	0.850
Q20_W1225_low	12.38	20.51	10.79	1.656	0.871
			High/Low	0.976	0.976

Table 5.4: Average singles rates divided by average beam current which is proportional to counts per charge. The last line shows the result of the higher beam current. The counts are suppressed by about 2.5% when the beam current is at $25\mu\text{A}$.

indicates no beam current dependent luminosity change. It is clear that the low Q^2 runs were below the boiling threshold and do not need any correction.

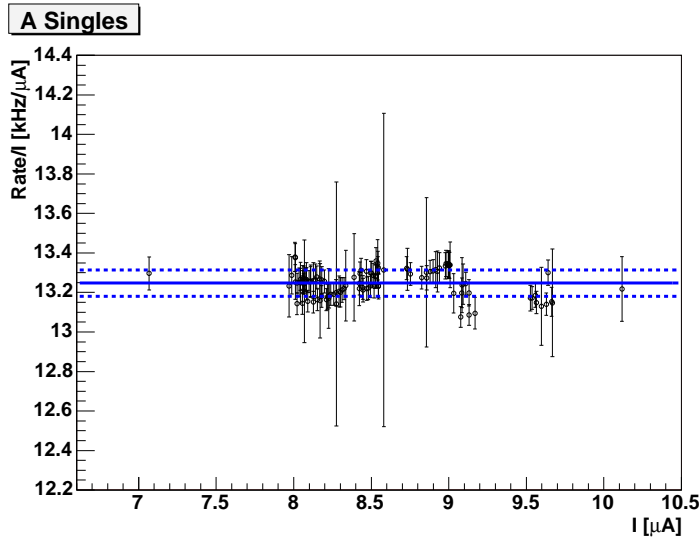


Figure 5-12: The singles rate in spectrometer A divided by the beam current for all the $Q^2 = 0.060 \text{ (GeV/c)}^2$ runs in the April beam time period. The lines show the average and RMS deviation of all the data points. Most of the data are within the errors. Even over a range of $3 \mu\text{A}$, there is no large target boiling effect.

However, other April data were taken with higher beam currents. Specifically, the parallel cross section comparison with Bates data (see Sec. 5.4.4) was taken with 25 to $30 \mu\text{A}$ of beam current. It is possible that these runs were taken above the boiling threshold. To test this, the singles rates from spectrometer A divided by the current was plotted in Fig. 5-13 for all the $Q^2 = 0.127 \text{ (GeV/c)}^2$ runs. In addition, a line was fit to the data of the form

$$y = C(1 - \delta x) \quad (5.6)$$

where C is a constant scaling factor and δ is the slope. The results of the fit in Fig. 5-13 are: $C = 4.66 \pm 0.13 \text{ kHz}/\mu\text{A}$ and $\delta = 0.0038 \pm 0.001 \mu\text{A}^{-1}$. This indicates a current dependent effect of 2% between 25 and 30 μA . The overall effect is even larger depending upon where the threshold is. However, the fitting errors encompass a large region which is consistent with a flat line as well as a boiling effect.

Notice in Fig. 5-13 that the Q127-q results are actually flat with respect to beam current. It is the other $Q^2 = 0.127 \text{ (GeV/c)}^2$ settings that are driving the slope. To investigate further, the parallel cross section was extracted from the 25 μA and 30 μA runs separately with identical cuts. The results are shown in Table 5.5. The errors are large compared to the difference but there is a difference of about 1.3% with the cross section showing the same trend versus beam current. Since the cross section is known to be flat versus beam current to 10 μA (from Fig. 5-12), this places an upper limit on the effect. Assuming the same trend that appears between 30 to 25 μA , the cross section at 10 μA would be 10.631 $\mu\text{b/sr}$. So, at most, this effect is almost 5% but it is most likely less. During the October run, the effect was measured to be 2.5% rather precisely. Assuming the threshold is actually at 12.5 μA , then the effect in April should be even smaller. The higher pressure will move the threshold to larger beam currents.

It is difficult to assign a final number to the effect due to the lack of data. However it is possible to adopt a correction factor which is consistent with the available data. The corrected luminosity, L_{corr} , is

$$L_{corr} = \frac{L}{1 - (I - 12.5)0.002} \pm 0.01L \quad (5.7)$$

where L is the otherwise fully corrected luminosity, and I is the beam current in μA . The error from this factor contributes to the overall systematic error. As mentioned above, only runs with beam currents above 12.5 μA will be affected by the correction. These settings are shown in Table 5.6 and do not include the primary low Q^2 data points.

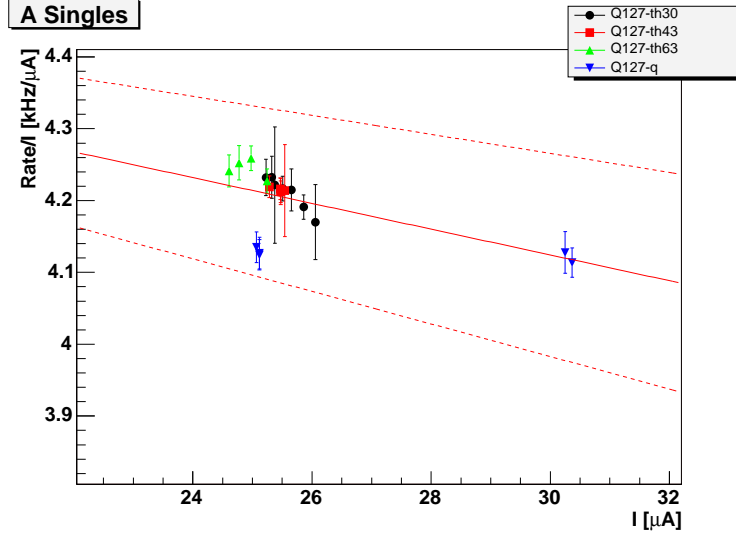


Figure 5-13: The singles rate in spectrometer A divided by the beam current for all the $Q^2 = 0.127 \text{ (GeV/c)}^2$ runs in the April beam time period. The line through the points clearly shows a non-zero slope most likely indicating target boiling. The upper and lower dashed lines represent the fitting errors.

I [μA]	XS [$\mu\text{b/sr}$]
25	10.250 ± 0.161
30	10.123 ± 0.196

Table 5.5: Parallel cross section results for $Q^2 = 0.127 \text{ (GeV/c)}^2$ as a function of beam current.

Q06_W1185
Q06_W1205
Q06_W1225
Q06_W1245
Q06_W1275
Q06_W1300_low
Q127-q
Q126_W1232
Q126_W1232_p1,2
Q127-w1140-p1,2
Q127-th30,43,63

Table 5.6: Settings which require the luminosity correction. Factors can be found in Tables 6.2 and 6.6.

5.3.5 Dead time

As mentioned in Sec. 5.1.3, the deadtime from the overall experimental setup is corrected by the Lumi software. Deadtime is the time during data taking when all the devices are on but an event is not detected. If an event arrives during a period when the setup is dead, then the event will be missed and these missed events must be corrected for. Deadtime can have many sources.

1. Intrinsic deadtime of the detectors.
2. Electronic deadtime of components.
3. Electronic deadtime of computer.

The intrinsic deadtime of the detectors is very small. If two events are extremely close to each other in time such that the wire chambers or the scintillators cannot tell the two apart, then the detector is effectively dead for the second particle. The intrinsic deadtime could become an issue at very high rates but as will be shown, other sources of deadtime will have long dominated the data rate.

The electronic deadtime of the components is also very small in comparison to the dominant deadtime, that of the data acquisition system. The frontend computer on each spectrometer takes approximately 1 ms to readout all of the channels [35]. There would then be 100% deadtime for a data rate of 1 kHz. The data rates were kept well below this but deadtime is still a factor.

Calculating or simulating all of the deadtimes is difficult so the practical approach is to use the BUSY outputs of the electronics. All of the electronic components have a BUSY output when they are busy. All of these signals are fed into a scaler unit VETO. The number of fast triggers from the scintillators is sent to a scaler. That scaler is not vetoed at all and a copy of it is vetoed by all the BUSY signals. By comparing these two numbers, Lumi can determine how many events were missed while the components were busy. Then, Lumi outputs a corrected luminosity number which can be used with the data. The error in this corrected luminosity depends

upon the number of counts in the scaler but for a typical run, is less than 0.5%. A more detailed explanation involving all the spectrometers is in [35].

5.3.6 Detector/trigger/chamber efficiencies and checks

Each detector in the experimental setup has an inefficiency which must be corrected for. During this experiment, not all of the individual inefficiencies were measured but the overall inefficiency was checked using the elastic cross section (see Sec. 5.4). However, from previous experiments, many of the inefficiencies have been determined.

From [71], the combined efficiency of the Spectrometer A and B scintillators is 98.7%. From [66], the efficiency of combining the two separate data streams for a coincidence measurement is 99.6%.

For the vertical drift chambers, there are two efficiencies, individual and overall efficiency. The individual chamber efficiencies can be determined by looking at the single wire efficiency. These plots are created event by event by first filling a tagged wire histogram. All of the wires between and including the two extreme wires in an event are tagged by placing a count in the bin corresponding to each of those wires. For example, if the extreme wires are 90 and 95, then one count is placed in the bins for wires 90, 91, 92, 93, 94, and 95. Then a second histogram is filled with actual counts from each wire (e.g. 90,91,92,94, and 95). After a run has been processed, the ratio of the total wire hits over the total tagged wires yields the single wire efficiency. A plot of a typical single wire efficiency histogram is shown in Fig. 5-14. The typical efficiency for x layers is $\geq 99\%$ and for s layers, $\geq 96\%$. Most s layers are closer to the x layers in efficiency but there are some which are lower.

The overall VDC efficiency for each Spectrometer would be $(0.99)^4$ if all 4 VDCs acted as independent detectors. However, the VDCs track particles and can recreate tracks even when missing many wires. From [71], a particle track can be safely reconstructed with as few as 3 wires in the x chambers and 3 wires in the s chambers. So, only when the joint multiplicity for a Spectrometer drops below 6 will there be any problems. The typical joint multiplicity is near 18 with very few events in the low count region. In [71], computer simulations were carried out for multiple

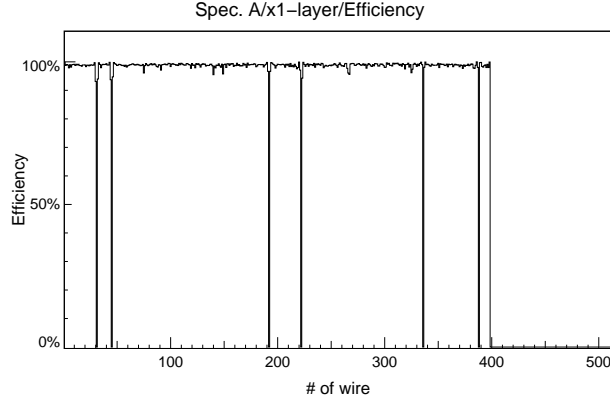


Figure 5-14: Single wire efficiency histogram for the x1 layer of Spectrometer A from setting Q06-t24-p1. Wires 31,45,192,222,336, and 388 have no response and so show up as gaps. The single wire efficiency for this chamber is $\approx 99\%$.

settings to determine the overall efficiency of the chambers. The average efficiency for Spectrometer A VDCs was 99.6%. The average efficiency for Spectrometer B VDCs was 99.9%. This gives an overall efficiency of 99.5% for the VDCs in coincidence.

The efficiency correction factor used on the data comes from the scintillator efficiency, coincidence efficiency, and overall VDC efficiency:

$$\epsilon_{tot} = \epsilon_{scint}\epsilon_{coinc}\epsilon_{VDC} = 0.987 \times 0.996 \times 0.995 = 0.978 \quad (5.8)$$

Therefore, the correction factor applied to the data is $1/0.978 = 1.022$. From [66] and [71], the systematic error in the inefficiency correction is estimated to be 1%.

Not included in the previous correction factor are the reconstruction errors. The algorithm that determines the track provides an error estimate derived from the fit to the track. In some cases, the fit is bad because the track cannot be properly reconstructed. This mostly results from delta production in the gas chambers. As a result, the electron continues on a much different path and the track reconstruction routine cannot get a good fit. These bad tracks can be cut out with the proper cut on the reconstruction error. (Only the electron has significant delta production and so only Spectrometer A is affected).

Fig. 5-15 shows the log-log plot of the counts versus the error in the focal plane

x coordinate for Spectrometer A. The right bump contains the poorly reconstructed events. A cut is then placed to allow only data for $\log \Delta x_A < -0.2$. The size of the correction is typically $\approx 1\%$. However, for a typical setting, the error in the correction is statistics limited to 1%. In practice, placing the Δx_A cut and correcting for it gives the same result as not using the cut so this cut is not used.

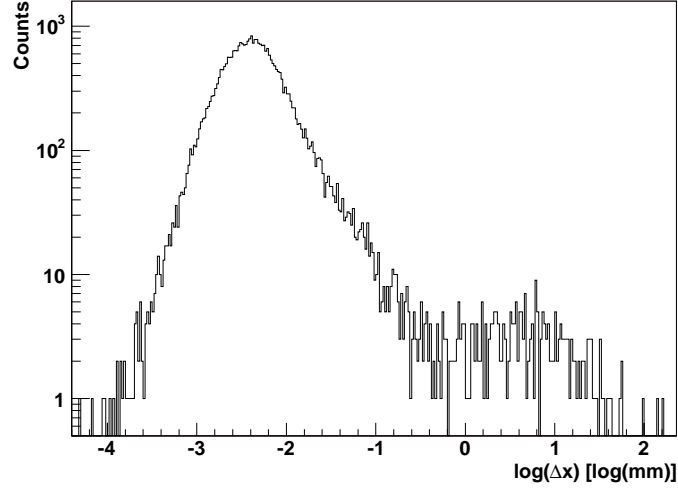


Figure 5-15: Log-log plot of counts versus $\log \Delta x$ for Spectrometer A. The small bump on the right near 0.8 are the poorly reconstructed events. For this setting, Q06-t24-p1, the bad events are about 1% of the total.

5.3.7 Phase space overlap

The pion production cross section seen by the spectrometers is a function of four variables: $W, Q^2, \theta_{\pi q}^*, \phi_{\pi q}^*$ (see Sec. 2.1). The extent of these variables is different for each setup. This is due to many things including different acceptance, boosts, correlations, etc. The extraction of the cross section involves collapsing them to a central point (see Sec. 5.3.9). However, to minimize the systematic errors of the collapse, while designing the experiment, the central kinematic values for each of the sequential measurement setups were made to agree. It was checked that the kinematics allowed for a large overlap of variables. Fig. 5-16 shows the extent of the overlap for the $\theta_{pq}^* = 24^\circ$ setup.

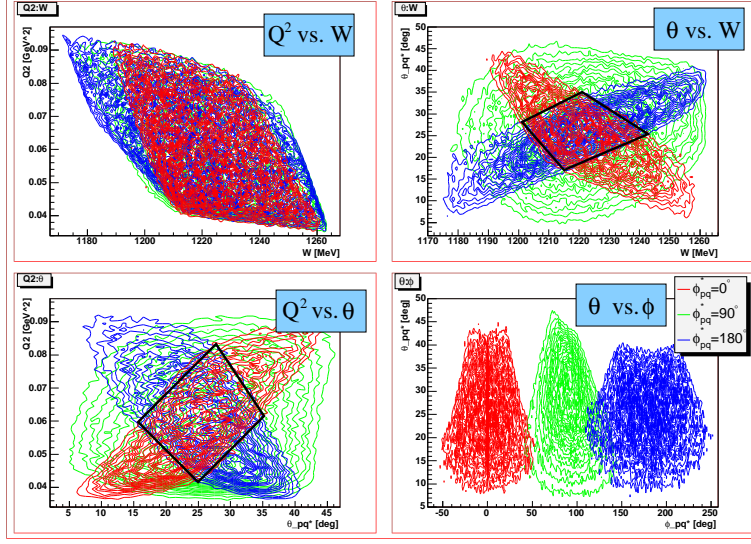


Figure 5-16: Plot of the overlap of the sequential settings for $Q^2 = 0.060$ $(\text{GeV}/c)^2$, $W = 1221$ MeV, $\theta_{pq}^* = 24^\circ$. Red corresponds to $\phi_{pq}^* = 0^\circ$, green to $\phi_{pq}^* = 90^\circ$ and blue to $\phi_{pq}^* = 180^\circ$. The overlap regions have been marked. The W overlap is approximately 40 MeV, the $\Delta Q^2 \approx 0.04$ GeV^2/c^2 , $\Delta\theta_{pq}^* \approx 10^\circ$, and $\Delta\phi_{pq}^* \approx 40^\circ$.

The setting used for $\theta_{pq}^* = 24^\circ$ was called a “cross” setting during the OOPS experiment [48] and has certain advantages. Asymmetries can be formed which allow for the easy separation of the σ s. In addition, the $\sin\phi$ term is a maximum allowing for a smaller error on $\sigma_{LT'}$. However, due to the kinematic constraints of the Mainz spectrometers, θ_{pq}^* above 24° at $W = 1221$ MeV and $Q^2 = 0.060$ $(\text{GeV}/c)^2$ could not be reached in the cross configuration. Larger θ_{pq}^* values are important because the cross sections tend to increase with increasing angle up to 45° for σ_{LT} and $\sigma_{LT'}$ and up to 90° for σ_0 and σ_{TT} (see Fig. 7-3).

The σ s can be extracted from any three ϕ angle settings but the errors typically increase for non-cross settings. It was found that keeping the three ϕ angles as far apart as possible was advantageous. The $\theta_{pq}^* = 37^\circ$ setting had two out-of-plane setups and one in-plane. However, there was a complicating factor. An interference between the spectrometers prevented reaching the most forward setting. As a result, the overlap for the larger angle is not as good as for the smaller angle (see Fig. 5-17). However, since a collapse method is used, strict overlap is not required and slight

differences can be accounted for but with an increase in systematic error.

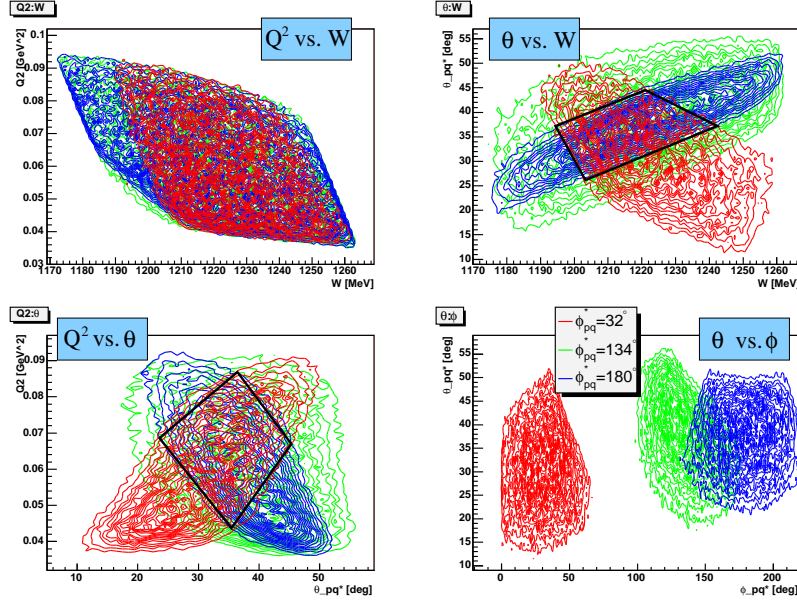


Figure 5-17: Plot of the overlap of the sequential settings for $Q^2 = 0.060$ (GeV/c) 2 , $W = 1221$ MeV, $\theta_{pq}^* = 37^\circ$. Red corresponds to $\phi_{pq}^* = 32^\circ$, green to $\phi_{pq}^* = 134^\circ$ and blue to $\phi_{pq}^* = 180^\circ$. The overlap regions have been marked. The W overlap is approximately 40 MeV, the $\Delta Q^2 \approx 0.04$ GeV $^2/c^2$, $\Delta \theta_{pq}^* \approx 20^\circ$, and $\Delta \phi_{pq}^* \approx 40^\circ$.

5.3.8 Definition of cuts

As mentioned in Secs. 5.3.1 and 5.3.2, timing and particle identification cuts are placed on the data. After the two dimensional pion/muon cut, a ± 3 ns cut is placed around the coincidence peak. The accidental background is subtracted and the remaining events are the true coincidences.

Typically there are cuts on the missing mass. However, the agreement between the data and the simulation diminishes as the missing mass increases (see Fig. 5-18). If the entire missing mass peak is used, then the difference is not important. The full radiative calculation is still used for each event but only the vertex correction will contribute an appreciable amount. (see Sec. 5.3.11).

After the coincidence timing cut and missing mass cut, spectrometer acceptance

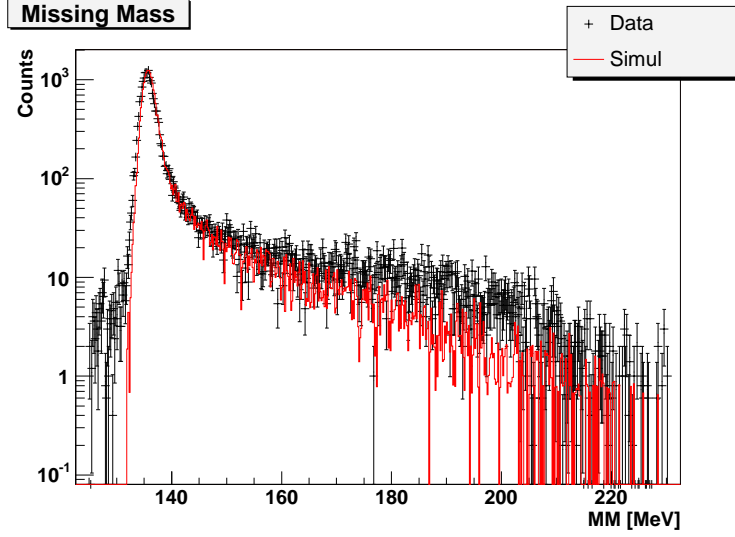


Figure 5-18: Comparison of the missing mass for data and simulation for the $Q^2 = 0.127 \text{ (GeV/c)}^2$ parallel cross section at $W = 1232 \text{ MeV}$.

cuts are placed. The momentum cuts are important because Simul does not simulate any events outside of the defined region. However, the real spectrometers have events outside the simulated region. For added verification that the cuts are not affected by being near an edge, the momentum cuts were decreased by 2% from each edge for Spectrometer A and 1% for Spectrometer B. The central momentum cuts were then $\pm 8\%$ for Spectrometer A and $\pm 6.5\%$ for Spectrometer B.

As mentioned in Sec. 3.3, the spectrometers have collimators inside of them. Simul uses these collimators to recreate the phase space. To ensure a clean cross section that is free of edge effects, the cuts in Table 5.7 are used. The numbers were found using the comparison of the simulation and the data shown in Fig. 5-19. The edges of the plots were then found and are used as the cuts. It should be noted that these cuts are to make sure that the extracted cross section comes from a region away from any edges. These cuts are meant to be general and so are not overly strict. The more precise cuts are detailed next.

As shown in Sec. 5.3.7, the phase space changes for each setup. This is mainly due to the different locations of the spectrometers relative to the momentum transfer direction. The Lorentz boosts are different and so the phase space volumes are not

Cut	Orig	Current
$ p_a <$	10%	8%
$ p_b <$	7.5%	6.5%
ϕ_0^A	$-5.16 \rightarrow 5.16$ deg	$-3 \rightarrow 2.5$ deg
θ_0^A	$-4.01 \rightarrow 4.01$ deg	$-3.5 \rightarrow 3.5$ deg
ϕ_0^B	$-1.15 \rightarrow 1.15$ deg	$-0.9 \rightarrow 0.9$ deg
θ_0^B	$-4.01 \rightarrow 4.01$ deg	$-3.6 \rightarrow 3.6$ deg

Table 5.7: Acceptance cut comparison.

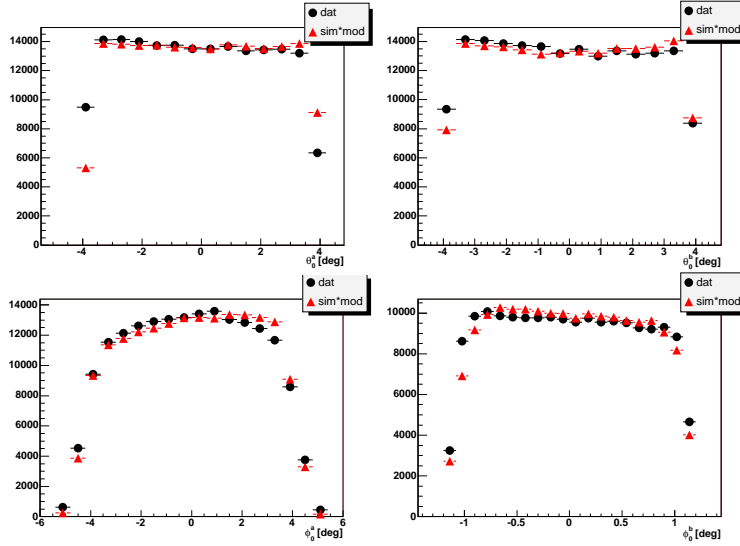


Figure 5-19: Comparison of data and simulation weighted by the Sato-Lee cross section for Q127-q spectrometer acceptance variables.

the same. For this reason, defining cuts on the physics variables (W , Q^2 , θ_{pq}^* , ϕ_{pq}^*) is difficult. Choosing a set width for all settings will not always be good for each setting. The method that was decided upon defines the cuts in a relative way. The first analysis pass finds the edges of the one dimensional distributions of W , Q^2 , θ_{pq}^* , ϕ_{pq}^* and z . The z variable is added to the list of physics variables because the comparison of the z vertex from the data and simulation varied over the runs. The differences were near the edges and these regions are avoided.

The first analysis pass finds the edges of the one dimensional distributions by taking the average of several of the central bins. The average is less susceptible to problems due to bin-to-bin variations. The one dimensional plots are all normalized

so that the central average is at 1.0. The macro then finds where the distribution differs by more than 50% from the central average. Typically, these points are about halfway down the shoulders on the edge of the distribution. However, occasionally the plots have a steady slope. In this case, the 50% cut still includes most of the distribution and is near the edges.

The first analysis pass cuts are then forced to be symmetric around the central value. The purpose is to prevent weighting the results with asymmetric cuts. The collapse should take asymmetries into account but the correction factors should also be kept as small as possible so that the systematic error from the collapse is small (see Sec. 5.3.9). The results of the first pass of the cuts are the outer vertical lines in Fig. 5-20. Those lines correspond to the point where the distribution is half the central value.

The second pass of the macro places cuts on the data based upon the width of the first pass cuts. Cuts were typically 50% or 75% of the width of the first pass cut. In Fig. 5-20, the innermost vertical lines mark 75% of the width of the outer cuts. Defining cuts in this way allows them to be determined consistently from setup to setup. Also, the cuts can then be varied in a simple way to check how sensitive the cross section results are to the cut widths. After studying the results across all of the kinematics in the data set, the width that gave the most consistent results was the 75% width using 50% of the maximum to define the edges (see Sec. 5.3.10).

This cut definition procedure yields cuts which are away from the edges of the acceptance and are stable to small changes in the cuts and can be determined in a consistent manner across setups. All of the central cut values and cut widths are in Appendix D.

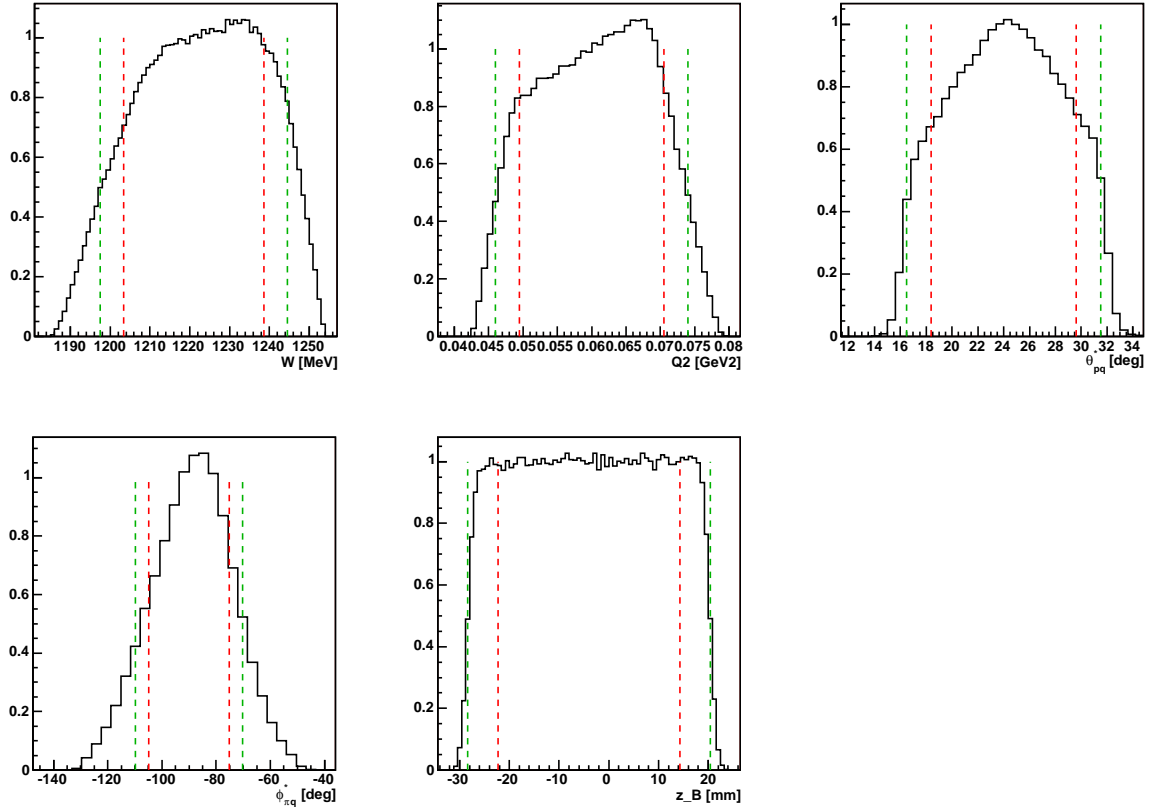


Figure 5-20: Physics variables for setup Q06-t24-p2 with cuts. The outer dashed lines mark the first pass cuts and the inner dashed lines show the second pass, final cuts.

5.3.9 Cross section extraction and collapse to point

The results of Simul, COLA, Lumi are all fed into special ROOT macros which yield cross sections. After the simulation and data are filtered with identical cuts (see Sec. 5.3.8), the background subtracted data are divided by the Jacobian and radiative correction weighted simulation and scaled by the luminosity to give the average cross section.

The average cross section, XS_{avg} is calculated by

$$XS_{avg} = \frac{H_{dat}N_{cts}}{H_{sim}L_{tot}} \quad (5.9)$$

where L_{tot} is the total, effective luminosity, N_{cts} is the number of counts thrown at the simulation, H_{dat} is the histogram containing counts, and H_{sim} is the histogram containing the simulated phase space. If the histograms contain only one bin, then the result, XS_{avg} is the average over the cuts in phase space. One can choose to use more than one bin in the histograms in which case the results are the average cross section as a function of the histogram bin variables. Either way, the results have been averaged and are not directly comparable to theory point cross sections.

To compare the averaged cross section to theory, a collapse procedure is applied to the data. This is also known as bin centering corrections [7] or transport. The issue is that the data are spread out over a large phase space in multiple dimensions. If possible, the best comparison of the data and theory is to run the simulation with the theory and compare. However, when the results are in more than two dimensions, it becomes difficult to quantify the level of agreement. Instead, if the theory varies in the same way across the phase space as the data varies, then the ratio of the theory point cross section to the theory average cross section can be used to scale the average data cross section to a point data cross section. This technique does not rely upon the absolute size of the theory but merely requires that the theory have the same shape throughout the phase space region of the cuts. A small (0.5%) systematic error is introduced with this method (see Sec. 5.5).

The first step is to obtain the average of a model over the same phase space. A

Setup	Collapse Factor for MAID2003
Q06-t0	1.007
Q06-t24-p1	0.989
Q06-t24-p2	1.030
Q06-t24-p3	1.006
Q06-t36-p1	1.124
Q06-t36-p2	1.028
Q06-t36-p3	1.022

Table 5.8: Collapse factors using MAID2003 for the various settings. Statistical errors on the factors are 0.005. The Q06-t36-p1 has the largest correction.

slight modification of Eq. 5.9 gives

$$XS_{avg}^{model} = \frac{H_{sim}^{model}}{H_{sim}} \quad (5.10)$$

where H_{sim}^{model} is the same as H_{sim} except that each event is weighted by the model cross section. Again, the binning of the histograms can be 1 bin for an overall average or several to see the variation of the cross section. Typically, the analysis uses one central bin.

The central assumption, which is checked by plotting versus several variables and using different models and cuts is that

$$\frac{XS_{cent}}{XS_{avg}} = \frac{XS_{cent}^{model}}{XS_{avg}^{model}}. \quad (5.11)$$

If Eq. 5.11 holds, then it can be rearranged to give

$$XS_{cent} = XS_{avg} \frac{XS_{cent}^{model}}{XS_{avg}^{model}} = XS_{avg} F_{point}^{model} \quad (5.12)$$

where F_{point}^{model} is the factor to collapse from the average cross section to the central, point cross section. Typical collapse factors are shown in Table 5.8. An examination of Table 5.18 shows that the collapse factors are all very similar leading to a model dependence about the same size as the statistical error.

As mentioned above, this method of collapse can be tested by varying the size of the cuts. As the cuts get smaller and smaller, then the average gets closer to the point

cross section. Unfortunately, the statistics also get worse and the errors are such that very small cuts do not give extra information. However, by varying the cuts smoothly and plotting the results, any instabilities in the extraction can be spotted. The goal is to settle in a stable region of cuts. More about this is covered in Sec. 5.3.10.

For the parallel cross section analysis, the collapse step is the final step since the cross section only contains σ_0 . However, for the rest of the analysis, more is required. For the non-parallel setups, there are three separate point cross sections for three different values of ϕ_{pq}^* . The form of the cross section (as shown in Sec. 2.2) is

$$\begin{aligned} \frac{d\sigma_v}{d\Omega} &= \frac{d\sigma_0}{d\Omega} + \sqrt{2\epsilon(1+\epsilon)} \frac{d\sigma_{LT}}{d\Omega} \cos \phi \\ &+ \epsilon \frac{d\sigma_{TT}}{d\Omega} \cos 2\phi + hP_e \sqrt{2\epsilon(1-\epsilon)} \frac{d\sigma_{LT'}}{d\Omega} \sin \phi \end{aligned} \quad (5.13)$$

Adding the cross section results taken with the positive and negative helicities cancels the h dependent part leaving three unknown cross sections. Since there are three known spectrometer cross sections, algebra can be used to extract the cross sections.

The extraction of the differential cross sections (σ_i) from the helicity independent spectrometer cross sections (X_i) starts with:

$$\begin{pmatrix} 1 & v_{LT} \cos \phi_1 & \epsilon \cos 2\phi_1 \\ 1 & v_{LT} \cos \phi_2 & \epsilon \cos 2\phi_2 \\ 1 & v_{LT} \cos \phi_3 & \epsilon \cos 2\phi_3 \end{pmatrix} \begin{pmatrix} \sigma_0 \\ \sigma_{LT} \\ \sigma_{TT} \end{pmatrix} = \begin{pmatrix} X_1 \\ X_2 \\ X_3 \end{pmatrix} \quad (5.14)$$

Once in matrix form, the algebraic results are clear:

$$\begin{pmatrix} \sigma_0 \\ \sigma_{LT} \\ \sigma_{TT} \end{pmatrix} = \begin{pmatrix} 1 & v_{LT} \cos \phi_1 & \epsilon \cos 2\phi_1 \\ 1 & v_{LT} \cos \phi_2 & \epsilon \cos 2\phi_2 \\ 1 & v_{LT} \cos \phi_3 & \epsilon \cos 2\phi_3 \end{pmatrix}^{-1} \begin{pmatrix} X_1 \\ X_2 \\ X_3 \end{pmatrix} \quad (5.15)$$

However, when multiple θ_{pq}^* settings are used, the errors are smaller if the spectrometer cross sections are sent to a fitter. This is due to only one extraction from

the data being performed instead of two. The two extractions are first extracting the three differential cross sections from the spectrometer cross sections and then extracting the multipoles from those results. Fitting the spectrometer cross sections is more direct and keeps the errors smaller. Fitting is detailed in Sec. 7.1. If only one setup is used, the algebra and the fitter give identical results.

The helicity dependent part of the cross section contains the $\sigma_{LT'}$ term. $\sigma_{LT'}$ can be extracted using

$$\sigma_{LT'} = \frac{X_{h>0} - X_{h<0}}{2P_e v_{LT'} \sin \phi}. \quad (5.16)$$

where $X_{h>0}$ and $X_{h<0}$ are the spectrometer cross sections using positive and negative beam helicity respectively.

5.3.10 Cut Robustness and Corrections

The cuts on the data have been defined in such a way that the region selected should be stable. Small changes in the cuts in one direction or the other should not change the cross section if the cuts are truly in a stable region. The procedure as defined in Sec. 5.3.8 allows for a simple definition of robustness. After selecting the full width, fractions of that width are used for the cuts. Looking at Fig. 5-20, the 75% cuts are typically on or very near the shoulders of the distributions. Using the 50% width does select a flatter region but with fewer events and so larger statistical error bars.

To investigate the effects of different cuts, several types of studies were performed. In all of them, the full width was defined using the location of 50% dropoff relative to the central bin. The first study set all but one of the variables to one width and varied the remaining variable. In Fig. 5-21, the 75% width was used for all variables and then the individual variables were set to 25%, 50%, 75%, 85% and 150%. The plot shows the absolute size of the cuts. The 75% setting is known to be very close to the edge so the step above (85%) was made smaller (10% versus 25% for the other steps) so as to stay in a nominally good region. The 150% setting is a stability check that is wide enough to include all of the data. It is important to know whether the

cross section drops off or is more in line with the other cuts. Ideally, all of the cut results will be flat but with larger error bars for the tighter cuts. Figure 5-21 shows that, except for z , the 85% result is very close to the 75% result. The Q^2 , θ_{pq}^* and ϕ_{pq}^* results are reasonably flat. The only real problem is a dropoff in W which has not been explained. However, even that change is about 2% for the 50% to 75% setting.

The comparison of the simulated z with the data shows that there tends to be less agreement near the edges (see Fig. 5-1). The simulation has a sharper edge than the data. As a result, the data are below the simulation for some parts and above for others. If all of the simulation is compared with all of the data, then the shape is no longer an issue and the results trend back up. However, including all the z could lead to greater uncertainty in the phase space volume since the data and simulation do not agree near the edges. The areas of disagreement are cut out to ensure a good phase space volume calculation.

Since there are five variables which can be varied (W , Q^2 , θ_{pq}^* , ϕ_{pq}^* , z) and five settings for each (0.25,0.5,0.75,0.85,1.5), there are 3125 possible variations. To cut this down to a more manageable number, the variables which are held constant were all set to the same fractional value. Since the 1.5 value is known to contain edge effects, only the 0.25, 0.50, and 0.75 widths were used. With the other variables held constant, each variable, in turn, was varied so that the effect could be seen. Fig. 5-21 shows the results of a scan of the cuts. Notice that the results are stable as a function of cuts. A summary of all of the results is shown in Fig. 5-22 where the average of the scan results for each variable is shown versus the fractional size of the cuts on the remaining variables. This way, trends in the cross section as the other variables are changed can be seen. Also, the RMS deviation and statistical errors are shown. Again, the idea is that the cross section should not vary with these cuts.

Looking at Fig. 5-22, the change in the cross section from the 50% setting to the 75% is clear in most variables. To test this effect more, finer scans were made for each kinematic setting. Instead of varying the individual variables, the same fractional cut was used for all (W , Q^2 , θ_{pq}^* , ϕ_{pq}^* , z).

Figure 5-23 shows the scans for the non-parallel, more forward angle $Q^2 = 0.060$

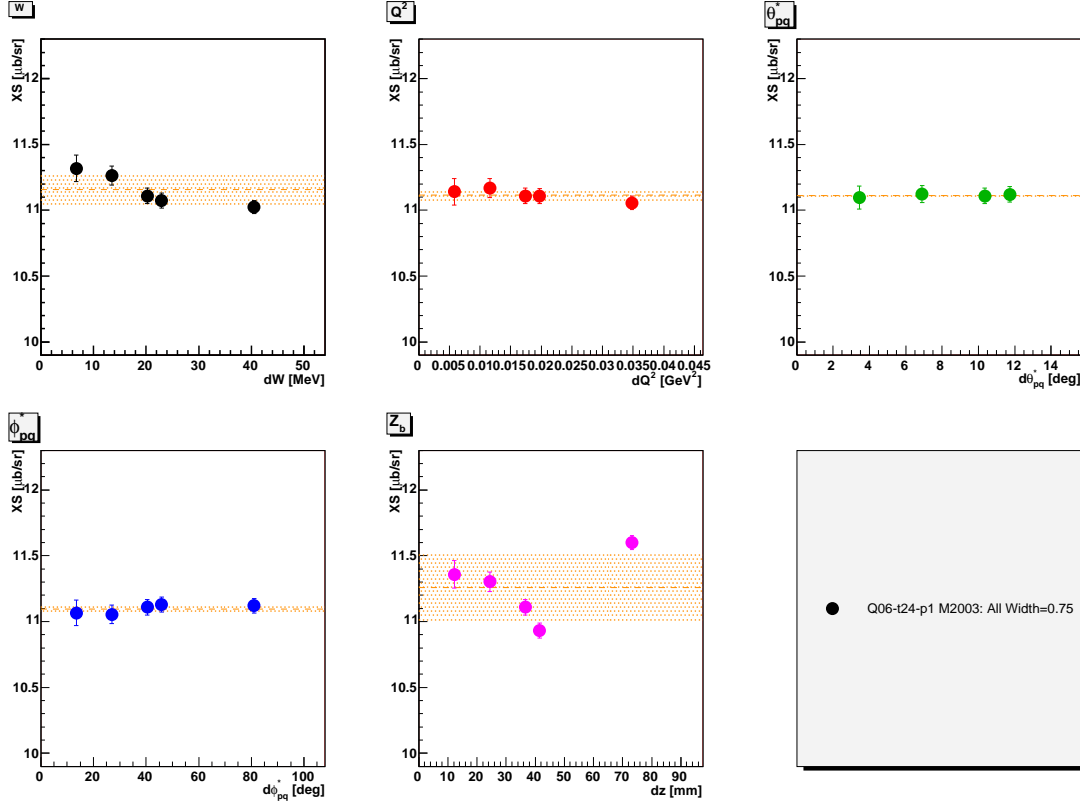


Figure 5-21: Cross sections as a function of cut width for one variable for the setup Q06-t24-p1 with 75% shoulder cuts on the other variables. Notice how most of the results are flat as the cuts are varied. There are known problems with z . The dotted region is the RMS deviation of the results.

(GeV/c) 2 settings. The x axis shows the fractional cut and the y axis shows the cross section normalized to the (0.5,0.5) cut result. The first 0.5 refers to the fraction of the average height for determining the full width and the second 0.5 refers to the fraction of the full width that was used. The shape is very similar for all of these scans. It appears that the 0.5 width results are in a flatter region than the 0.75 results. However, the error bar is smaller in the 0.75. Also, as will be shown shortly, the 0.75 cuts give more stable results for the helicity dependent cross sections. So, a phase space cut correction factor was determined by taking the ratios of the (0.5,0.5) cross section divided by the (0.5,0.75) cross section. The dark shaded bar shows the (0.5,0.75) result after the phase space cut correction with statistical errors. The lighter bar shows the total errors with the systematic error added in quadrature.

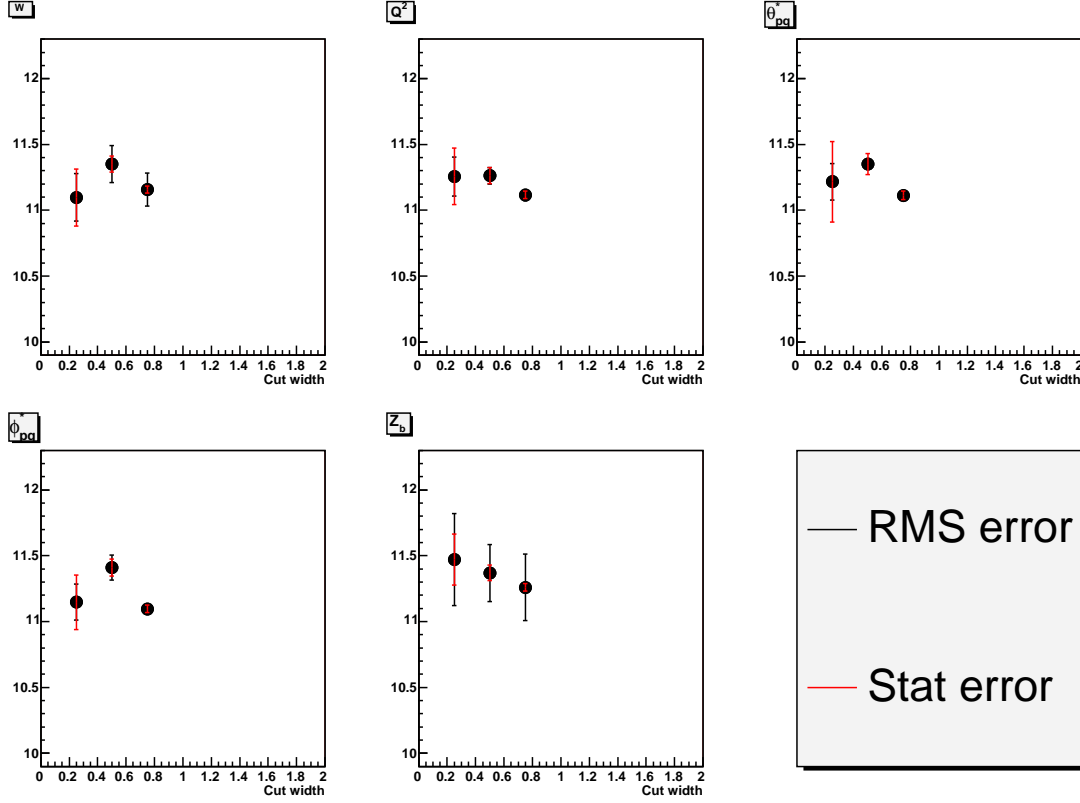


Figure 5-22: Summary of the cut scan study. All variables were held at widths shown on the x axis except for one which was varied over a range from 0.25 to 1.5. The points show the RMS deviation and the statistical errors. The goal is to have the cross sections not depend upon the cut width.

For these plots, systematic errors which affected all the points in the same way were ignored. Therefore, the systematic errors here consist of the estimated phase space cut correction error and the average deadtime error.

Figure 5-24 shows the scans for the in-plane, more backward angles. These results are much flatter and so do not need to be corrected. These type of results are the exception though as can be seen in Fig. 5-25. There, the scan results have a similar shape to the rest.

Finally, there are the helicity dependent results shown in Fig. 5-26. The Q06-t36-p1 setting is flat but the other settings have the same shape including a setting from the higher Q^2 . The corrected results are within the statistical errors of the flat region results.

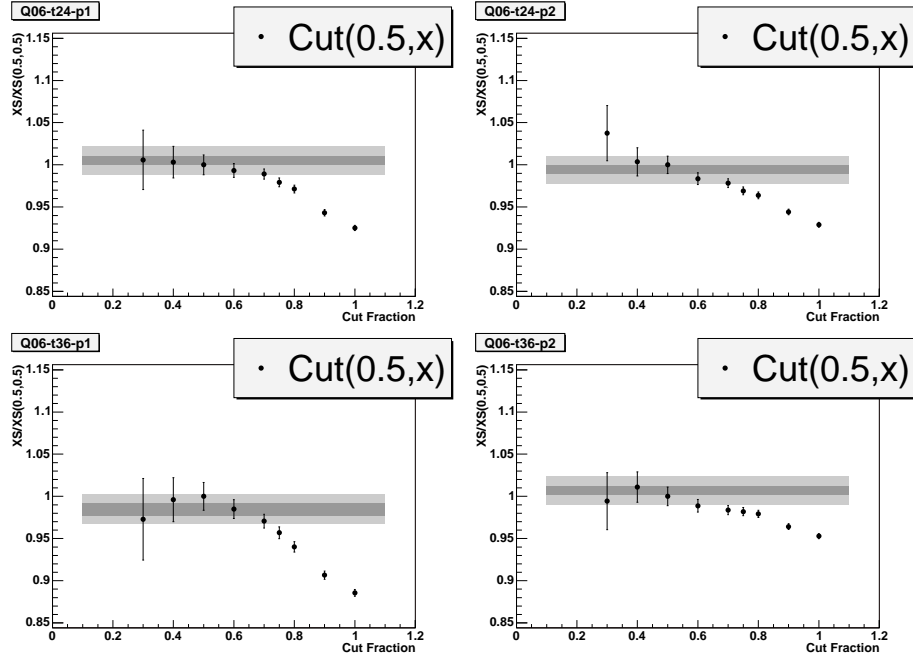


Figure 5-23: $Q^2 = 0.060 \text{ (GeV/c)}^2$, non-parallel, more forward settings cut scans. The bars are centered on the cut corrected result. The dark bar is the statistical error and the light bar shows the total error with the systematic error added in quadrature.

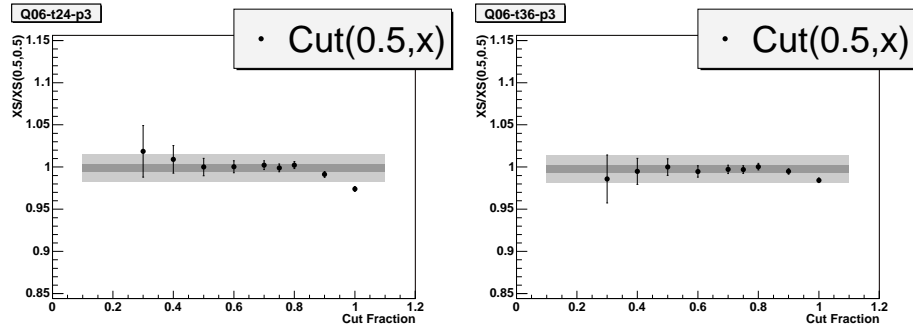


Figure 5-24: Scan of the cuts for the settings Q06-t24-p3 and Q06-t36-p3. The scans are different from the rest because they are flat and do not require a cut correction. See Fig. 5-23 for legend.

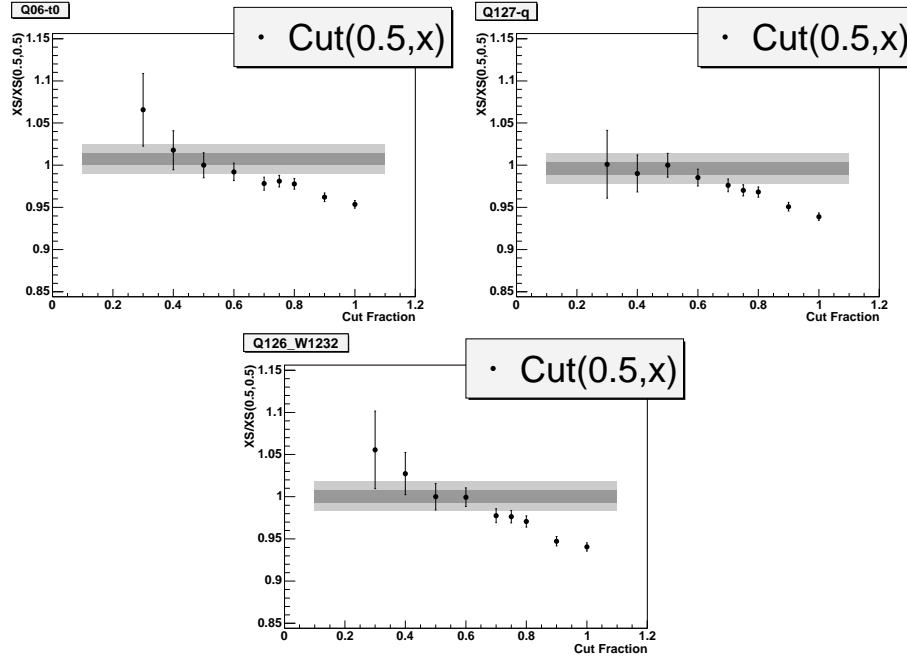


Figure 5-25: Scan of the cuts for the parallel cross section near the Δ resonance at $Q^2 = 0.060$ and 0.127 $(\text{GeV}/c)^2$. The shapes are similar to those in Fig. 5-23. See Fig. 5-23 for legend.

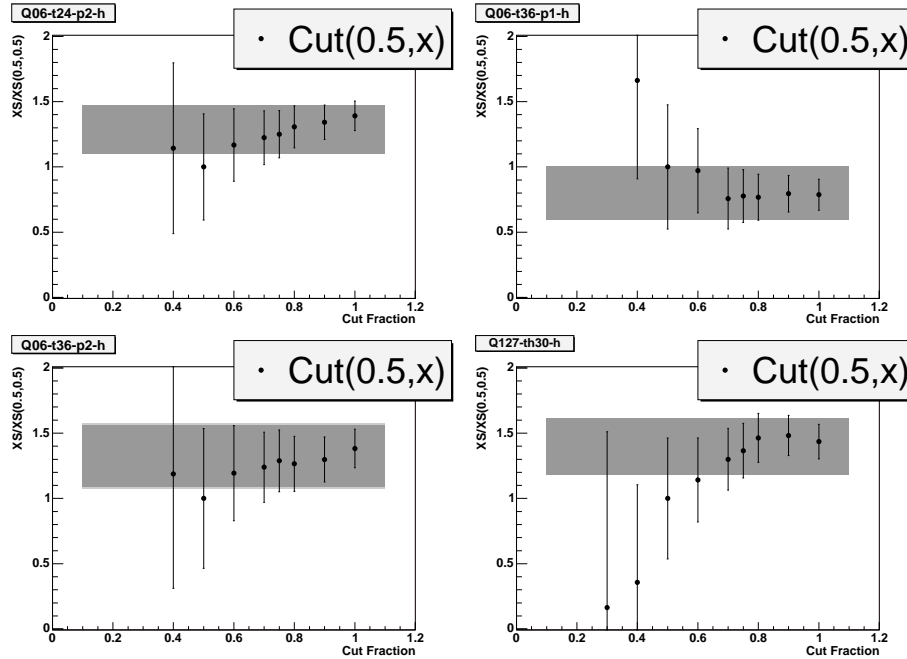


Figure 5-26: Helicity dependent cross section results for $Q^2 = 0.060$ and 0.127 $(\text{GeV}/c)^2$. See Fig. 5-23 for legend.

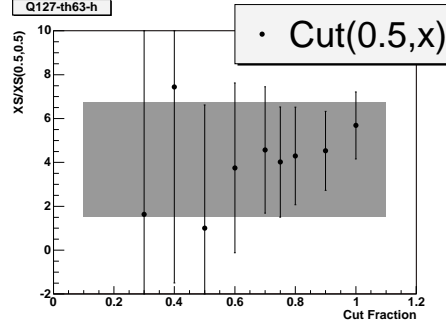


Figure 5-27: Scan for the $Q^2 = 0.127 \text{ (GeV/c)}^2$, $\theta_{pq}^* = 63^\circ$ setting. See Fig. 5-23 for legend.

The result that was the least clean is also the largest proton angle that was measured. The scan results are in Fig. 5-27 and show that the (0.5,0.5) region is rather unstable. The error bars are large and there are large swings in the central value to either side of zero. However, the region around (0.5,0.75) is much more stable and has smaller error bars. Again, the corrected result is within the error bars of the (0.5,0.5) result.

As all of these plots show, the (0.5,0.75) region is more stable for all of the settings and so was chosen as the final analysis cut. The phase space correction factors were found by averaging over the different data sets. The factors are summarized in Table 5.9. The table shows the average correction factor, the average of the error (statistical only) and the RMS deviation of the factors. The conclusion is that the correction can be safely applied with the systematic error being the average of the error of the correction factor.

Several setups have been excluded from Table 5.9. Setups Q06-W1205_rev, Q06-W1155_p1 and Q06-W1155_p2 were all taken in reverse kinematics (electron detected in Spectrometer B, proton in Spectrometer A). Since there were significantly fewer runs in the reverse kinematics, it is more difficult to find a trend. The average of the ratios indicates a correction factor less than 1%. So, it was decided that it is safer to leave those settings uncorrected but include an extra 2.3% systematic error for the $W = 1155 \text{ MeV}$ setups and 1.9% for the $W = 1205 \text{ MeV}$ setup. Those are the average errors on the phase space correction factor if it were used.

Setup	Ratio	Error	RMS
Q06-t0	1.019	0.017	
Q06-t24-p1	1.021	0.013	
Q06-t24-p2	1.032	0.012	
Q06-t36-p1	1.039	0.020	
Q06-t36-p2	1.018	0.012	
Q127-q	1.031	0.016	
Q126-W1232	1.025	0.018	
Average	1.026	0.015	0.008
Q06_W1125	1.024	0.024	
Q06_W1155	1.023	0.025	
Q06_W1185	1.023	0.022	
Q06_W1205	1.017	0.019	
Q06_W1225	1.023	0.021	
Q06_W1245	1.007	0.029	
Q06_W1275	1.029	0.027	
Q06_W1300_low	1.006	0.028	
Average	1.019	0.024	0.008
Q126_W1232_p1	1.035	0.018	
Q126_W1232_p2	1.008	0.014	
Average	1.021	0.016	0.019
Q127-w1140-p1	1.048	0.030	
Q127-w1140-p2	1.009	0.018	
Average	1.028	0.024	0.028
Q127-th30	1.031	0.017	
Q127-th43	1.042	0.020	
Q127-th63	1.002	0.019	
Average	1.025	0.019	0.021

Table 5.9: Cut correction factors and the settings used to calculate them.

Other runs excluded from Table 5.9 are the flat distributions mentioned earlier, Q06-t24-p3 and Q06-t36-p3, and the parallel run Q126-W1212 which also had a flat distribution. Again, an extra systematic error of 1.5% is used since that is close to the error in the unused correction factor. This error becomes a conservative estimate of the error in the phase space cuts.

5.3.11 Radiative Corrections and Energy Loss

The electron interacts with the target in this experiment via a single virtual photon. However, the electron can undergo other interactions prior to the interaction and prior to being detected. Figure 5-28 shows the various virtual photon diagrams while Fig. 5-29 shows the real photon diagrams.

The radiative effects act to create a tail in the distribution of electron energies that extend to the lower energies. If a cut is placed on the electron energy, the events below that cut will not be measured. However, the number of events that are cut out can be calculated and then corrected for using

$$\sigma_{true} = K(\Delta E)\sigma_{measured} \quad (5.17)$$

where ΔE is the difference between the peak of the scattered electron energy and the cutoff energy.

A standard approach to the radiative corrections is to break the calculation up into two parts, real and virtual [57, 71]. Then the correction factor takes the form

$$K = \frac{e^{\delta_{real}}}{1 + \delta_{virt}} \simeq e^{\delta_{real}}(1 - \delta_{virt}) \simeq e^{\delta_{real} - \delta_{virt}}. \quad (5.18)$$

As long as δ_{virt} stays reasonably small, the approximations will hold.

The diagrams in Fig. 5-28 all contribute to δ_{virt} which can be written as

$$\delta_{virt} = \frac{\alpha}{\pi} \left\{ \frac{13}{6} \left[\ln \frac{Q^2}{m_e^2} - 1 \right] - \frac{17}{18} - \frac{1}{2} \ln^2 \frac{E_i}{E'} - \frac{\pi^2}{6} + L_2 \left(\cos^2 \frac{\theta_e}{2} \right) \right\} \quad (5.19)$$

where E_i, E', θ_e, Q^2 are defined in Sec. 2.1, m_e is the mass of the electron, and L_2 is the Spence function

$$L_2(x) = - \int_0^x \frac{\ln(1-y)}{y} dy = \sum_{n=1}^{\infty} \frac{x^n}{n^2}. \quad (5.20)$$

The δ_{virt} term does not depend on ΔE and so is applied as a weight factor in

the simulation. The real term is implemented in the simulation using the equivalent radiator method. In this method, the real-photon part is approximated with two external radiators. One is placed before and one after the scattering. Each has thickness

$$\frac{t}{X_0} = \frac{\alpha}{\pi b} \left[\ln \frac{Q^2}{m_e^2} - 1 \right] \quad (5.21)$$

where

$$b = \frac{4}{3} \left[1 + \frac{1}{9} \frac{Z+1}{Z+\xi} \ln^{-1}(183Z^{-1/3}) \right], \quad (5.22)$$

t is the target thickness in g/cm², Z is the target atomic charge, and X_0 is the radiation length in g/cm² [71].

The final radiative correction is for external bremsstrahlung. This occurs while the electron is entering or exiting the hydrogen target and it differs from the internal correction by not involving the Coulomb field of the target nucleus. These also tend to be rare but large losses. External bremsstrahlung is handled in Simul using the inverse of the external bremsstrahlung energy loss formula found in [62]. The correction has a random element to it such that over large numbers of simulated events, the energy distribution will be the same as in reality.

More details about radiative corrections can be found in [79],[71], and [57].

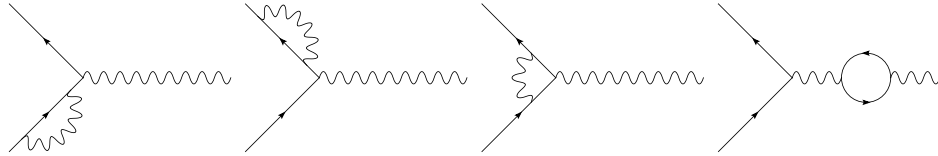


Figure 5-28: Diagrams containing, from left to right, the self-energy terms, the vertex correction, and the vacuum polarization.

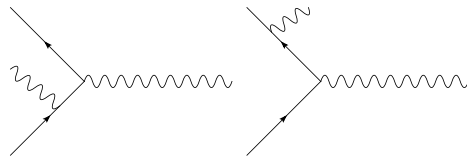


Figure 5-29: Diagrams showing the soft, real, Bremsstrahlung photon being emitted.

5.3.12 Energy Loss

The radiative corrections properly correct for some losses for the electron but the proton, being much more massive, has negligible radiative losses. However, both will lose energy as they pass through the various materials in and around the target and the spectrometers. For protons ($m_p \gg m_e$), the energy loss is given by this form of the Bethe-Bloch formula [50]

$$-\frac{dE}{dx} = 4\pi N_a r_e^2 m_e \rho \frac{Z}{A} \frac{z^2}{\beta^2} \left[\ln \left(\frac{2m_e \gamma^2 \beta^2}{I} \right) - \beta^2 - \frac{\delta}{2} - \frac{C}{Z} \right] \quad (5.23)$$

where N_a is Avogadro's number, r_e is the classical electron radius, m_e is the mass of an electron, β is velocity of the incident particle divided by the speed of light, $\gamma = (1 - \beta^2)^{-1/2}$, Z is the charge of the target, A is the atomic weight of the target, z is the charge of the incident particle, I is the mean excitation potential, δ is a density correction, and C is the shell correction. All of the constants can be combined as

$$4\pi N_a r_e^2 m_e \rho = 0.3069 \rho (\text{MeV/cm}) \quad (5.24)$$

where ρ is in units of gm/cm^3 .

The shell and density corrections are only important at low and high energies respectively. The density correction comes from the tendency of high energy particles to polarize atoms along its path. The default Bethe-Bloch formula will then overestimate the energy loss because it does not account for the shielding that arises from the polarization. The shell corrections become important when the particle is traveling at a velocity similar to that of the orbital electrons of the atoms in the target material. However, at the energies of this experiment, neither correction is significant.

To calculate the energy loss for electrons, the Bethe-Bloch formula must be modified to take into account the electron's much smaller mass. This modified Bethe-Bloch is [50]

$$-\frac{dE}{dx} = 2\pi N_a r_e^2 m_e c^2 \rho \frac{Z}{A} \frac{1}{\beta^2} \left[\ln \frac{\tau^2 (\tau + 2)}{2(I/m_e c^2)^2} + F(\tau) - \delta - 2 \frac{C}{Z} \right] \quad (5.25)$$

where τ is the kinetic energy of the the particle in units of $m_e c^2$ and $F(\tau) \rightarrow 0.125$ for electrons and $F(\tau) \approx -0.53$ for positrons in our energy range.

Finally, the simulation corrects for Landau energy straggling. As a particle passes through matter, the actual energy loss will depend upon exactly how it interacts with the matter. The mean energy loss can be calculated using the previous formulas but the distribution is not necessarily symmetric. The distribution follows a Landau distribution which peaks and then has a tail. The most probable energy loss is then different from the mean energy loss. However, from [57], the effects of Landau straggling can be ignored for target thicknesses less than 0.05 of the radiation length of the target material. Liquid hydrogen has a radiation length of 866 cm [32] and the target is about 5 cm long (see Sec. 3.2) giving a ratio of about 0.006.

Once the total energy loss is calculated for both particles, that energy is added back in both in COLA and Simul. Again, the final check of the procedure is if the simulation and data agree which they do (see Figs. 5-1 and 5-2).

5.4 Cross checks

During the April run period, elastic runs were performed before and after each in-plane setup. During the October run, elastic runs were performed at the beginning and end of each Q^2 setting. For most elastic runs, the scale factors were set so that the data stream contains coincidence data for spectrometers A and B as well as single arm data for each spectrometer.

In addition to the elastic runs, several measurements were performed which overlap with previous results. All of these overlap results will be shown and discussed.

5.4.1 Coincidences

Figures 5-32, 5-33 and 5-34 show the elastic coincidence results (electrons in Spectrometer A, protons in Spectrometer B). The same rough spectrometer cuts were used as for the production runs (see Sec. 5.3.8). However, the cuts on the physical variables were different since elastic and pion production have different kinematics.

Whereas Q^2 and W are used in pion production, E' and θ_e are used in elastics. The E' is left untouched and the cross section is binned versus θ_e . Also, there is no cut on the proton. The target z cut is slightly different from the production runs but a study on Q127-q-elas showed that the effect is less than 1%. Also, the offset for z in the software was slightly different for some runs (October) but a similar study on Q127-q-elas showed the effect to be less than 0.5% which is very close to the statistical error. The z cut error is less than the systematic error on the luminosity.

The systematic error for these elastic runs is similar to the systematic error for the production runs (see Sec. 5.5). However, for the plots in this section, the luminosity error has been suppressed because the luminosity error should affect all the runs in the same way. There could have been a difference from April to October but the results indicate that the luminosity was under control and stable. The non-luminosity related systematic error for the elastics is estimated at 2.3% (deadtime + cut + resolution + beam position + detector inefficiency).

The oscillations seen in the cross section plots versus θ_e (Figs. 5-32, 5-33 and 5-34) are typical of elastic cross sections measured with the Mainz spectrometers [82]. In the elastic region, only a small part of the focal plane is illuminated (see Fig. 5-35). It is believed that single wire position uncertainties (sagging wires) in the wire chambers lead to the oscillations seen in the cross section. To test this idea, the chamber wires were tightened in late 1999. A comparison of the counts versus angle from before and after the tightening is shown in Fig. 5-30.

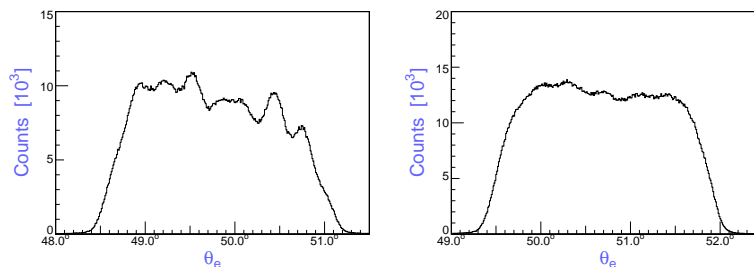


Figure 5-30: The effect of tightening the wires in the wire chambers can be seen in these plots of counts versus θ_e . The left plot is from June 1999 and the right plot is from after the repair in November/December 1999. Figure from [82].

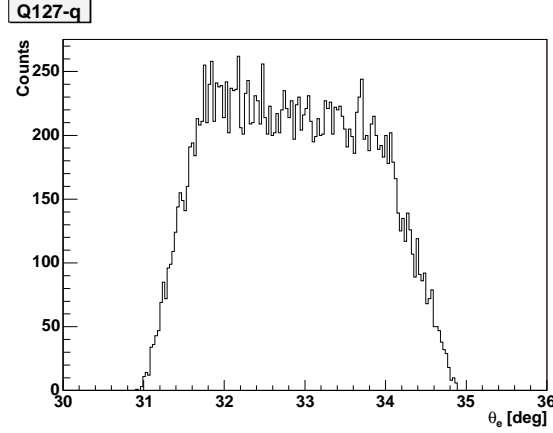


Figure 5-31: A plot of counts versus θ_e for a parallel cross section, pion production run at $Q^2 = 0.126 \text{ GeV}^2/\text{c}^2$, $W = 1232 \text{ MeV}$. Note the lack of structure in the plot even with cuts.

Since a $\gamma^*N \rightarrow \Delta$ production run illuminates the entire focal plane (see Fig. 5-35), the effect is expected to average out. As further evidence, see Fig. 5-31 where a plot of counts versus θ_e is shown from a parallel cross section, pion production run. Timing, missing mass and acceptance cuts have been applied to Fig. 5-31 and yet there is still no structure visible.

To eliminate the effect of the structure in the elastic plots, the cross section is averaged over the θ_e acceptance. Since the structure appears to have approximately as many positive deviations as negative, the average should be stable. Table 5.10 shows the elastic coincidence results after averaging over the central region. For comparison purposes, the acceptance averaged elastic cross section from [52] was averaged over the same region and can also be seen in Table 5.10. The acceptance averaged world fit was calculated in the same way as described in Sec. 5.3.9 but using an elastic cross section fit instead of a pion production model. There ends up being very little difference between the acceptance averaged world cross section and the unaveraged cross section because the acceptance in the elastic region is very small. There are so many kinematic correlations (i.e. θ_e is directly linked to E') that there cannot be much variation in a given bin.

The θ_e cut width was defined in a similar way to the pion production cuts. Since

the (0.5,0.5) region is flat and there is no shortage of counts, that θ_e region was used.

Note that some elastic runs are not listed in Table 5.10. The setting 0.06-th24-phi180-elastic used the lowest current measured with the rough scale on the Förster probe leading to greater uncertainty. There appear to be some systematic problems with using the rough scale on low currents so that combination was avoided. Other runs had higher currents or used the fine scale. Q126_elas_1 had a timing offset that could not be corrected afterward that lead to a 30% discrepancy. The timing was fixed for the pion production run after it.

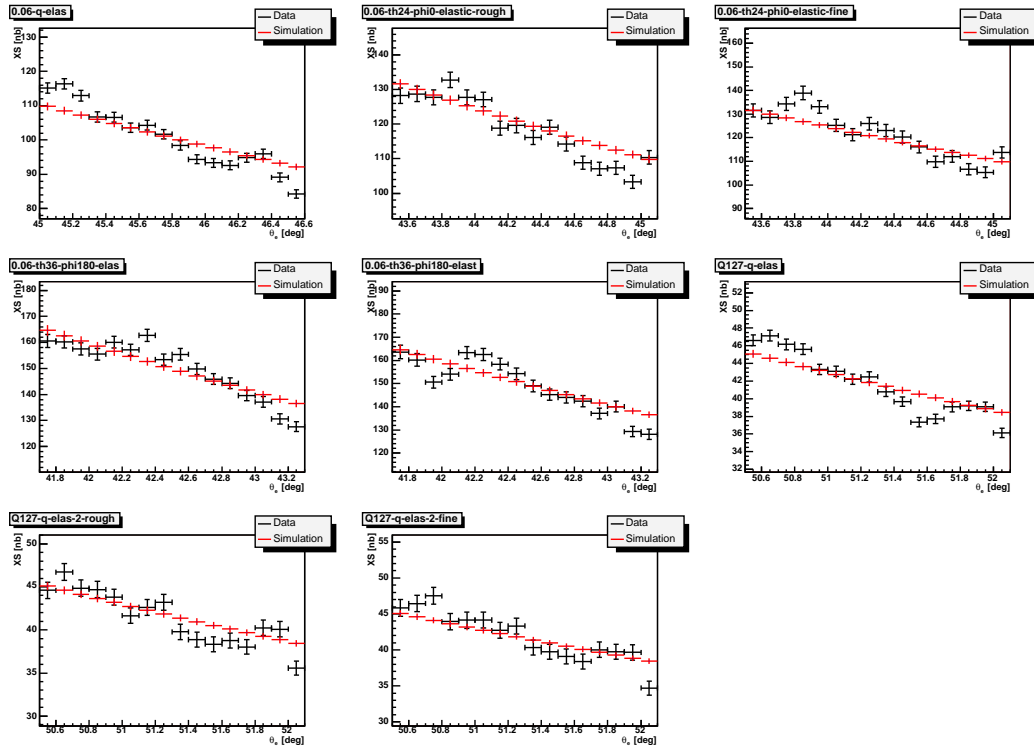


Figure 5-32: Elastic coincidence cross section (black crosses with endcaps) in nb plotted against θ_e along with the acceptance averaged dispersion analysis fit of Ref. [52] (red crosses). Errors are statistical only. These are all from the first part of the April 2003 run.

Figure 5-32 shows that the results are stable over time and most are consistent within systematic errors with the 1996 dispersion-theoretical analysis fit to the world elastic data [52]. There are two runs which are a bit lower than the rest and they correspond to a lower beam energy. The settings were studied, but no reason for the

Setup	E MeV	Q^2 GeV ²	θ_e^{min} °	θ_e^{max} °	XS_{avg} $\mu\text{b/sr}$	Disp 96 $\mu\text{b/sr}$	% diff
0.06-q-elas	795	0.30	45.0	46.5	101.7 \pm 0.4 (0.4%)	101.3	0.4
0.06-th36- phi180-elas	795	0.28	41.8	43.2	150.7 \pm 0.6 (0.4%)	150.0	0.4
0.06-th36- phi180-elast	795	0.28	41.8	43.2	149.3 \pm 0.7 (0.5%)	150.0	-0.5
0.06-th24-phi0- elastic-rough	795	0.29	43.5	45.0	119.1 \pm 0.5 (0.5%)	121.1	-1.6
0.06-th24-phi0- elastic-fine	795	0.29	43.5	45.0	122.1 \pm 0.7 (0.5%)	121.1	0.9
Q127-q-elas	855	0.41	50.5	52.0	42.0 \pm 0.1 (0.4%)	41.9	0.2
Q127-q-elas-2- rough	855	0.41	50.5	52.0	41.8 \pm 0.2 (0.6%)	41.9	-0.3
Q127-q-elas-2- fine	855	0.41	50.5	52.0	42.3 \pm 0.3 (0.7%)	41.9	1.1
Q20-q-elas-1	855	0.48	57.0	58.5	21.8 \pm 0.1 (0.3%)	22.0	-1.2
Q20-q-elas	855	0.48	57.0	58.5	21.5 \pm 0.1 (0.5%)	22.0	-2.3
Q20-t33-p1-elas	855	0.44	53.9	55.4	29.0 \pm 0.2 (0.6%)	29.7	-2.4
Q20-t33-p1-elas2	855	0.44	53.9	55.4	29.3 \pm 0.1 (0.4%)	29.7	-1.5
Q20-t33-p3-elas	855	0.44	53.9	55.4	29.3 \pm 0.1 (0.5%)	29.7	-1.4
Q20-th57-p3-elas	855	0.38	48.3	49.8	53.0 \pm 0.2 (0.4%)	53.5	-1.0
Q20-th57-p3-elas2	855	0.38	48.3	49.8	52.8 \pm 0.2 (0.4%)	53.5	-1.3
Q06_minus_elas_2	855	0.19	31.0	32.5	533.7 \pm 1.8 (0.3%)	544.9	-2.1
Q126_elas_2	855	0.37	47.0	49.0	59.8 \pm 0.3 (0.5%)	59.9	-0.2
Q06_elas_1_fine	705	0.16	34.8	36.0	541.5 \pm 2.5 (0.5%)	570.0	-5.0
Q06_elas_2	705	0.16	34.8	36.0	532.6 \pm 2.5 (0.5%)	570.0	-6.6
Q06_minus_elas_1	855	0.19	31.5	32.3	535.1 \pm 2.6 (0.5%)	530.7	0.8
Q06_minus_elas_2	855	0.19	31.5	32.3	535.0 \pm 2.5 (0.5%)	530.7	0.8
Q06_elas_rev	855	0.28	39.3	40.2	172.7 \pm 1.2 (0.7%)	167.2	3.3
Q126_elas_2	855	0.37	47.5	48.8	59.1 \pm 0.4 (0.6%)	58.8	0.6

Table 5.10: Averaged elastic coincidence results in chronological order with statistical errors. The top section results are from April. The bottom section results are from October. The rev or minus settings were taken with the reverse configuration where Spectrometer B detected electrons and Spectrometer A detected protons. The rest were taken in the regular configuration where the roles of the Spectrometers are reversed. The absolute systematic error is 3.1% which is the same as the pion production runs. The systematic error on the variation between setups is the estimated error in the phase space cuts, which comes from the pion production studies, and is 1.5%.

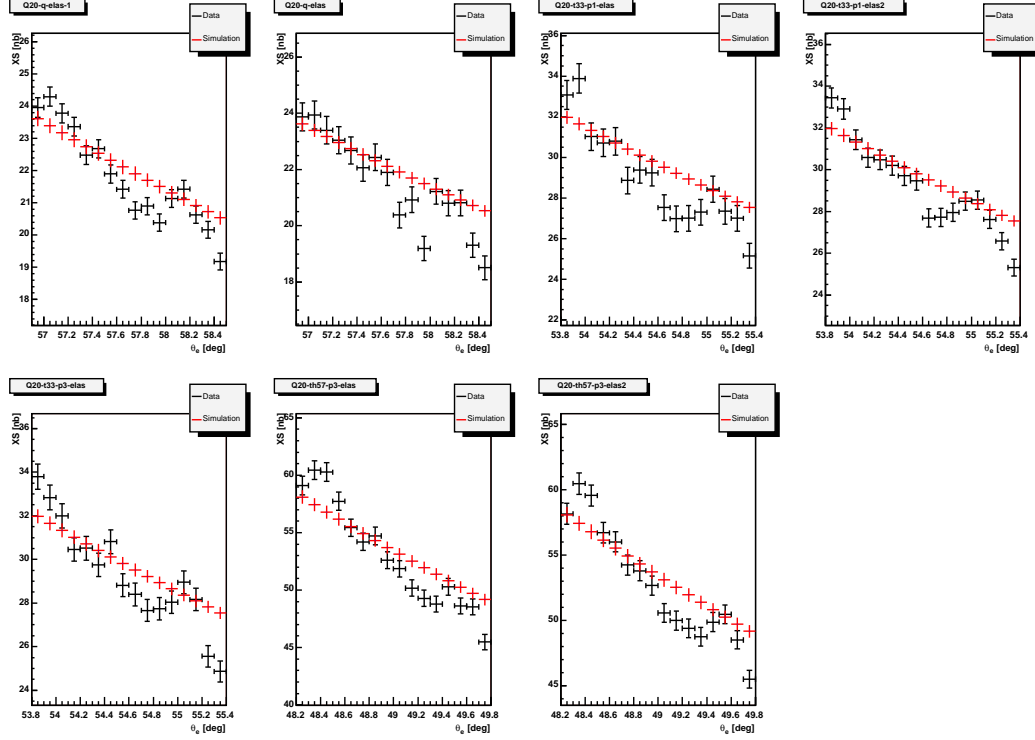


Figure 5-33: Elastic coincidence cross section (black crosses with endcaps) in nb plotted against θ_e along with the acceptance averaged dispersion analysis fit of Ref. [52] (red crosses). Errors are statistical only. The green vertical lines indicate the integration region. These are all from the second part of the April 2003 run.

low results could be found so the results are reported as they are. These elastic runs were on either side of the low Q^2 W scan and so could indicate a possible systematic shift.

There is an updated version of the 1996 dispersion-theoretical analysis by Hammer (Ref. [41]). In our kinematic region, the new version is about 1% below the 1996 fit (see Fig. 5-37). In addition to the updated Hammer fit, there are several other fits that have been obtained and Fig. 5-37 shows how close the various fits are at $E=855$ MeV. There is a small amount of spread between the fits but they appear to agree at about $98.5\% \pm 1.5\%$. For reference, the low end $\theta_e = 40^\circ$ of Fig. 5-37 corresponds to $Q^2 = 0.28 \text{ GeV}^2$ and the high end $\theta_e = 60^\circ$ corresponds to $Q^2 = 0.50 \text{ GeV}^2$.

The conclusion from the coincidence elastic analysis is that the measured cross sections are stable over time and agree well with previous elastic results. This indi-

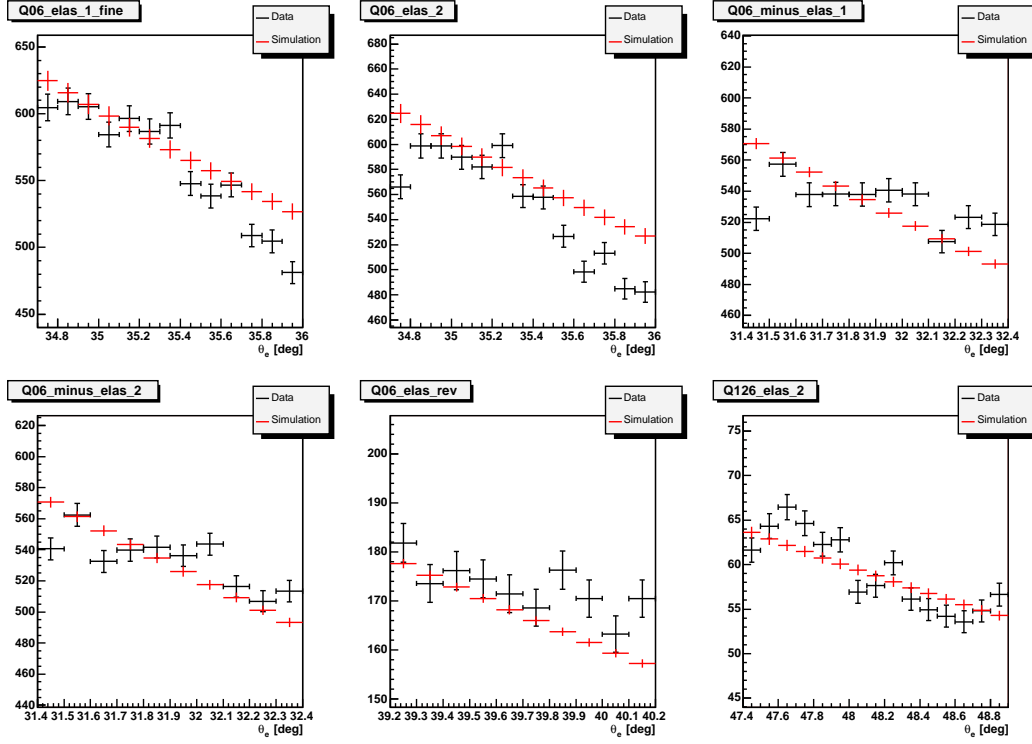


Figure 5-34: Same as Fig. 5-32 but for the October run period.

cates stability in the luminosity, target density, and beam position. It also indicates that the spectrometers can be placed reliably and that the central momenta are well known.

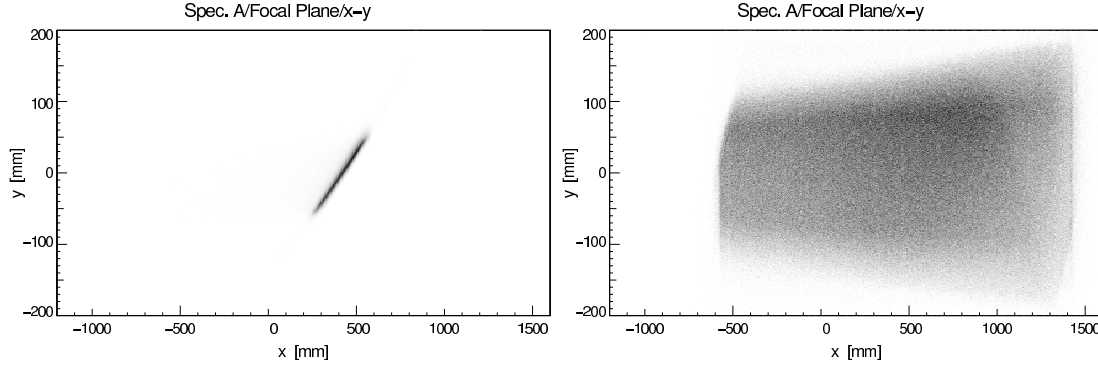


Figure 5-35: Plot of hits versus the horizontal and vertical coordinates in the focal plane. The left plot is for an elastic run and the right plot is for a $\gamma^*N \rightarrow \Delta$ production run.

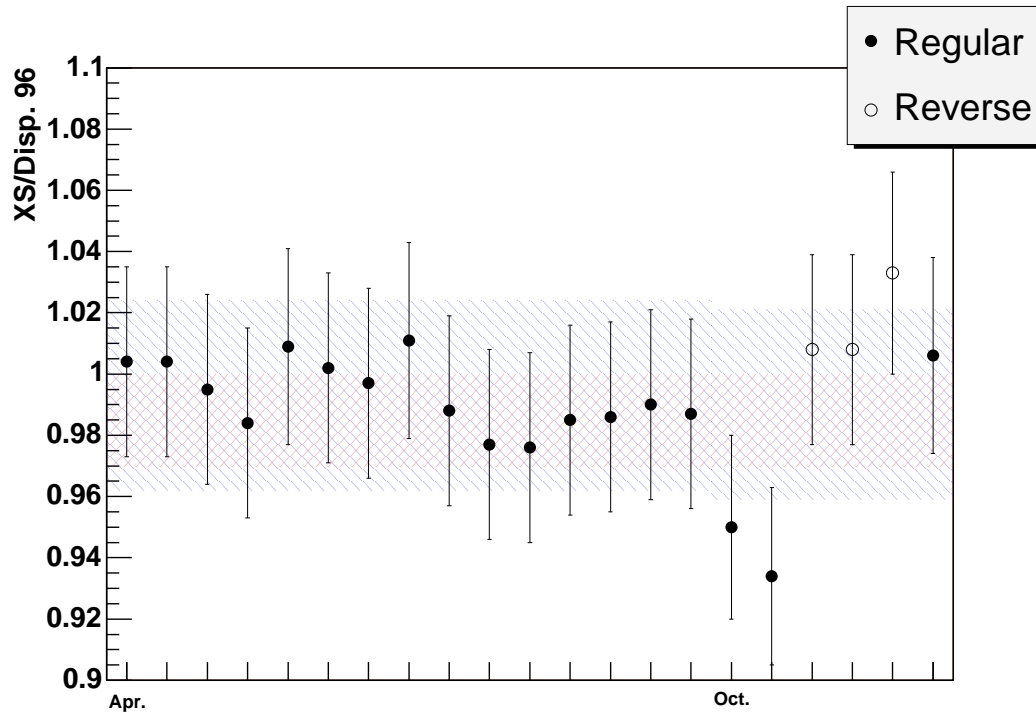


Figure 5-36: Comparison of ratio of the elastic cross section to the Dispersion 96 prediction [52]. Errors are the total statistical and systematic added in quadrature. The results are stable over time and close to the various world models. The red / represents the region where the various elastic models overlap (see Fig. 5-37). The blue \ regions are the average ratio and average error for the April (left) and October (right) run times.

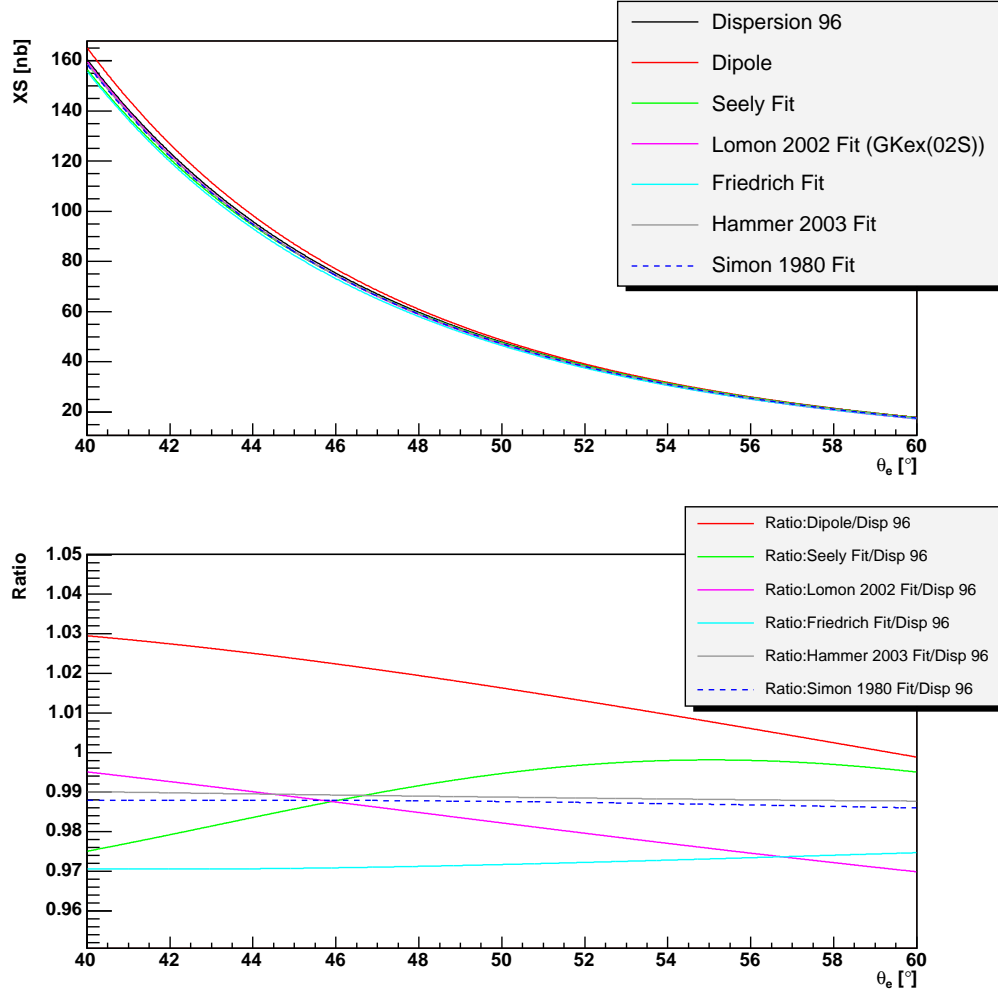


Figure 5-37: Comparison of elastic form factor fits at $E=855$ MeV. The top plot shows the absolute size of the fits and the bottom plot shows the ratio of each fit to the “standard” 1996 fit [52]. The fits are: Dispersion 1996 [52], Dipole $1.0/(1.0 + (Q^2/0.71))^2$, the Seely fit [68], Lomon [51], Friedrich [36], Simon [69] (which is equivalent to Hoehler), Hammer 2003 [41]. (The 1996 fit is the standard used for comparison because it is what has been compared against the Mainz elastic data since at least the April 2003 run time).

5.4.2 Single Arm

As mentioned earlier, the data stream also contains single arm data. However, for some runs the scale factors were set too low to get large numbers of single arm counts and those runs have been suppressed. Several representative setups were analyzed for their singles to confirm that the cross sections are as expected. Figures 5-38 and 5-39 show the single arm results for spectrometer A (detecting electrons). The integration region is wider for the single arm A because the physical acceptance of Spectrometer A is larger than Spectrometer B. In coincidence, Spectrometer B's smaller acceptance limits the region seen in coincidence in A. However in single arm, a larger part of the spectrometer can be used since it does not have to be in coincidence with B.

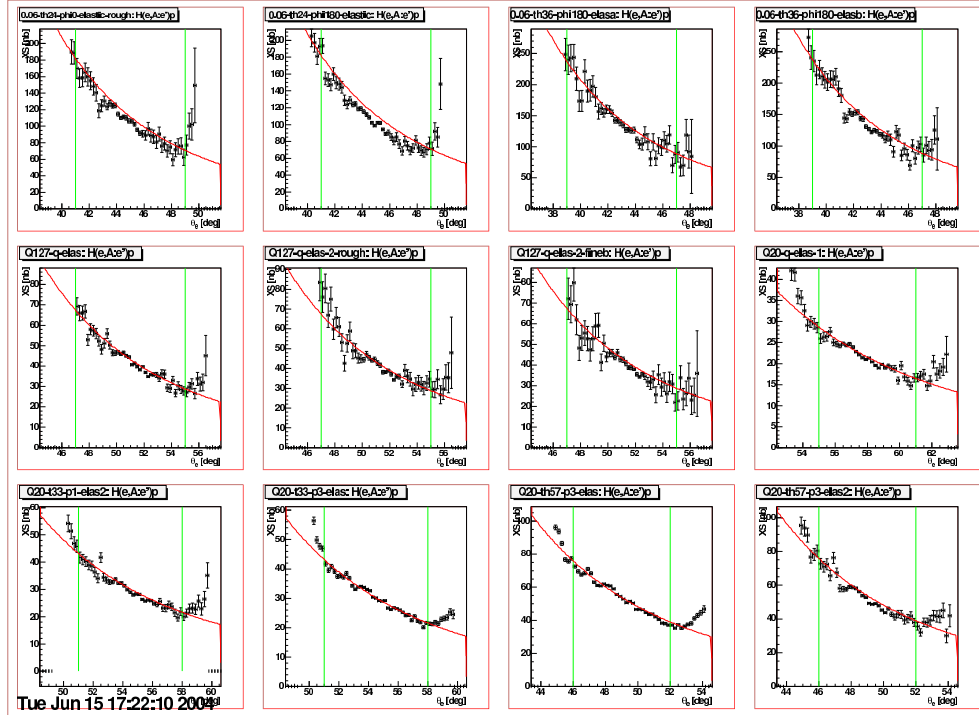


Figure 5-38: Elastic single results plotted against the dispersion analysis of Ref. [52] (red solid line). Errors are statistical only. Data do not have the inefficiency factor taken into account (2.2%). Vertical lines indicate the integration region. These runs are all from April 2003.

The numerical results can be seen in Table 5.11. A few of the runs are lower than the rest but the majority of runs appear to be very close to the world average.

The single arm analysis required some more analysis than the coincidences. This

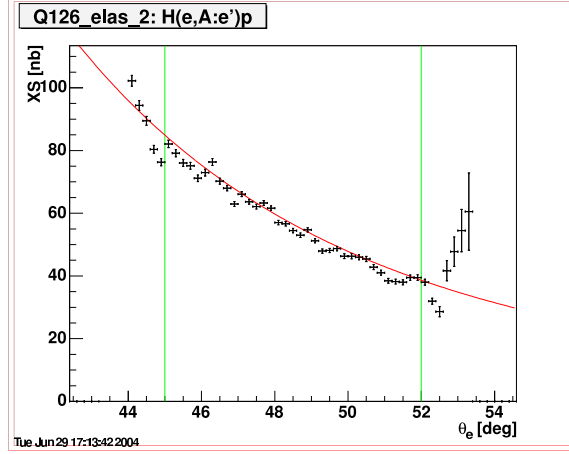


Figure 5-39: Elastic single results plotted against the dispersion analysis of Ref. [52] (red solid line). Errors are statistical only. Data do not have the inefficiency factor taken into account (2.2%). Vertical lines indicate the integration region. This run is from October 2003.

is because the single and coincidence data streams must be merged properly. In the single arm analysis, the single arm events are binned normally but coincidence events are weighted by the ratio of the effective single arm luminosity over the effective coincidence luminosity. Ignoring deadtime effects, this is just the ratio of the scale factors. By using the effective luminosities, the small deadtime effects are included. Then, the histogram is divided by the Simul single arm result (using a 4π collimator for spectrometer B). The results are divided by the single arm luminosity yielding a cross section. Fig. 5-40 shows an example of data from the various streams and how they fit together.

Overall, the single arm analysis shows the same stability and agreement with the world data as the coincidence analysis. Taken together, the results indicate that the spectrometer efficiency is well understood within the cuts.

Setup	E MeV	Q^2 GeV ²	θ_e^{min} °	θ_e^{max} °	XS_{avg} $\mu\text{b/sr}$	Disp 96 $\mu\text{b/sr}$	% diff %
0.06-th36-phi180-elasa	795	0.28	39.0	47.0	147.8 ± 2.0	148.1	-0.2
0.06-th36-phi180-elasb	795	0.28	39.0	47.0	145.9 ± 1.5	148.1	-1.5
0.06-th24-phi0-elastic-rough	795	0.29	41.0	49.0	111.1 ± 1.2	115.6	-6.0
Q127-q-elas	855	0.41	47.0	55.0	45.0 ± 0.3	44.7	0.6
Q127-q-elas-2-rough	855	0.41	47.0	55.0	46.4 ± 0.6	44.7	3.8
Q127-q-elas-2-fine	855	0.41	47.0	55.0	44.5 ± 0.7	44.7	-0.5
Q20-q-elas-1	855	0.48	55.0	61.0	21.9 ± 0.1	21.8	0.3
Q20-t33-p1-elas2	855	0.44	51.0	58.0	30.8 ± 0.2	30.6	0.5
Q20-t33-p3-elas	855	0.44	51.0	58.0	31.3 ± 0.1	30.6	2.2
Q20-th57-p3-elas	855	0.38	46.0	52.0	55.9 ± 0.1	54.7	2.2
Q20-th57-p3-elas2	855	0.38	46.0	52.0	54.4 ± 0.4	54.7	-0.6
Q126_elas_2	855	0.37	45.0	52.0	57.9 ± 0.1	58.2	-0.4

Table 5.11: Selected averaged elastic single arm results for spectrometer A in chronological order. The top section is from April 2003 and the bottom section is from October 2003. The same inefficiency correction used for the coincidence elastics and production runs was used (1.022). The systematic error and phase space cut errors are estimated to be the same as the elastic coincidence runs (see Table 5.10).

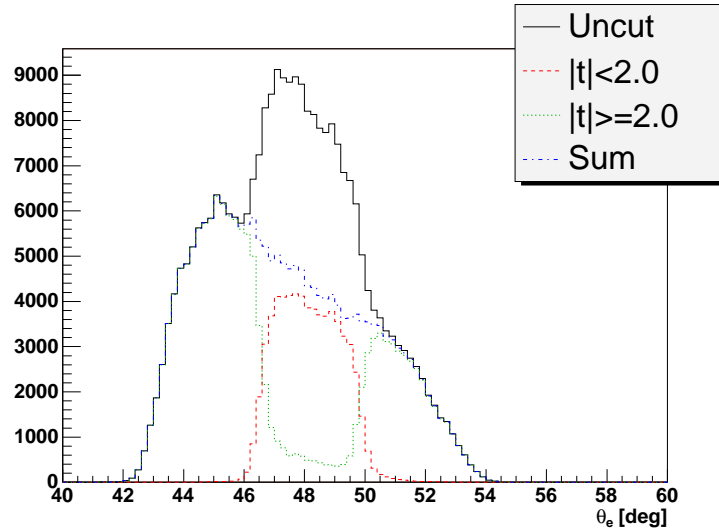


Figure 5-40: Example of the two data streams for the single arm analysis of Q126_elas_2. The solid black line shows the raw counts versus θ_e . The red dashed line shows the properly scaled coincidence alone. The green dotted line shows the singles alone. The blue dot-dashed line is the sum and is smooth.

5.4.3 δ scan

A delta scan was performed using electrons in both Spectrometer A and B. To complete a δ scan, the peak from the elastic cross section is moved across the focal plane by varying the central momentum of each spectrometer. In this way, a narrow region of the focal plane is illuminated with a well known cross section. The efficiency of the focal plane can be tested using this approach. The results showed a slight dropoff in the cross section near the edges of the acceptance. For this reason, we are avoiding these regions in our analysis. The other cuts placed on the data (W , Q^2) tend to limit the acceptance even more in Spectrometer A.

The W and Q^2 cuts do not limit the acceptance of Spectrometer B so the primary limit on the size of the acceptance is the cut placed on the central momentum. Again, the size of the central momentum cuts were chosen based upon the pion production results but the δ scans were basically in agreement. Those results favored the central region over the edges.

5.4.4 Parallel cross section

As mentioned previously (see Sec. 4.2), the parallel cross section at $Q^2 = 0.127$ (GeV/c)² was taken during both runtimes to act as an overall check of our absolute cross sections. The check can be performed because this measurement has been carried out previously at Bates [55, 54, 80, 74, 73]. The beam energy for each of these past experiments was slightly different and so the ϵ factor is slightly different. To correct for this, we use the ratio of σ_T to σ_L from a model like so:

$$\sigma_0 = \sigma_T + \epsilon\sigma_L \quad (5.26)$$

$$\sigma'_0 = \sigma_T + \epsilon'\sigma_L \quad (5.27)$$

$$\sigma'_0 = \sigma_0 \frac{f + \epsilon'}{f + \epsilon} = \sigma_0 F \quad (5.28)$$

$$f = \frac{\sigma_T}{\sigma_L} \quad (5.29)$$

Model	σ_T [$\mu\text{b/sr}$]	σ_L [$\mu\text{b/sr}$]	f
MAID 2003	10.436	1.892	5.52
DMT	9.428	1.649	5.72
Sato-Lee	10.113	0.708	14.28
SAID	10.361	0.359	28.87

Table 5.12: Cross sections used to account for the different factors of ϵ in the existing data.

The factors from the various models at $W = 1232$ MeV, $Q^2 = 0.127$, and $\theta_{pq}^* = 0^\circ$ (GeV/c)² can be found in Table 5.12. MAID 2003 agrees best with the existing data [74] and so is the model used in the conversion. Using MAID 2003, the correction factor is about 1%. With the other models, the correction is even smaller.

Table 5.13 shows all of the parallel cross section comparisons for the previous Bates data and the current experiment. For reference, the original, unconverted values are included. An easier way to see the comparison is shown in Fig. 5-41 where the Bates and Mainz values are plotted along with the total error band for each. There is a reasonable overlap region since the systematic errors are accounted for in the plot. The Mainz results are stable over time from April 2003 to October 2003. Another item to consider is that the variation in the Bates measurements is about 4% and the difference from Mainz to the lowest Bates point is about the same. The conclusion drawn is that the current measurement agrees with previous measurements within the systematic error.

The conclusion for agreement was drawn after extensive checking for systematic shifts. Among the checks performed were:

- VDC efficiency compared with scintillators (fine)
- Relative efficiency of the separate VDCs (fine)
- Different optics offsets (fine)
- Beam position offsets (fine)
- Central vertex offsets (fine)

Data set	ϵ	XS [$\mu\text{b/sr}$]	Stat. [$\mu\text{b/sr}$]	Syst. [$\mu\text{b/sr}$]	Model [$\mu\text{b/sr}$]
Mertz-Vellidis	0.614	11.20 ± 0.61	0.22	0.57	0.003
Sparveris	0.768	11.98 ± 0.41	0.16	0.36	0.11
Mertz-Vellidis	0.707	11.40 ± 0.62	0.22	0.58	0.003
Sparveris	0.707	11.85 ± 0.41	0.16	0.36	0.11
Q127-q(25)	0.707	10.84 ± 0.37	0.08	0.35	0.08
Q127-q(30)	0.707	10.97 ± 0.38	0.10	0.36	0.08
Q126-W1232(20)	0.707	10.85 ± 0.37	0.08	0.35	0.08

Table 5.13: Comparison of the parallel cross section from previous experiments and from the current experiment.

- Phase space cuts checks (fine, see Sec. 5.3.10)
- Background subtraction (fine, see Sec. 5.3.3)
- Acceptance and central momentum cuts (fine, see Sec. 5.3.8)
- Search for stable part of spectrometer across setups which gave good agreement with models (negative result)
- Cross checks between S. Stave and N. Sparveris using the same data set (fine)

Most of the checks performed showed stability and consistency of the results and were not particularly sensitive. No reason for the systematic shift between the two data sets could be found but they do agree within the systematic errors.

One more check of the systematic errors was performed during the low Q^2 W scan. Settings Q06-W1205 and Q06-W1205_rev measured the same cross section but with the roles of the spectrometers reversed. The cross section results are shown in Table 6.1. The final results come within $0.16 \mu\text{b/sr}$ of agreeing. This along with the low elastic results on either side (see Sec. 5.4.1) seem to indicate a possible several percent systematic shift down during the W scan. However, a detailed study of the settings have not given any reason for the shift. Therefore, the W scan results are shown without any additional corrections. This systematic shift does not affect the primary low Q^2 data or the shape of the W results.

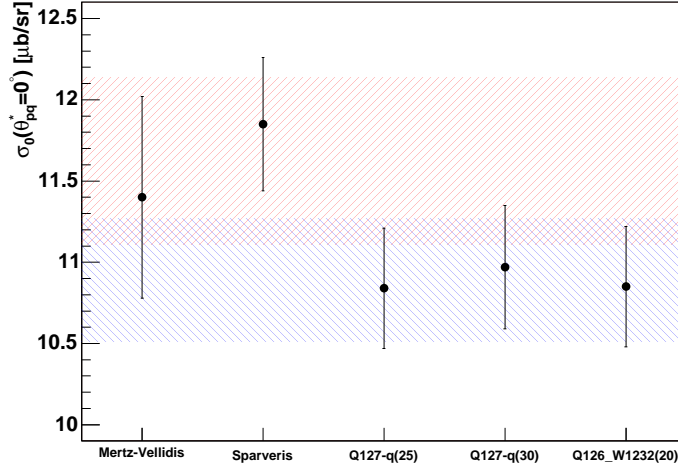


Figure 5-41: Comparison of the parallel cross section from previous experiments and from the current experiment. The red / lines are the average of the central values and the errors for Bates. The blue \ lines are the values for Mainz. The overlap region is easily seen.

5.4.5 More Bates Overlap

In addition to the parallel cross section at resonance and $Q^2 = 0.127 \text{ (GeV/c)}^2$, other data were taken which either directly overlap with previous data taken at Bates or are close.

One direct overlap is the measurement of the asymmetry

$$A_{0\pi} = \frac{\sigma(\phi_{pq} = 0) - \sigma(\phi_{pq} = 180)}{\sigma(\phi_{pq} = 0) + \sigma(\phi_{pq} = 180)} = \frac{-v_{LT}\sigma_{LT}}{\sigma_T + \epsilon\sigma_L + \epsilon\sigma_{TT}} \quad (5.30)$$

and σ_{LT} at $W = 1232 \text{ MeV}$, $Q^2 = 0.126 \text{ (GeV/c)}^2$, and $\theta_{pq}^* = 28^\circ$. The results from Bates [80] and the cross check results from Mainz are in Tables 5.14 and 5.15. The Mainz results are systematically below the Bates results but are within the statistical error bars let alone the total errors. This is also a difficult comparison because the cross section is very small.

Another direct overlap is the parallel cross section at $Q^2 = 0.127 \text{ (GeV/c)}^2$ and $W = 1212 \text{ MeV}$. The comparison of the results from Bates [80] is shown in Table 5.16. The difference between the the Mainz and Bates average result is larger than

Data	$A_{0\pi}$	Stat. Err.	Sys. Err.	Model Err.	Total Err.
Bates	-0.227	0.024	0.018	0.009	0.031
Mainz	-0.198	0.015	0.029	—	0.025

Table 5.14: Comparison of the Bates and Mainz $A_{0\pi}$ at $W = 1232$ MeV, $Q^2 = 0.126$ (GeV/c)² and $\theta_{pq}^* = 28^\circ$. The Mainz statistical error contains the estimated setup-to-setup (cut) error (see Sec. 5.5). The model error was not estimated for the Mainz results.

Data	σ_{LT}	Stat. Err.	Sys. Err.	Model Err.	Total Err.
Bates	1.94	0.20	0.17	0.07	0.27
Mainz	1.62	0.13	0.16	—	0.21

Table 5.15: Comparison of the Bates and Mainz σ_{LT} at $W = 1232$ MeV, $Q^2 = 0.126$ (GeV/c)² and $\theta_{pq}^* = 28^\circ$. The Mainz statistical error contains the estimated setup-to-setup (cut) error (see Sec. 5.5). The model error was not estimated for the Mainz results. The cross section from [80] has been converted to the conventions in [29].

what was previously seen for the parallel cross section at $W = 1232$ MeV. However, the Bates data were taken at two different beam energies $E = 719$ and 799 MeV and the results were averaged. The new Mainz results agree within the errors with the Bates data taken at the higher beam energy. That higher energy is closer to the beam energy used for the Mainz data. The conclusion is that while the results are still systematically low, the new results agree with the Bates results within the errors.

The next cross check did not have an exact overlap because the data were taken to extend the database at $Q^2 = 0.127$ (GeV/c)². The cross section $\sigma_{LT'}$ was measured at $W = 1221$ MeV and at three $\theta_{pq}^*, \phi_{pq}^*$ combinations. This was then compared with

Data	$\sigma(\theta_{pq}^* = 0)$	Stat. Err.	Sys. Err.	Model Err.	Total Err.
Bates-719	16.13	0.60	0.85	0.10	1.05
Bates-799	14.79	0.53	0.85	0.13	1.01
Bates-Avg	15.37	0.40	0.85	0.12	0.95
Mainz	13.58	0.24	0.38	—	0.45

Table 5.16: Comparison of the Bates and Mainz $\sigma(\theta_{pq}^* = 0)$ at $W = 1212$ MeV and $Q^2 = 0.126$ (GeV/c)². The Mainz statistical error contains the estimated setup-to-setup (cut) error (see Sec. 5.5). The model error was not estimated for the Mainz results.

data from Bates taken at $W = 1232$ MeV, $Q^2 = 0.127$ (GeV/c) 2 , $\theta_{pq}^* = 51^\circ$ [49]. Figure 5-42 shows that the new results are consistent with the previous Bates results within the errors. With only three Mainz data points and the large error bars, it is difficult to select one model over another in this plot. For this reason, it is being included to show overall consistency with the previous results but is not being used for physics interpretation.

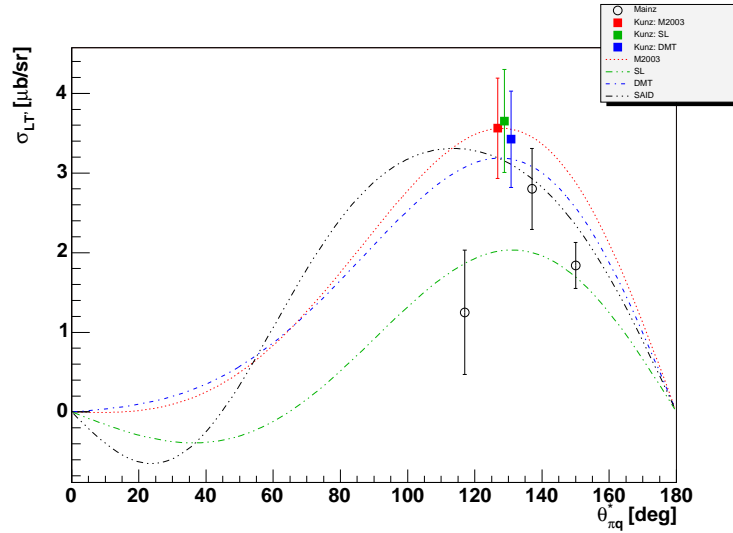


Figure 5-42: Comparison of the Bates and Mainz $\sigma_{LT'}$ results at $W = 1221$ MeV, $Q^2 = 0.127$ (GeV/c) 2 and the predictions from several models. The Bates data point has been transported from $W = 1232$ MeV using three models (MAID, Sato-Lee, and DMT) but the results are similar. The error bars reflect the total error, statistical plus systematic added in quadrature. However, the error is mostly ($> 95\%$) statistical in nature.

One final overlap involves the $Q^2 = 0.126$ (GeV/c) 2 data all taken at either 28 or 30 degrees. The helicity dependent part of the 30 degree data has been used above but not the helicity independent part. The two in-plane measurements at 28 degrees along with the out-of-plane measurement at 30 degrees are close to the same configuration used for $Q^2 = 0.060$ (GeV/c) 2 at 24 degrees. In the low Q^2 case, there were two in-plane and one maximally out-of-plane measurement all at the same proton angle. In this case, the out-of-plane proton angle differs slightly from the two in-plane measurements. However, the difference is small and using various

	M_{1+} [$10^{-3}/m_{\pi^+}$]	EMR [%]	CMR [%]
Bates	$41.4 \pm 0.3 \pm 0.4$	$-2.3 \pm 0.3 \pm 0.6$	$-6.1 \pm 0.2 \pm 0.5$
Mainz	$40.2 \pm 0.7 \pm 0.5$	$-2.6 \pm 0.4 \pm 0.5$	$-5.6 \pm 0.3 \pm 0.3$

Table 5.17: Comparison of the three parameter resonant fit results using the independent Bates [74] and Mainz results. The first error is the statistical and systematic error combined in quadrature. The second error is the model error.

models, the error can be estimated. In addition, there is the parallel cross section at $W = 1232$ MeV. These four data points are sufficient to allow a three resonant parameter fit (explained in detail in App. A). From this, the M_{1+} , EMR and CMR can be extracted and compared with the previous Bates analysis [74].

The comparison is shown in Table 5.17 where the MAID model was used to fit the Bates results [74] and the new Mainz results are the average of using four models to fit: DMT [47, 46], MAID [28], Sato-Lee [67] and SAID [4]. The EMR is in agreement within the experimental errors and the CMR agrees if the model errors are taken into account. The M_{1+} results agree on the outside edges of the error bars and show a $\approx 3\%$ lower result for Mainz. Since the cross section is proportional to $|M_{1+}|^2$, the fits indicate a $\approx 6\%$ difference between the labs. This is consistent with the parallel cross section comparison shown in Sec. 5.4.4. Model errors were estimated in different ways for the two analyses but it is gratifying that the estimates are similar. The Bates analysis estimated the effect of higher order multipoles within one model while the Mainz analysis took the standard deviation of the results of fits using the four representative models listed above. This latter method is also used in Sec. 7.1.2 to estimate the model errors at $Q^2 = 0.060$ (GeV/c) 2 .

5.5 Systematic Errors

The systematic error estimates come from either previous work or from the analysis of the current data. The quantity in question was varied and the new cross section was found. The difference for various quantities gave the estimated systematic error.

The luminosity was described in Sec. 5.3.4. The systematic error on the total charge is small ($<0.1\%$) since the Förster probe measures the charge very precisely (see Sec. 3.1.4). The error on the target length is estimated at 1% and the density error is also estimated at 1%. The total estimated error that was recommended for the luminosity is then 2% [53]. The stable elastic results shown in Sec. 5.4.1 verify this estimate. In addition, the singles rates in Spectrometer C (the luminosity monitor) during runs were very stable.

As mentioned in Sec. 5.3.6, from [66] and [71], the systematic error in the detector inefficiency correction is estimated to be 1%.

As mentioned in Sec. 5.3.5, the deadtime correction comes from counts and so the error from counting statistics.

The phase space cut uncertainties were found by looking at the difference in the cross section when using the flat, central region, and the larger region which included some of the shoulders (see Sec. 5.3.10). The large, in-plane angle settings had very little difference, but for the rest of the settings, the difference was typically 2 to 3%. The systematic error in the cut correction was estimated to be the average of the errors in the ratios of the small and large cut regions (see Table 5.9). The systematic error in the cut correction is between 1.5% and 2.5%.

Since the phase space cut varies with the kinematics, the error in the cut contributes to the statistical error from one setup to another. In addition, the deadtime correction is statistical in nature and can vary from setup to setup. So, the phase space cut error and deadtime error are combined in quadrature to get the setup-to-setup error and that is then combined with the statistical error in quadrature. This is the error that is used as the statistical error in all the plots and in the fitting procedure (see Sec. 7.1).

As mentioned in Sec. 5.3.9, models of the cross section were used to collapse the cross section to a point. By using several models and comparing the differing cross sections (see Table 5.18), an estimate of the model error was made. The models MAID2003, Sato-Lee, DMT, and SAID were used and the RMS deviation of the various resulting cross sections gave the estimate. For most runs, the model error

Setup	M2003 [$\mu\text{b/sr}$]	DMT [$\mu\text{b/sr}$]	SL2000 [$\mu\text{b/sr}$]	SAID [$\mu\text{b/sr}$]	Stat. [$\mu\text{b/sr}$]	Avg \pm RMS [$\mu\text{b/sr}$]	RMS/Avg
Q06-t0	11.78	11.71	11.77	11.70	0.08	11.74 \pm 0.04	0.004
Q06-t24-p1	11.11	11.09	11.14	11.106	0.06	11.11 \pm 0.02	0.002
Q06-t24-p2	17.80	17.76	17.89	17.72	0.08	17.79 \pm 0.07	0.004
Q06-t24-p3	15.06	15.06	15.12	14.97	0.07	15.05 \pm 0.06	0.004
Q06-t36-p2	22.29	22.27	22.40	22.20	0.11	22.29 \pm 0.09	0.004
Q06-t36-p3	17.49	17.46	17.57	17.36	0.08	17.47 \pm 0.08	0.005
Q06-t36-p1	14.90	15.09	15.24	14.83	0.11	15.02 \pm 0.19	0.013

Table 5.18: Model dependence of uncorrected cross sections. The statistical error is the same for each model in each setting. Also notice that the RMS deviation spread in the models is less than or equal to the statistical error. The only exception is the Q06-t36-p1 run which was off-center.

was about 0.4%. However, for the Q06-t36-p1 run the error is larger. This was due to the larger collapse interval. Because of unforeseen constraints (see Chap. 4), the spectrometers were not placed at the design kinematics but rather about 7 degrees lower in θ_{pq}^* . As a result, the collapse is more dependent on the model and the model error is 1.3%.

The beam current dependent luminosity correction is mentioned in Sec. 5.3.4 and the estimated error on the correction is 1%.

The momentum and angular resolution of the spectrometers were given in Sec. 3.3. These numbers were checked using elastic scattering elastic relations. Since the elastic kinematics are constrained once one variable is measured ($E', \theta_e, P', \theta_p$), the other variables can be calculated from one and compared to the measured values. This acts as a self-consistency check. Figure 5-43 shows the comparison for one variable. The calculations show that the simulation and data agree very well. The energy results would be at zero if the radiated losses were added back in. However, the simulation is radiated to match the data. The data and simulation should agree but then the difference will be non-zero.

To see the effect of the resolution errors, the central momentum and angle settings for the spectrometers were changed in the simulation and the new results used to extract cross sections. Using various combinations of the resolutions and for several,

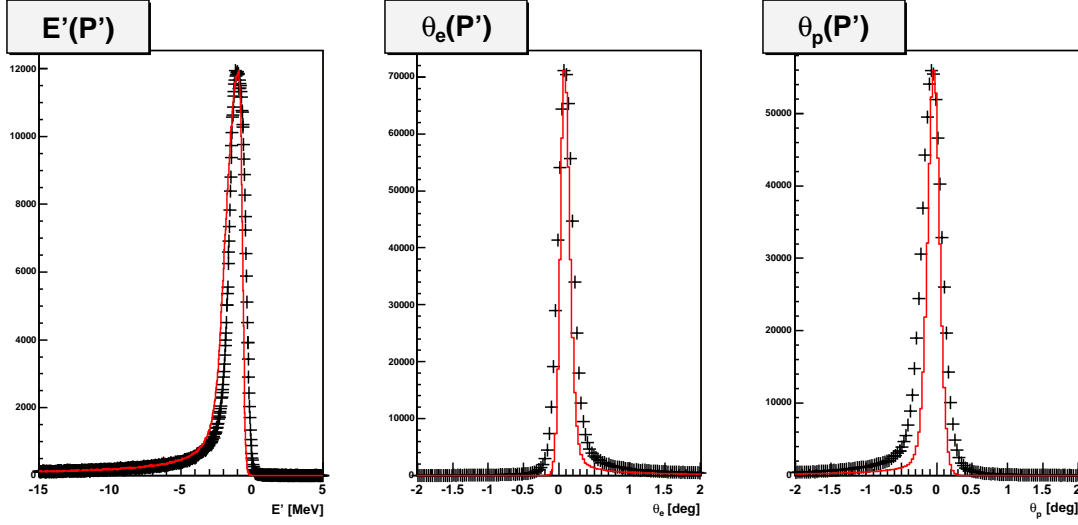


Figure 5-43: Comparison of the elastic kinematic relations for the data (black crosses) and the simulation (line) for the proton momentum P' . For each plot, the calculated kinematic value is subtracted from the measured value. When in agreement, the results should be centered around zero. This is nearly the case for the angular relations. The energy loss calculation leads to an offset in the momentum comparison.

representative setups, the resolution error was estimated at 1%. Since the elastic relations study did show some larger discrepancies in the electron momentum (0.3 MeV/c), even larger deviations of the momentum alone were checked with the simulations. The pion production cross sections changed by less than 0.5%. The overall 1% estimate should then be good. It is also possible that the offsets seen in the elastic will be averaged out more in production runs since the kinematics are no longer constrained. This can be seen in the plots of data and simulation (Fig. 5-1). The agreement in Q^2 and W is very good.

The spectrometer positioning errors of 0.6 mm and 0.1 mrad (see Sec. 3.3) are much smaller than the resolution errors and so were assumed to not affect the results in a significant way.

The beam position can affect the cross section. A study showed that this effect is also about 1%.

For the runs which used the beam polarization, there is an additional systematic error of 1.2% from the Möller polarimeter measurement. However, those runs typically

Error	Size [%]
Luminosity	2
Detector inefficiency correction	1
Deadtime correction error per setup	< 0.5
Phase space cut error	1.5→2.4
Model error in collapse	0.4,1.3
Beam current lumi correction	1
Momentum and angular resolution	1
Beam position	1
Total in quadrature	3.3→3.7
Beam polarization	1.2

Table 5.19: Summary of systematic errors.

suffer from large statistical errors so the systematic errors are not significant.

Table 5.19 summarizes all of the systematic errors and their sources. The final systematic error is consistent with estimates given in [12].

Chapter 6

Results

In the previous chapter, certain specific results were shown as examples. In this chapter, all of the remaining cross sections will be shown for $Q^2 = 0.060$ and $Q^2 = 0.127$ (GeV/c)². The analysis procedure outlined in Chap. 5 was applied to the data. Corrections for luminosity, phase space cuts, and inefficiency were applied and each correction carries a different systematic error.

6.1 $Q^2 = 0.060$ (GeV/c)² data

The main focus of this thesis is the low Q^2 data. These are the data that test the Q^2 variation of the models and CPT the most.

Table 6.1 shows the final cross section results with the correction factors and the total error added in quadrature. The helicity dependent cross sections are designated with the suffix “:h” and are defined as

$$XS_h = \sigma(h < 0) - \sigma(h > 0) = -hv_{LT'}\sigma_{LT'} \sin \phi_{\pi q}^* \quad (6.1)$$

where the various terms are defined in Sec. 2.2. The values of XS_h are used instead of $\sigma_{LT'}$ in the fitter to minimize the errors (see Sec. 5.3.9).

The individual errors that comprise the total error for each $Q^2 = 0.060$ (GeV/c)² data point are listed in Table 6.1. The statistical error is mainly from the counts

inside the cuts and partly the number of counts in the simulation. The setup-to-setup error consists of the terms which could vary from one setting to another and so must be included in the errors used to fit the data (χ^2 minimization requires full statistical errors). These were primarily the phase space cut uncertainties (1.5% to 2.5%) along with the error in the total charge ($< 0.1\%$). The rest of the systematic errors are expected to affect all of the points equally. For example, if the luminosity is overestimated because the target length is shorter than that used for the calculation, then all of the setups will be affected equally. The phase space cut uncertainty, though, has a kinematic dependence and so can vary from setup to setup.

Table 6.2 shows the individual parts that comprise the correction factors. The factors are uniform except for the luminosity correction which varied with beam current and the phase space cut correction which varied with kinematics. Table 6.3 shows the summary of the systematic errors. These errors are also uniform except for the presence of the luminosity correction error (if required), the different model error for the mis-aligned setting (see Sec. 5.3.7) and the error in the phase space cut correction. The differences between all of these are not very large.

To facilitate further comparison with the models, the spectrometer cross sections were combined using the formulas in Sec. 5.3.9 to give the cross sections σ_0 , σ_{TT} , σ_{LT} and $\sigma_{LT'}$. Those cross sections are in Table 6.4. The systematic errors were estimated by combining the statistical and phase space acceptance errors in quadrature to form a new error which was used for error propagation. The remaining systematic error was then used to shift the spectrometer cross sections up and down. The range for the extracted σ_0 , σ_{TT} and σ_{LT} before and after the systematic shifts gave the estimate for the systematic error. This procedure gives approximately the same error for σ_0 but half the error for σ_{TT} and σ_{LT} than if all the errors were combined in quadrature before the extraction.

Setup	W [MeV]	θ_{pq}^* [$^\circ$]	ϕ_{pq}^* [$^\circ$]	XS [$\mu\text{b}/\text{sr}$]	Stat. [$\mu\text{b}/\text{sr}$]	StS [$\mu\text{b}/\text{sr}$]	Sys. [$\mu\text{b}/\text{sr}$]
Q06-t0	1221	0	—	12.35 ± 0.39	0.09	0.20	0.38
Q06-t24-p1	1221	24	0	11.65 ± 0.37	0.06	0.18	0.36
Q06-t24-p2	1221	24	90	18.67 ± 0.59	0.09	0.30	0.58
Q06-t24-p3	1221	24	180	15.39 ± 0.48	0.07	0.24	0.48
Q06-t36-p1	1221	37	32	15.67 ± 0.54	0.12	0.25	0.52
Q06-t36-p2	1221	37	134	23.38 ± 0.74	0.12	0.37	0.73
Q06-t36-p3	1221	37	180	17.87 ± 0.56	0.08	0.28	0.56
Q06-t24-p2:h	1221	24	90	-1.05 ± 0.16	0.15	0.02	0.03
Q06-t36-p1:h	1221	37	32	-0.68 ± 0.18	0.18	0.01	0.02
Q06-t36-p2:h	1221	37	134	-1.03 ± 0.19	0.19	0.02	0.03
Q06_W1155_p1	1155	26	0	5.57 ± 0.21	0.05	0.13	0.20
Q06_W1155_p2	1155	26	180	6.38 ± 0.23	0.04	0.15	0.23
Q06_W1125	1125	0	—	2.40 ± 0.09	0.02	0.06	0.09
Q06_W1155	1155	0	—	5.48 ± 0.21	0.06	0.13	0.20
Q06_W1185	1185	0	—	10.27 ± 0.40	0.10	0.25	0.39
Q06_W1205	1205	0	—	12.58 ± 0.48	0.11	0.31	0.47
Q06_W1205_rev	1205	0	—	13.69 ± 0.47	0.11	0.27	0.45
Q06_W1225	1225	0	—	10.88 ± 0.42	0.10	0.27	0.41
Q06_W1245	1245	0	—	7.21 ± 0.29	0.09	0.18	0.27
Q06_W1275	1275	0	—	3.17 ± 0.12	0.04	0.08	0.12
Q06_W1300_low	1300	0	—	1.48 ± 0.06	0.02	0.04	0.06

Table 6.1: $Q^2 = 0.060 \text{ (GeV/c)}^2$ cross sections. The error is the total statistical plus systematic error in quadrature. The individual errors are the statistical error, the setup-to-setup error (primarily the phase space cut correction error) and the total systematic error. The setup-to-setup error is the size of the error expected between setups and, combined with the statistical error, is the error that is used in the χ^2 minimization fits (see Sec. 7.1.2). Other parts of the systematic error are expected to affect all the setups equally. The systematic error for the Q06-t36-p1 setting is larger because of the larger model error. The second set of results with the suffix “:h” is for the helicity dependent cross section. The errors are statistically dominated for those results. The third set of results are from the background amplitude test. The lower set of results is the W parallel cross section scan. For the details on the systematic errors and the correction factor, see Tables 6.2 and 6.3.

Setup	I [μ A]	Scint. ineff.	Coinc. ineff.	VDC ineff.	Lumi. corr.	Cut corr.	Total corr.
Q06-t0	8.18	1.013	1.004	1.005	1.000	1.026	1.049
Q06-t24-p1	8.18	1.013	1.004	1.005	1.000	1.026	1.049
Q06-t24-p2	8.82	1.013	1.004	1.005	1.000	1.026	1.049
Q06-t24-p3	8.90	1.013	1.004	1.005	1.000	1.000	1.022
Q06-t36-p1	8.62	1.013	1.004	1.005	1.000	1.026	1.049
Q06-t36-p2	8.81	1.013	1.004	1.005	1.000	1.026	1.049
Q06-t36-p3	8.36	1.013	1.004	1.005	1.000	1.000	1.022
Q06_W1155_p1	3.05	1.013	1.004	1.005	1.000	1.000	1.022
Q06_W1155_p2	5.37	1.013	1.004	1.005	1.000	1.000	1.022
Q06_W1125	10.08	1.013	1.004	1.005	1.000	1.019	1.041
Q06_W1155	11.90	1.013	1.004	1.005	1.000	1.019	1.041
Q06_W1185	13.44	1.013	1.004	1.005	1.002	1.019	1.043
Q06_W1205	13.96	1.013	1.004	1.005	1.003	1.019	1.044
Q06_W1205_rev	2.54	1.013	1.004	1.005	1.000	1.000	1.022
Q06_W1225	13.98	1.013	1.004	1.005	1.003	1.019	1.045
Q06_W1245	14.12	1.013	1.004	1.005	1.003	1.019	1.045
Q06_W1275	20.65	1.013	1.004	1.005	1.017	1.019	1.059
Q06_W1300_low	25.23	1.013	1.004	1.005	1.026	1.019	1.069

Table 6.2: Correction factors for $Q^2 = 0.060 \text{ (GeV/c)}^2$ data. Detailed descriptions of all the factors are in Secs. 5.3.4, 5.3.6 and 5.3.10. The total correction factor is the product of each individual factor. Helicity dependent cross sections have the same correction factors as the helicity independent versions.

Setup	Lumi.	Det. ineff.	Dead- time	Lumi. corr.	Cut err.	Model err.	Res. err.	Beam pos.	Tot. err.
Q06-W1221	0.02	0.01	0.005	0.00	0.015	0.004	0.01	0.01	0.031
Q06-t36-p1	0.02	0.01	0.005	0.00	0.015	0.013	0.01	0.01	0.033
Q06_W1155_px	0.02	0.01	0.005	0.00	0.023	0.004	0.01	0.01	0.036
W scan I<12.5 μ A	0.02	0.01	0.005	0.00	0.024	0.004	0.01	0.01	0.036
W scan	0.02	0.01	0.005	0.01	0.024	0.004	0.01	0.01	0.038
W scan rev.	0.02	0.01	0.005	0.00	0.019	0.004	0.01	0.01	0.033
		Hel. dep.		Hel. indep.		Beam Pol.		Tot. err.	
		Q06-W1221		0.031		0.012		0.033	
		Q06-t36-p1		0.033		0.012		0.035	

Table 6.3: Systematic error summary for $Q^2 = 0.060 \text{ (GeV/c)}^2$. Individual error estimates are all described in Sec. 5.5. The Cut error is the phase space cut correction (Sec. 5.3.10). The Model error is from the RMS deviation of the models used to collapse the cross sections (Sec. 5.5 and Table 5.18). The Res. error is the resolution error arising from the angular and position resolution study (Sec. 5.5). The Beam pos. error is the error arising from the change in the beam position (Sec. 5.5). The error from the phase space cut correction and dead time are the values which can change from setup-to-setup (StS in Table 6.1). The lower table contains the additional errors arising from the polarized beam. The helicity dependent cross sections have the same systematic errors as the helicity independent cross sections but with the beam polarization error added in quadrature.

W [MeV]	Q^2 [(GeV/c) 2]	θ_{pq}^* [$^\circ$]	σ	XS [$\mu\text{b/sr}$]	Stat. + Sts. Err. [$\mu\text{b/sr}$]
1221	0.060	24.0	σ_0	16.10 ± 0.47	0.17
1221	0.060	24.0	σ_{TT}	-3.30 ± 0.24	0.22
1221	0.060	24.0	σ_{LT}	1.12 ± 0.10	0.09
1221	0.060	37.0	σ_0	21.02 ± 0.66	0.31
1221	0.060	37.0	σ_{TT}	-7.99 ± 0.66	0.63
1221	0.060	37.0	σ_{LT}	1.85 ± 0.14	0.13
1155	0.060	26.0	σ_{LT}	0.22 ± 0.09	0.06
1155	0.060	26.0	$\sigma_0 + \epsilon\sigma_{TT}$	5.97 ± 0.15	0.11
1221	0.060	24.0	$\sigma_{LT'}$	1.23 ± 0.18	0.18
1221	0.060	37.0	$\sigma_{LT'}$	1.59 ± 0.36	0.35

Table 6.4: Summary of the extracted values for σ_0 , σ_{TT} , σ_{LT} , and $\sigma_{LT'}$. The error in the cross section is the total statistical and systematic error, added in quadrature. See text for details of the error estimation procedure.

Setup	W [MeV]	θ_{pq}^* [$^\circ$]	ϕ_{pq}^* [$^\circ$]	XS [$\mu\text{b/sr}$]	Stat. [$\mu\text{b/sr}$]	StS [$\mu\text{b/sr}$]	Sys. [$\mu\text{b/sr}$]
Q127-w1140-p1	1140	58.6	45	6.93 ± 0.27	0.08	0.17	0.26
Q127-w1140-p2	1140	58.6	135	5.53 ± 0.21	0.04	0.14	0.21
Q127-w1140-p1:h	1140	58.6	45	-0.66 ± 0.17	0.17	0.02	0.02
Q127-w1140-p2:h	1140	58.6	135	-0.42 ± 0.09	0.09	0.01	0.02
Q127-th30	1221	30	90	22.61 ± 0.81	0.16	0.47	0.80
Q127-th43	1221	43	135	26.97 ± 0.97	0.21	0.56	0.95
Q127-th63	1221	63	150	29.51 ± 1.06	0.23	0.61	1.04
Q127-th30:h	1221	30	90	-1.70 ± 0.27	0.26	0.04	0.06
Q127-th43:h	1221	43	135	-1.84 ± 0.34	0.33	0.04	0.06
Q127-th63:h	1221	63	150	-0.58 ± 0.36	0.36	0.01	0.02

Table 6.5: $Q^2 = 0.127 \text{ (GeV/c)}^2$ results. The error is the total error in quadrature. The individual errors are the statistical error, the setup-to-setup error and the total systematic error. See caption for Table 6.1 for more details. The suffix “:h” denotes helicity dependent results. For the details on the systematic errors and the correction factor, see Tables 6.7 and 6.6.

6.2 $Q^2 = 0.127 \text{ (GeV/c)}^2$ data

As outlined in Sec. 4.2, the database at $Q^2 = 0.127 \text{ (GeV/c)}^2$ was extended. The goal of the extension was to investigate the background amplitudes in more detail and complement the existing data. The results are shown in Table 6.5. The details behind the correction factors are shown in Table 6.6 and the systematic errors are in Table 6.7. As in the previous section, the separated σ s have been calculated and are shown in Table 6.8.

Setup	I [μ A]	Scint. ineff.	Coinc. ineff.	VDC ineff.	Lumi. corr.	Cut corr.	Total corr.
Q127-w1140-p1	20.36	1.013	1.004	1.005	1.016	1.028	1.067
Q127-w1140-p2	19.15	1.013	1.004	1.005	1.013	1.028	1.065
Q127-th30	25.62	1.013	1.004	1.005	1.027	1.025	1.076
Q127-th43	25.43	1.013	1.004	1.005	1.027	1.025	1.075
Q127-th63	24.97	1.013	1.004	1.005	1.026	1.025	1.074

Table 6.6: Correction factors for the $Q^2 = 0.127$ (GeV/c) 2 data. Detailed descriptions of all the factors are in Secs. 5.3.10, 5.3.6, and 5.3.4. The total correction factor is the product of each individual factor. Helicity dependent cross sections have the same correction factors as the helicity independent versions.

Setup	Lumi.	Det. ineff.	Deadtime	Lumi. corr.	Cut err.	Model err.	Res. err.	Beam pos.	Tot. err.
Q127-w1140-px	0.02	0.01	0.005	0.01	0.024	0.004	0.01	0.01	0.038
Q127-thxx	0.02	0.01	0.005	0.01	0.020	0.004	0.01	0.01	0.035
Hel. dep.			Hel. indep.	Beam Pol.		Tot. err.			
Q127-w1140-px:h			0.038	0.012		0.040			
Q127-thxx:h			0.035	0.012		0.037			

Table 6.7: Systematic error summary for $Q^2 = 0.127$ (GeV/c) 2 . See caption for Table 6.3 for an explanation for each term.

W [MeV]	Q^2 [(GeV/c) 2]	θ_{pq}^* [$^\circ$]	σ	XS [μ b/sr]	Stat. + Sts. Err. [μ b/sr]
1140	0.127	58.6	σ_0	6.23 ± 0.17	0.12
1140	0.127	58.6	σ_{LT}	-0.58 ± 0.14	0.10
1140	0.127	58.6	$\sigma_{LT'}$	0.94 ± 0.16	0.16
1221	0.127	30.0	$\sigma_{LT'}$	1.84 ± 0.29	0.28
1221	0.127	43.0	$\sigma_{LT'}$	2.80 ± 0.51	0.51
1221	0.127	63.0	$\sigma_{LT'}$	1.25 ± 0.78	0.78

Table 6.8: Summary of the extracted values for σ_0 , σ_{LT} , and $\sigma_{LT'}$. The error in the cross section is the total statistical and systematic error, added in quadrature.

Chapter 7

Interpretation and Discussion

Now that the results have been shown in tabular form, they will be compared with models and models fit to the data. In addition, the extracted resonant multipoles will be given that were obtained by fitting the data with the different models described in Sec. 2.7. All of the near resonance and background sensitive results will then be interpreted and discussed.

7.1 Models and Fitting

7.1.1 Comparison with Models

Plotting the data with model predictions provides a qualitative comparison. The large scale model predictions can be tested. Also, for calculations like EFT which yield cross sections but not many multipoles, a comparison at the cross section level can be illuminating. However, precision multipoles and the extraction of the non-spherical terms will wait until the next section.

The upper panels of Figures 7-1 and 7-2 show the cross sections at $W = 1221$ MeV, $Q^2 = 0.060$ (GeV/c)² as a function of $\phi_{\pi q}^*$ along with the predictions from several models. These spectrometer cross sections are then fit (see Sec. 7.1.2) and the resulting fitted models are plotted in the lower panels of Figures 7-1 and 7-2. Spectrometer cross sections are a linear combination of the various σ s. Figures 7-

1 and 7-2 show the full cross section along with the ϕ dependent components: σ_0 (constant with ϕ), σ_{TT} ($\cos 2\phi$) and σ_{LT} ($\cos \phi$). The predictions from four models before fitting are shown in the upper panels and the agreement or disagreement between the components is apparent. All the models cluster tightly for σ_{TT} but show more dispersion in σ_{LT} and σ_0 . These differences then translate into the dispersions seen in the total cross section. Since both the σ_0 and σ_{TT} cross sections contain the E_{1+} multipole (see Eq. A.7), the clustered σ_{TT} and spread σ_0 make interpretation of the EMR difficult. However, σ_{LT} contains S_{1+} (Eq. A.7) and the spread among the models indicates disagreement in the CMR. The next section will check these qualitative arguments.

The lower panels in Figures 7-1 and 7-2 show the convergence of the models after fitting. More examples of the convergence of the models after fitting will be shown shortly. The significance of the convergence is discussed in the next section.

The $Q^2 = 0.060 \text{ (GeV/c)}^2$ results are summarized in Fig. 7-3 along with the model predictions in the upper panel and models after fitting (the EFT calculation from PV was not fitted) in the lower panel (see Sec. 7.1.2). The PV EFT calculation is consistent with the data but the errors are rather large. Even so, this indicates that the assumptions made in the calculation appear to be valid. This comparison of data and cross sections is the most direct link with QCD in this analysis. All other comparisons are more reliant upon models.

In Figure 7-3, the clustering of σ_{TT} seen in Figs. 7-1 and 7-2 is still present as well as the dispersion in σ_0 and σ_{LT} . Figure 7-3 also shows the comparison for $\sigma_{LT'}$ and the W scan. The $\sigma_{LT'}$ results are spread out from model to model and indicate differences in the backgrounds. The Sato-Lee model follows the data very well but the other models are higher. The W scan also shows significant spread among the models especially near the resonance before the fit. Convergence of the models is clearly shown in the lower panel of Fig. 7-3. More detail is given in the next section.

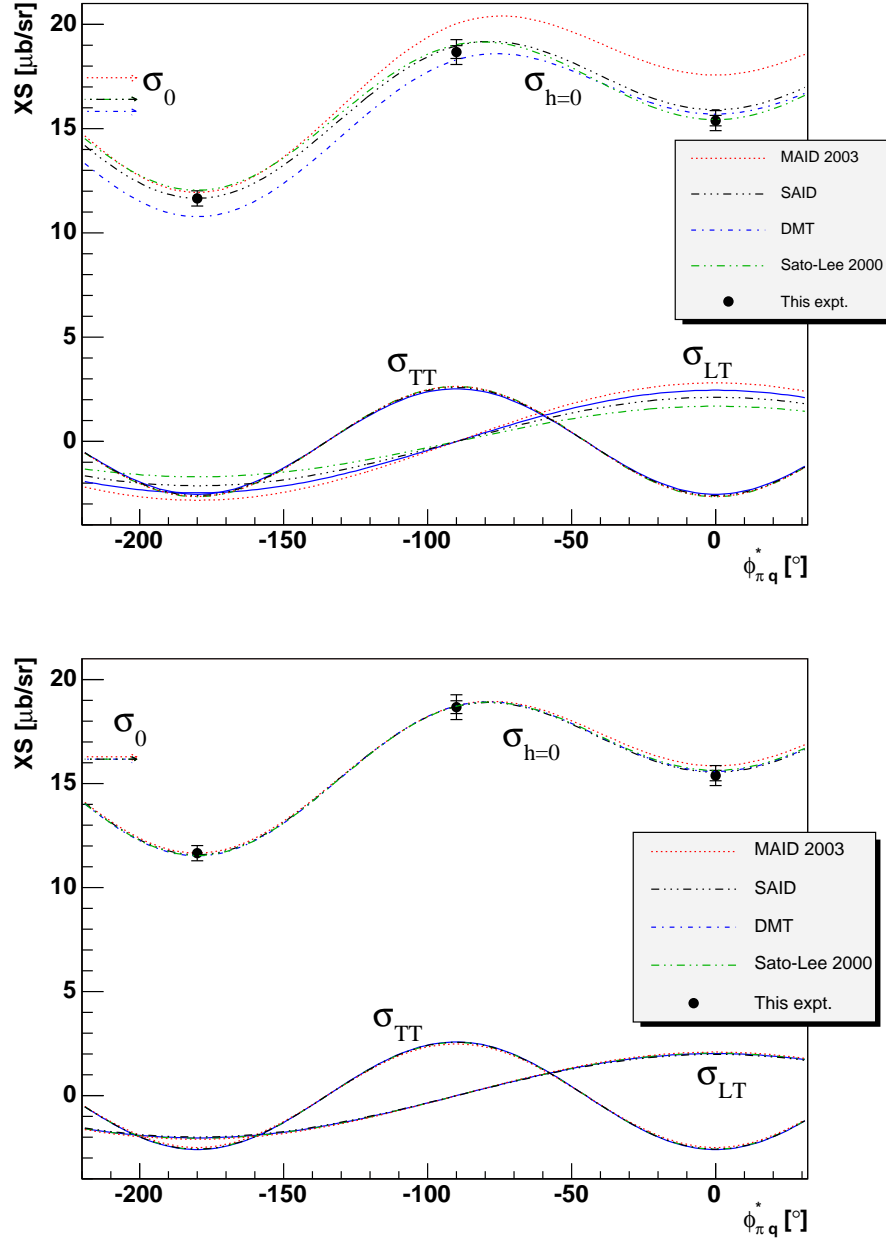


Figure 7-1: The upper panel shows the new data at $W = 1221$ MeV, $Q^2 = 0.060$ $(\text{GeV}/c)^2$, $\theta_{pq}^* = 24^\circ$ plotted plotted versus ϕ_{pq}^* with the model predictions. The wide error bars are the total systematic and statistical errors added in quadrature. The narrower error bars are the statistical only. The models are MAID2003 [28, 29], DMT [47, 46], Sato-Lee [67] and SAID [4]. In addition to the full helicity independent cross section, the various components are plotted. σ_0 from each model is a horizontal arrow since there is no ϕ dependence. The σ_{TT} component goes with $\cos 2\phi$ and varies more rapidly than the σ_{LT} with its $\cos \phi$ dependence. The lower panel shows the same data but with the three parameter fitted models described in Sec. 7.1.2. The convergence is significant.

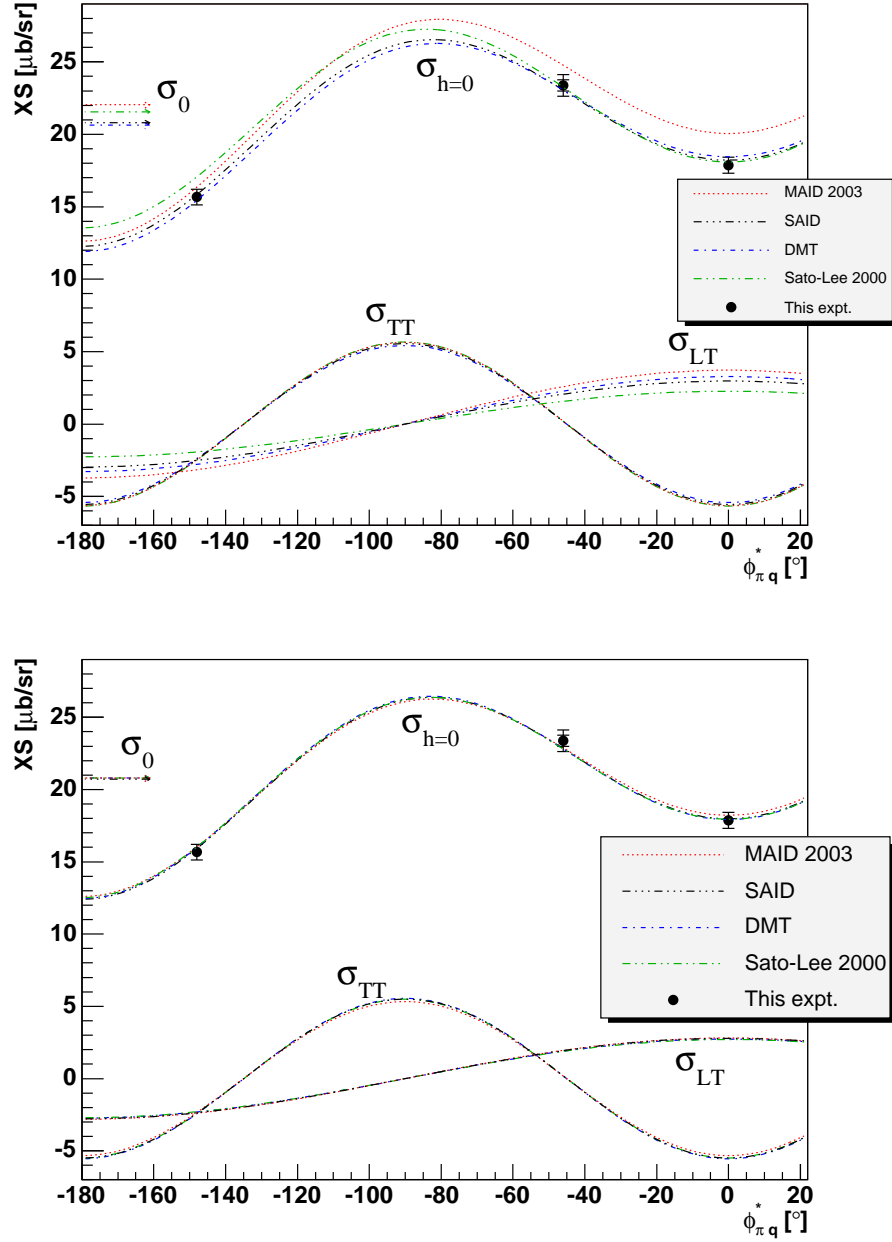


Figure 7-2: The upper panel shows the new data at $W = 1221$ MeV, $Q^2 = 0.060$ $(\text{GeV}/c)^2$, $\theta_{pq}^* = 37^\circ$ plotted versus ϕ_{pq}^* with the model predictions. The lower panel shows the same data but with the three parameter fitted models described in Sec. 7.1.2. The convergence is significant as in Fig. 7-1. See caption for Fig. 7-1 for more details.

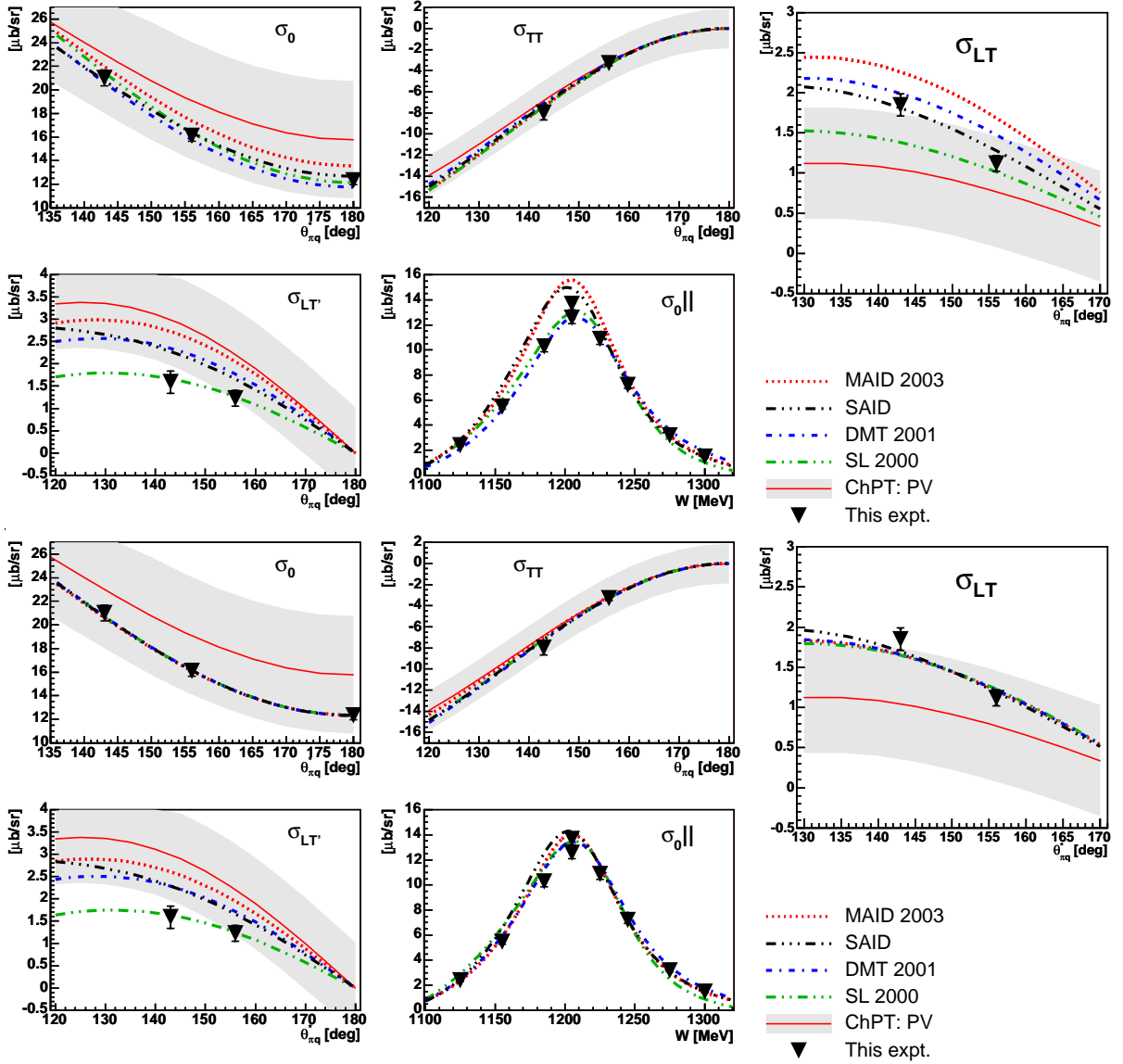


Figure 7-3: Summary of the new Mainz data at $Q^2 = 0.060 (\text{GeV}/c)^2$ plotted with the model predictions (upper panel) and fitted models (lower panel). The wide error bars are the total systematic and statistical errors added in quadrature. The narrower error bars (not always visible) are the statistical only. The models are MAID2003 [28, 29], DMT [47, 46], Sato-Lee [67] and SAID [4]. Note the convergence of the models after fitting in the lower panel.

7.1.2 $Q^2 = 0.060 \text{ (GeV/c)}^2$ fits

Interpretation of the final cross sections can be performed in different ways. One method is to plot the results against various models as was done in the previous section. This does allow the models to be tested and even parts of the models can be refined. It is also important for comparing with the chiral EFT calculations which only provide limited predictions for the resonant multipoles but can give cross section predictions. However, to get a more quantitative result, fitting of the cross sections can be performed to extract the resonant amplitudes.

The fitting procedure used in this analysis is described in detail in Appendix A. Briefly, the procedure takes the background multipoles from any given model and varies the amplitude of the resonant, isospin 3/2 multipoles to attain a best fit. Those three multipoles are $M_{1+}^{3/2}$, $E_{1+}^{3/2}$ and $S_{1+}^{3/2}$. The $E_{1+}^{3/2}$ and $S_{1+}^{3/2}$ multipoles indicate the amount of deviation from spherical symmetry. Different models contain different sizes of background terms and different sizes of resonance terms as well. Figure 7-3 showed that the dispersion of the models is significant.

The fitting of the data started with the primary $Q^2 = 0.060 \text{ (GeV/c)}^2$ helicity independent results, the three θ_{pq}^* angles with the ϕ_{pq}^* dependence. Those seven spectrometer cross section results were fit using the three resonant parameter fit with different models. The results are shown in Table 7.1 and all the fits had χ^2 per degree of freedom near one indicating good fits. The lower panel of Figure 7-3 shows a plot of the data and the different fitted models. The plot shows a convergence of the models which is rather significant. Despite different background terms, the models still converged with a three parameter resonant multipole fit. Figure 7-4 also shows this convergence for the EMR and CMR. The convergence in M_{1+} was not as significant but the values for M_{1+} have been modified by the various model authors in order to fit previous data. Therefore, it is not surprising that the three parameter fit did not force it to converge.

It is important to note that in the lower panel of Fig. 7-3, only the primary low Q^2 results have been fit and yet the agreement is also reasonable for the W scan. The

	EMR (%)	CMR (%)	$M_{1+}^{3/2}$	$\chi^2/\text{d.o.f.}$
SAID	-2.18(31)[-1.80]	-4.87(29)[-5.30]	40.81(29,57)[40.72]	0.68
SL	-2.26(30)[-2.98]	-4.46(25)[-3.48]	40.20(27,56)[41.28]	1.04
DMT	-2.11(28)[-2.84]	-4.85(26)[-5.74]	40.78(27,57)[40.81]	0.88
MAID	-2.56(27)[-2.16]	-5.07(26)[-6.51]	39.51(26,57)[40.53]	1.24
Avg.	-2.28(29,01,20)	-4.81(27,03,26)	40.33(27,57,61)	—
GH	-2.66	-6.06	41.15	—
PV	-2.88(70)	-5.85(140)	39.75(387)	—

Table 7.1: Values of EMR, CMR, and M_{1+} (in units of %, % and $(10^{-3}/m_{\pi^+}$ respectively) for the EFT predictions and fitted models. The EFT predictions are Gail and Hemmert (GH) [38] and Pascalutsa and Vanderhaeghen (PV) [60, 61]. The models are the three resonant parameter fitted SAID [4], MAID [28], Sato-Lee(SL) [67], and DMT [47, 46] models at $W = 1232$ MeV (1227.3 MeV for SAID [3]) and $Q^2 = 0.060$ $(\text{GeV}/c)^2$. The original model predictions are in the square brackets. The first number in parentheses is the statistical and setup-to-setup errors added in quadrature. The second number is the systematic errors. The systematic errors for the EMR and CMR are suppressed because they were very small. For the average, the third number is the model errors defined as the RMS deviation of the results from the four different models.

$\sigma_{LT'}$ results are only close for the Sato-Lee model but then those cross sections were not included in this fit. In addition, the $\sigma_{LT'}$ cross section is sensitive primarily to the background amplitudes and a resonant fit is not expected to improve the agreement. A comparison of the upper and lower panels of Fig. 7-3 shows this to be the case. Table 7.1 also shows the original model results and the predictions from the two chiral effective field theory calculations.

The chiral effective field theory results from Pascalutsa and Vanderhaeghen (PV) [60] in Fig. 7-3 were not fit but are included in the plots for comparison. They agree with the σ_0 and σ_{TT} results but not as well for σ_{LT} and $\sigma_{LT'}$. However, the theory error bars are rather large. The error bars come from an estimate of the size of higher order terms (see Sec. 2.6). When the next order calculation is complete, it will be interesting to see the level of agreement with the data. In addition, the error bars should get smaller as they will then reflect even higher order uncertainties.

It is also good to see that the resonant fit has model convergence versus W . The spread of the models was rather significant in the W scan plot in Fig. 7-3 but is now

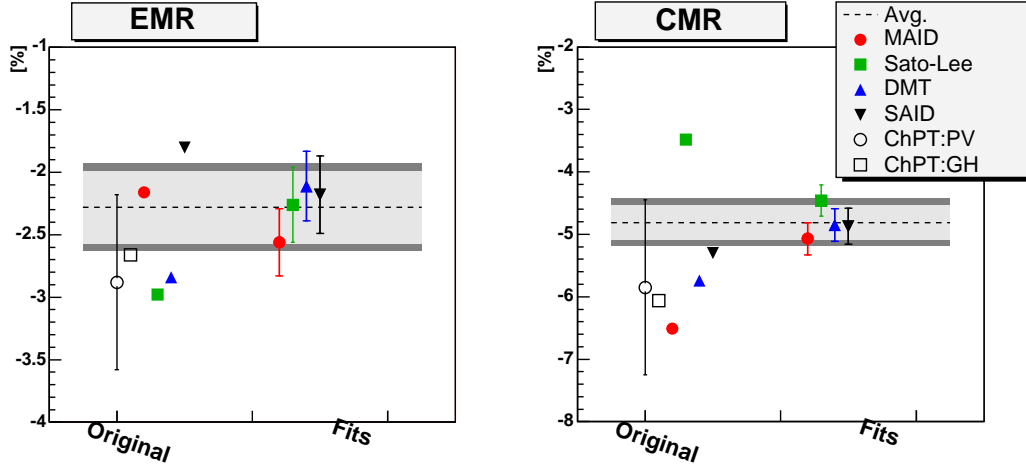


Figure 7-4: Example of the convergence of the EMR and CMR values with fitting. The light error band is the average of the fitting errors and the darker band is the RMS deviation of the models added in quadrature. The models are MAID 2003 [28, 29], DMT [47, 46], Sato-Lee [67] and SAID [4]. The chiral effective field theory predictions of Pascalutsa and Vanderhaeghen (PV) [60, 61] and Gail and Hemmert (GH) [38] are included.

much smaller. The shape is not in perfect agreement but the differences are thought to be due to the background terms which were not varied in the resonant fit.

Table 7.1 contains three different types of errors. The first is the regular statistical error combined in quadrature with the setup-to-setup errors described in Sec. 5.5. This is the error which is used when fitting the data. The minimization of χ^2 requires errors which are statistical in nature and not systematic. The systematic errors are handled differently and are the second type of error in Table 7.1. To take proper account of the systematic errors, all of the fitted cross sections were moved to the maximum of their systematic errors (calculated without the phase space cut error) and to the minimum and fit at each. The range of fit values then gives the estimate of the systematic error.

Finally, Table 7.1 also contains the model errors. The model errors were found by taking the root mean square deviation of the results from the four models. The final result that is quoted is an average of the four models with the average of their statistical and systematic errors along with the RMS deviation model errors. These

errors are a bit arbitrary in that they rely upon which models are used. However, the four models used are representative so adding more models should not affect the results greatly. Also of note is that the model error and experimental errors are very similar in size, especially for the EMR and CMR. This was also seen at $Q^2 = 0.127$ (GeV/c)² in Ref. [74]. Therefore, one can conclude that the current experimental limit has been reached and further gains can only be achieved after improving the models.

The final, averaged results of the three resonant parameter fits are shown in Fig. 7-5 along with the available data in the low Q^2 region and the model predictions. It is gratifying that the final fitted results are in agreement with previous data. In the M_{1+} plot, the model predictions are so closely bunched that the new data point cannot discriminate between the models. This was expected though and any differences between the models will be seen in the more sensitive EMR and CMR plots.

For both the EMR and the CMR, Fig. 7-5 shows that the quark model predictions do not agree with the old or the new data. This is more evidence of the importance of including the pion cloud.

As Q^2 decreases, the EMR predictions from the models tended to converge at the photon point. This is also expected since the models typically fit the photon point. So, no model (other than the quark models) can be ruled out with the new EMR measurement. However, it is consistent with both EFT predictions. Recall that the EFT calculations are more reliable at lower values of Q^2 . The errors increase in the PV calculation and the variability of the GH calculation increases with Q^2 . It is important to note that the fairly large errors in the Pascalutsa and Vanderhaeghen calculation come from an estimate of the size of the next higher order terms (see Sec. 2.6). The new data point at $Q^2 = 0.060$ (GeV/c)² is also consistent with the lattice QCD calculation.

The CMR plot has more divergence at low Q^2 and so the new data point has more power to separate the models there. The new point is in qualitative agreement with the two dynamic models. It is also very close to the SAID results. However, both SAID and MAID are largely fits to other data and do not have predictive power. The

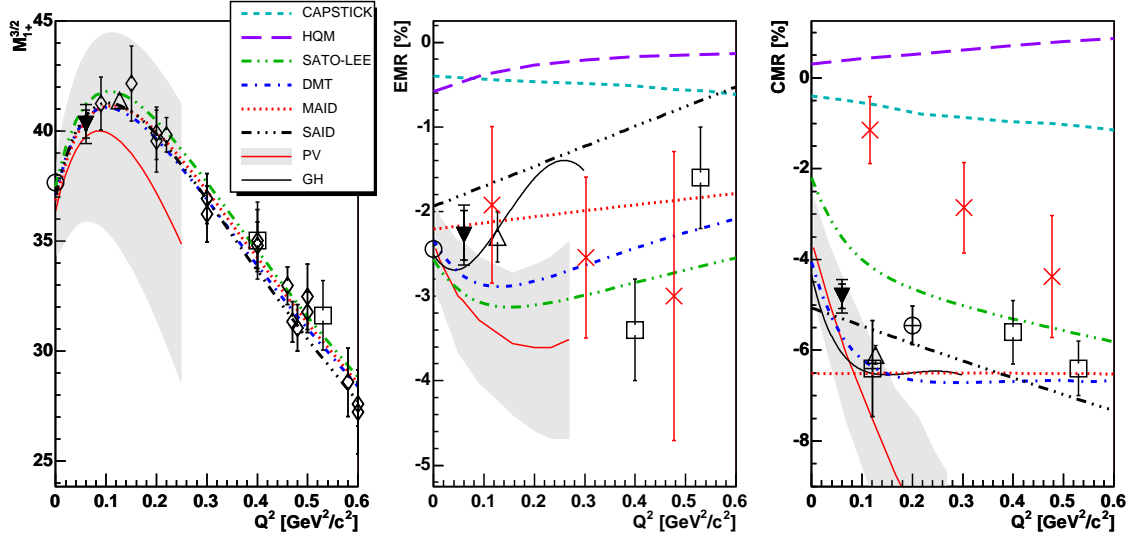


Figure 7-5: Results for $M_{1+}^{3/2}$ (in units of $10^{-3}/m_{\pi}^+$), EMR and CMR extracted with fit for $Q^2 = 0.060$ $(\text{GeV}/c)^2$ at $W = 1232$ MeV compared with other data in the low Q^2 range and the same models as in Fig. 7-3. The newly measured data are the filled triangles \blacktriangledown and include statistical and setup-to-setup errors (first error bars), systematic errors (second error bars), and model errors (third error bars) added in quadrature. The SAID model is plotted at their fitted resonance position of $W = 1227.3$ MeV [3]. The other data are the photon point \bigcirc [13], CLAS \square [45], Bates \triangle [74], Elsner \oplus [33], M_{1+} inclusive \diamond [8], and Pospischil \boxplus [63]. Recent lattice QCD calculations are shown \times [2] as well as recent chiral effective field theory calculations from Pascalutsa and Vanderhaeghen (PV) [60] and Gail and Hemmert (GH) [38]. The GH prediction for $M_{1+}^{3/2}$ is very close to the MAID2003 results up to $Q^2 \approx 0.2$ $(\text{GeV}/c)^2$ and so has been suppressed. The HQM [25] and Capstick [22] quark models have been included to emphasize that those models do not agree with the data. The dynamical models and EFT results tend to agree well with both the new and the existing data.

qualitative agreement of the dynamical models indicates the importance of including the pion cloud. The CMR result is also consistent with both EFT predictions (assuming a similar sized error in the Gail and Hemmert prediction as in the Pascalutsa and Vanderhaeghen) further indicating the importance of the pion cloud. When the next order is calculated, these errors bars will shrink.

The lattice QCD prediction for the CMR is rather different from the data and other predictions and the new result demonstrates the importance of using a chiral extrapolation versus a linear extrapolation to the physical pion mass. As shown in Fig. 2-5, the EMR extrapolation is close to the data but the CMR is very different.

Recall that the Pascalutsa and Vanderhaeghen prediction for the σ_{LT} cross section was below the new data (see Fig. 7-3). However, in Fig. 7-5, the CMR is close to the data. This is because the prediction for M_{1+} is below the data but cancels out in the ratio. This shows the importance of comparing the absolute size of the multipoles, at least for one, while also looking at the ratios. A model or calculation can get the ratio right but the scale wrong.

It is interesting that good fits were achieved in the resonant region despite the differing model backgrounds. Figure 7-6 shows the absolute size of all of the s and p multipoles and the largest \overline{F} (parameterization of the $L \geq 2$ multipoles shown in Eqn. A.3) that appear in the leading multipole approximation (see Appendix A, Eqs. A.6-A.9). The M_{1+} term is clearly dominant but the background multipoles are of a similar size to the resonant multipoles. The reason that the fitting routine is able to be rather insensitive to the backgrounds is due, in part, to their angular dependence. Figure 7-7 shows the full, helicity independent LMA cross section (see Eqs. 2.12 and A.6-A.9) versus $\theta_{\pi q}^*$ at $W = 1221$ MeV, $Q^2 = 0.060$ (GeV/c)², $\phi_{\pi q}^* = 30^\circ$ for each multipole interfering with M_{1+} . (The ϕ angle was chosen so that the TT and LT terms would both be present in the total cross section.) The primary $|M_{1+}|^2$ term has been suppressed so that the angular dependence of the multipoles is more easily seen.

Figure 7-7 shows that the primary contributors to the cross section (excepting the suppressed M_{1+}) are the resonant E_{1+} and S_{1+} and the background E_{0+} and

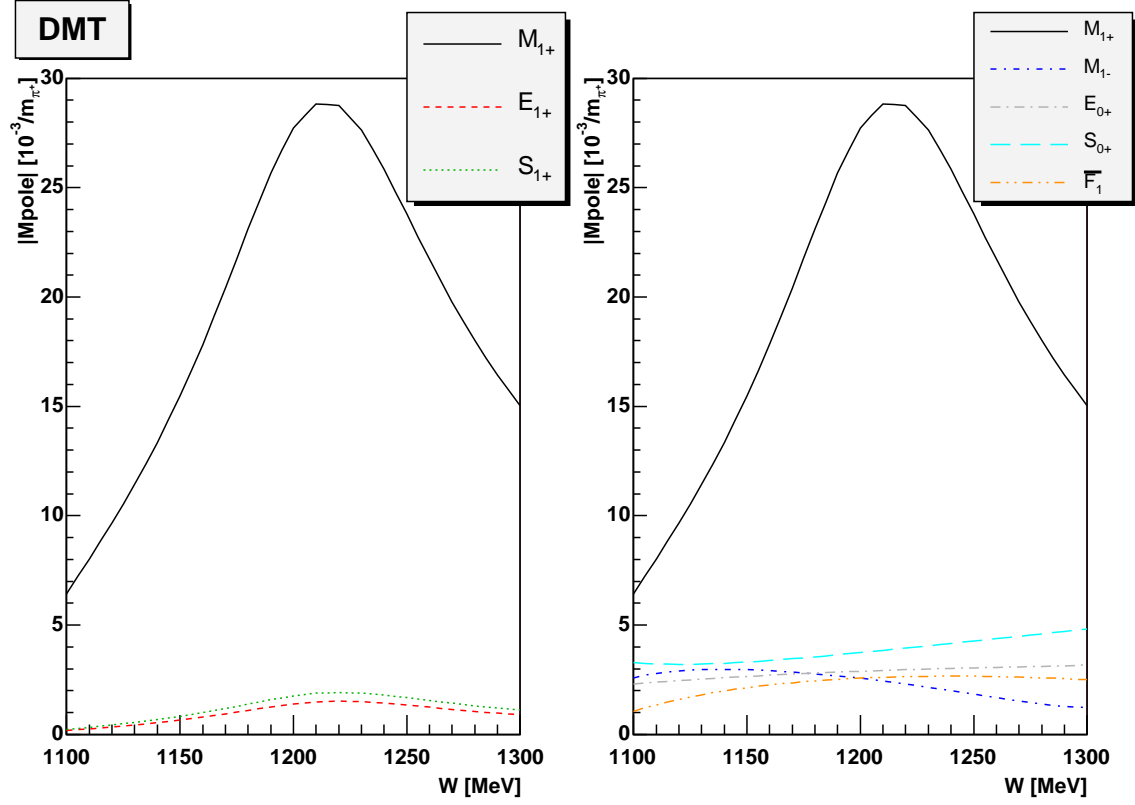


Figure 7-6: Comparison of the magnitudes of several $\pi^0 p$ charge channel multipoles from the DMT model [47] versus W at $Q^2 = 0.060 \text{ (GeV/c)}^2$. \overline{F}_1 is a function of $\theta_{\pi q}^*$ and is shown for $\theta_{\pi q}^* = 180^\circ$.

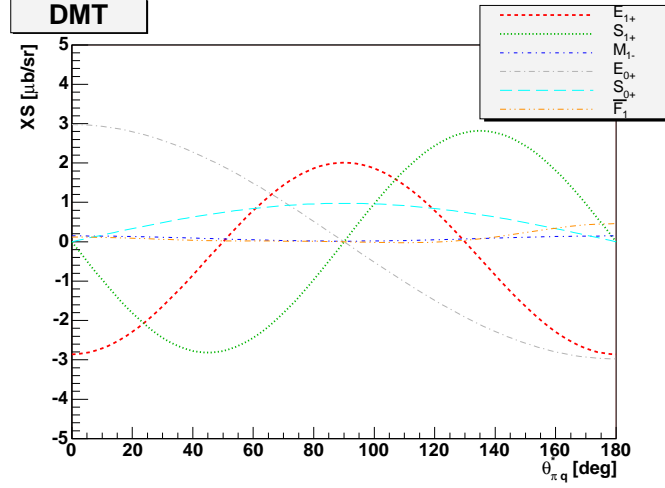


Figure 7-7: Comparison of helicity independent LMA cross sections for multipoles interfering with M_{1+} plotted versus $\theta_{\pi q}^*$ for $W = 1221$ MeV, $Q^2 = 0.060$ (GeV/c)², $\phi_{\pi q} = 30^\circ$ for the DMT model [47, 46].

S_{0+} . All those multipoles have different angular shapes which the fitter can use to separate the components. (This is also one of the reasons why large angular acceptance is desirable. A larger region will allow even better discrimination between the background and resonance amplitudes.) The M_{1-} and \overline{F}_1 terms only have a small effect on the cross section even though they have a comparable magnitude. This is due to their having a different phase which has been suppressed in these plots. Near resonance, the resonant multipoles along with E_{0+} and S_{0+} are mostly imaginary while the M_{1-} and \overline{F}_1 are primarily real. Since the M_{1+} term near resonance is almost pure imaginary, the interference with M_{1-} and \overline{F}_1 is very small. In addition, the E_{0+} multipole also does not differ very much from model to model so while it has a large effect, it does not affect the resonant fits from model to model. These plots clearly show why the three parameter resonant fits using different models were so successful despite the different model backgrounds.

7.2 Background Amplitude Test

7.2.1 $Q^2 = 0.060 \text{ (GeV/c)}^2$

Background sensitive data were taken at $Q^2 = 0.060 \text{ (GeV/c)}^2$ to test the reaction models. In order to declare whether or not a model describes these data, and hence has realistic background amplitudes, certain criteria must be met. The model must agree with: 1. Data in the low W region (presented in this section). 2. $\sigma_{LT'}$ near resonance (Sec. 7.1). 3. Points in the parallel cross section W scan (Sec. 7.1), especially at high and low W . This agreement should be for models that have already had their three resonant multipoles fit to the data near $W = 1232 \text{ MeV}$. Comparing over a wide range of W is a rigorous test of the background multipoles and the shape of M_{1+} . Also, the background multipoles are more important at low W (see Fig. 7-6 near $W = 1155 \text{ MeV}$). Although the extraction of specific background multipoles was not expected, model predictions can be compared to the data to see whether they agree or not. In addition, some fitting including background terms can tell which amplitudes may be significant. Similar studies were performed in Ref. [74] on the Bates $Q^2 = 0.127 \text{ (GeV/c)}^2$ data. Since the new data cover a similar kinematic region, the results are expected to be similar.

The upper panel of Fig. 7-8 shows a low W test of the background amplitudes at $Q^2 = 0.060 \text{ (GeV/c)}^2$. The low W region is useful for testing the background amplitudes since it is far from other resonances. In addition, the M_{1+} term is not purely imaginary in that region and interferences from real background amplitudes will not be suppressed as much. Returning to the upper panel of Fig. 7-8, only the DMT model is close to the data but still does not reproduce both points. The other models differ in size and shape due to the different background amplitudes contained in them.

The same low W data points are plotted in the lower panel of Fig. 7-8 along with the model fits found in Sec. 7.1.2. These data points were not included in those fits. Two of the fitted models are close to the $\phi_{\pi q}^* = 0^\circ$ point but they all fail on the $\phi_{\pi q}^* = -180^\circ$ point. This is indicating disagreement among the models for the various

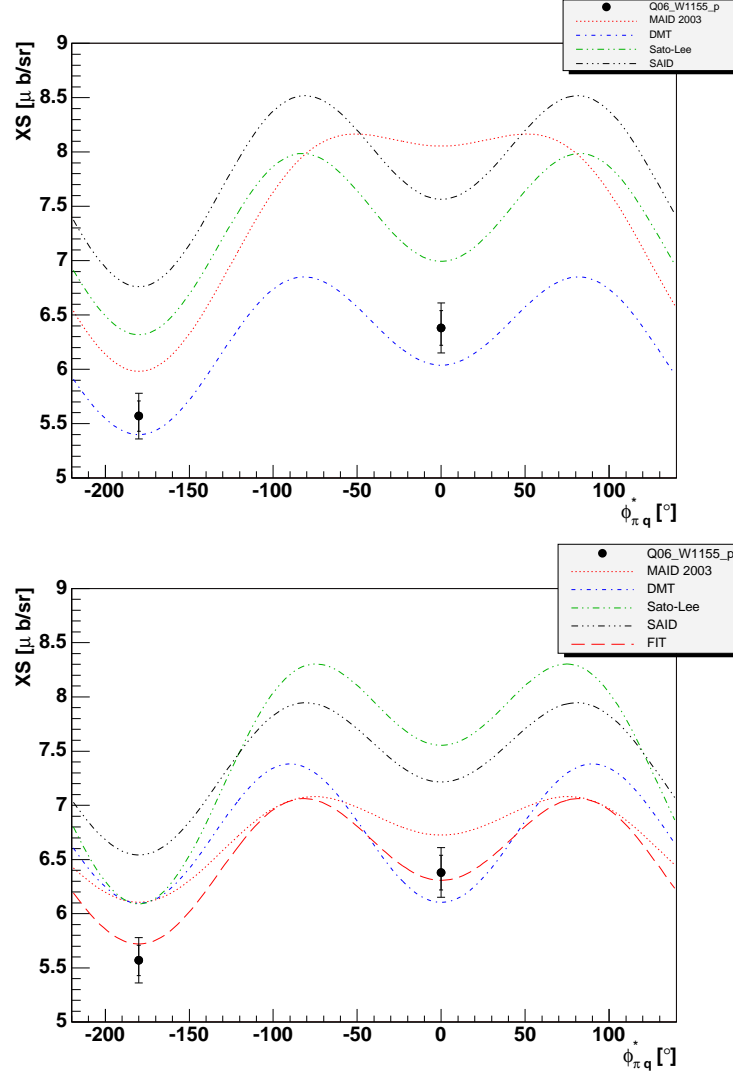


Figure 7-8: The upper panel shows a plot of spectrometer cross sections for $W = 1155$ MeV, $Q^2 = 0.060$ $(\text{GeV}/c)^2$, $\theta_{pq}^* = 26^\circ$ along with several models. The wide error bars are the total systematic and statistical errors added in quadrature. The narrower error bars are the statistical only. The lower panel shows the same data but with models fitted with the three resonance parameters near resonance. Also included in the lower plot is one of the best four parameter fits (3 resonance parameters + M_{1-}).

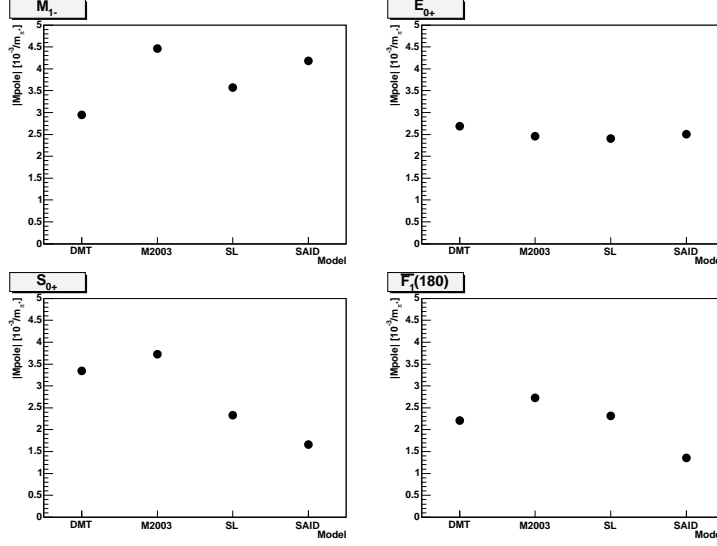


Figure 7-9: Comparison of several non-resonant (background) $\pi^0 p$ charge channel multipoles from the DMT model [47, 46], MAID [28], Sato-Lee (SL) [67] and SAID [4] at $W = 1155$ MeV and $Q^2 = 0.060$ (GeV/c) 2 .

background amplitudes. The model-to-model background differences are shown in Fig. 7-9. However, these amplitudes would not be helped using a resonant parameter fit. Taken together, the two panels in Figure 7-8 are indicating that, as expected, more than a three parameter resonant fit is required away from the resonance region. One of the best four parameter fits is also included in the lower panel of Fig. 7-8. It will be discussed in more detail shortly.

Based upon the criteria for agreement listed earlier and Figs. 7-8 and 7-3, the DMT model does have the best overall agreement with all of the $Q^2 = 0.060$ (GeV/c) 2 data. The fitted DMT results in Fig. 7-8 are the closest to the data of all the models. The fitted DMT results for $\sigma_{LT'}$ in Fig. 7-3 are fairly close to the data and no worse than MAID and SAID. Finally, the fitted DMT results for the W scan in 7-3 look very good overall and only disagree at a few points. While no model agrees perfectly with all the data, the DMT with the three resonant parameter fit does appear to describe the new low Q^2 data the best.

Appendix A lists other fitting parameters in addition to the three resonant fit parameters. Two studies were performed to find candidates for the largest contributors.

Model	Most Important Background Multipoles
MAID	$M_{1-}, E_{0+}, E_{1+}^{1/2}, \overline{F}_1, M_{1+}^{1/2}, L_{1+}^{1/2}$
DMT	$E_{0+}, E_{1+}^{1/2}, M_{1-}, \overline{F}_1, M_{1+}^{1/2}, L_{1+}^{1/2}$
Sato-Lee	$M_{1-}, E_{0+}, E_{1+}^{1/2}, \overline{F}_1, M_{1+}^{1/2}, L_{1+}^{1/2}$
SAID	$\overline{F}_6, E_{0+}, M_{1-}, E_{1+}^{1/2}, M_{1+}^{1/2}, L_{1-}$

Table 7.2: Background amplitudes from four models contributing the most to the $Q^2 = 0.060$ (GeV/c)² data arranged from largest to smallest (left to right). The top six amplitudes are listed for each model. The χ^2 increased by a factor of approximately two or more when any one of the amplitudes was turned off in the model.

The first study checked for correlations between fitting parameters. (Details about correlation coefficients are shown in Appendix B.) That study yielded inconclusive results and a second type of study was performed. All of the new $Q^2 = 0.060$ data were used to find the χ^2 using each fitted model. Then, each of the fit parameters was set to zero in turn and the resulting values of χ^2 were recorded. Multipoles with small contributions will change the χ^2 only slightly whereas larger multipoles will affect the χ^2 more. Using all four models (SAID, Sato-Lee, MAID and DMT), certain multipoles were found that had consistently large effects. The top six for each model are shown in Table 7.2. More contributors could be listed but their effect gets smaller and smaller and six was chosen as an arbitrary cutoff. This cutoff also corresponds approximately to a doubling of the χ^2 . Three of the models agree on the largest contributors to the cross sections after the three resonant parameters. The SAID model has some differences but also agrees on four of the six contributors.

Another study was performed which combined the findings from the two previous studies. Instead of focusing on the values of the background amplitudes, the effect of the unknown background amplitudes on the resonant amplitudes was examined. Fitting parameters which are large and also highly correlated were identified. Through studying the effect on the extracted M_{1+} , EMR and CMR, two criteria for significance were found. 1. A parameter must be highly correlated with another (i.e. their correlation coefficient $|r|$ is greater than 0.7, see App. B). 2. The χ^2 using all of the data should at least double when a parameter is zeroed out. Using these criteria, background amplitudes which are correlated with the resonant amplitudes and have

Sensitive Background Multipoles		
E_{1+}	vs.	$E_{1+}^{1/2}, M_{1+}^{1/2}, M_{1-}, \overline{F_1}, \overline{F_2}$
M_{1+}	vs.	$E_{1+}^{1/2}, L_{1+}^{1/2}, L_{0+}, E_{0+}$
L_{1+}	vs.	$L_{1+}^{1/2}$

Table 7.3: Background amplitudes identified as significant for the $Q^2 = 0.060$ (GeV/c)² data. All of these amplitudes were highly correlated with one of the resonant parameters ($|r| > 0.7$) and caused the χ^2 to double when they were turned off.

a large effect can be identified. Table 7.3 shows the terms which meet these criteria. Figure 7-10 then shows deviations from the three parameter fit using those terms. Most of the terms identified as significant did affect the extraction of the resonant parameters. Also, if the central value of the extraction was not affected, the size of the error did increase for the sensitive terms. However, the $\chi^2/\text{d.o.f.}$ was not significantly improved using any of these extra parameters. One of the best four parameter fits (using the three resonant parameters with M_{1-}) is shown in the lower panel of Fig. 7-8 and with the remaining low Q^2 data in Fig. 7-11. While that fit does a good job for the two low W data points, it is still off for the background sensitive $\sigma_{LT'}$ data near resonance and for some of the parallel cross section W scan results especially at the low and high W tails. (Note that the error bars in the high and low W region are fairly small so small deviations from the fitted curve can lead to large χ^2 .) Because of the sensitivity of these few points, the overall χ^2 was not improved very much. However, as mentioned above, since the data set is limited, it is not a surprise that no single background multipole allows a good fit. The effect of background amplitudes from the models can be compared to data but the amplitudes themselves cannot be determined.

This study shows that the resonant multipoles do have some sensitivity to the background multipoles. However, since none of these background multipoles were determined, the values of the resonant multipoles are not changed but the internal model errors increase. This internal model error is different from the model to model or external error since it does not rely upon any other models for the results. It is a

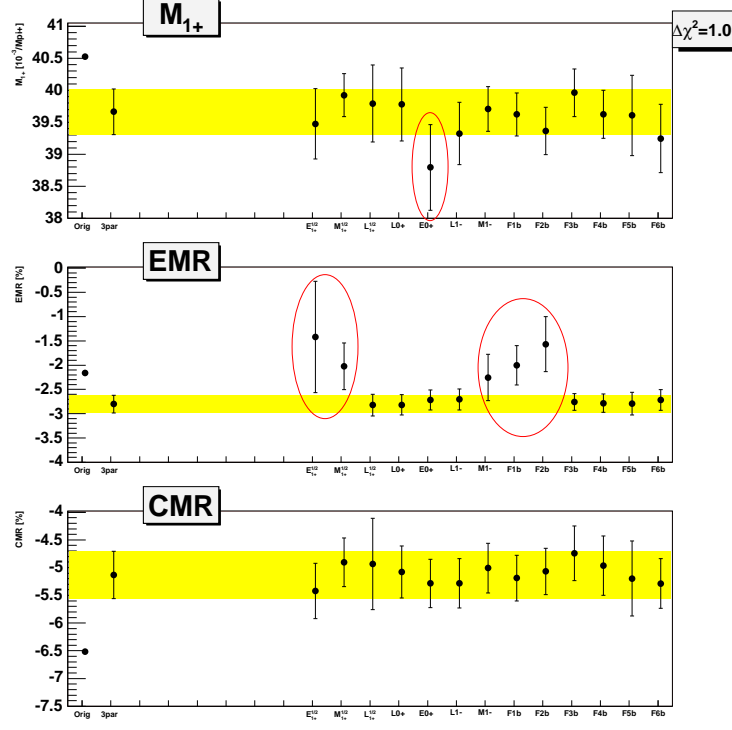


Figure 7-10: Extracted M_{1+} , EMR and CMR for various fits using MAID 2003. The sensitivity to some of the background multipoles manifests itself as a variation in the extracted value. The fourth fitting parameter for each fit is listed on the x axis. In addition, the original model prediction (Orig) and the value using the three resonant parameter fits (3par) are shown. Several of the background parameters identified as significant are circled. The errors increased for the others.

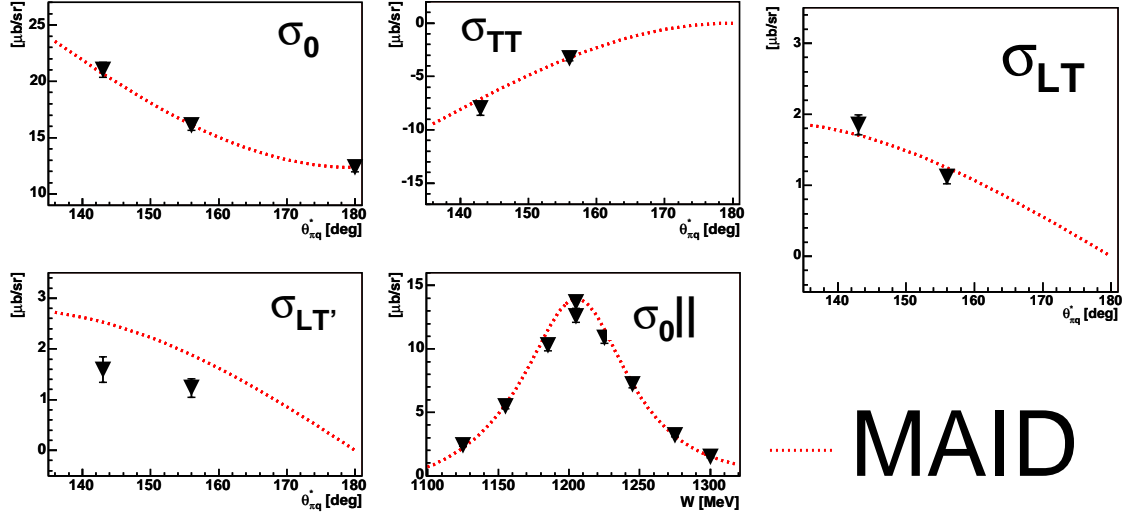


Figure 7-11: Summary of the new Mainz data at $Q^2 = 0.060 \text{ (GeV/c)}^2$ (\blacktriangledown) plotted with one of the best four parameter fits using MAID 2003. This fit is with the three resonant parameters and the M_{1-} background amplitude.

way of estimating the uncertainty in the resonant amplitudes caused by uncertainties in the background while using a single model. Its approximate size is estimated by looking at the root mean square of the deviations in the resonant values using the various four parameter fits.

A similar study was performed using the more extensive Bates data at $Q^2 = 0.127 \text{ (GeV/c)}^2$. Each term identified as significant had a visible effect in a plot similar to that of Fig. 7-10. However, even that set of data with more background sensitive points was not fit much better using the parameters identified as significant. That study also showed that the internal model errors were about the same as the model to model errors. Furthermore, another slightly different procedure was used in Ref. [74] to estimate the internal model error with similar results. Therefore, only the model to model errors are quoted in this work.

The method of looking for the significant contributors and varying them individually could potentially miss combinations of multipoles which may be able to fit the data better (i.e. a “perfect” six parameter fit). It can also miss possible correlations between multipoles. Already, the collective effect of the $L \geq 2$ multipoles is evident

since the EMR exhibits a sensitivity to \overline{F}_1 and \overline{F}_2 (see App. A for details about the \overline{F}_i terms). Two large scans were performed to look for other combinations of multipoles which may be useful in fitting. In one scan the three resonant parameters were allowed to vary and in the other, they were fixed. Then all combinations of the remaining 13 parameters (\overline{F}_i , s and p wave multipoles, $I = 1/2$ multipoles) were also allowed to vary in a fit of all the new $Q^2 = 0.060$ (GeV/c)² data. The parameters and the $\chi^2/\text{d.o.f}$ were recorded for each fit and the results were then searched for the best fit. There was not significant improvement over the three parameter fit and, without limits, some of the fitting parameters went to unreasonable (>10 times original) values. The conclusion is that no “perfect” combination of parameters was missed that would have given a good fit to all of the low Q^2 data.

Two more scans were performed on the more limited primary data set of $Q^2 = 0.060$ (GeV/c)² data (the seven data points for the three θ_{pq}^* angles at the various ϕ_{pq}^*). With only seven data points, seven parameter fits would, of course, give perfect agreement. This limited the fits to at most six parameters. All possible four, five and six parameter fits were cycled through always including the resonant parameters but either fixing them or allowing them to vary. For fixed resonant parameters, no better fit was found. For varied resonant parameters, only one better fit was found. In that fit, the E_{0+} multipole was varied. The M_{1+} and S_{0+} multipoles did not change very much but E_{1+} decreased. However, the E_{0+} had almost 30% error in it. So, the small data set fit may give some information about background terms but it is fairly limited.

The message from this low Q^2 background study is that none of the models agrees perfectly with the background sensitive data. This alone indicates that the models must be improved. The DMT model did have the best overall agreement though. The studies indicate a path to follow for improvement. The problem encountered with the fitting method used in this thesis is that the parameters apparently do not give the models enough freedom to fit the background amplitudes. As is clear in the W scan plot in Fig. 7-3, the models simply have the wrong shape. This mostly has to do with how the background amplitudes are defined and determined in the models. The

approach of identifying the significant contributors will work to a point and that point has been reached. The next step to try to constrain the background would be to go back a step in the models and fit coupling constants and other internal model terms which affect many multipoles at once. This would hopefully add enough freedom to allow the models to fit. However, this type of fitting has not been developed for use yet so this analysis cannot go beyond the resonant three parameter fit. Some model creators are able to do the fits described. All of the fits shown here have been performed by the author with assistance from the model authors. Additional fits will require more software development.

In addition to improving the fits, more data over a larger kinematic range would be helpful in constraining the models. Part of the current problem is the limited size of the data set. Even the larger Bates data set at $Q^2 = 0.127 \text{ (GeV/c)}^2$ has problems determining the background terms. A concerted effort is needed to obtain more data that has enough variation to constrain the model backgrounds more.

7.2.2 $Q^2 = 0.127 \text{ (GeV/c)}^2$

As mentioned previously, the low W measurement is a good test of the background amplitudes since it is farther away from the effects of the higher resonances. At $Q^2 = 0.127 \text{ (GeV/c)}^2$, $W = 1140 \text{ MeV}$ and $\theta_{pq}^* = 58.6^\circ$, both helicity dependent and independent cross sections were measured. The results are plotted in Figs. 7-12 and 7-13. The results show some considerable dispersion in the models for the helicity independent cross section. As for the $Q^2 = 0.060$ low W data, the DMT model does describe the data the best. Still, though, one model is favored for one angle, and another for the other angle. Taken together, it is clear that there is still considerable variation in the backgrounds of the models at $Q^2 = 0.127 \text{ (GeV/c)}^2$ similar to the variation at $Q^2 = 0.060 \text{ (GeV/c)}^2$.

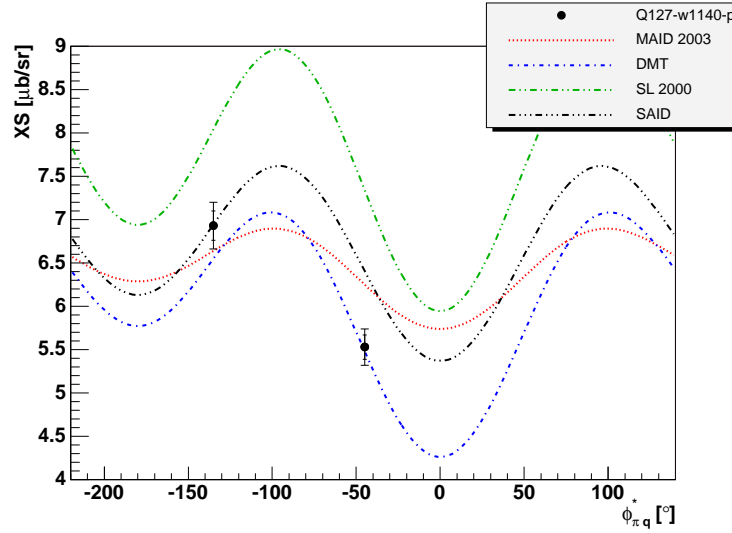


Figure 7-12: Plot of spectrometer cross sections for $W = 1140 \text{ MeV}$, $Q^2 = 0.127 \text{ (GeV/c)}^2$, $\theta_{pq}^* = 58.6^\circ$ along with several models. The wide error bars are the total systematic and statistical errors added in quadrature. The narrower error bars are the statistical only

These new data were added to the existing $Q^2 = 0.127 \text{ (GeV/c)}^2$ database in an effort to demonstrate a method for extracting information about background terms.

A fitting procedure similar to the one used in 7.1.2 was carried out for the $Q^2 = 0.127 \text{ (GeV/c)}^2$ database in [74]. A study has been performed adding the new low W

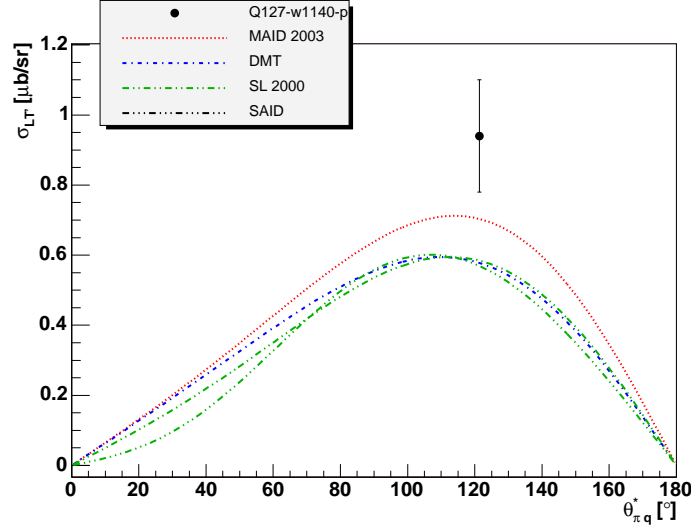


Figure 7-13: Plot of $\sigma_{LT'}$ for $W = 1140$ MeV, $Q^2 = 0.127$ (GeV/c) 2 , $\theta_{pq}^* = 58.6^\circ$ along with several models. The statistical error dominates here.

data to that database. One problem is that there are many other data points in the database and the significance of new points can be lost. In order to test the effect of the new low W points at $Q^2 = 0.127$ (GeV/c) 2 in a sensitive way, the three resonant parameters were locked and a background term, S_{0+} , was allowed to vary. Then that term was locked and the three resonant parameters were refit to see the difference in the fits. A final check allowed all four parameters to vary to see the difference.

Table 7.4 shows the results of the fits. The $\chi^2/\text{d.o.f.}$ was lowered slightly and the background multipole was changed a bit. However, Table 7.5 shows the effect on the EMR and CMR. First, the current fit agrees very well with the fit published in [74]. Second, the resonant parameters are not affected by a large amount. The S_{0+} affects the CMR because the S_{1+} and S_{0+} mix. This can be seen by looking at Eq. A.8. The $\cos\theta$ term allows some separation of the two but there is still some tradeoff between the terms. Even so, the CMR does not vary outside of the error bars for the fit with the one varied term. The CMR is slightly outside the error bars when the resonant terms are also allowed to vary.

This study clearly shows that more work must be done to understand the backgrounds in the models. These new data can assist with that task.

Fit	λE_{1+}	λM_{1+}	λS_{1+}	λS_{0+}	χ^2/dof
Bates	1.098 ± 0.038	1.001 ± 0.002	0.950 ± 0.011	—	2.29
+Mainz low W	1.098	1.001	0.950	1.083 ± 0.039	2.28
Locked S_{0+}	1.099 ± 0.037	1.000 ± 0.002	0.966 ± 0.011	1.083	2.15
4 par.	1.095 ± 0.037	0.998 ± 0.002	0.982 ± 0.016	1.138 ± 0.055	2.23

Table 7.4: Results of a test of the sensitivity of the background to the new Mainz data. Only statistical errors from MINUIT are shown.

Fit	EMR	CMR
Sparveris [74]	-2.3 ± 0.3	-6.1 ± 0.2
Bates	-2.32 ± 0.08	-6.18 ± 0.07
Bates locked S_{0+}	-2.32 ± 0.08	-6.29 ± 0.07
4 par.	-2.32 ± 0.08	-6.40 ± 0.10

Table 7.5: Comparison of the EMR and CMR for the various fits at $Q^2 = 0.127$ $(\text{GeV}/c)^2$ with and without the background terms. The Sparveris data errors contain the statistical and systematic errors while the remaining results are statistical errors only from MINUIT.

Chapter 8

Summary and Conclusion

The previously published results at $Q^2 = 0.127 \text{ (GeV/c)}^2$ demonstrated the dominance of the pion cloud and the importance of including its effects. The new data from Mainz confirm that finding and go on to show the significant (and predicted) Q^2 variation.

The Mainz facility provided high quality, precision data whose accuracy was verified with several cross checks. The experiment was carefully designed to reach the lowest possible Q^2 (while taking the physical limits of the spectrometers into account) in pion electroproduction to date in order to test the chiral effective field theory predictions. Also, the value of $Q^2 = 0.060 \text{ (GeV/c)}^2$ was chosen because of the significant variation of the multipoles with Q^2 .

Comparing the extracted cross sections directly with chiral effective field theory results shows good consistency between the two and indicates that the EFT calculations are reliable. Also, a three resonant parameter fit to the data allowed convergence of the various models despite the differing background amplitudes. The fits indicate the presence of non-spherical terms that are approximately the same size as several predictions. In addition, the fit results show the failure of the quark models to predict the size of the magnetic dipole or the quadrupole terms correctly.

The extent of the new data at $Q^2 = 0.060 \text{ (GeV/c)}^2$ has allowed testing of specific models and predictions for the resonant multipoles. These results showed qualitative agreement with the chiral extrapolation of the lattice QCD results, two chiral pertur-

bation theory results and two pion cloud models thus indicating the importance of the pion cloud and providing a connection to QCD. However, further refinement of the models is required before they can achieve quantitative agreement with the data.

The new Mainz results and previous Bates results have reached a limit on their accuracy and cannot easily be improved. The experimental error as a percentage of the extracted value for M_{1+} is $< 1\%$, for CMR is $\approx 6\%$ and for EMR is $\approx 13\%$. The model errors are about the same size as the experimental errors. Therefore, not much improvement in understanding can be expected until the models are refined further. In addition, the comparisons with the background sensitive data indicated that while one fitted model (DMT) can describe the data fairly well, there are still significant problems with the background amplitudes in all the models. This can only be resolved with improvement of the models or more data or both.

Improvement of the EFT calculations can be achieved by calculating the next higher order effects. In addition, the fitting using the models could be improved by fitting not only individual multipoles but the internal model parameters such as form factors and coupling constants which affect many multipoles simultaneously in different ways.

Improved models will then require improved data to test them. The current experiment used the existing setup at the Mainz A1 hall which had limited angular coverage. Larger angular coverage will increase the sensitivity to the non-spherical amplitudes and allow more constraint of the background amplitudes. However, the experiment in this thesis measured only 5 of the 36 possible cross sections. The remaining cross sections require target and/or recoil polarization. More complete experiments will allow models to be constrained not only for the resonant amplitudes but for the background amplitudes as well. A totally complete experiment with target and recoil polarization would allow an entirely model independent analysis. Of course, this type of experiment is currently very difficult to perform due to the low count rates that come from using low density polarized targets and recoil polarimeters with low analyzing power. However, as this analysis has shown, model errors can be significant and eliminating the need for models in the analysis phase would be ideal.

This experiment showed that our understanding of the physics in the low Q^2 region is improving but there is more work to be done.

Appendix A

Fitting formalism

The procedure for fitting the data begins with a model. That model provides the background terms as well as the base multipoles which will be fit. Next, a fitting routine is run using MINUIT [44] inside ROOT [21] which minimizes χ^2 by changing a multiplicative factor in front of various multipoles. The observables are then calculated using the updated multipoles (see Sec. 2.3). The same factor is used for real and imaginary parts of the multipole to preserve the multipole phase. All of the model fits use the three resonant multipoles

$$R_i = M_{1+}^{3/2}, E_{1+}^{3/2}, L_{1+}^{3/2}.$$

The resonant parameters are varied using λ s in the following way:

$$A_{\pi^0 p} = A_p^{1/2} + \lambda(R_i) \frac{2}{3} A^{3/2}. \quad (\text{A.1})$$

Only the $I = 3/2$ part of the charge channel resonant multipole is modified.

Assuming the dominance of s and p waves gives four more multipoles to modify

$$B_i = E_{0+}, L_{0+}, M_{1-}, L_{1-}.$$

For these non-resonant multipoles, the entire multipole is modified ignoring the isospin basis.

$$A_{\pi^0 p} = \lambda(B_i) \left(A_p^{1/2} + \frac{2}{3} A_{3/2} \right) \quad (\text{A.2})$$

So that there is not a heavy dependence on the assumption of s and p wave dominance, all the higher order multipoles are gathered together based upon the definition of the CGLNFs (see Sec. 2.3). The higher order multipoles can then be summed together into the new parameters, \overline{F}_i s, which are:

$$\begin{aligned} \overline{F}_1 &= F_1 - (E_{0+} + 3M_{1+} \cos \theta + 3E_{1+} \cos \theta) \\ \overline{F}_2 &= F_2 - (M_{1-} + 2M_{1+}) \\ \overline{F}_3 &= F_3 - 3(E_{1+} - M_{1+}) \\ \overline{F}_4 &= F_4 \\ \overline{F}_5 &= F_5 - (L_{0+} + 6L_{1+} \cos \theta) \\ \overline{F}_6 &= F_6 - (L_{1-} - 2L_{1+}). \end{aligned} \quad (\text{A.3})$$

The \overline{F} s are not exactly like the multipoles because they depend on $\theta_{\pi q}^*$. However, the \overline{F} s are used in the fit the same way the non-resonant multipoles are used:

$$\overline{F}_i' = \lambda_i \overline{F}_i, \quad (\text{A.4})$$

that is, placing a multiplicative factor in front of the entire term so that the phase is not affected.

In addition to these thirteen parameters (three $\lambda(R_i)$, four $\lambda(B_i)$, six λ_i), three extra $\lambda_i^{1/2}$ s are introduced to the $I = 1/2$ parts of the resonant multipoles

$$A_{\pi^0 p} = \lambda_i^{1/2} A_p^{1/2} + \lambda(R_i) \frac{2}{3} A_{3/2} \quad (\text{A.5})$$

which can be varied separately from the other λ s. While the $I = 3/2$ multipoles contain the resonance, the $I = 1/2$ multipoles are sensitive to the background terms. By including these parameters, the fit can then try to accommodate more variations

in the background.

Inside the fit routine, the λ scaled multipoles and \overline{F}_i s are summed to give modified CGLNFs which are then combined using the formulas in Sec. 2.3 to give the cross sections.

While the fitting routine takes all of the multipoles into account, it is useful to look at the cross sections in the leading multipole approximation or LMA. The LMA assumes s and p wave dominance and that the M_{1+} multipole is much larger than the other multipoles which are good approximations in the Δ resonance region. In the expansions below, the \overline{F} terms which interfere with M_{1+} are also kept so that all the significant terms can be seen.

$$\begin{aligned}
\sigma_T^{LMA} &\propto \left(\frac{5}{2} - \frac{3}{2} \cos^2 \theta \right) |M_{1+}|^2 \\
&+ 6 \cos^2 \theta \Re [E_{1+}^* M_{1+}] \\
&- \sin^2 \theta (3 \Re [E_{1+}^* M_{1+}] + \Re [M_{1+}^* \overline{F}_3]) \\
&+ (1 - 3 \cos^2 \theta) (\Re [M_{1+}^* M_{1-}] + \Re [M_{1+}^* \overline{F}_2]) \\
&+ 2 \cos \theta (\Re [E_{0+}^* M_{1+}] + \Re [M_{1+}^* \overline{F}_1])
\end{aligned} \tag{A.6}$$

$$\begin{aligned}
\sigma_{TT}^{LMA} &\propto -\Re [M_{1+}^* (3E_{1+} + 3\overline{F}_2 + \overline{F}_3 + 3M_{1-})] \sin^2 \theta \\
&- \frac{3}{2} |M_{1+}|^2 \sin^2 \theta
\end{aligned} \tag{A.7}$$

$$\sigma_{LT}^{LMA} \propto \sin \theta \Re [M_{1+}^* (\overline{F}_5 + L_{0+} + 6L_{1+} \cos \theta)] \tag{A.8}$$

$$\sigma_{LT'}^{LMA} \propto \sin \theta \Im [M_{1+}^* (\overline{F}_5 + L_{0+} + 6L_{1+} \cos \theta)] \tag{A.9}$$

The σ s are related to the response functions, R_i , by the kinematic factors described in Sec. 2.3. The LMA forms show that σ_T is dominated by M_{1+} but σ_{TT} has some E_{1+} , $\overline{F_2}$ and $\overline{F_3}$ terms. σ_{LT} contains the sensitivity to L_{1+} and $\overline{F_5}$ terms while $\sigma_{LT'}$ is sensitive to the background of the two. This is because the real parts of the M_{1+} and L_{1+} terms are small leaving nothing very large for the imaginary part of the $M_{1+}^* L_{1+}$ operation.

The LMA form also shows that only certain \overline{F} s appear and need to be considered.

For completeness, the LMA form of the construction

$$\sigma_{E2} = \sigma_0(\theta) + \sigma_{TT}(\theta) - \sigma_0(\theta = \pi) \quad (\text{A.10})$$

is given:

$$\begin{aligned} \sigma_{E2}^{LMA} &= -12 \sin^2 \theta \Re [E_{1+}^* M_{1+}] \\ &- 2 \Re [M_{1+}^* \overline{F_3}] \sin^2 \theta \\ &+ (2 \cos \theta + 2) (\Re [E_{0+}^* M_{1+}] + \Re [M_{1+}^* \overline{F_1}]) \end{aligned} \quad (\text{A.11})$$

This combination was chosen because it cancels the leading $|M_{1+}|^2$ term and enhances the interference between M_{1+} and E_{1+} . However, this was not used in favor of fitting the spectrometer cross sections directly.

Appendix B

Correlations

B.1 Curvature Matrix and Eigenvectors

This Appendix contains supplementary information about fitting and correlations. The sections show the derivation of the correlation angle from the curvature matrix and how to interpret the correlation coefficient. These were useful in determining the multipoles to include in the fits before the current method using χ^2 to identify “large” multipoles.

B.1.1 Correlation angle from curvature matrix

When performing a fit, it is likely that the various parameters will have correlations. The correlations can be seen quite clearly when the results of many fits are plotted against each other. These many results form a scatter plot. If the scatter plot forms an ellipse with axes along with plot axes, then the variables are uncorrelated. However, if the ellipse is rotated, the angle is related to the correlation. This will be shown through the derivation of the relation between the rotation angle and the parameter errors.

Fig. B-1 shows the one σ ellipse for two parameters that are uncorrelated in x' space. Fig. B-2 shows those same two parameters but in x space where they are correlated. The angle the major axis makes with the x_1 axis is ϕ .

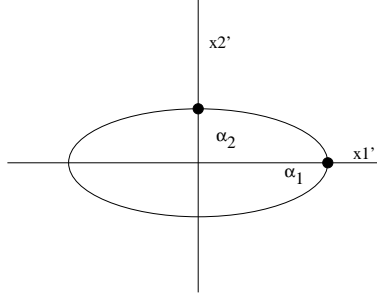


Figure B-1: $\Delta\chi^2=1.0$ curve for two parameters that are uncorrelated in x' space.

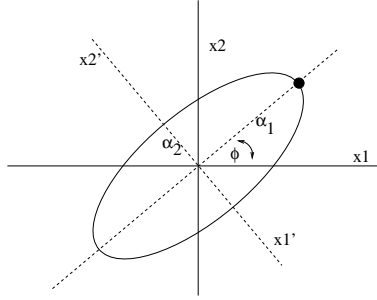


Figure B-2: $\Delta\chi^2=1.0$ curve for two parameters that are correlated in x space.

So, the relation between the x and x' spaces is

$$\begin{pmatrix} x'_1 \\ x'_2 \end{pmatrix} = \begin{pmatrix} \cos \phi & \sin \phi \\ -\sin \phi & \cos \phi \end{pmatrix} \begin{pmatrix} x_1 \\ x_2 \end{pmatrix} \quad (\text{B.1})$$

The formula for the $\Delta\chi^2=1$ ellipse in x' space is:

$$\frac{x'^2_1}{\alpha_1^2} + \frac{x'^2_2}{\alpha_2^2} = \Delta\chi^2 = 1 \quad (\text{B.2})$$

and substituting for x'_1 and x'_2 gives

$$\frac{(x_1 \cos \phi + x_2 \sin \phi)^2}{\alpha_1^2} + \frac{(-x_1 \sin \phi + x_2 \cos \phi)^2}{\alpha_2^2} = 1. \quad (\text{B.3})$$

The ellipse in x space is

$$x_1^2 \left(\frac{\cos^2 \phi}{\alpha_1^2} + \frac{\sin^2 \phi}{\alpha_2^2} \right) + x_2^2 \left(\frac{\sin^2 \phi}{\alpha_1^2} + \frac{\cos^2 \phi}{\alpha_2^2} \right) + 2x_1x_2 \left(\frac{\cos \phi \sin \phi}{\alpha_1^2} - \frac{\sin \phi \cos \phi}{\alpha_2^2} \right) = 1. \quad (\text{B.4})$$

Next, is an examination of the χ^2 surface. χ^2 is a minimum at the best fit and is approximated as a parabola near the minimum. With these assumptions, only a few numbers are needed to describe the parabola as a function of the fit parameters.

$$\Delta\chi^2 = \begin{pmatrix} x_1 & x_2 \end{pmatrix} \begin{pmatrix} \epsilon_{11} & \epsilon_{12} \\ \epsilon_{21} & \epsilon_{22} \end{pmatrix} \begin{pmatrix} x_1 \\ x_2 \end{pmatrix} \quad (\text{B.5})$$

Carrying out the multiplication gives

$$\Delta\chi^2 = \epsilon_{11}x_1^2 + 2\epsilon_{12}x_1x_2 + \epsilon_{22}x_2^2. \quad (\text{B.6})$$

The ϵ terms make up the curvature matrix and are all the terms needed to describe the shape of the χ distribution near the minimum assuming a parabolic shape.

Comparing Eq. B.6 and Eq. B.4, the relations between the variables become clear.

$$\epsilon_{11} = \frac{\cos^2 \phi}{\alpha_1^2} + \frac{\sin^2 \phi}{\alpha_2^2} \quad (\text{B.7})$$

$$\epsilon_{22} = \frac{\sin^2 \phi}{\alpha_1^2} + \frac{\cos^2 \phi}{\alpha_2^2} \quad (\text{B.8})$$

$$\epsilon_{12} = \cos \phi \sin \phi \left(\frac{1}{\alpha_1^2} - \frac{1}{\alpha_2^2} \right) \quad (\text{B.9})$$

Solving for α_1^2 and α_2^2 and using some trigonometric relations gives

$$\alpha_1^2 = \frac{\cos(2\phi)}{\epsilon_{11} \cos^2 \phi - \epsilon_{22} \sin^2 \phi} \quad (\text{B.10})$$

$$\alpha_2^2 = \frac{-\cos(2\phi)}{\epsilon_{11} \sin^2 \phi - \epsilon_{22} \cos^2 \phi}. \quad (\text{B.11})$$

Substituting Eqs. B.10 and B.11 in Eq. B.9, simplifying and using another trigonometric relation gives

$$\epsilon_{12} = \frac{1}{2} \sin(2\phi) \left(\frac{\epsilon_{11} - \epsilon_{22}}{\cos(2\phi)} \right). \quad (\text{B.12})$$

Rearranging and simplifying once more yields

$$\tan(2\phi) = \frac{2\epsilon_{12}}{\epsilon_{11} - \epsilon_{22}} \quad (\text{B.13})$$

So far, all of the work has dealt with the curvature matrix. Another useful matrix is the error or covariance matrix. The error matrix is the inverse of the curvature matrix.

$$\begin{pmatrix} \epsilon_{11} & \epsilon_{12} \\ \epsilon_{21} & \epsilon_{22} \end{pmatrix}^{-1} = \begin{pmatrix} \sigma_{11}^2 & \sigma_{12} \\ \sigma_{21} & \sigma_{22}^2 \end{pmatrix} \quad (\text{B.14})$$

For reference, for a 2 dimensional array the inverse relation is

$$\begin{pmatrix} a & b \\ c & d \end{pmatrix}^{-1} = \frac{1}{ad - bc} \begin{pmatrix} d & -b \\ -c & a \end{pmatrix} \quad (\text{B.15})$$

Substituting the inverse results in Eq. B.13 gives

$$\tan(2\phi) = \frac{2\sigma_{12}}{\sigma_{11}^2 - \sigma_{22}^2}. \quad (\text{B.16})$$

Eq. B.16 is identical to the equation shown in the Particle Data Handbook [32]. The relation between the correlation angle and the error matrix has been derived. Even more, now the correlation can be shown and understood graphically.

B.1.2 Correlation angle from eigenvectors

A second more direct way to find the correlation angle is to diagonalize the curvature matrix. This will find the uncorrelated eigenvectors in the x' space. These eigenvectors will define the axes of the ellipse. Finding the angle the eigenvectors make with the x axis will yield the correlation angle. The derivation starts with the curvature matrix as before

$$\begin{pmatrix} \epsilon_{11} & \epsilon_{12} \\ \epsilon_{12} & \epsilon_{22} \end{pmatrix} \begin{pmatrix} x_1 \\ x_2 \end{pmatrix} = \epsilon \begin{pmatrix} x_1 \\ x_2 \end{pmatrix} \quad (\text{B.17})$$

Solving for the eigenvalues in the standard way gives

$$\lambda = \frac{\epsilon_{11} + \epsilon_{22} \pm \sqrt{(\epsilon_{11} - \epsilon_{22})^2 + 4\epsilon_{12}^2}}{2}. \quad (\text{B.18})$$

Setting up the matrix equation

$$\begin{pmatrix} \epsilon_{11} & \epsilon_{12} \\ \epsilon_{12} & \epsilon_{22} \end{pmatrix} \begin{pmatrix} x_1 \\ x_2 \end{pmatrix} = \begin{pmatrix} \lambda_1 x_1 \\ \lambda_2 x_2 \end{pmatrix} \quad (\text{B.19})$$

and solving for the components of the eigenvectors yields the angle the eigenvector makes with the x axis through

$$\tan \phi = x_2/x_1 \quad (\text{B.20})$$

where x_2 and x_1 are the components of one of the eigenvectors. The components of the first eigenvector are

$$\epsilon_{11}x_1 + \epsilon_{12}x_2 = \lambda_1 x_1. \quad (\text{B.21})$$

Solving for x_2/x_1 gives

$$\frac{x_2}{x_1} = \frac{\lambda_1 - \epsilon_{11}}{\epsilon_{12}} = \tan \phi. \quad (\text{B.22})$$

Substituting for λ_1 and simplifying gives

$$\tan \phi = \beta + \sqrt{1 + \beta^2} \quad (\text{B.23})$$

where $\beta = \frac{\epsilon_{22} - \epsilon_{11}}{2\epsilon_{12}}$. Using the trigonometric relation

$$\tan 2\alpha = \frac{2 \tan \alpha}{1 - \tan^2 \alpha} \quad (\text{B.24})$$

we can find that Eq. B.23 simplifies to

$$\tan 2\phi = \frac{-1}{\beta} = \frac{2\epsilon_{12}}{\epsilon_{11} - \epsilon_{22}} \quad (\text{B.25})$$

which is the same as Eq. B.13. That equation was shown to be the same as the original Particle Data Group relation.

So, the eigenvectors do indeed have a relation to the correlation angles.

B.1.3 Errors

Next is the derivation of the relations between the eigenvalues and the eigenvector errors. Looking at Eqs. B.10 and B.11 for α_1 and α_2 , the results for the eigenvectors can be obtained by setting the rotation angle to 0. This yields

$$\alpha_1^2 = \frac{1}{\epsilon'_{11}} \quad (\text{B.26})$$

$$\alpha_2^2 = \frac{1}{\epsilon'_{22}}. \quad (\text{B.27})$$

The primed notation on the ϵ s is now used because by setting the correlation to 0, the equation has switched to the diagonalized matrix.

Next, the same operation is performed on Eq. B.18, dropping ϵ_{12} and switching to the primed notation.

$$\lambda_1 = \epsilon'_{11} \quad (\text{B.28})$$

$$\lambda_2 = \epsilon'_{22} \quad (\text{B.29})$$

Of course, this has shown that the diagonalized matrix is just the eigenvalue matrix as expected. In addition, there is a relation to the α s. By definition, the α s are the required size of the eigenvector to reach the $\Delta\chi^2=1$ curve. This corresponds to a one standard deviation uncertainty.

Finally, using Eqs. B.26, B.27, B.28 and B.29

$$\alpha_i = \frac{1}{\sqrt{\lambda_i}} = \sigma'_{ii}. \quad (\text{B.30})$$

In words, the square root of the inverse of the eigenvalue gives the one sigma uncertainty in the eigenvector.

B.2 Correlation Coefficient

B.2.1 Definition

A problem with using the correlation angle as defined in B.16 is that it is sensitive to the absolute size of each parameter. As an example, see Fig. B-3. On the left, the multipoles are plotted in parameters that are relative to the MAID 2003 default values [28, 29]. On the right is the absolute scale. The major axis appears to shift. In Fig. B-4, the relative scale shows an ellipse whereas the absolute scale shows a circle. Looking once again at Eq. B.16, notice that the difference in the denominator does not allow the scale to cancel. If a fit parameter is scaled such that it only needs to be half the size to still fit the data, then its error will scale down by half as well. The problem occurs when the parameters are scaled by different factors. Those factors will not cancel and will change the correlation angle. As a result, changing the scale can change the apparent correlation angle making it an ambiguous tool for finding correlations.

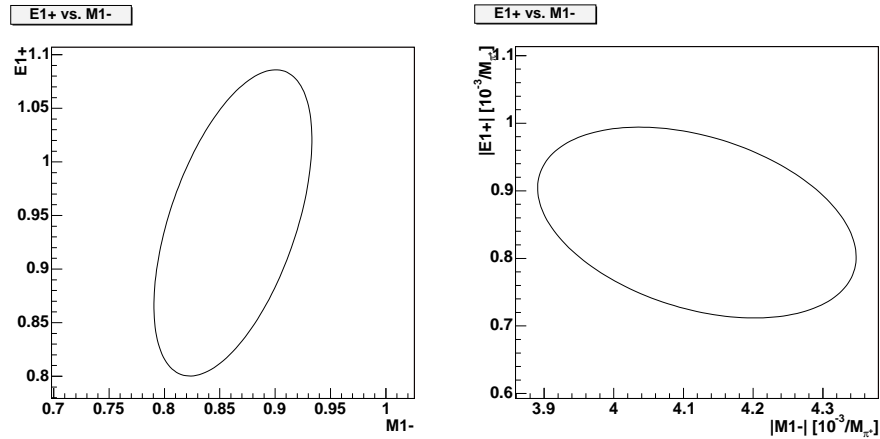


Figure B-3: E_{1+} vs. M_{1-} fit parameters for data using MAID2003 plotted against each other. On the left is the normalized scale. On the right is the absolute scale.

A more robust factor is the correlation coefficient defined as

$$r = \frac{\sigma_{12}}{\sigma_1 \sigma_2}. \quad (\text{B.31})$$

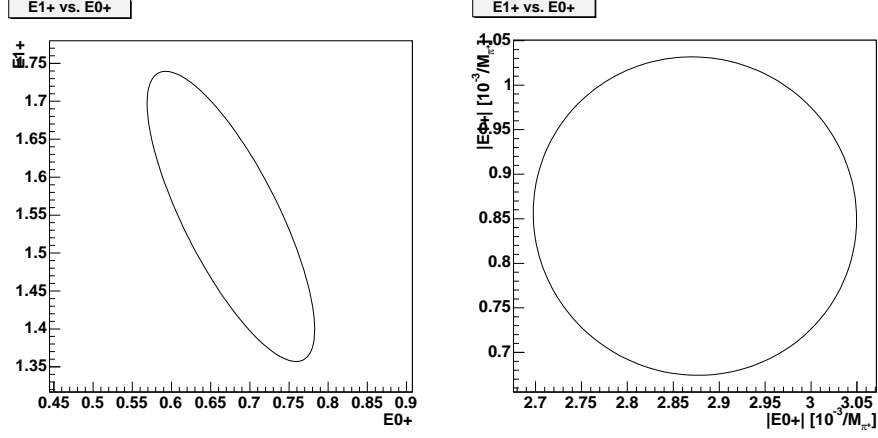


Figure B-4: E_{1+} vs. E_{0+} fit parameters for data using MAID2003 plotted against each other. On the left is the normalized scale. On the right is the absolute scale.

Since the denominator is multiplicative, any scale changes will cancel. The correlation coefficient measures how much of the variance in the distribution of points is accounted for by a linear relationship between the two variables.

A more complete definition comes from the results of a linear regression analysis (from [56]).

When fitting points to a line, the sum

$$Q = \sum_{i=1}^n (Y_i - a - bX_i)^2 \quad (\text{B.32})$$

should be a minimum. Appendix A of [56] shows the procedure in detail. The idea is to take derivatives of Q with respect to a and b , equate the results to zero and solve for the least squares estimators. The result of the procedure is

$$a = \mu_y - b\mu_x \quad (\text{B.33})$$

and

$$b = \frac{\sigma_{xy}}{\sigma_x} \quad (\text{B.34})$$

where μ_i are the mean values and σ_i are the standard deviations.

Substituting the correlation coefficient, r gives

$$a = \mu_y - r \frac{\sigma_y}{\sigma_x} \mu_x \quad (\text{B.35})$$

and

$$b = r \frac{\sigma_y}{\sigma_x}. \quad (\text{B.36})$$

These results show that the average value of y for a given x is

$$\mu_{Y|X} = \left(\mu_y - r \frac{\sigma_Y}{\sigma_X} \mu_X \right) + r \frac{\sigma_Y}{\sigma_X} X. \quad (\text{B.37})$$

Next, to find the variance, take the bivariate normal distribution for two variables, labeled $f(x, y)$ and calculate the variance in the usual way

$$\sigma^2 = \int_{-\infty}^{\infty} \int_{-\infty}^{\infty} f(x, y) (y - (a + bx))^2 dx dy = \sigma_y^2 (1 - r^2). \quad (\text{B.38})$$

The function $f(x, y)$ is normalized to one which is why it was not explicitly divided by when calculating σ^2 .

B.2.2 Interpretation of r

The previous section, showed how to define r . Now r must be interpreted.

Equation B.38 and the fact that all the variances must be positive, limits the range of r to -1 to 1. In addition, this relation shows how much of the variance is due to a linear fit using the variables. For example, if there is no variance, then the points all fall on the same line. This would correspond to $r = \pm 1$ and indicate that the parameters are 100% correlated. Similarly, the maximum variance occurs when $r = 0$ indicating that a line explains none of the variance. This would mean the results are totally uncorrelated.

The problem is how to interpret values of $|r|$ which are in between 0 and 1. The interpretation useful for this analysis is that r^2 is the proportion of the variance that is explained by a linear relation between x and y [56].

A website [70] listed some general guidelines for interpreting r .

r	r^2	Correlation
$0.7 \rightarrow 1.0$	$0.5 \rightarrow 1.0$	Strong positive
$0.3 \rightarrow 0.7$	$0.1 \rightarrow 0.5$	Weak positive
$-0.3 \rightarrow 0.3$	$0.0 \rightarrow 0.1$	Little to no
$-0.7 \rightarrow -0.3$	$0.1 \rightarrow 0.5$	Weak negative
$-1.0 \rightarrow -0.7$	$0.5 \rightarrow 1.0$	Strong negative

So, in general, if more than half the variance is from the relation between y and x , then y and x are strongly correlated. Below about 10%, there is no correlation.

The correlation coefficient is a tool which will not depend on the size of the parameters but truly on their correlation.

Appendix C

Kinematics Summary

C.1 April 2003 Central Kinematics Summary

E [MeV]	Q^2 [(GeV/c) ²]	W [MeV]	θ_{pq}^*	ϕ_{pq}
795	0.060	1221	0	\vec{q}
795	0.060	1221	29.60	28.80
795	0.060	1221	36.50	134.00
795	0.060	1221	36.50	180.00
795	0.060	1221	23.90	0
795	0.060	1221	23.90	90
795	0.060	1221	23.90	180
855	0.127	1232	0	\vec{q}
855	0.127	1221	63.00	150.02
855	0.127	1221	43.00	135.00
855	0.127	1221	30.19	90.00
855	0.127	1140	58.60	45.00
855	0.127	1140	58.60	135.00

C.1.1.1 $Q^2 = 0.060 \text{ (GeV/c)}^2$ Kinematics Details

$W_{\text{center}}=1221 \text{ MeV}$

$E \text{ [MeV]}$	θ_e	$E' \text{ [MeV]}$	$Q^2(\text{GeV/c})^2$	θ_q
795.00	23.97°	437.70	0.060	24.23°

	ϕ_1	ϕ_2	ϕ_3	ϕ_4
ϕ_{pq}	28.80°	134.00°	180.00°	—
α_e	23.97°	23.97°	23.97°	—
β_e	0.00°	0.00°	0.00°	—
θ_{pq}	11.26°	13.85°	13.85°	—
$\theta_{\pi q}^*$	150.40°	143.50°	143.50°	—
α_p	14.34°	33.95°	38.08°	—
β_p	5.40°	9.92°	0.00°	—
$p_p \text{ (MeV/c)}$	554.79	544.70	544.70	—

	ϕ_1	ϕ_2	ϕ_3	ϕ_4
ϕ_{pq}	0.00°	90.00°	180.00°	\vec{q}
α_e	23.97°	23.97°	23.97°	23.97°
β_e	0.00°	0.00°	0.00°	0.00°
θ_{pq}	9.10°	9.10°	9.10°	0.00°
$\theta_{\pi q}^*$	156.10°	156.10°	156.10°	180.00°
α_p	15.13°	24.23°	33.33°	24.23°
β_p	0.00°	9.10°	0.00°	0.00°
$p_p \text{ (MeV/c)}$	561.60	561.60	561.60	574.48

C.1.2 Central Kinematics for $Q^2 = 0.127 \text{ (GeV/c)}^2$

$W_{\text{cent}} = 1221 \text{ MeV}$

$E \text{ [MeV]}$	θ_e	$E' \text{ [MeV]}$	$Q^2 \text{ (GeV/c)}^2$	θ_q
855.00	32.94°	462.00	0.127	28.26°

	ϕ_1	ϕ_2	ϕ_3	ϕ_4
ϕ_{pq}	—	150.02°	—	—
α_e	—	32.94°	—	—
β_e	—	0.00°	—	—
θ_{pq}	—	20.33°	—	—
$\theta_{\pi q}^*$	—	117.00°	—	—
α_p	—	46.06°	—	—
β_p	—	10.00°	—	—
$p_p \text{ (MeV/c)}$	—	562.20	—	—

	ϕ_1	ϕ_2	ϕ_3	ϕ_4
ϕ_{pq}	—	135.00°	—	—
α_e	—	32.94°	—	—
β_e	—	0.00°	—	—
θ_{pq}	—	14.22°	—	—
$\theta_{\pi q}^*$	—	136.76°	—	—
α_p	—	38.42°	—	—
β_p	—	10.00°	—	—
$p_p \text{ (MeV/c)}$	—	611.52	—	—

	ϕ_1	ϕ_2	ϕ_3	ϕ_4
ϕ_{pq}	—	90.00°	—	—
α_{e}	—	32.94°	—	—
β_{e}	—	0.00°	—	—
θ_{pq}	—	10.00°	—	—
$\theta_{\pi\text{q}}^*$	—	149.81°	—	—
α_{p}	—	28.26°	—	—
β_{p}	—	10.00°	—	—
p_{p} (MeV/c)	—	634.92	—	—

	ϕ_1	ϕ_2	ϕ_3	ϕ_4
ϕ_{pq}	-	-	-	\vec{q}
α_{e}	-	-	-	32.94°
β_{e}	-	-	-	0.00°
θ_{pq}	-	-	-	0.00°
$\theta_{\pi\text{q}}^*$	-	-	-	180.00°
α_{p}	-	-	-	28.26°
β_{p}	-	-	-	0.00°
p_{p} (MeV/c)	-	-	-	657.69

$W_{\text{cent}}=1140 \text{ MeV}$

θ_e	E' [MeV]	$Q^2(\text{GeV}/c)^2$	θ_q	
29.74°	563.91	0.127	37.44°	
	ϕ_1	ϕ_2	ϕ_3	ϕ_4
ϕ_{pq}	45.00°	135.00°	—	—
α_e	29.74°	29.74°	—	—
β_e	0.00°	0.00°	—	—
θ_{pq}	14.22°	14.22°	—	—
$\theta_{\pi q}^*$	121.40°	121.40°	—	—
α_p	27.28°	47.60°	—	—
β_p	10.00°	10.00°	—	—
p_p (MeV/c)	473.83	473.83	—	—

C.2 October 2003 Central Kinematics Summary

E' [MeV]	Q^2 [(GeV/c) ²]	W [MeV]	θ_{pq}^*	ϕ_{pq}^*
705	0.060	1125	0	\vec{q}
705	0.060	1155	0	\vec{q}
705	0.060	1185	0	\vec{q}
705	0.060	1205	0	\vec{q}
855	0.060	1205	0	\vec{q}
705	0.060	1225	0	\vec{q}
705	0.060	1245	0	\vec{q}
705	0.060	1275	0	\vec{q}
705	0.060	1300	0	\vec{q}
855	0.060	1155	26	0
855	0.060	1155	26	180
855	0.126	1212	0	\vec{q}
855	0.126	1232	0	\vec{q}
855	0.126	1232	28	0
855	0.126	1232	28	180

C.2.1 $Q^2 = 0.060 \text{ (GeV/c)}^2$ Kinematic Details

Parallel Cross Section W scan

E	Q^2	W	SpecA			SpecB			θ_{pq}^*	ϕ_{pq}^*
[MeV]	[(GeV/c) ²]	[MeV]	pt	alpha	mom	pt	alpha	mom	[°]	[°]
705	0.060	1125	e	24.63	467.72	p	34.86	410.04	0	—
705	0.060	1155	e	25.67	431.27	p	30.57	463.26	0	—
705	0.060	1185	e	26.88	393.86	p	26.72	514.25	0	—
705	0.060	1205	e	27.81	368.39	p	24.38	547.77	0	—
855	0.060	1205	p	26.77	547.77	e	21.20	518.39	0	—
705	0.060	1225	e	28.87	342.49	p	22.20	581.16	0	—
705	0.060	1245	e	30.07	316.16	p	20.16	614.52	0	—
705	0.060	1275	e	32.25	275.88	p	17.33	664.70	0	—
705	0.060	1300	e	34.53	241.57	p	15.14	706.74	0	—

$\sigma_{LT}, \sigma_0 + \epsilon\sigma_{TT}$ extraction

E	Q^2	W	SpecA			SpecB			θ_{pq}^*	ϕ_{pq}^*
[MeV]	[(GeV/c) ²]	[MeV]	pt	alpha	mom	pt	alpha	mom	[°]	[°]
855	0.060	1155	p	24.23	452.00	e	20.01	581.27	26	0
855	0.060	1155	p	41.34	452.00	e	20.01	581.27	26	180

C.2.2 $Q^2 = 0.126 \text{ (GeV/c)}^2$ Kinematic Details

Parallel Cross Section

E	Q^2	W	SpecA			SpecB			θ_{pq}^*	ϕ_{pq}^*
[MeV]	[(GeV/c) ²]	[MeV]	pt	alpha	mom	pt	alpha	mom	[°]	[°]
855	0.126	1212	e	32.37	474.20	p	29.19	642.51	0	—
855	0.126	1232	e	33.32	448.15	p	27.13	673.70	0	—

$\sigma_{LT}, \sigma_0 + \epsilon\sigma_{TT}$ extraction

E	Q^2	W	SpecA			SpecB			θ_{pq}^*	ϕ_{pq}^*
[MeV]	[(GeV/c) ²]	[MeV]	pt	alpha	mom	pt	alpha	mom	[°]	[°]
855	0.126	1232	e	33.32	448.15	p	17.64	653.32	28	0
855	0.126	1232	e	33.32	448.15	p	36.61	653.32	28	180

Appendix D

Cut Details

D.1 Central Cut Values

Setup	W [MeV]	Q^2 [(GeV/c) ²]	θ_{pq}^* [deg]	ϕ_{pq}^* [deg]	z_B [mm]
Q06-t0	1221.0	0.060	0.0	—	-4.0
Q06-t24-p1	1221.0	0.060	24.0	0.0	-4.0
Q06-t24-p2	1221.0	0.060	24.0	90.0	-4.0
Q06-t24-p3	1221.0	0.060	24.0	180.0	-4.0
Q06-t36-p1	1221.0	0.060	29.0	32.0	-4.0
Q06-t36-p2	1221.0	0.060	37.0	134.0	-4.0
Q06-t36-p3	1221.0	0.060	37.0	180.0	-4.0
Q06_W1125	1125.0	0.060	0.0	—	-4.0
Q06_W1155	1155.0	0.060	0.0	—	-4.0
Q06_W1185	1185.0	0.060	0.0	—	-4.0
Q06_W1205	1205.0	0.060	0.0	—	-4.0
Q06_W1205_rev	1205.0	0.060	0.0	—	-4.0
Q06_W1225	1225.0	0.060	0.0	—	-4.0
Q06_W1245	1245.0	0.060	0.0	—	-4.0
Q06_W1275	1275.0	0.060	0.0	—	-4.0
Q06_W1300_low	1300.0	0.060	0.0	—	-4.0

Setup	W [MeV]	Q^2 [(GeV/c) ²]	θ_{pq}^* [deg]	ϕ_{pq}^* [deg]	z_B [mm]
Q06-W1155_p1	1155.0	0.060	26.0	0.0	-4.0
Q06-W1155_p2	1155.0	0.060	26.0	180.0	-4.0
Q127-q(25)	1232.0	0.126	0.0	—	-4.0
Q127-q(30)	1232.0	0.126	0.0	—	-4.0
Q126-W1232	1232.0	0.126	0.0	—	-4.0
Q126-W1212	1212.0	0.126	0.0	—	-4.0
Q126-W1232_p1	1232.0	0.126	28.0	0.0	-4.0
Q126-W1232_p2	1232.0	0.126	28.0	180.0	-4.0
Q127-w1140-p1	1140.0	0.127	58.6	45.0	-4.0
Q127-w1140-p2	1140.0	0.127	58.6	135.0	-4.0
Q127-th30	1221.0	0.127	30.0	90.0	-4.0
Q127-th43	1221.0	0.127	43.0	135.0	-4.0
Q127-th63	1221.0	0.127	63.0	150.0	-4.0

D.2 Cut Widths

Setup	ΔW [MeV]	ΔQ^2 [(GeV/c) ²]	$\Delta\theta_{pq}^*$ [deg]	$\Delta\phi_{pq}^*$ [deg]	Δz_B [mm]
Q06-t0	32.25	0.0210	10.6	—	36.6
Q06-t24-p1	20.25	0.0174	10.4	40.5	36.6
Q06-t24-p2	35.25	0.0210	11.3	29.7	36.6
Q06-t24-p3	33.75	0.0186	9.5	45.9	36.6
Q06-t36-p1	24.75	0.0198	10.4	24.3	36.6
Q06-t36-p2	33.75	0.0210	11.3	24.3	36.6
Q06-t36-p3	38.25	0.0186	10.4	35.1	36.6
Q06_W1125	20.25	0.0198	15.9	—	36.6
Q06_W1155	26.55	0.0198	14.1	—	36.6
Q06_W1185	29.25	0.0186	12.9	—	36.6
Q06_W1205	32.85	0.0186	12.7	—	36.6
Q06_W1205_rev	36.45	0.0078	13.6	—	37.8
Q06_W1225	32.85	0.0174	12.3	—	36.6
Q06_W1245	31.05	0.0162	11.8	—	36.6
Q06_W1275	26.55	0.0150	11.6	—	36.6
Q06_W1300_low	22.95	0.0138	11.1	—	36.6

Setup	ΔW [MeV]	ΔQ^2 [(GeV/c) ²]	$\Delta\theta_{pq}^*$ [deg]	$\Delta\phi_{pq}^*$ [deg]	Δz_B [mm]
Q06-W1155_p1	20.25	0.0078	13.1	45.9	37.8
Q06-W1155_p2	33.75	0.0090	11.3	62.1	37.8
Q127-q(25)	42.75	0.0294	10.7	—	36.6
Q127-q(30)	42.75	0.0294	10.7	—	36.6
Q126-W1232	42.75	0.0306	10.5	—	37.8
Q126-W1212	39.75	0.0306	11.2	—	37.8
Q126-W1232_p1	30.75	0.0282	13.1	35.1	37.8
Q126-W1232_p2	45.75	0.0294	10.4	40.5	37.8
Q127-w1140-p1	20.25	0.0306	16.7	24.3	36.6
Q127-w1140-p2	51.75	0.0354	17.6	18.9	36.6
Q127-th30	42.75	0.0318	14.9	24.3	36.6
Q127-th43	45.75	0.0306	11.3	24.3	36.6
Q127-th63	45.75	0.0294	9.5	18.9	36.6

Appendix E

Mainz $\gamma^* N \rightarrow \Delta$ Collaboration

A.M. Bernstein, S. Stave

M.I.T.

I. Nakagawa

MIT/U. Kentucky/RIKEN

P. Achenbach, C. Ayerbe Gayoso, D. Baumann, J. Bernauer, R. Böhm, M. Ding,

M. O. Distler, L. Doria, J. Friedrich, J. García Llongo, I. Goussev, W. Heil, P.

Jennewein, K. W. Krygier, A. Liesenfeld, M. Lloyd, H. Merkel, U. Müller,

R. Neuhausen, L. Nungesser, A. Piegsa, J. Pochodzalla, M. Seimetz, Th. Walcher,

M. Weis

U. Mainz

A. Christopoulou, A. Karabarounis, C.N. Papanicolas, N. Sparveris, S. Stiliaris

U. Athens and I.A.S.A.

D. Bosnar, M. Makek

U. Zagreb

T. Botto

Bates, M.I.T.

D. Dale

U. Kentucky

S. Širca, M. Potokar

U. Ljubljana

Bibliography

- [1] J. C. Alder et al. Measurements of inclusive hadron momentum distributions in deep inelastic electroproduction. *Nucl. Phys.*, B46:415–428, 1972.
- [2] C. Alexandrou et al. The N to Delta electromagnetic transition form factors from lattice QCD. *Phys. Rev. Lett.*, 94:021601, 2005.
- [3] R. A. Arndt. Private communication.
- [4] R. A. Arndt, W. J. Briscoe, I. I. Strakovsky, and R. L. Workman. Analysis of pion photoproduction data. *Phys. Rev.*, C66:055213, 2002.
- [5] R. A. Arndt, R. L. Workman, Z. Li, and L. D. Roper. Pion photoproduction resonance couplings in the second resonance region. *Phys. Rev.*, C42:1864–1866, 1990.
- [6] Richard A. Arndt, Ron L. Workman, Zhujun Li, and L. David Roper. Partial wave analysis of pion photoproduction. *Phys. Rev.*, C42:1853–1863, 1990.
- [7] John R. Arrington. *Inclusive Electron Scattering from Nuclei at $x > 1$ and High Q^2* . PhD dissertation (unpublished), California Institute of Technology, 1998.
- [8] Inna Aznauryan. Private communication of fit to inclusive data from [9, 10, 75, 1, 72].
- [9] K. Baetznner et al. Separation of $\sigma(s)$ and $\sigma(t)$ in the region of the $\delta(1236)$ resonance and determination of the magnetic dipole transition form-factor. *Phys. Lett.*, B39:575–578, 1972.

- [10] W. Bartel et al. Electroproduction of pions near the Delta(1236) isobar and the form-factor of $G^*(M)(q^2)$ of the (γ N Delta) vertex. *Phys. Lett.*, B28:148–151, 1968.
- [11] P. Bartsch. *Aufbau eines Moeller-Polarimeters fuer die Drei-Spektrometer-Anlage und Messung der Helizitaetsasymmetrie in der Reaktion $p(\vec{e}, e'p)\pi^0$ im Bereich der Delta-Resonanz*. PhD dissertation, Johannes Gutenberg-Universitaet Mainz, Insitute fuer Kernphysik, 2001.
- [12] P. Bartsch et al. Measurement of the beam-helicity asymmetry in the $p(e(\text{pol.}), e'p)\pi^0$ reaction at the energy of the Delta(1232) resonance. *Phys. Rev. Lett.*, 88:142001, 2002.
- [13] R. Beck et al. Determination of the E2/M1 ratio in the γ N to Delta(1232) transition from a simultaneous measurement of $p(\gamma(\text{pol.}), p)\pi^0$ and $p(\gamma(\text{pol.}), \pi^+)n$. *Phys. Rev.*, C61:035204, 2000.
- [14] A. M. Bernstein. Deviation of the nucleon shape from spherical symmetry: Experimental status. *Eur. Phys. J.*, A17:349–355, 2003.
- [15] A. M. Bernstein, I. Nakagawa, and S. Stave. Mainz N to Delta Progress Report. Unpublished internal report, February 2003.
- [16] G. Blanpied et al. $N \rightarrow \Delta$ transition and proton polarizabilities from measurements of $p(\gamma \text{ polarized}, \gamma)$, $p(\gamma \text{ polarized}, \pi^0)$, and $p(\gamma \text{ polarized}, \pi^+)$. *Phys. Rev.*, C64:025203, 2001.
- [17] K. I. Blomqvist et al. The three-spectrometer facility at the Mainz microtron MAMI. *Nucl. Instrum. Meth.*, A403:263–301, 1998.
- [18] W. U. Boeglin. Coincidence experiments with electrons. *Czech. J. Phys.*, 45:295–335, 1995.
- [19] Ralph Boehm. *Messung des Wirkungsquerschnitts der Reaktion $d(e, e'p)n$ fuer fehlende Impulse bis 950 MeV/c und Trennung der longitudinalen und transver-*

salen Reaktionsanteile fuer fehlende Impulse bis 350 MeV/c. PhD dissertation (unpublished), Johannes Gutenberg-Universitaet Mainz, Insitute fuer Kernphysik, 2001.

- [20] B.H. Bransden and R.G. Moorhouse. *The Pion-Nucleon System.* Princeton University Press, 1973.
- [21] R. Brun and F. Rademakers. ROOT: An object oriented data analysis framework. *Nucl. Instrum. Meth.*, A389:81–86, 1997.
- [22] Simon Capstick. Photoproduction amplitudes of P(11) and P(33) baryon resonances in the quark model. *Phys. Rev.*, D46:1965–1972, 1992.
- [23] Simon Capstick and Gabriel Karl. E(1+) / M(1+) and S(1+) / M(1+) and their Q^2 dependence in gamma neutrino $N \rightarrow \Delta$ with relativized quark model wave functions. *Phys. Rev.*, D41:2767, 1990.
- [24] A1 Collaboration. Mainz A1 Website at <http://wwwa1.kph.uni-mainz.de/A1/>.
- [25] M. De Sanctis, M. M. Giannini, E. Santopinto, and A. Vassallo. Electromagnetic form factors in the hypercentral constituent quark model. *Nucl. Phys.*, A755:294–297, 2005.
- [26] Michael O. Distler, Harald Merkel, and Markus Weis. Data acquisition and analysis for the 3-spectrometer-setup at MAMI. In *Proceedings of the 12th IEEE Real Time Congress on Nuclear and Plasma Sciences Symposium on the Theory of Computing*, 2001.
- [27] T. W. Donnelly and A. S. Raskin. Considerations of polarization in inclusive electron scattering from nuclei. *Annals Phys.*, 169:247–351, 1986.
- [28] D. Drechsel, O. Hanstein, S. S. Kamalov, and L. Tiator. A unitary isobar model for pion photo- and electroproduction on the proton up to 1-GeV. *Nucl. Phys.*, A645:145–174, 1999.

- [29] D. Drechsel, S.S. Kamalov, and L. Tiator. An online version of the numerical program for [28] is accessible at <http://www.kph.uni-mainz.de/MAID/maid2003/maid2003.html>.
- [30] D. Drechsel and L. Tiator. Threshold pion photoproduction on nucleons. *J. Phys.*, G18:449–497, 1992.
- [31] D. Drechsel and L. Tiator, editors. *Proceedings of the Workshop on the Physics of Excited Nucleons*. World Scientific, 2001.
- [32] S. Eidelman et al. Review of particle physics. *Phys. Lett.*, B592:1, 2004.
- [33] D. Elsner et al. Measurement of the LT-asymmetry in electroproduction at the energy of the (1232)-resonance. *Eur. Phys. J.*, A27:91–97, 2006.
- [34] Bernard T. Feld. *Models of Elementary Particles*. Blaisdell Publishing Company, 1969.
- [35] Richard E. J. Florizone. *The Longitudinal and Transverse Response of the $(e, e'p)$ reaction in Helium-3 and Helium-4 in the Quasielastic Region*. PhD dissertation (unpublished), Massachusetts Institute of Technology, 1999.
- [36] J. Friedrich and T. Walcher. A coherent interpretation of the form factors of the nucleon in terms of a pion cloud and constituent quarks. *Eur. Phys. J.*, A17:607–623, 2003.
- [37] V. V. Frolov et al. Electroproduction of the Delta(1232) resonance at high momentum transfer. *Phys. Rev. Lett.*, 82:45–48, 1999.
- [38] Tobias A. Gail and Thomas R. Hemmert. Signatures of chiral dynamics in the nucleon to Delta transition. 2005.
- [39] Sheldon L. Glashow. The unmillisonant quark. *Physica*, A96:27–30, 1979.
- [40] R. Gothe. *Proceedings of the Workshop on the Physics of Excited Nucleons*. World Scientific, 2001.

- [41] H. W. Hammer and Ulf-G. Meissner. Updated dispersion-theoretical analysis of the nucleon electromagnetic form factors. *Eur. Phys. J.*, A20:469–473, 2004.
- [42] K. Herter. *Entwicklung und Erprobung eines Verfahrens zur Messung der absoluten Energie des Elektronenstrahls von MAMI*. Diploma thesis (unpublished), Insitute fuer Kernphysik, Universitaet Mainz, 1992.
- [43] Nathan Isgur, Gabriel Karl, and Roman Koniuk. D waves in the nucleon: A test of color magnetism. *Phys. Rev.*, D25:2394, 1982.
- [44] F. James and M. Roos. 'MINUIT' A system for function minimization and analysis of the parameter errors and correlations. *Comput. Phys. Commun.*, 10:343–367, 1975.
- [45] K. Joo et al. Q^2 dependence of quadrupole strength in the $\gamma^* p \rightarrow \Delta(1232)^+ \rightarrow p \pi^0$ transition. *Phys. Rev. Lett.*, 88:122001, 2002.
- [46] S. S. Kamalov, Guan-Yeu Chen, Shin-Nan Yang, D. Drechsel, and L. Tiator. π^0 photo- and electroproduction at threshold within a dynamical model. *Phys. Lett.*, B522:27–36, 2001.
- [47] S. S. Kamalov and Shin Nan Yang. Pion cloud and the Q^2 dependence of $\gamma^* N \longleftrightarrow \Delta$ transition form factors. *Phys. Rev. Lett.*, 83:4494–4497, 1999.
- [48] C. Kunz. *Simultaneous Measurement of the R_{TL} , $R_{TL'}$ and $R_T + \epsilon R_L$ Responses of the $H(\vec{e}, e'p)\pi^0$ Reaction in the $\Delta(1232)$ Region*. PhD dissertation (unpublished), Massachusetts Institute of Technology, 2000.
- [49] C. Kunz et al. Measurement of the transverse-longitudinal cross sections in the $p(e(\text{pol.}), e' p)\pi^0$ reaction in the Delta region. *Phys. Lett.*, B564:21–26, 2003.
- [50] W. R. Leo. Techniques for nuclear and particle physics experiments: A how to approach. Berlin, Germany: Springer (1987) 368 p.

- [51] Earle L. Lomon. Effect of recent $R(p)$ and $R(n)$ measurements on extended Gari-Kruempelmann model fits to nucleon electromagnetic form factors. *Phys. Rev.*, C66:045501, 2002.
- [52] P. Mergell, Ulf G. Meissner, and D. Drechsel. Dispersion theoretical analysis of the nucleon electromagnetic form-factors. *Nucl. Phys.*, A596:367–396, 1996.
- [53] H. Merkel. Private communication.
- [54] C. Mertz. *The response functions R_{LT} and $R_T + \epsilon_L R_L$ for the $H(e, e'p)\pi^0$ reaction at the $\Delta(1232)$ resonance*. PhD dissertation (unpublished), Arizona State University, 1998.
- [55] C. Mertz et al. Search for quadrupole strength in the electro-excitation of the $\Delta(1232)^+$. *Phys. Rev. Lett.*, 86:2963–2966, 2001.
- [56] Mickey, Dunn, and Clark. *Applied Statistics*. John Wiley and Sons, 2004.
- [57] Luke W. Mo and Yung-Su Tsai. Radiative corrections to elastic and inelastic $e p$ and μp scattering. *Rev. Mod. Phys.*, 41:205–235, 1969.
- [58] J. W. Negele. What we are learning about the quark structure of hadrons from lattice QCD? 2005.
- [59] NIST. <http://webbook.nist.gov/chemistry/fluid/>.
- [60] Vladimir Pascalutsa and Marc Vanderhaeghen. Electromagnetic nucleon to Delta transition in chiral effective-field theory. *Phys. Rev. Lett.*, 95:232001, 2005.
- [61] Vladimir Pascalutsa and Marc Vanderhaeghen. Chiral effective-field theory in the $\Delta(1232)$ region: Pion electroproduction on the nucleon. *Phys. Rev.*, D73:034003, 2006.
- [62] M. Pieroth, J. Friedrich, P. Semmel, N. Voegler, John Leroose, and Peter D. Zimmerman. Radiation tail in electron scattering: Approximations in the calculation and comparison to measurements. *Nucl. Inst. Meth.*, B36:263–275, 1989.

- [63] Th. Pospischil et al. Measurement of the recoil polarization in the $p(e(\text{pol.}), e' p(\text{pol.}))\pi^0$ reaction at the $\Delta(1232)$ resonance. *Phys. Rev. Lett.*, 86:2959–2962, 2001.
- [64] William H. Press, Saul A. Teuloksky, William T. Vetterling, and Brian P. Flannery. *Numerical Recipes in C*. Cambridge University Press, 1992.
- [65] A. S. Raskin and T. W. Donnelly. Polarization in coincidence electron scattering from nuclei. *Ann. Phys.*, 191:78, 1989.
- [66] A. W. Richter. *Trennung des longitudinalen, transversalen und longitudinal-transversal interferierenden Anteils des Wirkungsquerschnitts der Reaktion $H(e, e'\pi^+)$ in der Nahe der Pionschwelle*. PhD dissertation (unpublished), Universitaet Mainz, Institut fuer Kernphysik, 1994.
- [67] T. Sato and T. S. H. Lee. Dynamical study of the Δ excitation in $N(e, e' \pi)$ reactions. *Phys. Rev.*, C63:055201, 2001.
- [68] J. Seely. Polynomial fit in Q^2 to form factor database. Private communication, 2004.
- [69] G. G. Simon, C. Schmitt, F. Borkowski, and V. H. Walther. Absolute electron proton cross-sections at low momentum transfer measured with a high pressure gas target system. *Nucl. Phys.*, A333:381–391, 1980.
- [70] S. Simon. www.cmh.edu/stats/definitions/correlation.htm.
- [71] Simon Širca. *The axial form factor of the nucleon from coincident pion electro-production at low Q^2* . PhD dissertation (unpublished), University of Ljubljana, Faculty of Mathematics and Physics, 1999.
- [72] Cole Smith. Private communication.
- [73] N. Sparveris. *Study of the conjecture of a deformed nucleon through the $\gamma^* N \rightarrow \Delta^*(1232)$ reaction*. PhD dissertation (unpublished), University of Athens, 2003.

- [74] N. F. Sparveris et al. Investigation of the conjectured nucleon deformation at low momentum transfer. *Phys. Rev. Lett.*, 94:022003, 2005.
- [75] S. Stein et al. Electron scattering at 4-degrees with energies of 4.5-GeV - 20-GeV. *Phys. Rev.*, D12:1884, 1975.
- [76] Anthony W. Thomas and Wolfram Weise. The structure of the nucleon. Berlin, Germany: Wiley-VCH (2001) 389 p.
- [77] L. Tiator. N to Delta Reaction Calculations with MAID. Hadron Deformation Workshop, MIT, Cambridge, MA, August 7-9, 2004.
- [78] Lothar Tiator and Sabit Kamalov. Maid analysis techniques. 2006.
- [79] Herbert Uberall. *Electron Scattering from Complex Nuclei*. Academic Press, 1971.
- [80] C. Vellidis. *Search for quadrupole strength in the excitation of the $\Delta^+(1232)$ with measurements of response functions in the reaction $H(e, e'p)\pi^0$* . PhD dissertation (unpublished), University of Athens, 2001.
- [81] G. A. Warren et al. Induced proton polarization for π^0 electroproduction at $q^2 = 0.126-(\text{GeV}/c)^2$ around the Delta(1232) resonance. *Phys. Rev.*, C58:3722, 1998.
- [82] Markus Weis. *Elektroproduktion neutraler Pionen und Entwicklung eines Steuerungssystems fuer die Drei-Spektrometer-Anlage am Mainzer Mikrotron*. PhD dissertation (unpublished), Johannes Gutenberg-Universitaet Mainz, Institute fuer Kernphysik, 2003.
- [83] S. S. M. Wong. Introductory nuclear physics. New York, USA: Wiley (1998) 460 p.
- [84] S. N. Yang. DMT Model for Pion Electroproduction. Hadron Deformation Workshop, MIT, Cambridge, MA, August 7-9, 2004.

Acknowledgments

First I would like to thank my parents, Chris and Mary Beth, for always encouraging my interest in science. Many magazine subscriptions, after-school programs, science fairs and summer camps later, here I am. I want to thank my siblings, Sonia, Sasha, and Seth for all they have done over the years. They were very encouraging and willing to listen to a bit of physics. In addition, I thank my grandparents for their love and support. It has been great to have so many people behind me.

Next, I want to thank all my teachers along the way but especially Dewey Beadle for his excellent physics class. The hands-on experiments and intuitive style made physics fun. I hope to teach and when I do, I will be sure to incorporate his style into the class.

Next I must thank Prof. Karl Pitts for the opportunity to work in physics over several summers. I was really able to get a feel for research from the inside through that work and it was very useful. His lab was also a fun one with lots of activity. It really demonstrated that physics should not be done alone but in a group.

Much thanks is due to my adviser, Prof. Aron Bernstein, whose constant guidance kept the experiment and analysis going along. His love of physics shows everyday and his positive attitude is contagious. I know I have learned a great deal from him and I am fortunate to have had such a great teacher. I also want to thank Prof. Costas Papanicolas for all of his guidance as well. He always has his eye on the beauty of the underlying physics and allowing it to shine though. Itaru Nakagawa was very helpful and an excellent guide not only for physics but also during my visit of his home country of Japan. Nikos Sparveris was critical for getting the analysis done in a timely manner. He always cut to the heart of the problem and showed what was

important. I am also thankful to Simon Širca for all his help. He was a constant reminder that there are more subjects than physics in the world. I am lucky to have worked closely with such fine physicists and I thank them all.

Next, I must thank all of the Mainz physicists and students without which the experiment could not have run. I especially thank Michael Distler and Harald Merkel for all of their assistance before, during and after the experiment. Their expert advice clarified many analysis issues and helped to improve the results.

Thank you to the other thesis committee members, Prof. Min Chen and Dr. William Donnelly, for many helpful suggestions over the years. I know that you have helped to improve the experiment and the presentation of the results.

I also thank all my fellow graduate students who were always ready to get cookies or a beer at the end of a long day of analysis. I've known Aaron Maschinot since our days at Kentucky and he was always good for a nice conversation. We spent many lunches and evenings discussing world events which helped to broaden my interests. Jason Seely and Ben Clisie have also always been available for advice or unwinding and for that I thank them. Plus, they always had the right bit of ROOT or L^AT_EX code to solve my problems. It really is the human part of MIT which makes it work and I was lucky to have such nice people around.

I also want to thank my undergraduate buddies Jason Perry and Mark Jones for their continued support throughout my time at MIT. They made the four years at Kentucky fly by and have continued to help me after going their separate ways. Mark especially helped the thesis writing process to be much more bearable.

Before the music begins to play ushering me off the stage, I would like to thank Jean Hager who has always been there for me throughout my time at MIT. Whenever I felt that I couldn't see the finish line, she always gave me a hug and said everything would be fine. Well, with her help, I finally finished and now we can see what other adventures await us.

Biographical Note

Sean Stave was born December 16, 1976 in Akron, Ohio. After graduating from Seneca High School in Louisville, Kentucky in 1995, he attended the University of Kentucky, majoring in Physics. He received his B.S. in Physics from Kentucky in 1999 graduating Summa Cum Laude and started his Ph.D. studies at MIT later that year. In 2003, he lived in Germany for ten months to take the data for this thesis and begin the analysis.